Seismic activity near Ulannbaatar : implication for seismic hazard assessment

Munkhsaikhan Adiya

To cite this version:

Munkhsaikhan Adiya. Seismic activity near Ulannbaatar : implication for seismic hazard assessment. Geophysics [physics.geo-ph]. Université de Strasbourg, 2016. English. NNT : 2016STRAH007 . tel-01443798

HAL Id: tel-01443798
https://theses.hal.science/tel-01443798

Submitted on 23 Jan 2017

UNIVERSITÉ DE STRASBOURG

ÉCOLE DOCTORALE: Sciences de la terre et Environnement ED 413

UMR7516 Institut de Physique du Globe de Strasbourg

Thèse présentée par:

Munkhsaikhan ADIYA

Soutenue le: **29 Septembre 2016**

Pour obtenir le grade de:

Docteur de l'université de Strasbourg

Discipline/ Spécialité: Science de la terre/Géophysique

Activité sismique de la région d'Oulan Bator : Implication pour l'évaluation de l'aléa sismique

Seismic activity near Ulaanbaatar : Implication for seismic hazard assessment

THÈSE dirigée par:

Dr. Jérôme VAN DER WOERD	Université de Strasbourg-Unistra

RAPPORTEURS:

Prof. Jacques DÉVERCHÈRE	Université de Bretagne Occidentale -UBO
Dr. Anne DESCHAMPS	Université de Sophia Antipolis - Géoazur

AUTRES MEMBRES DU JURY:

Dr. Antoine SCHLUPP	Université de Strasbourg – Unistra (Co-encadrant)
Dr. Laurent BOLLINGER	CEA/DIF/DASE/LDG

Table of contents

Acknowledgements

Firstly, I would like to express my deepest thanks to my successive PhD supervisors Dr.Catherine Dorbath, from 2010 to 2015, Dr.Jérôme Van Der Woerd, from 2015 to 2016, and Dr.Antoine Schlupp, co-supervisor all along my PhD, for their continuous supports and valuable advises in my thesis.

I am very honored to express my appreciation to my first PhD supervisor, Dr.Catherine Dorbath who accepted me as her student. Her consecutive support, including financial support for my last stay at Strasbourg, and real trust have been encouraging me all the time of my research and writing of this thesis. I was very glad to being her student until her retirement. I thank Dr.Jérôme Van Der Woerd for accepting to follow the end of my PhD.

My sincere thanks are due to my advisor Dr.Antoine Schlupp for his great support, guidance, and valuable advices that made this dissertation possible. This dissertation could not have been written without all his contribution. I could not have imagine having the best advisor and mentor for my PhD study. He is not only served as my advisor but also encouraged and challenged me throughout my academic program. He showed me different ways to approach a research problem and the need to be persistent to accomplish any goal. Also, I am grateful to his wife Nathalie Arnould and Jehanne Bouzy for helping me during my stays in Strasbourg. I would like to express deepest thanks to their generous kind support to me, alike my parents along with me, in every curious moment especially while I had health issues.

Also I would like to express my gratitude and thanks to Dr.Marco Calo. Catherine and Marco gave me all along my PhD their experienced guidance to learn and apply the seismic tomography method for my study.

It has been a wonderful experience and great opportunity to work with them and I can never appreciate Antoine, Catherine and Marco enough for them understanding of the human problems of their student.

Beside my advisors, I would like to thank the rest of my thesis committee: Prof.Jacques Déverchère and Dr.Anne Deschamps who reviewed in details my work and for their insightful comments and encouragement to improve it; and Dr.Laurent Bollinger for its valuables questions and comments. They motivated me to widen my research from various perspectives.

I would like to express my gratitude and thanks to the French Embassy in Mongolia that generously provided me funding for this research by financing me several stays of few months in the laboratory of seismology of EOST at Strasbourg. Without their precious support, and the help of Campus France, it would not be possible to conduct this research.

I would like to express sincere gratitude to our long-term collaborator, Département Analyse, Surveillance, Environnement (DASE) of CEA in France, which supported our institute for the deployment of permanent and mobile seismic stations networks around Ulaanbaatar. These high-qualified data, recording the seismicity near Ulaanbaatar, gave me a great opportunity to do this PhD and to improve our knowledge about this activity.

My sincerely gratitude to the head of the Institute of Astronomy and Geophysics (IAG) of the Mongolian Academy of Sciences (MAS), Prof.Demberel Sodnomsambuu and head of Department of Seismology (DS) of the IAG, Dr.Ulziibat Munkhuu, who gave me great chance to start my PhD study in France and their supporting during the whole period of my study. Many thanks to Dr.Odonbaatar Chimed, head of Laboratory of Seismic Hazard Analysis of the (DS), for its help for the calculation of the seismic scenarios. Also, thanks to my colleagues and friends for the stimulating discussions and for all the fun we have had in the last few years.

Last but not the least, special thanks go to my family. Their love and support made me spiritually throughout writing this thesis and my life in general.

Abstract

Key words: ***Mongolia, Ulaanbaatar, seismic hazard, swarm, velocity model, Double-Difference tomography, Emeelt fault.***

We observe since 2005 a high seismic activity at 10 km from Ulaanbaatar that allowed us to identify a new active fault, Emeelt, on the field.

After computing a 3D velocity model, I applied Double-Difference tomography to obtain a precise localization of earthquakes. They trace at least three parallel branches oriented N147^0 like the fault seen at surface. The seismic activity on the Main Emeelt Fault (MEF) is along at least 15 km, on the West and East branches, less active, along 10 km. The depth of the seismicity extends between 4 and 15 km. The activity seems concentrated at the intersection with Mesozoic faults and Vp/Vs contrast suggests the presence of fluids. The 10 swarms identified show an increasing activity and a spatial migration with time.

The calculation of 2 possible scenarios, one M ~ 6.4 and one M ~ 7, shows an important impact on Ulaanbaatar, with a minimum intensity of VIII and IX for M=6.4 and X for M=7

Introduction

Mongolia is a landlocked country, which covers an area of about 1.57 million square kilometers bordered by the Russian Federation to the north, the People's Republic of China to the east, south and west and Kazakhstan to the west (Figure 0.1). Its vast steppes are the transition between the southernmost fringe of the Great Siberian forest and the northernmost Central Asian deserts. It is one of the world's highest elevated countries with an average elevation of 1580 m above sea level.

Mongolia can be divided into three major topographic zones: the mountain chains that dominate the northern and western areas (the Mongolian Altai and Gobi-Altai Mountains, the Khangai Mountains (Khangain Nuruu), and the Khentiin Mountains (Khentiin nuruu), the basin areas situated between and around them, and the large upland plateau belt that lies across the southern and eastern sectors (Gobi). The Mongolian Altai in the west and southwest constitute the highest and the longest of these ranges. Extending eastward from the Mongolian Altai are the Gobi-Altai Mountains, a smaller range that disappear eastward in the Gobi. To the north, the Sayan Mountain lies along the border with Siberia and Russia. The Khangai Mountains, is a wide mountain at the centre of the country. The top of the range is at about 3700 m, with the highest point at about 4025 m in the northwest. The Khangai has gentle slopes covered with pastureland. The Khentiin Mountains, oriented SW-NE, extends from the SW of Ulaanbaatar into Siberia in the NE. The highest peak reaches about 2800 m, but in general the maximum elevations are about 2130 m. Ulaanbaatar lies at the southwestern edge of the range. Around and between the main ranges lie an important series of basins. The Great Lakes region, with more than 300 lakes, is between the Mongolian Altai, the Khangai, and the mountains along the border with Siberia.

The population of Mongolia reaches about 3.0 million. Mongolia is one of the least densely populated countries of the world, with 1.9 inhabitants per square kilometer.

The capital Ulaanbaatar is the largest city of Mongolia, at an elevation of about 1350 m, along the valley of Tuul River and at the foot of the Bogd Mountain (about 1900 m) (Figure 0.2). Ulaanbaatar is also the economic and industrial center of the country. After a recent growth of population in the capital during the last 20 years, from 700.000 to about 1.3 million inhabitants, today about 46 % of the whole population of Mongolia is concentrated in the capital.

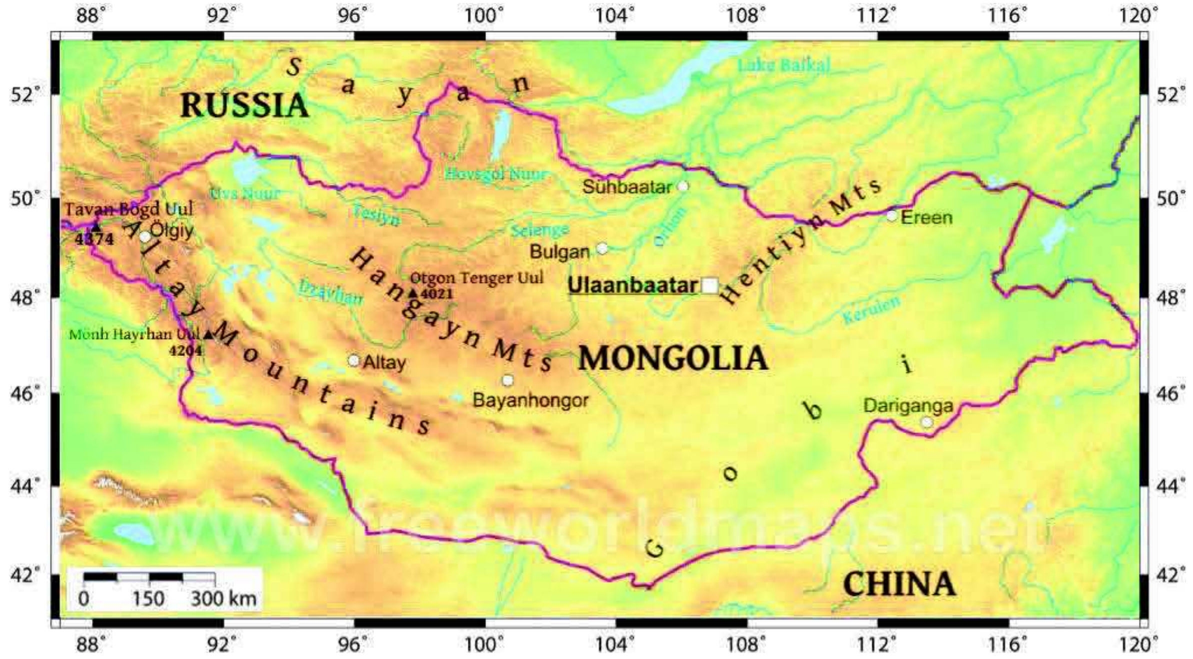

Figure 0.1. Geography of Mongolia.

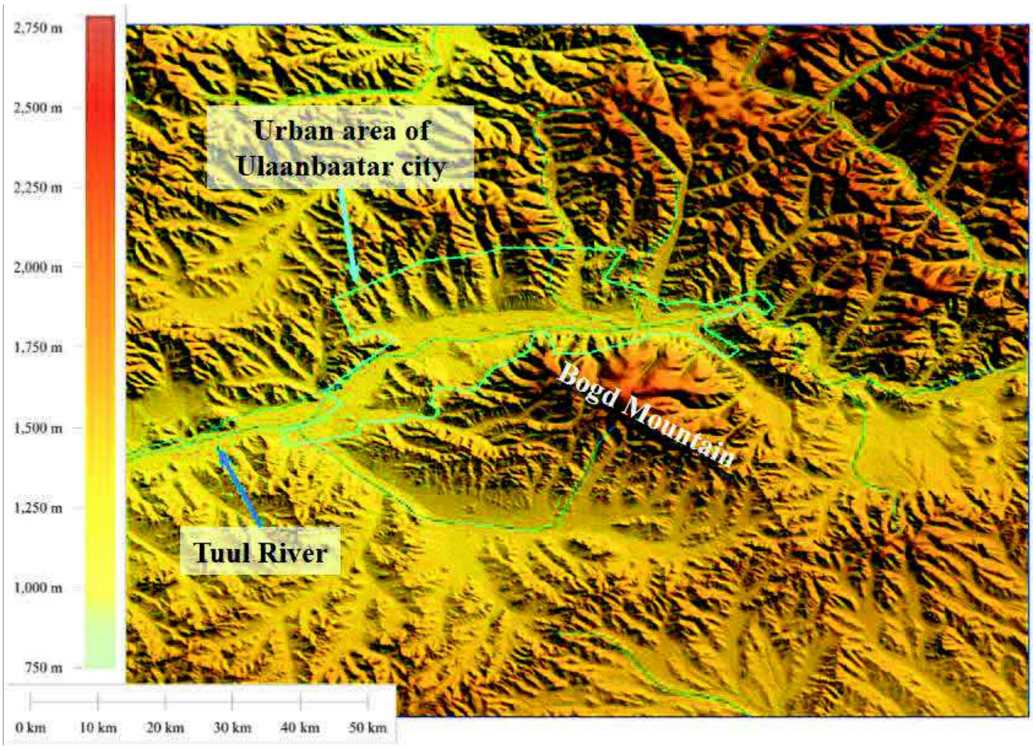

Figure 0.2. Location of Ulaanbaatar city area.

Mongolia is one of the countries in the world affected by large earthquakes (M>8). Seismic hazard estimated in Mongolia is considered of high level (Figure 0.3) but it is surprising that only regions where M>8 occurred last century are with high hazard. The estimation of the probability of future destructive earthquakes in Mongolia is important for human protection and economic stability and cannot be limited to this global view. Moreover the seismic hazard assessment for Ulaanbaatar, where stakes are concentrated, is a target of first importance. It is necessary for citizens and authorities to decide what is the adapted protection that they have to consider (building code, earthquake preparedness, safety and rescue organization, etc).

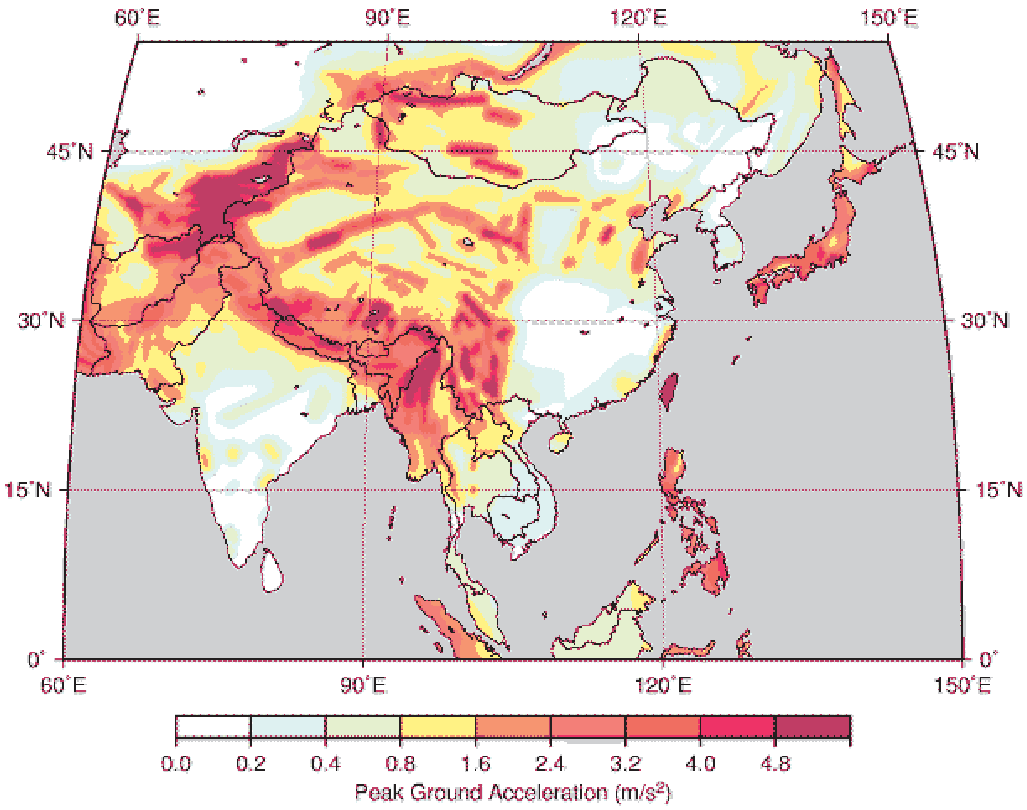

Figure 0.3. Seismic hazard map of East-Asia (from Global Seismic Hazard Assessment Program).

Seismic hazard assessment depends on parameters such as active faults and seismic activity, attenuation of seismic waves with distance and site effects. One crucial information for seismic hazard analysis is the identification of active faults and their seismic activity. Strong earthquakes occur along active seismic structures, the maximum possible event on them is related to the length of the fault, relation that has been studied in details, for instance, by Wells and Coppersmith (1994). The earthquakes are today recorded by seismic networks, and in the last centuries, they are known by the description of their effects (macroseismic information). But older events, even very large ones, are unknown. Therefore, scientists search for traces of active faults and for evidence of their previous activity. The only way is to identify active faults by morphotectonic approaches followed by paleoseismic trenching to recover their seismic activity. Therefore, the identification of active faults in the capital region and their seismic potential is of primary importance for the seismic hazard assessment and the civil protection of Ulaanbaatar.

In April of 2005, we started to observe new seismic activity to the west of the capital less than 10 km from the urban area and 3 km to the north of the international airport. Due to this activity, initial relocation has been done at the Institute of Astronomy and Geophysics (IAG) (Ulziibat Munkhuu) to precise the area of interest. Then we organized, with a French team, a field survey in the area of the seismic activity observed in 2008. Ulziibat Munkhuu (IAG) and Antoine Schlupp (EOST) discovered eroded surface paleo-ruptures, consistent with the seismicity, that characterize a new active fault, called the Emeelt fault. At the site, they observed about 5 to 7 km-long surface ruptures, despite very subdued surface traces. In addition, the seismicity distribution has a length of about 35 km and is, with the available data from NDC, located more to the north and the south of the surface ruptures with the same orientation, i.e. a mean strike of N147. It is clear that in the case of the Emeelt fault, we could not define the whole surface structure related with the seismic activity. Notice that if an earthquake breaks a 35 km-long fault, the associated magnitude Mw could reach about 6.8-6.9 (Wells and Coppersmith, 1994).

Several questions arise :

- Did this fault break in the past with large magnitude events?
- How precise is the available localization of the seismicity?
- What are the depths of the events?
- Does the extension of seismicity for about 35 km with only 5 to 7 km of surface rupture imply that the other parts are hidden or “blind”?
- How are earthquakes generated and distributed along the Emeelt fault?
- What is the evolution of the characteristics of the seismicity with time?
- What can we learn from the numerous small events recorded in the area?

To answer these questions, except the first one for which paleoseismic investigations are necessary, we need to get very precise localizations of the seismicity in the area, which will be an important part of my work during my PhD. For example, it is possible to identify a fault area based on the precise earthquakes distribution with depth, if an active fault did not produce surface ruptures or if they have been eroded. However, the precise localization of the seismicity in the fault area depends on a well-constrained crustal 3D velocity structure. For this purpose, we used the method of local earthquake tomography to better constrain the 3D structure. This method has been applied in many studies before, as for example: Thurber et al., 2003; Tomomi et al., 2006; Jeanne et al., 2007; Nakamichi et al., 2007; Dorbath et al., 2008; Moretti et al., 2009; Pei et al., 2010; Nugraha et al., 2013; etc...

Therefore, in my PhD, I will apply the TomoDD method to better identify the fault area and to characterize the seismic activity of the Emeelt fault zone.

Finally, the goal of my PhD research is to understand the space and time evolution of the seismicity in the Emeelt fault area using the TomoDD method and to analyze the implication for the seismic hazard assessment of Ulaanbaatar. Answers to these questions are awaited by the authorities as well as by the citizens.

This work is the continuation of several studies, done in the frame of the French-Mongolian scientific cooperation, with Dr. Antoine Schlupp, in order to improve the seismic hazard assessment of Ulaanbaatar.

The methodology of the study

The aim of this study is to chracterize the 3D velocity structure around the Emeelt fault and the structure itself using seismic events that occurred in the area. The methodology is summarized hereunder.

I will first present the geological and tectonic context (Chapter 1) and describe the observed seismicity in Mongolia and around the Emeelt area (Chapter 2). Second, I will constrain a one-dimensional (1D) velocity model for the area (Chapter 3). Then, the TomoDD procedure is applied on the recorded seismicity to get a three-dimensional (3D) velocity model and precise localization of the seismicity around the Emeelt fault (Chapter 4). Then, with the precise location, I discuss the space and time evolution of the seismicity and the relation with the known active faults in the area and the implication for the seismic hazard of Ulaanbaatar (Chapter 5) (Figure 0.4).

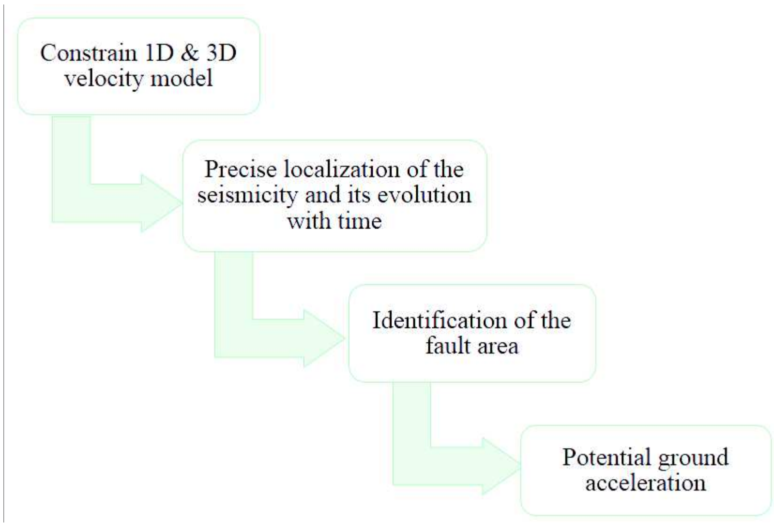

Figure 0.4. Workflow diagram for the characterization of active faults in the study area

To constrain the 1D & 3D velocity structure of the study area, I applied the following methodology :

- the solutions of three-dimensional seismic tomography are obtained by solving the coupled hypocenter locations-velocity model inverse problem, which is highly dependent on the data quality and on the 1-D reference velocity model (Kissling et al., 1994). I constrain a 1D velocity model using earthquake data, recorded by seismic stations in and around Ulaanbaatar area (see chapter 3).

- for the 3D inversion, I use the results from the 1D inversion (1D velocity model) and I find a 3D velocity structure of the study area (see chapter 4). The seismic swarms of Emeelt fault area are an ideal case for conducting a local seismic tomography study, as they have frequent earthquakes and dense stations coverage. I used the tomoDD code, developed by Zhang and Thurber (2003), which provides highly resolved Vp and Vs models and hypocenter locations. The tomoDD software, based on the HypoDD location code of Waldhauser & Ellsworth (2000), calculates local velocity structures using a double-difference method. The advantage of tomoDD is that it uses relative arrival times with their quality values together with absolute arrival times.

With the precise earthquakes location, I am able to determine the minimum subsurface rupture length and width of the Emeelt fault, and then to discuss the potential magnitude of events on the Emeelt fault, and to calculate some ground motion parameters at specific points of Ulaanbaatar.

1 Chapter 1: Geological and tectonic context

1.1 Geological context of Mongolia

Mongolia is located in the Central Asian Orogenic Belt (CAOB) (Kröner et al., 2007) (Figure 1.1). The CAOB is a wide region situated between the Siberian craton to the north and the Sino-Korean and Tarim cratons to the south. It corresponds to large accretionary terrains, which record an about 800 Ma history of arc and microcontinent accretions, from south to north (Kröner et al., 2007). The broad history of this huge territory is now reasonably well understood but there are still major unanswered questions such as the rate and volume of crustal growth, the origin of the continental fragments, the detailed mechanism of accretion and collision, the role of terrane rotations during the orogeny, and the age and composition of the lower crust.

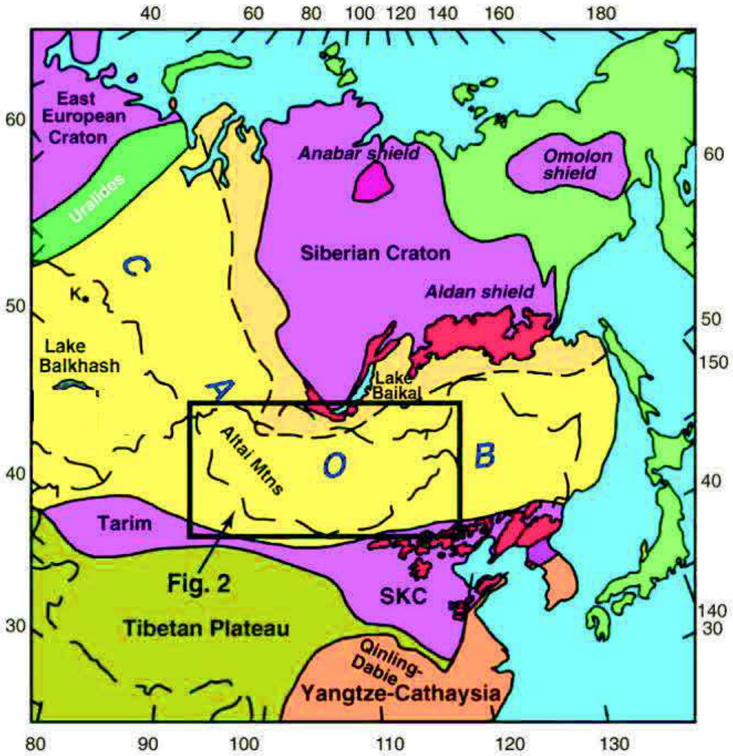

Figure 1.1. Simplified tectonic divisions of central Asia. Red areas are exposed Archean to Paleoproterozoic rocks. Yellow-brown area surrounding Siberian craton is late Meso- to Neoproterozoic part of the CAOB. Brown area is Paleo- to Neoproterozoic Yangtze-Cathaysia craton. Green pattern, including the Japanese islands, represents Pacific fold belts. K—Kokchetav (in northern Kazakhstan); SKC—Sino-Korean craton. CAOB=The Central Asian Orogenic Belt (after Kröner at al., 2007). Black rectangle represents location of Mongolia.

Overall the CAOB records the formation of small forearc and backarc ocean basins that probably evolved between island arcs and microcontinents and were closed during continuous accretion between the Neoproterozoic and Paleozoic.

Due to this geological history, we can observe at the surface in Mongolia that is located inside the CAOB, a variety of rock types and structures, which are representative of all geological ages from Precambrian to Quaternary.

Mongolia is traditionally subdivided into two tectonic domains, a northern and a southern one, separated by the so-called Main Mongolian Lineament – an approximate regional topographic and structural boundary separating dominantly Precambirian and Lower Paleozoic rocks to the north, from dominantly Lower to Upper Paleozoic rocks to the south (black bold line in Figure 1.2) (Badarch et al., 2002; Zorin et al., 2002; Minjin et al., 2006).

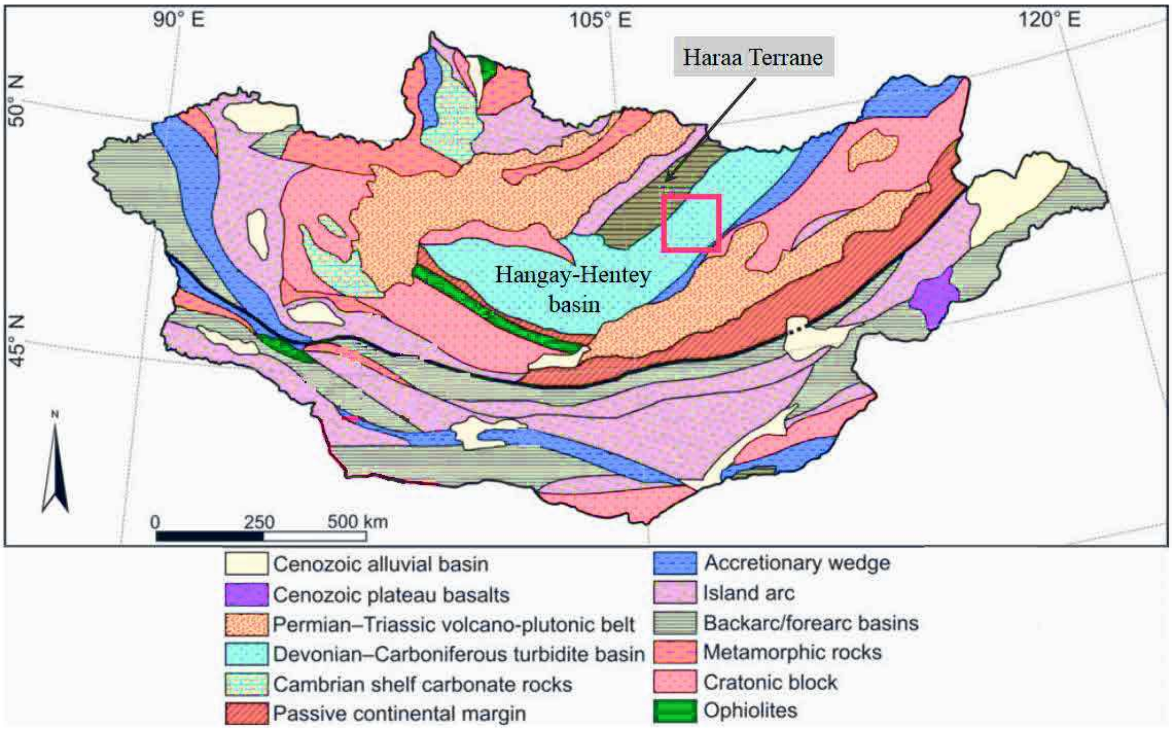

Figure 1.2. Geological subdivision of Mongolia (after Badarch et al., 2002). Study area is delineated by red square.

The northern domain is usually classified as"Caledonian" and contains Proterozoic to lower Paleozoic terranes composed of a collage of island-arc volcanic, ophiolitic, granitic, and volcanoclastic sedimentary rocks. They are interpreted to be the product of island arc collisions and active margin accretions that occurred through subduction of oceanic plates beneath the Siberian Craton.

The southern domain is composed of an assemblage of lower to middle Paleozoic arc-related volcanic, volcanoclastic sediments, ophiolite terranes, serpentinite mélanges, and fossiliferous limestone rocks all of which have been intruded by granitic plutons and covered by Mesozoic non-marine (molasse) sedimentary rocks.

More recently, during past decades, several researchers considered the geology of Mongolia in term of a collage of many tectonostratigraphic terranes. Badarch et al. (2002) has divided Mongolia into forty-five terranes that are grouped into eight different categories or zones : cratonal blocks, passive continental margins, metamorphic rocks of uncertain tectonic origin, island arcs, backarc/forearc basins, accretionary wedges, ophiolites, and volcanic/sedimentary overlap assemblages (Figure 1.2). Interestingly the boundaries of these terranes can be associated to fault zones that are in some case reactivated during subsequent tectonic events, and the previous structuration of Mongolia plays probably a role into the present-day location of large active faults. Some terrane boundaries are concealed by younger cover rocks, intrusions, and alluvial sediments and are thus located only approximately (Badarch et al., 2002).

1.2 Active tectonics and recent seismicity

1.2.1 Indo-Asian collision and large faults in Mongolia

The Central Asian deformation domain has been described since the seventies and numerous studies by different researchers explain that the active deformation and active fault systems of western and central Mongolia are dominantly the result of the India-Eurasia collision (Tapponnier and Molnar, 1979).

The Indo-Eurasian convergence-collision generated large en-échelon right-lateral strike-slip faults to the west and left-lateral strike-slip faults in the east, inducing eastward “block-extrusion” accommodating lateral displacements between these blocks (Figure 1.3).

Central Asia is characterized by large intracontinental basins that include the Tarim and Junggar basins, separated by intracontinental orogens such as the Tien Shan and north of it the Altai Sayan, Mongolian Altai, Gobi-Altai, and intracontinental rift zones such as the Baikal rift system.

The eastward to southeastward motion of central and eastern Mongolia is accommodated by left-lateral slip on the E-W trending Tunka, Bulnai, and Gobi-Altai faults (2 ± 1.2, 2.6 ± 1.0, and 1.2 mm/yr, respectively) and by about 4 mm/yr of extension across the Baikal rift zone. Present active tectonic deformation in Mongolia results from the far field effects of the India-Eurasia collision zone.

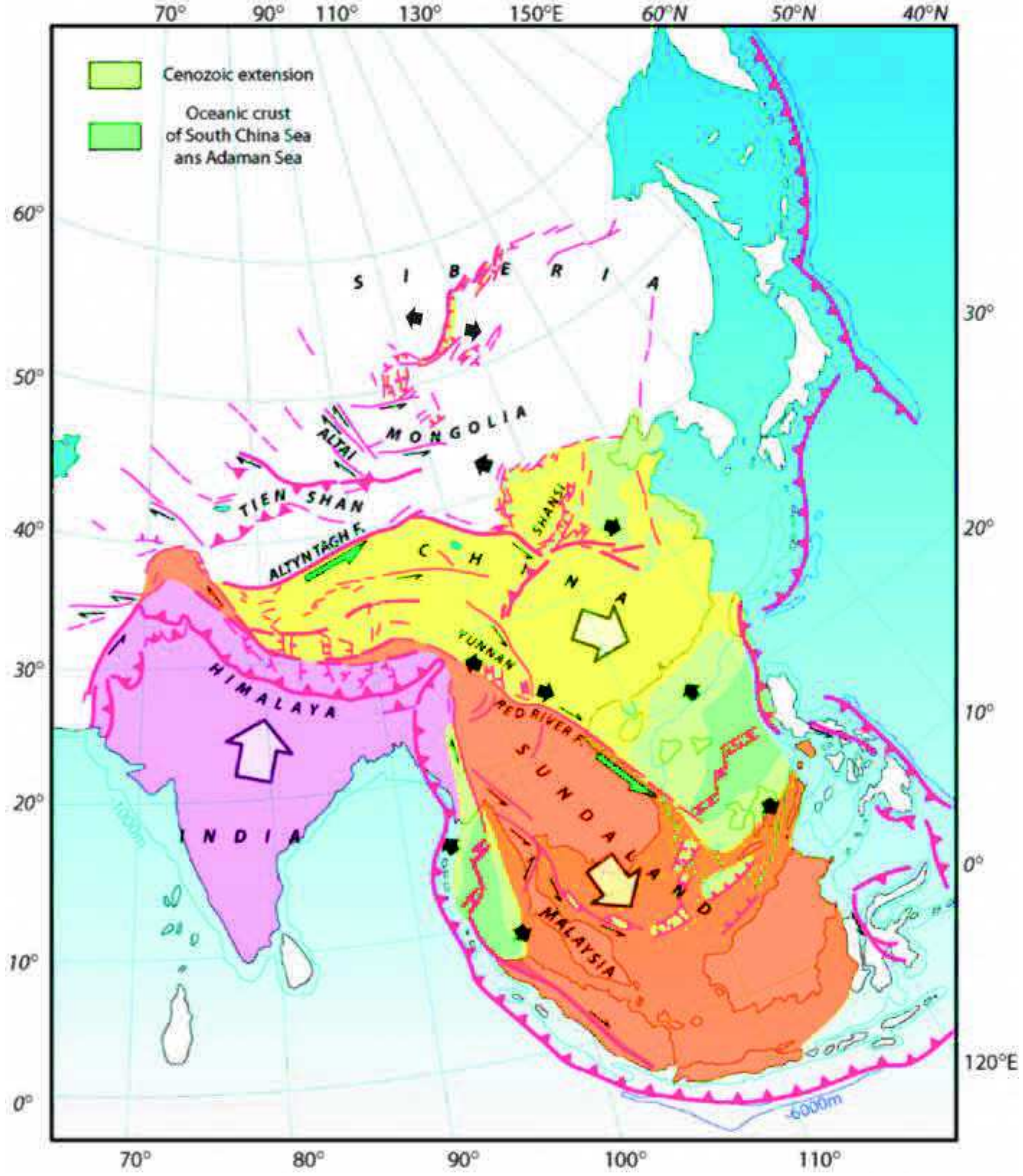

Figure 1.3. Schematic map of regional tectonics (Cenozoic extrusion) and large faults in eastern Asia. White arrows represent qualitatively major block motions with respect to Siberia. Black arrows indicate direction of extrusion-related extension (after Tapponnier et al., 1982).

The present deformation is highlighted by continuous global positioning system (GPS). Clearly, we observe the India-Asia collision with aconvergence of about 4 cm/yr (Calais et al., 2006) and the present extrusion of the South China block at 1cm/yr.

In central Asia ,first GPS observations started in 1994. They show that all the deformation in Mongolia is much smaller than the regions south of it (Figure 1.4) (Calais and Amarjargal, 2000; Calais et al., 2003; Calais et al., 2006).

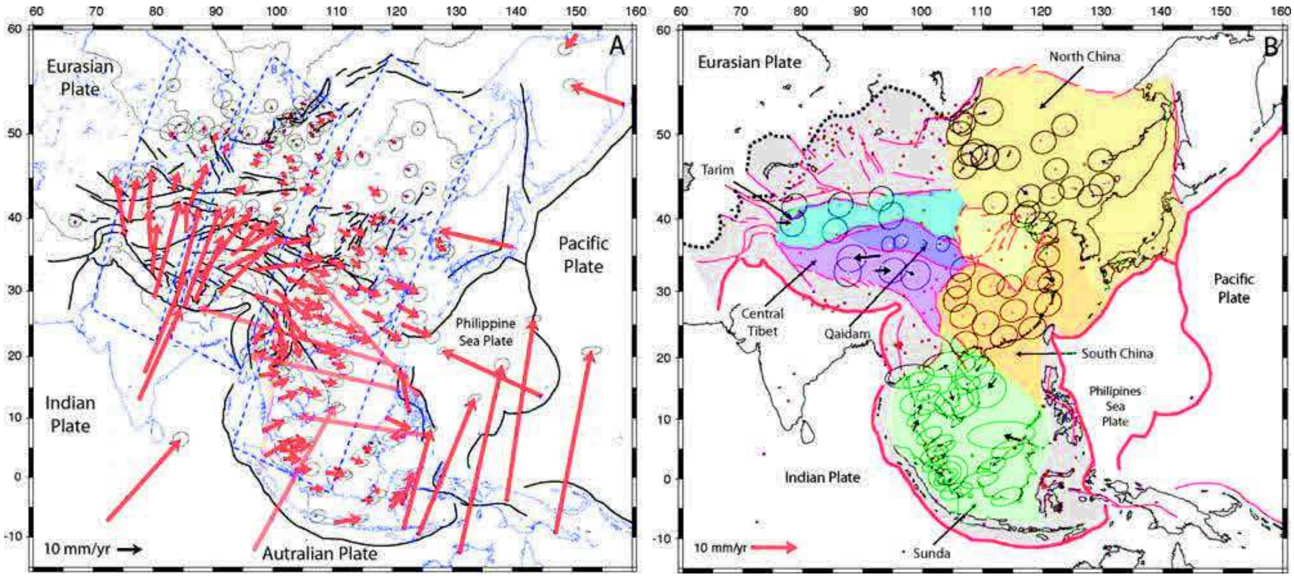

Figure 1.4. (A) Horizontal GPS velocities shown with respect to Eurasia. Large velocities at sites on adjacent plates are shown transparent for a sake of readability. (B) Residual velocities after subtracting rigid block rotations. Dots show locations of all GPS sites. Major blocks are shown with colour backgrounds. White areas are not included in analysis. Error ellipses are 95% confidence interval on both figures (after Calais et al., 2006).

Calais et al. (2003) indicate that 15% of the India-Eurasia convergence is accommodated north of the Tien Shan by N-S shortening combined with dextral shear in the Mongolian Altai and by eastward displacements along major left-lateral strike-slip faults in central and eastern Mongolia (Figure 1.8).

1.2.2 Seismic activity at the scale of Mongolia

This active deformation in Western and Central Mongolia leads to high seismicity throughout the region and the occurrence of strong earthquakes. Western Mongolia has been the most seismically active intracontinental region in the world during the last century where four earthquakes of magnitude 8 and greater (Appendix 1) have occurred (Bulnai 1905/07/09, Tsetserleg 1905/07/23, Altai/Fu-Yun 1931/08/10 and Gobi-Altai 1957/12/04). They ruptured three major fault systems for about nine hundred kilometres (Figure 1.5). These events are associated with coseismic displacement along the faults between 5 and 12 m (Baljinnyam et al., 1993; Schlupp, 1996; Schlupp and Cisternas, 2007; Klinger et al., 2011; Choi et al., 2012).

The recurrence period estimated of these large earthquakes is more than 3000 yrs related to the low deformation rate along the faults (estimated between 1 to 3 mm/yr, Ritz et al., 2003, 2006 ; Calais et al., 2003 ; Vergnolle et al., 2003 ; Rizza et al., 2015). The cumulative deformation along these faults show that the return period of such great earthquakes are between ~2700-4500; 3000-

4000 yrs for Gobi-Altai (Ritz et al., 2006), 4500 yrs (Calais et al., 2003) and ~2700-4000 yrs for Bulnai (Rizza et al., 2015). Active faults are numerous and large but the occurrence of these four large earthquakes in less than one century are unusually high (Schlupp, 1996).

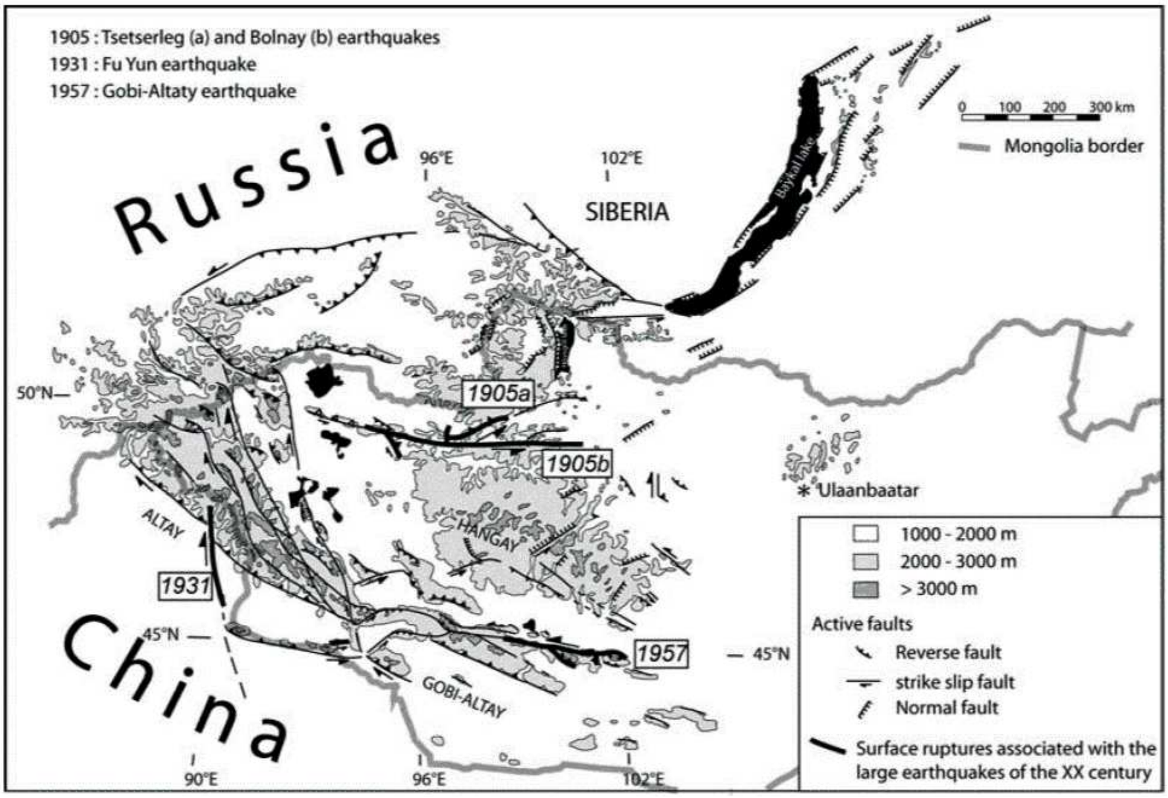

Figure 1.5. Main active faults in Mongolia and large earthquakes of the XXth century (after Schlupp and Cisternas, 2007).

Postseismic relaxation gradually causes a significant stress change (0.1-0.9 bar) over large distances. Using a spring-slider model to simulate earthquake interaction and it is shown that viscoelastic stress transfer may be responsible for the earthquake time clustering observed in active tectonic areas (Chery et al., 2001).

Vergnolle et al. (2003) proposed that the occurrence of these and many other smaller earthquakes are related and controlled to a large extent by stress changes generated by the compounded static deformation of the preceding earthquakes and subsequent viscoelastic relaxation of the lower crust and upper mantle beneath Mongolia.

1.2.3 Main characteristics of large active faults and seismicity of western and central Mongolia

1.2.3.1 Bulnai:

In 1905, two strong earthquakes with magnitude Mw≥8 occurred to the north of Khangai (Figure 1.5, Figure 1.6 and Figure 1.7).

The first one, the Tsetserleg earthquake, occurred the 9 July 1905. It produced clear 130 km-long surface ruptures, oriented about N60^0, with left lateral strike-slip with a reverse component. Schlupp and Cisternas (2007), based on the source inversion of these two events, indicate that the total rupture length of the Tsetserleg earthquake could have reached 190km (in an area difficult to reach), and they estimated a magnitude, by body waves inversion, of Mw=8 (Figure 1.6).

The second one, bigger than the first, occurred 2 weeks later (23 July 1905) and induced surface ruptures over a length of 375 km on the main fault with a left lateral strike slip component and horizontal displacement measured up to 11±2 m (Florensov and Solonenko, 1965; Baljinnyam et al., 1993; Schlupp and Cisternas, 2007).

The most recent work using 1905 historical seismic records and with source inversion (Schlupp and Cisternas, 2007) indicates that the Bolnay earthquake nucleation was at the intersection between the main fault (EW, 375 km of left lateral strike-slip) and the Teregtiin fault (N160, 80 km of right lateral strike-slip with a vertical component near the intersection with the main fault). They precise that the rupture was bilateral along the main fault: 100 km to the west and 275 km to east. It also propagated 80 km to the southeast along the Teregtiin fault. The moment magnitude Mw obtained with the inversion varies between 8.3 and 8.5.

The ruptures associated to the Tsetserleg earthquake reached the middle part of the main fault that ruptured two week later during the Bolnay great event.

Morphotectonic analyses carried out at three sites along the eastern part of the Bolnay fault allowed estimating a mean horizontal slip rate of 3.1±1.7mm/year over the Late Pleistocene–Holocene period and paleoseismological investigations show evidence for two earthquakes prior to the 1905 event, with a recurrence intervals of ~2700-4000 yrs (Rizza et al., 2015).

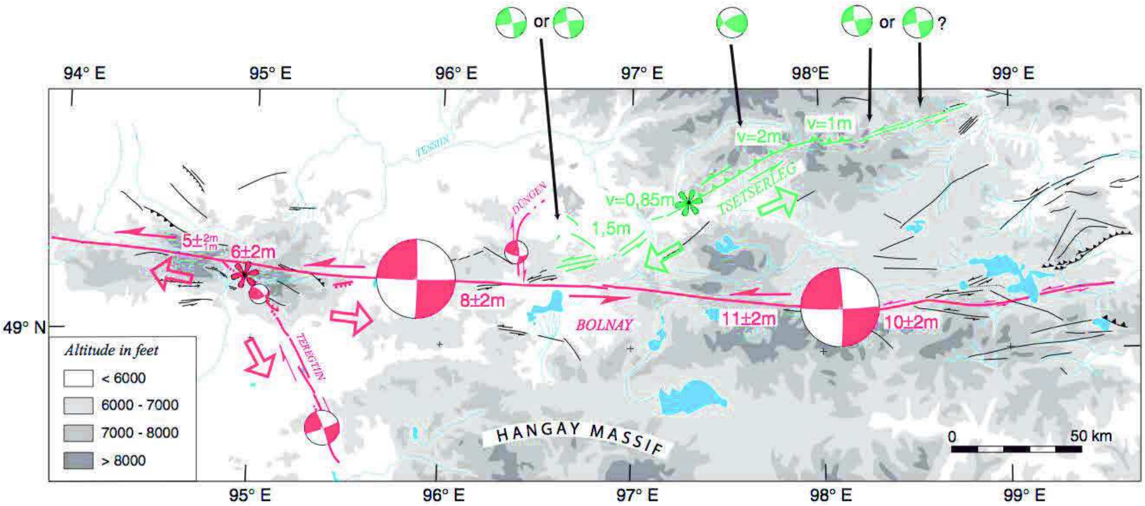

Figure 1.6. Surface ruptures, epicentre (star), focal mechanism of each segment, and rupture propagation direction (open arrows) for Tsetserleg (green) and Bolnay (red) earthquakes (after Schlupp and Cisternas, 2007).

The observed seismicity since 1964 shows that the highest activity is still along the Tsetserleg and Bolnay earthquake ruptures. It characterizes late aftershocks of the two 1905 events (Sodnomsambuu et al., 2014) (Figure 1.7).

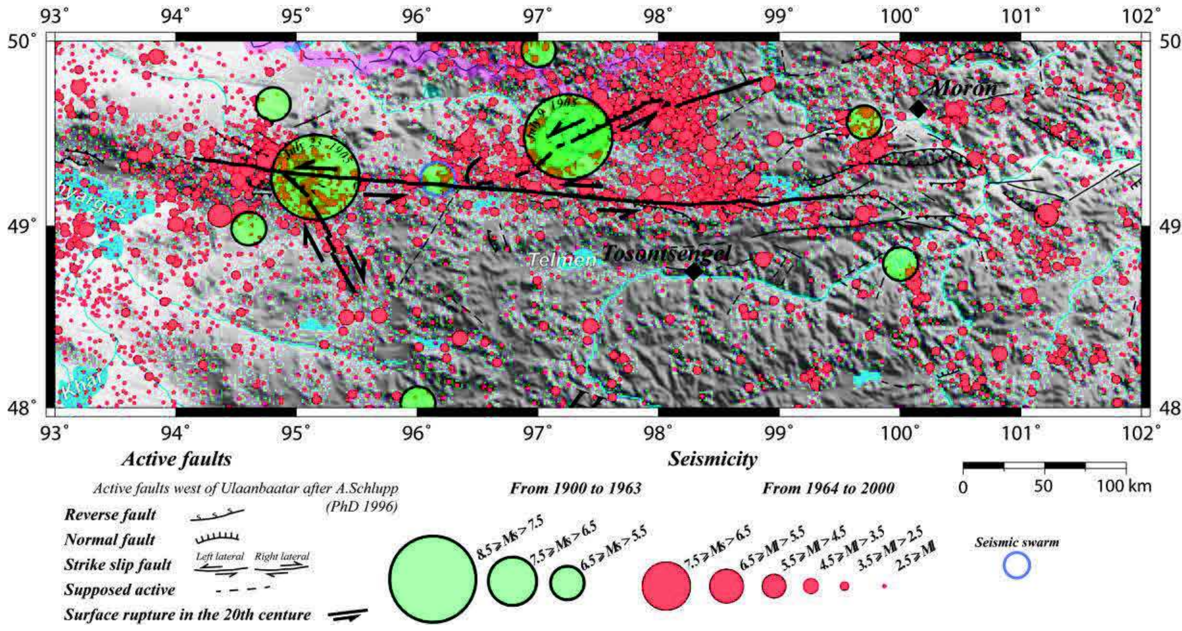

Figure 1.7. Seismicity observed between 1900 and 2000 (In Green for July 1905 after Schlupp 1996 and Schlupp and Cisternas 2007, in red with the network of Mongolia since 1964) in the area of Tsetserleg and Bolnay faults (modified from "One century of seismicity in Mongolia [1900-2000]).

1.2.3.2 Altai:

The deformation of the Mongolian Altai is dominated by active NW striking thrust faults and NNW right lateral strike-slip faults. On average, the major strike slip fault systems are separated by

25±5 km and intervening areas appear tectonically inactive, like non deformed blocs, at the surface (Cunningham et al., 2003). The beginning of the deformation is estimated at about 1 to 5 Ma ago (Vassalo, 2006).

Munkhuu (2006) described in details the active faults of Altai with the main right-lateral strike-slip faults of the range (Khovd, Tolbo, Sagsai) as well as, to the south of the Altai range, the left-lateral strike-slip faults associated with reverse slip (Bulgan, Sharga) (Figure 1.8). He observed cumulated horizontal displacement on the largest faults between 1.4 and 4.8 km. Several late Quaternary surface ruptures, or paleodislocations, are known. They were produced by large earthquakes along Chihtei, Sagsai, Ar-Hotol and Bulgan segments (Munkhuu, 2006).

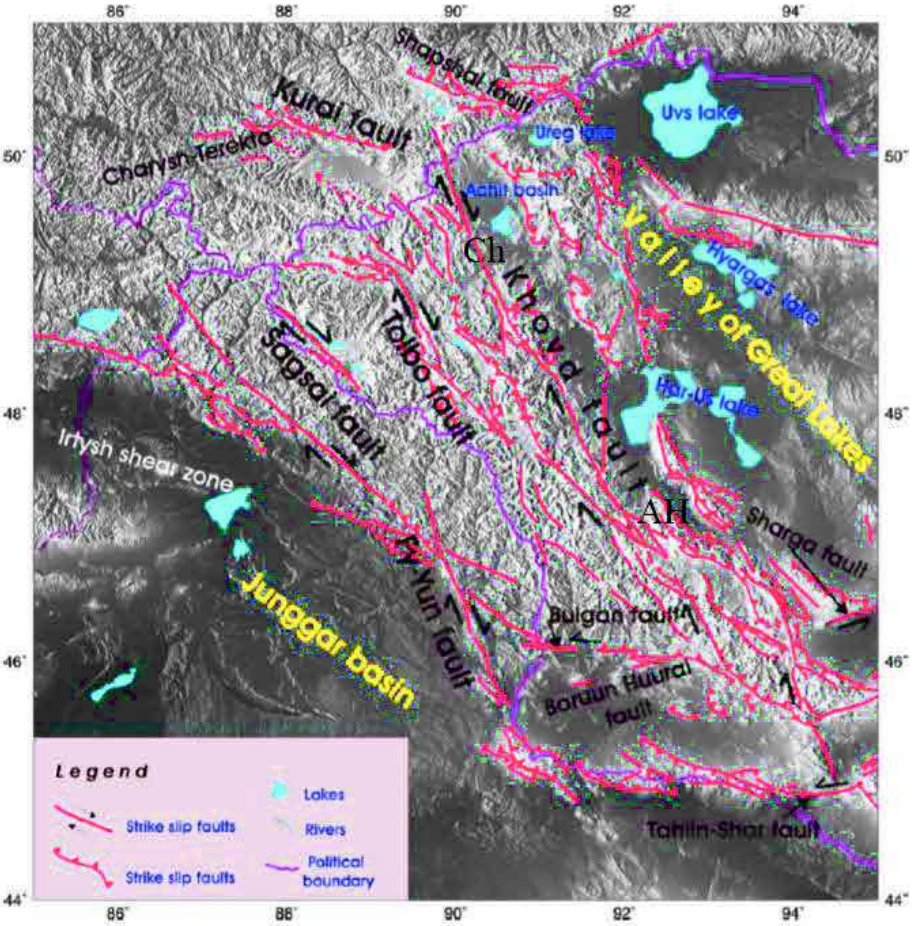

Figure 1.8. Main active structures of Mongolian Altai interpreted using SPOT and Landsat satellite images overlapped on GTOPO30 topography (Ch = Chihtei and AH = Ar Hotol) (modified from Munkhuu, 2006).

Considering the seismological observations, the Altai region is one of the active regions of Central Asia. Since 1903, 60 earthquakes with magnitude of more than 5.5 occurred and several large earthquakes produced surface ruptures and landslides such as during Fu-Yun (1931, Ms=7.9), Uureg-

Nuur (1970, M_L=7), Takhiin-Shar (1974, M_L=6.9) (Figure 1.9) and Chuya (2003, M_S=7.2) earthquakes (Munkhuu, 2006; Dorbath et al., 2008) (Figure 1.11).

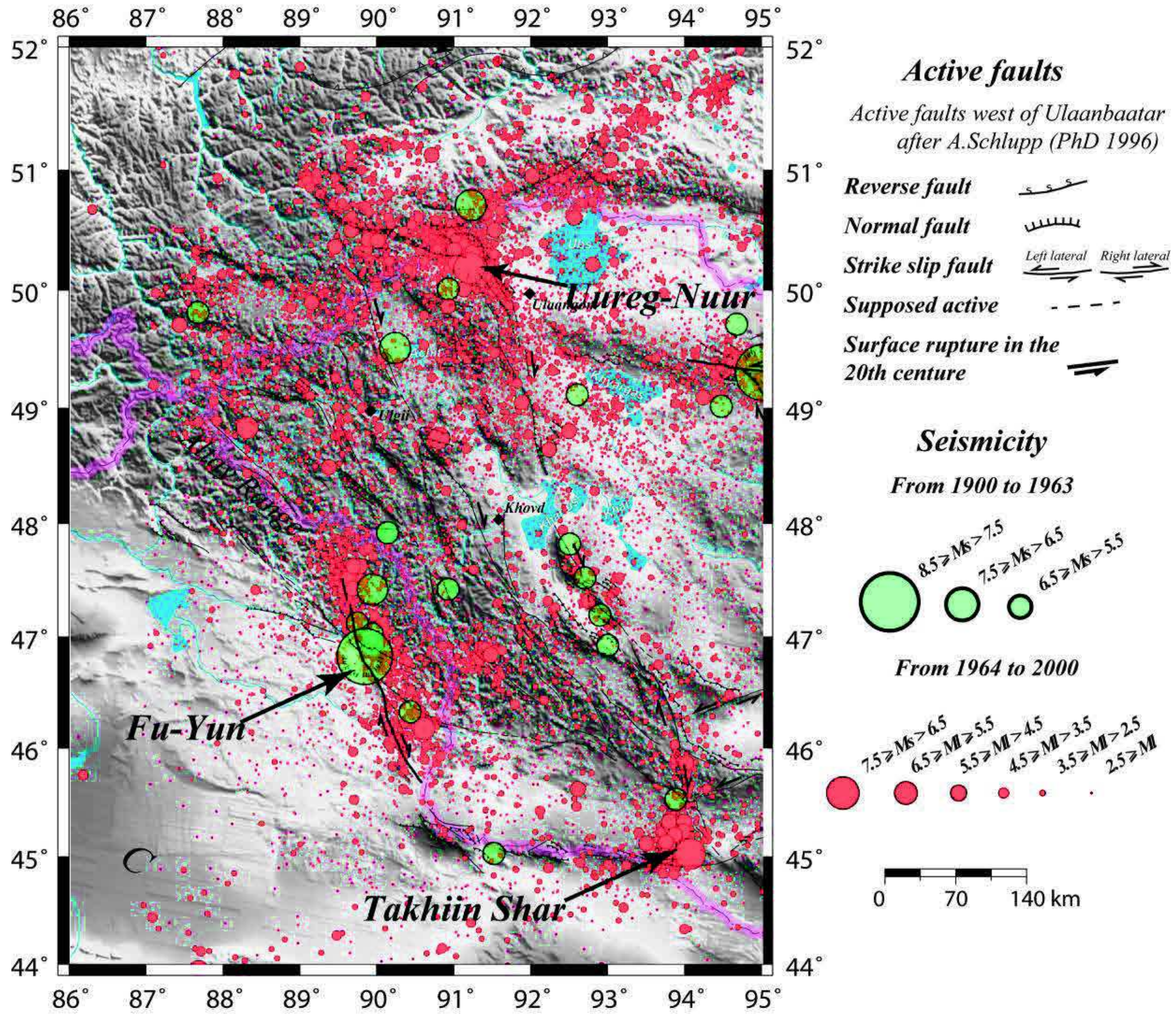

Figure 1.9. Seismicity observed between 1900 and 2000 (in red with the network of Mongolia since 1964) in the area of Tsetserleg and Bolnay faults (modified from "One century of seismicity in Mongolia [1900-2000]).

On 11 August, 1931, an earthquake with M_S 7.9 ruptured the right lateral Fu-Yun fault (Figure 1.8 and Figure 1.10) in the southern Altai Mountains of Northwest China. The most recent work on that fault (Klinger et al., 2011) indicates that the well known 160 km of surface ruptures are distributed over three fault segments. They measured 290 stream channels and terraces offsets that give an average co-seismic slip of 6.3 m (Figure 1.10). The highest seismicity observed in the Altai range is still along the Fu-Yun surface ruptures of the 1931 earthquake, interpreted as late aftershocks (Sodnomsambuu et al., 2014).

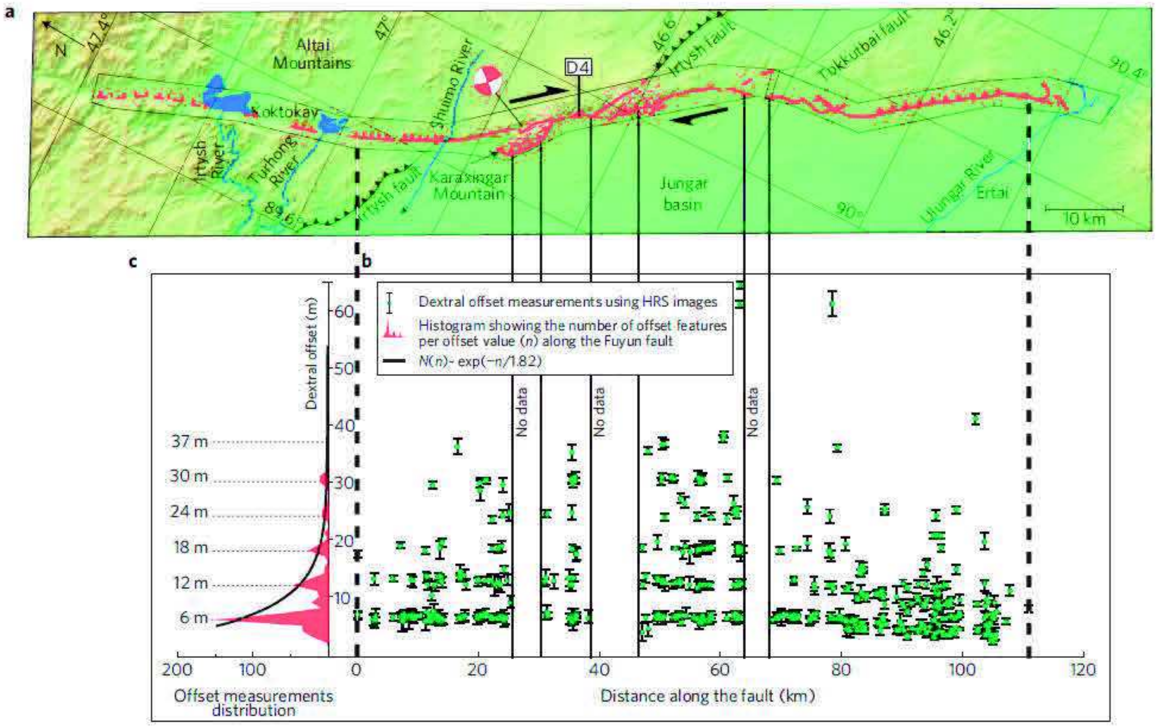

Figure 1.10. Rupture map of 1931 Fuyun earthquake from field and satellite image analysis. Geomorphic offsets are interpreted as the repetition of earthquakes with about 6 m of right-lateral slip (Klinger et al., 2011).

The average surface displacement observed in the field, the surface of the fault plane determined by the aftershocks distribution (80x17km) gives a magnitude M_W~7.2. The characteristics of the Altai event suggest that the Gorny Altai region (Figure 1.11), similar to Mongolia and Gobi, is characterized by large infrequent M 7-8 earthquakes along faults moving at rates of a few mm/yr or less (Dorbath et al., 2008).

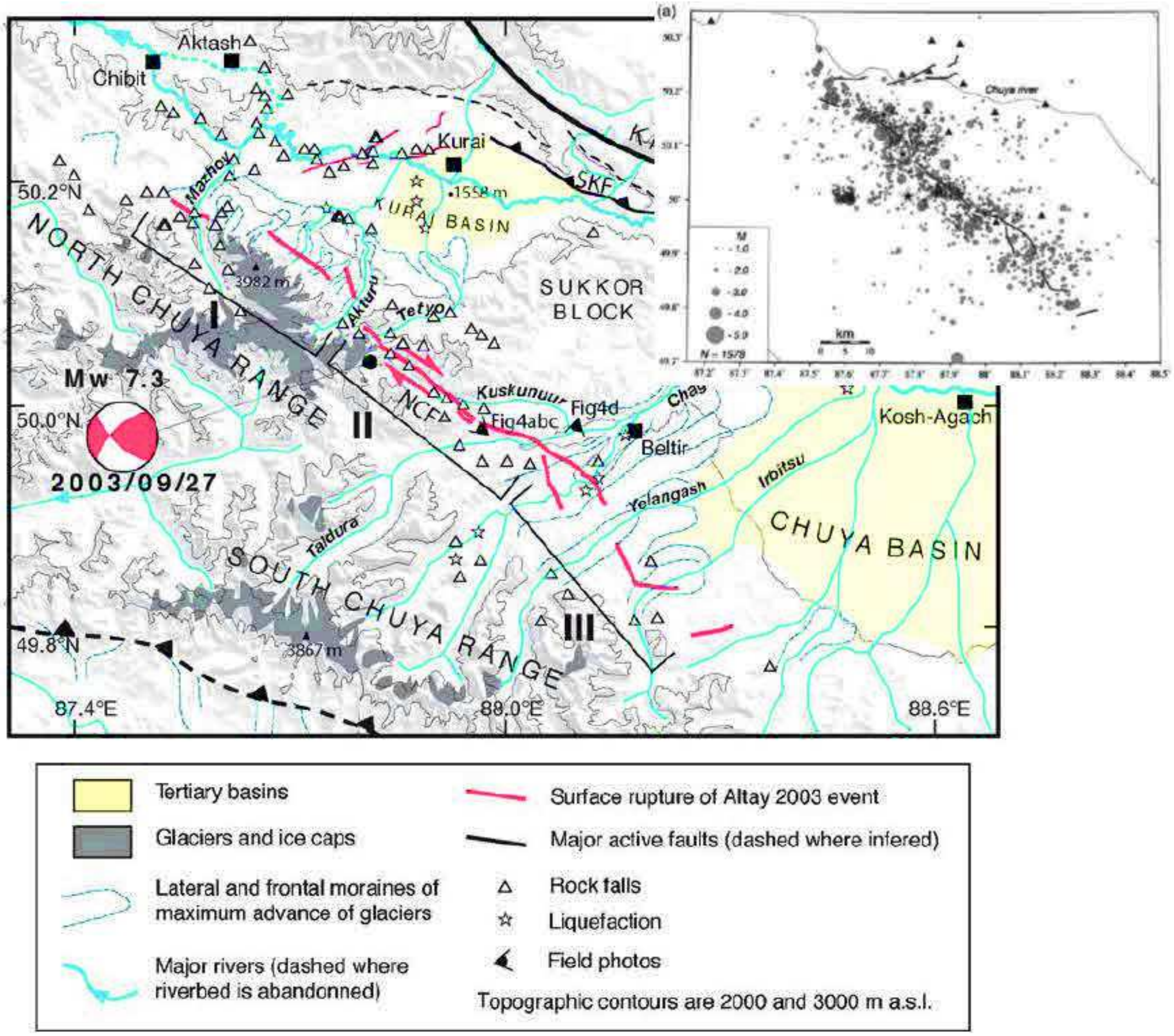

Figure 1.11. Seismotectonic map of epicentral area. Main surface rupture (bold red lines) of the 2003 Gorny Altai earthquake follows the northern edge of the Chuya range along the North Chuya fault (NCF). The Chuya and Kurai basins filled with Tertiary sediments are limited north and south by growing ranges: the Kurai and Chuya mountains, respectively. The Kurai fault (KF), the major right-lateral strike-slip fault in the area, was not activated during the 2003 earthquake. Map of well-located aftershocks (rms <0.2) shown in upper right corner. Black triangles are seismic stations. Stars are positions of main aftershocks from the International Seismological Centre (Dorbath et al., 2008).

1.2.3.3 Gobi-Altai:

Extending eastward from the Mongolian Altai to the Gobi, the Gobi-Altai Mountains is an active deforming intraplate and intracontinental mountain range that forms part of the complex deformation field of Central Asia.

The main faults of Gobi-Altai trend N100E and correspond to left lateral strike slip faults (Khilko et al., 1985, Schlupp, 1996). The range is 900 km long from east to west and between 250 and 350 km wide from north to south. The beginning of the reactivation of the range is estimated at 5±3Ma (Vassallo et al., 2007).

The Bogd fault system is one of the best known strike slip fault systems in the region as it recently ruptured during the great Gobi-Altai earthquake of December 4, 1957 with magnitude of 8,1 (Khilko et al., 1985; Baljinnyam et al., 1993; Ritz et al., 2003, 2005; Schlupp, 1996; Rizza et al., 2011) (Figure 1.12 and Figure 1.13).

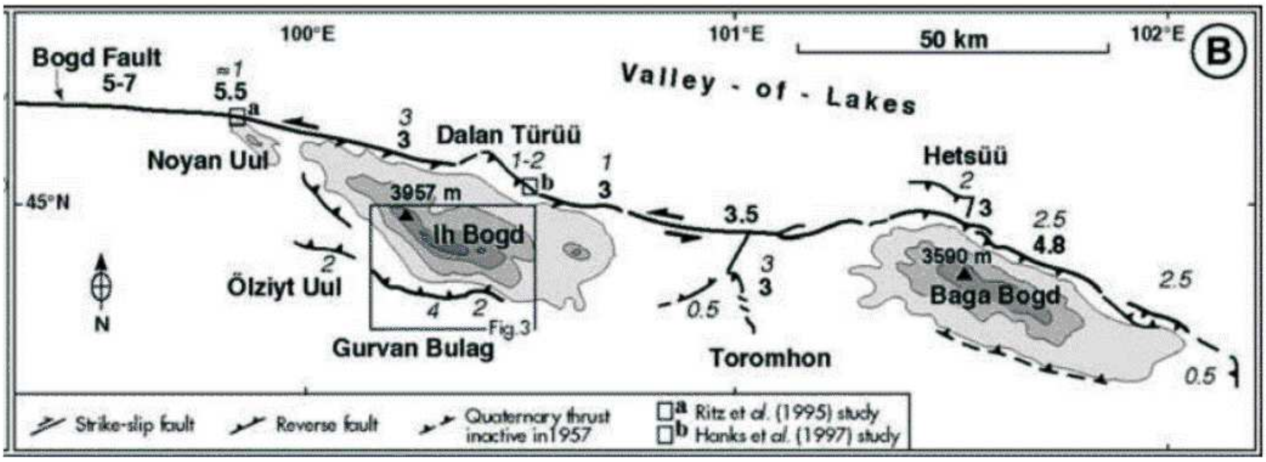

Figure 1.12. Surface rupture of the earthquake of 1957. Horizontal and vertical displacement indicated by bold and italic numbers, respectively (after Ritz et al., 2003).

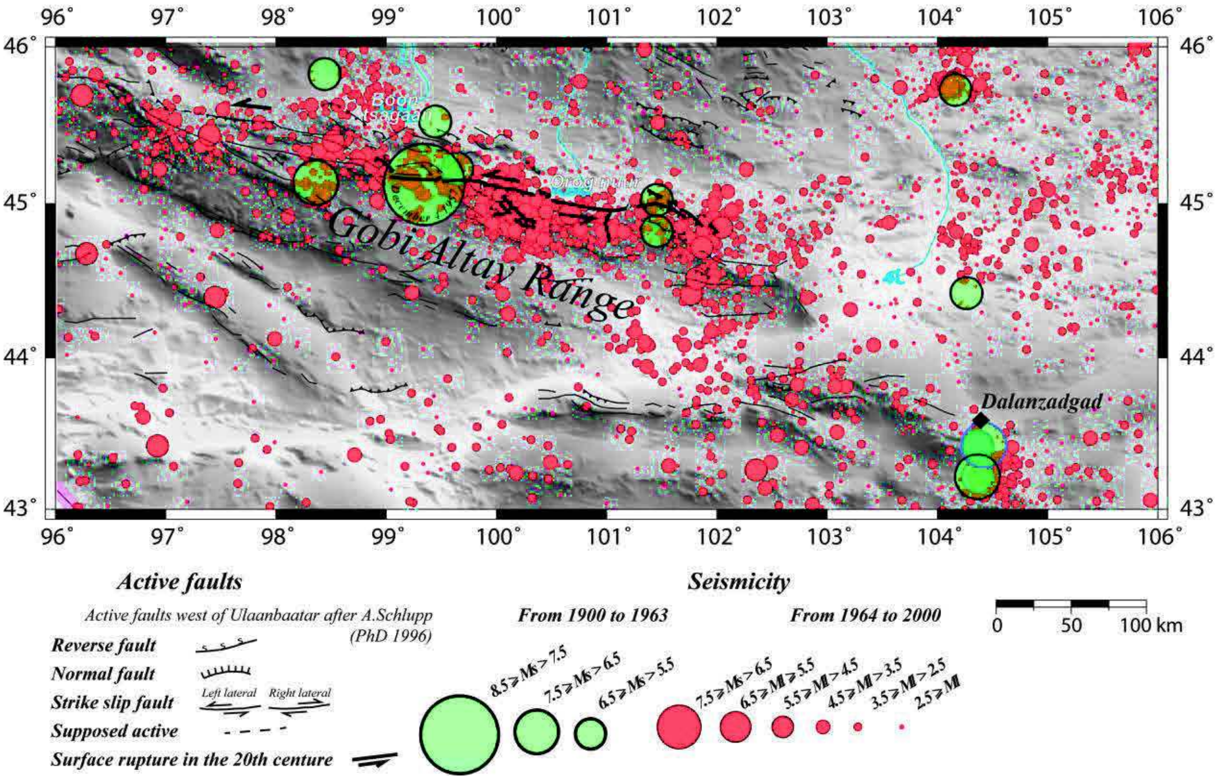

Figure 1.13. Seismicity observed between 1900 and 2000 (in red with the network of Mongolia since 1964) in the area of Tsetserleg and Bolnay faults (modified from "One century of seismicity in Mongolia [1900-2000]).

Ritz et al., (2006) confirmed the low horizontal and vertical slip rates within the massifs of the Gurvan Bogd mountain range for the Late Pleistocene–Holocene period. The Bogd fault has a maximum horizontal left-lateral slip rate of ~1.5 mm/yr, while reverse fault segments along the Gurvan Bogd fault system have vertical slip rates between 0.1 and 0.2 mm/yr (Ritz et al., 2006). Characteristic dislocations observed along the Bogd fault suggest return periods of earthquakes similar to 1957 between 3000 and 4000 yr (Rizza et al., 2011).

1.2.3.4 Khangai:

The Khangai mountain (summits at about 3700 m asl, highest top at ~4000m) is located in central Mongolia and oriented about N123^0. Its length (WNW-ESE) is ~500 km and its width is ~200 km. It has a dome shape, the mountain is also called "Khangai dome". The Khangai dome is located at the western end of the Khangai-Hentey geological structure (Badarch et al., 2002) (Figure 1.2) and consists of granites, gneisses and other metamorphosed rocks of Pre-Cambrian and early Mesozoic age (Cunningham, 2001).

Several evidence suggest that the Khangai mountain developed recently and that the geodynamic processes, which are also responsible for its uplift, are still active.

Central Mongolia is characterized by a thick crust and thin lithosphere. For example, Barruol et al. (2008), based on geophysical and geochemical arguments, suggest a lithosphere thinner than 90 km beneath central Mongolia, contrasting with a thick (at least 200 km) Siberian platform. Moreover, Petit et al. (2008) indicate that the Bouguer gravity anomaly is, on average, much lower in Western Mongolia than in the Baikal region, suggesting a greater crustal thickness and/or a thinner lithosphere.

Chen et al. (2015) proposed that the mantle upwelling induced decompression melting in the uppermost mantle and that excess heat associated with melt transport modified the lithosphere that isostatically compensates the surface uplift at upper mantle depths (>80 km).

In and around the uplifted Khangai Mountains are small-volume alkali-basaltic cones and lavas erupted since 30 Ma, which are parts of one of the largest region of intra-plate Cenozoic volcanism that extends from Baikal Rift through central Mongolia to China (Hunt et al., 2012) (Figure 1.14). These lavas have been used by Schlupp (1996) for paleo-magnetism measurements to identify clockwise rotations of several tens of degrees since the Cenozoic that could record the rotation of the whole dome (Figure 1.14).

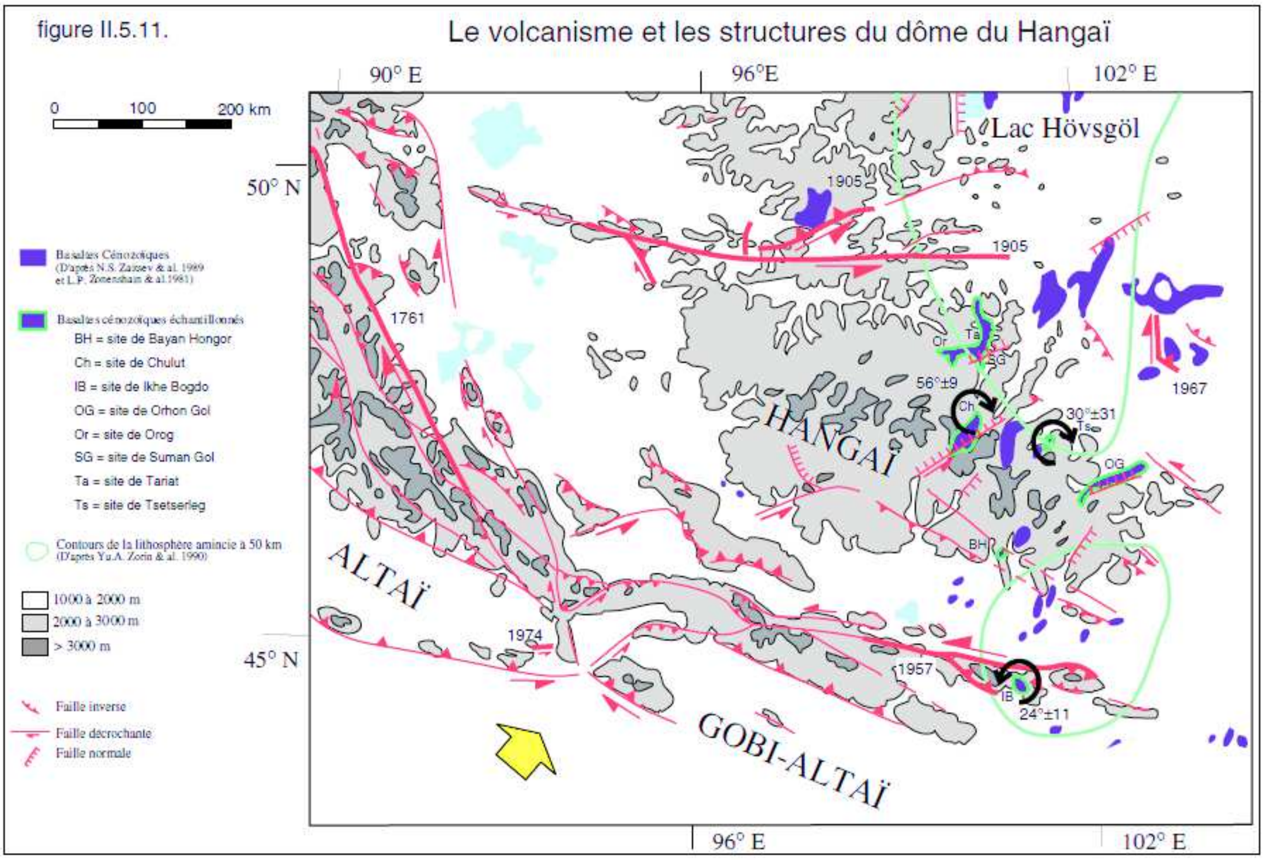

Figure 1.14. Main volcanism, measured rotation on lavas deposits and major faults of Khangai Dome (after Schlupp, 1996).

From the tectonic point of view, there is a series of east–west left-lateral strike-slip faults (named the Songino-Margats, the Hag Nuur, the Uliastay and the South Khangai fault systems) in the south and west part of the Khangai. Total bedrock displacements of ~3 km have been measured on both the Songino-Margats and South Khangai fault systems and 11 km across the Hag Nuur fault. Cumulative offsets across the Uliastay fault systems are unknown but are unlikely to be large (Figures 1.15-1.16) (Walker et al., 2008).

At the SE edge of Khangai dome, there is a clear NE-SW trending normal fault of Egiin Dawaa (Khilko et al., 1985; Schlupp, 1996; Schlupp and Cisternas, 2007) consistent with the main stress orientation. We notice that the WNW–ESE trending Bayan Hongor fault is still under discussion and has been described both as a reverse or as a normal fault (Baljinnyam et al., 1993; Schlupp, 1996; Cunningham, 2001; Walker et al., 2007, 2008) (Figure 1.14 - Figure 1.16).

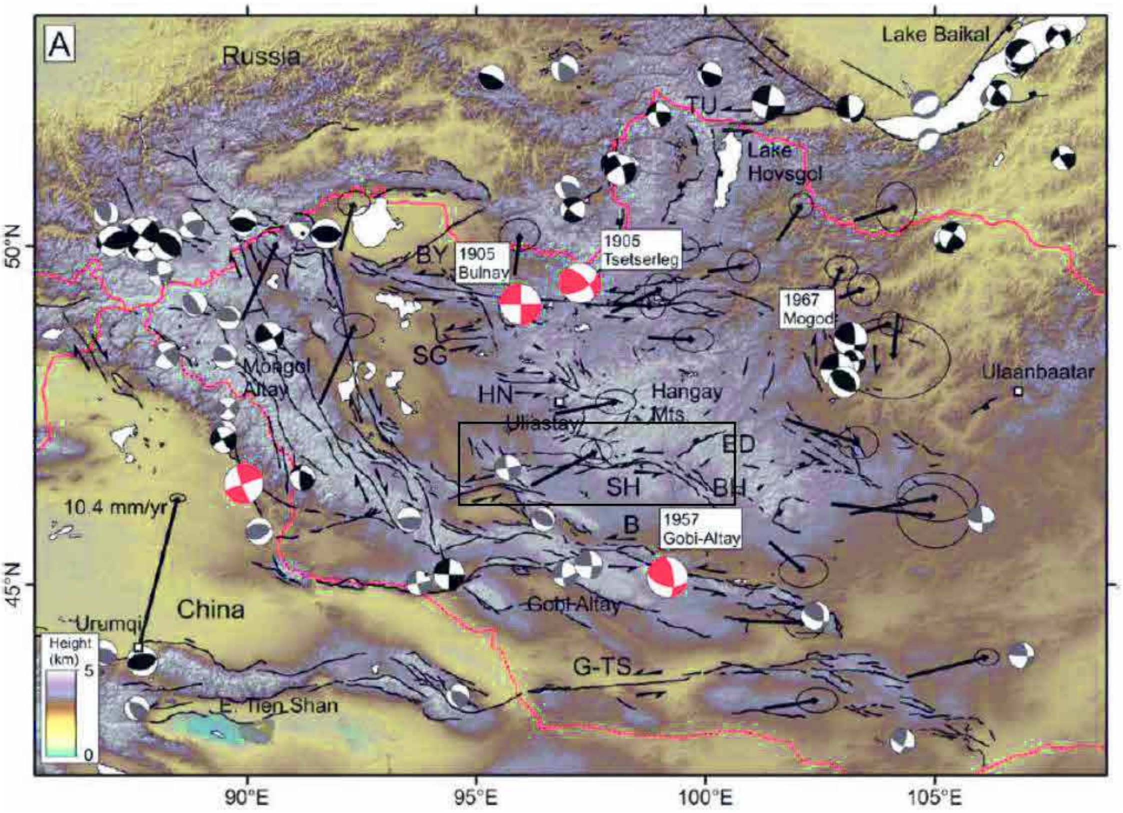

Figure 1.15. Shaded-relief topographic map of western and central Mongolia and CGPS velocities relative to stable Eurasia. Active faults are shown as black lines. The east–west strike-slip faults of central Mongolia are labelled as TU=Tunka, BY=Bulnai, SG=Songino-Margats, HN=Hag Nuur, SH=South Khangai, B=Bogd, G-TS=Gobi-Tien Shan, ED=Egiin Dawaa fault, BH=Bayan Hongor fault (after Walker et al., 2008).

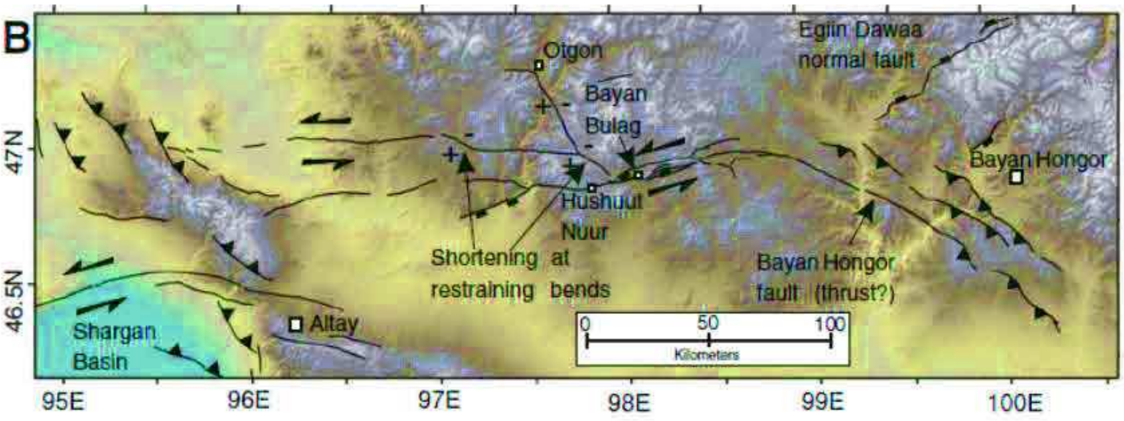

Figure 1.16. Shaded-relief topographic map of south Khangai shown in Figure 1.15 by the black rectangle (after Walker et al, 2007).

The observed seismicity of the Khangai dome shows a low level (Figure 1.17) in comparison with other active areas of Mongolia, with no large earthquake since 1900. The moderate activity is mainly concentrated to the south of the Khangai, near the active structures and also widespread over the whole range (Figure 1.16 and Figure 1.17). Nevertheless, the uncertainty of the localization is too important to associate earthquakes to specific structures and a part of the apparent "widespread" seismicity could be in fact concentrated along some active structures, like Egiin Dava. The maximum known magnitude in Khangai since 1900 is about 5.5.

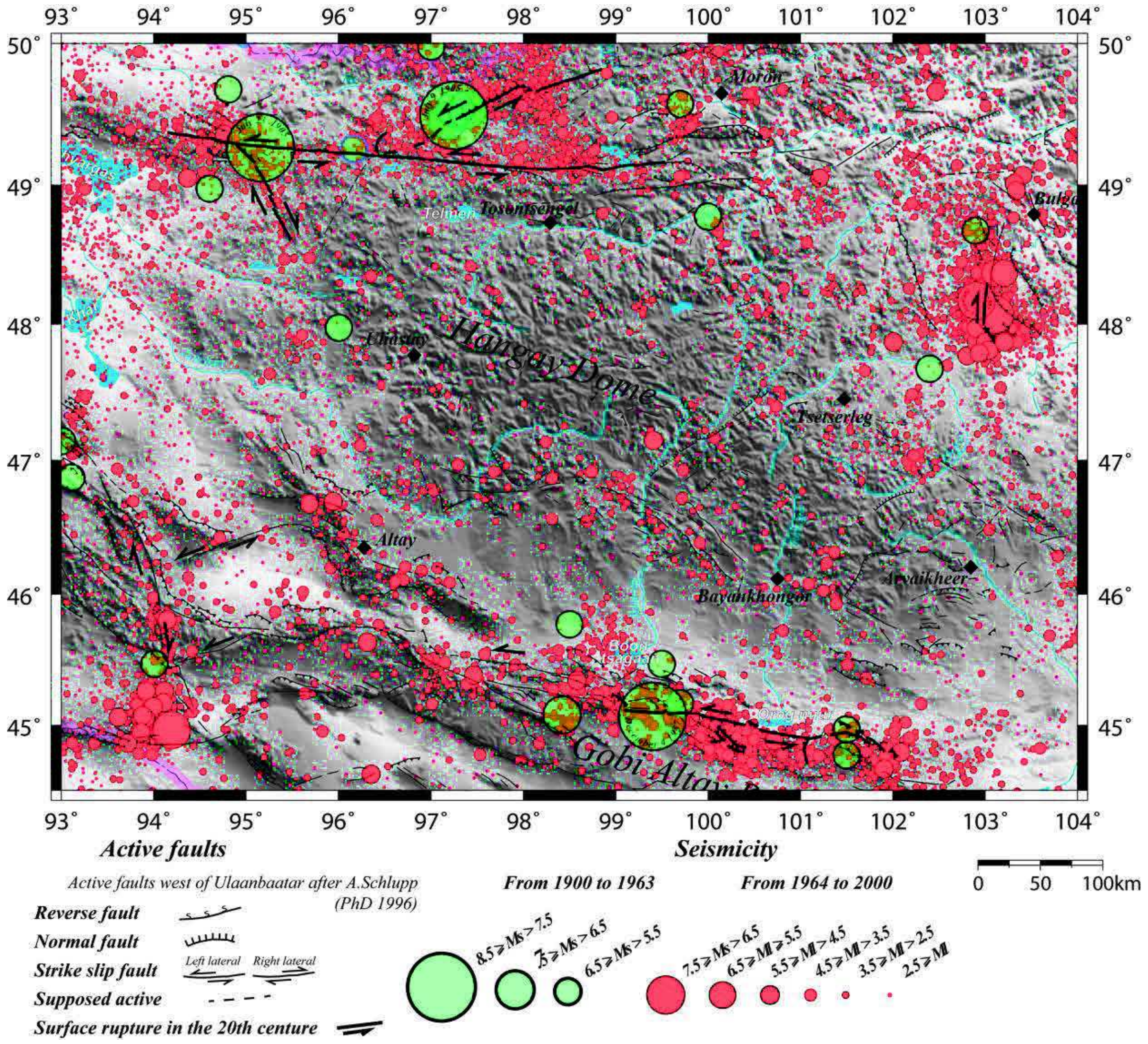

Figure 1.17. Seismicity observed between 1900 and 2000 (in red with the network of Mongolia since 1964) in the area of Tsetserleg and Bolnay faults (modified from “One century of seismicity in Mongolia [1900-2000]).

1.2.3.5 Between Khangai and Ulaanbaatar, the region of Mogod

The Mw=7.0 Mogod earthquake of 1967/01/05 is the largest recent event in this region and was located at about ~260 km from Ulaanbaatar, near the NE edge of the Khangai Dome where we observe also a set of late Cenozoic volcanic eruptions.

The main shock ruptured in three subevents occurring sequentially from north to south, all of them associated with segments of coseismic surface faulting. The first and second subevents involved predominantly N-S right-lateral strike slip, with the second, larger one occurring on a fault dipping steeply east with a significant reverse component of slip. The third subevent involved thrust faulting with a NW-SE strike at the southern end. A large (Mw 6.4) aftershock on January 20 was associated with a different thrust fault segment, which terminates the southern end of the strike-slip rupture of the first subevent (Bayasgalan 1999, Bayasgalan and Jackson, 1999) (Figure 1.18).

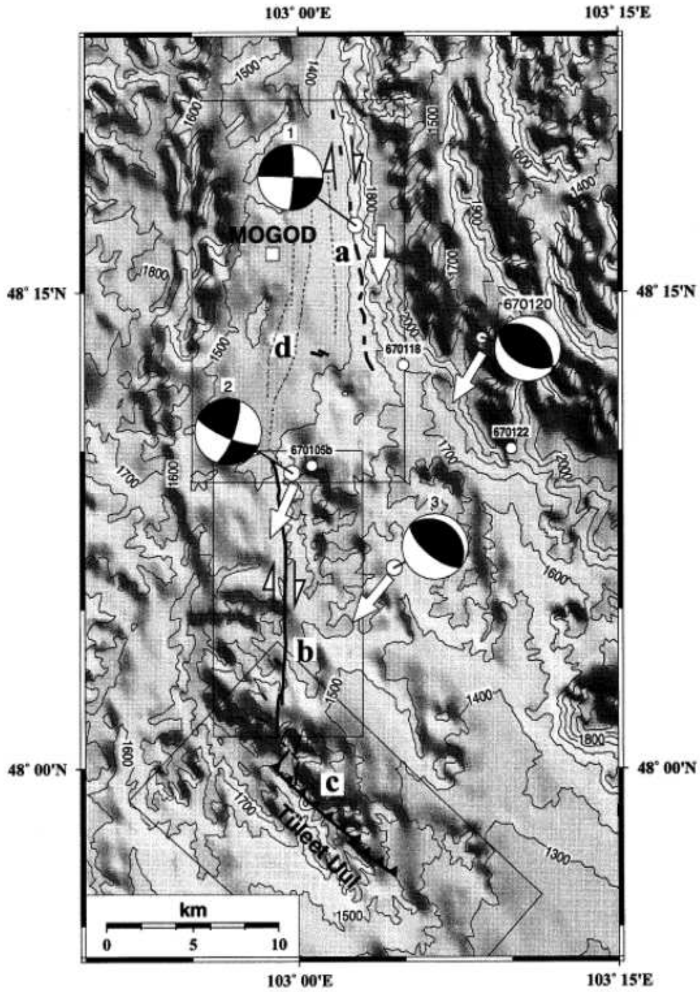

Figure 1.18. Main surface fault ruptures of the Mogod earthquake (a, b and c) . The three main shock subevents (marked 1, 2 and 3) and the mechanism of the principal aftershock (1967-01-20). Slip vectors are shown as large white arrows (after Bayasgalan and Jackson, 1999).

The event of Mogod is very important for the seismic hazard of Ulaanbaatar as it was the nearest large event and it was felt in the capital, therefore it is still in the memory of many citizens. The residents of Ulaanbaatar felt this event with an intensity between IV to VI (MSK-64) (Figure 1.19). It was used to show that the basin under the city induced site effects. Considering the epicentral distance (~260km), it is clear that this intensity variation (IV to VI) is related to the local geology of Ulaanbaatar that has an impact on the ground motion (Chimed, 2011).

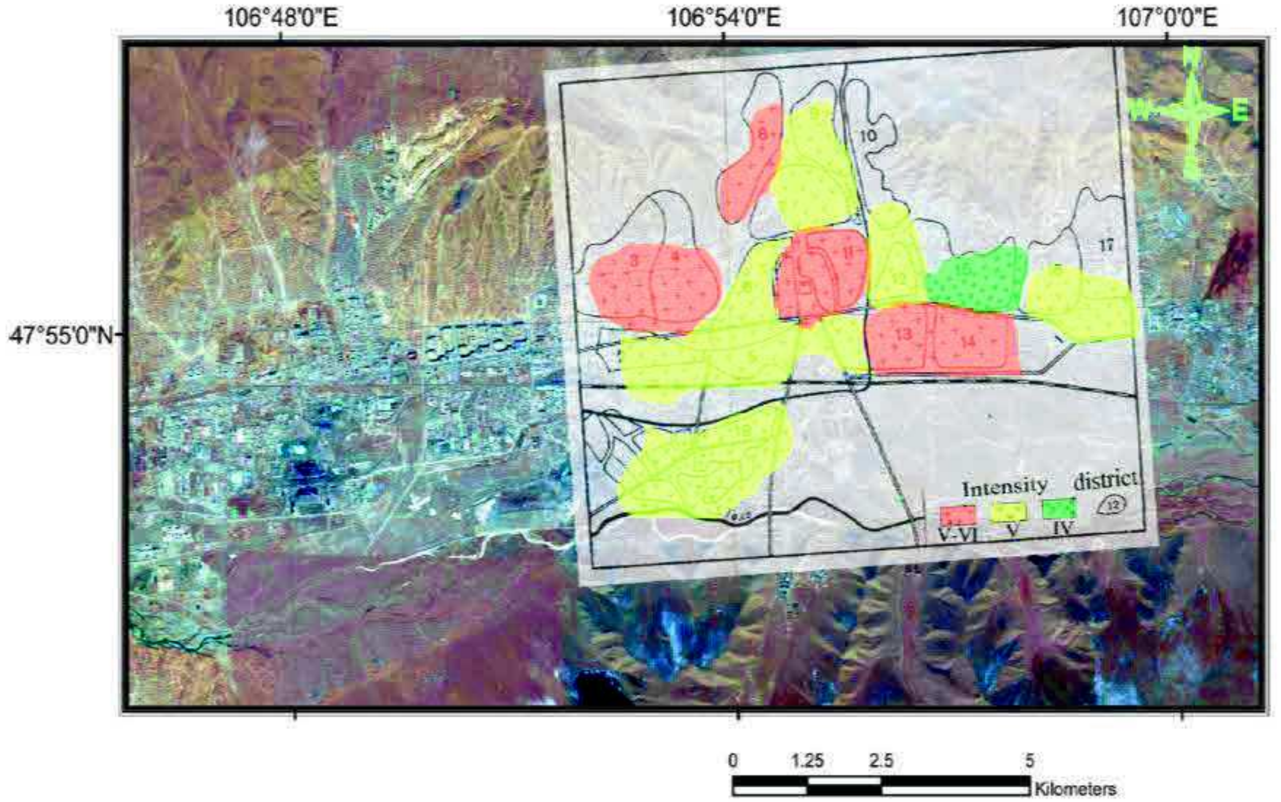

Figure 1.19. 1967 Mogod earthquake MSK Intensity map of Ulaanbaatar city. In background actual city urban area observed in a satellite image from GoogleEarth (after Chimed, 2011)

1.2.3.6 Link between Altyn Tagh and East Gobi faults in southern Mongolia

To the southeast of Mongolia, near the boundary of China, the largest fault system named East Gobi Fault has been identified (Figure 1.20). The East Gobi fault zone is a wide sinistral shear zone that seems to be accommodating little extension (Webb and Johnson, 2006; Richon et al, 2015). It is inferred that the East Gobi Fault Zone is kinematically linked, via the Alxa Fault Zone, to the Altyn Tagh fault of NW Tibet. The Altyn Tagh fault is the largest left lateral fault striking towards Mongolia and extends from the northern Himalayan collisional zone towards north China (Yin et al., 2002).

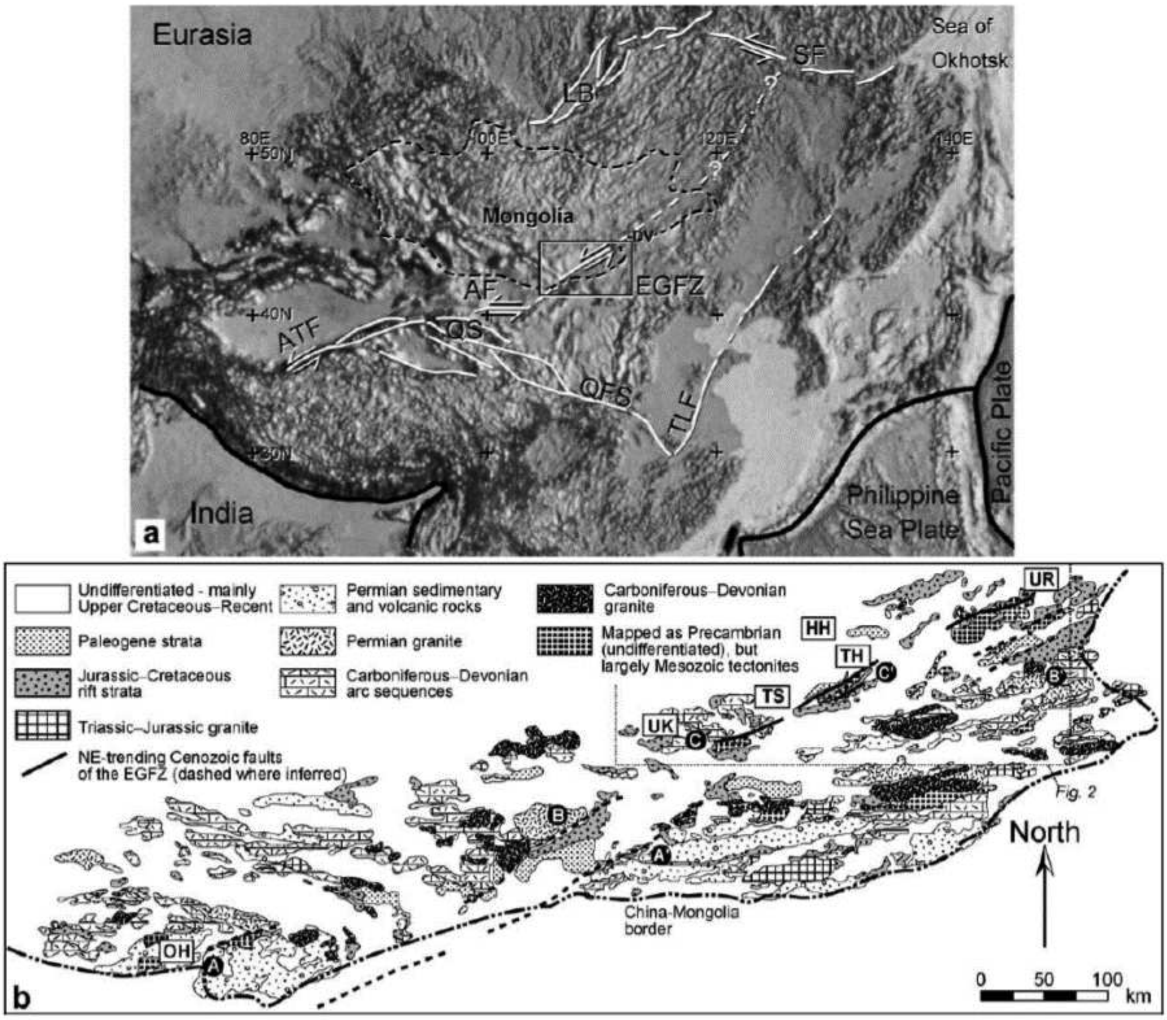

Figure 1.20. a) Regional map showing major tectonic elements of China and Mongolia. Primary plate boundaries are shown in black and regional faults in white. Rectangle denotes area shown in b. AF = Alxa fault system, ATF = Altyn Tagh fault, DV = Dariganga volcanic field, EGFZ = East Gobi Fault zone, LB = Lake Baikal, QFS = Qinling fault system, QS = Qilian Shan, SF = Stanovoy fault system, TLF = Tan Lu fault. b) Simplified geologic map of southeastern Mongolia based and modified after Tomurtogoo (1999). OH = Onch Hayrhan, UK = Ulgay Khid, TS = Tsagan Subarga, HH = Har Hotol, TH = Tavan Har; UR = Urgun. The map shows possible offset markers across the EGFZ (after Webb and Johnson, 2006).

1.2.3.7 Khuvsgul and Baikal:

The Baikal rift system (BRS) spreads along the edge of the Siberian Platform and through the mountain structures of East Siberia and extends over 1500 km in a NE-SW direction. It is prolonged to the NE by the Stanovoy strike-slip zone, which joins the Sea of Okhotsk and Sakhalin deformation zones. To the SW, it is connected to the system of left-lateral strike-slip faults of western Mongolia (Figure 1.21). The Baikal rift structure is asymmetric and appears strongly controlled by the geometry of the suture zone bounding the Siberian craton (Petit et al., 2008). The rift grabens and half-grabens are bordered by active normal faults. Moreover, faults with sub-latitudinal and sub-meridional strikes depict left-lateral and right-lateral strike-slip components, respectively (Sankov et al., 2000). The displacement amplitudes of the major normal faults reach 1500-2000 m, while some limited horizontal displacements are reported on the wings of the Baikal rift system.

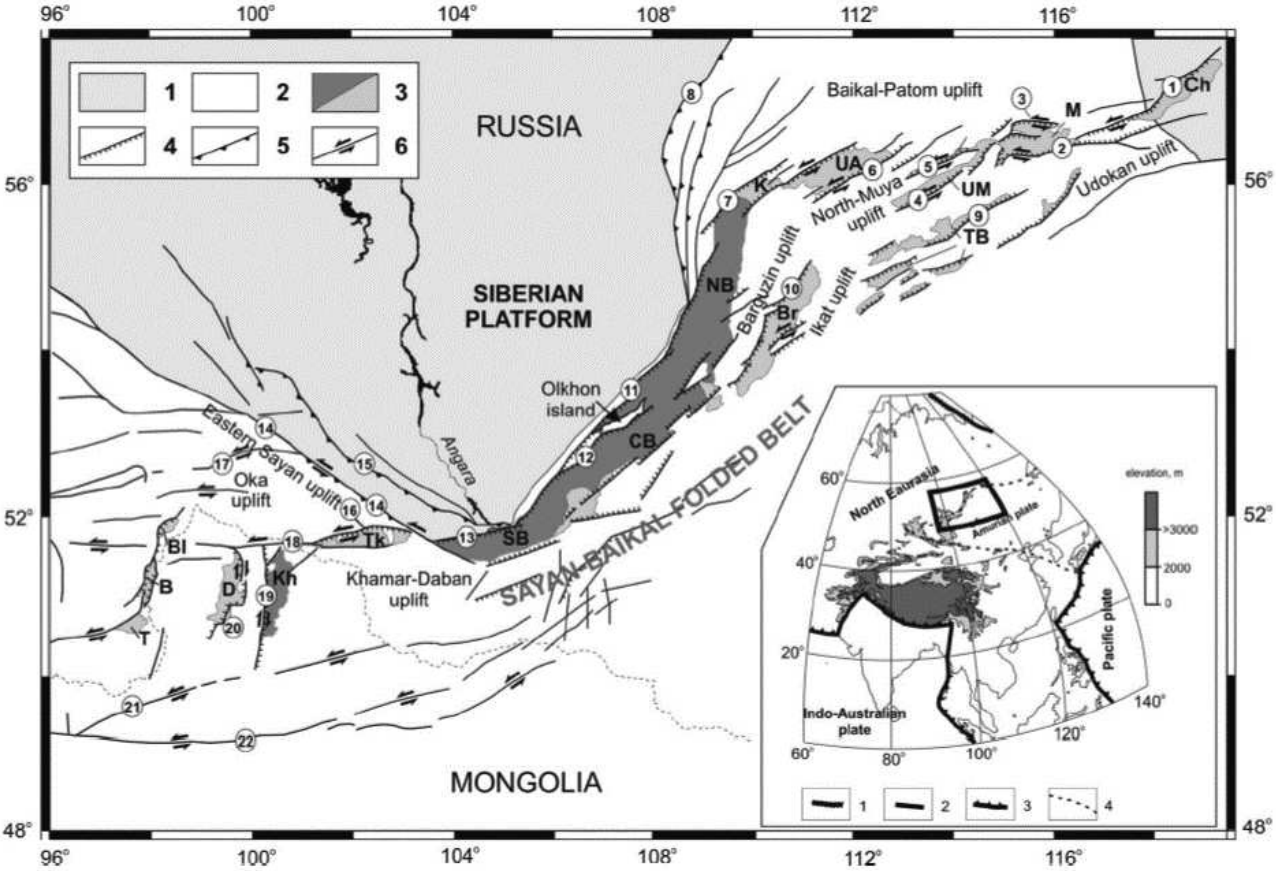

Figure 1.21. Neotectonic scheme of the Baikal rift system and surroundings. 1-Siberian platform; 2-Sayan-Baikal folded area; 3-Cenozoic rift basins: Ch-Chara, M-Muya, UM-Upper Muya; TB-Tsipa-Baunt; UA-Upper Angara; K-Kitchera; NB-North Baikal; Br-Barguzin; CB-Central Baikal; SB-South Baikal; Tk-Tunka; Kh-Khubsugul; D-Darkhat; Bl-Belinskaya; B-Busingol; T-Terekhol; 4-normal fault; 5-thrust and reverse fault; 6-strike-slip fault. Numbers within circles denote main faults: 1-Kodar; 2-South-Muya; 3-North-Muya; 4-Upper Muya; 5-Muyakansky; 6-Upper Angara; 7-Kitchera; 8-Akitkan; 9-Tsipa-Baunty; 10-Barguzin; 11-Primorsky; 12-Morskoy; 13-Obruchev; 14- Main Sayan Fault; 15-Peredovoy; 16-Tunka; 17- Okino-Zhombolok; 18-Baikal-Mondy; 19-Khubsugul; 20-Darkhat; 21-Tsetserleg; 22-Bolnai (Khangai) (after Dobrynina, 2016).

The Baikal rift is seismically active, and several large earthquakes occurred in history. The maximum magnitude of earthquakes recorded instrumentally is M_S=7.6 for a strike-slip event in the NE part of the Baikal rift system (27/06/1957) and M_S=6.8 (29/08/1959) for a normal fault earthquake in the central part of the rift system. The number of weak and moderate events is fairly large, about 3-4000 earthquakes per year (Radziminovich et al., 2013).

There are three seismic NS basins in north Mongolia: Busiin-Gol, Darkhad and Khubsugul lake area (Figure 1.21 and Figure 1.22). Most epicentres are concentrated in the Busiin-gol zone connected with the Sayan active zone to the west and the Baikal active rifting zone to the NE (Munkhuu, 2006). The largest earthquake occurred on 27th December 1991, called Busiin-Gol, with a magnitude of Mw = 6.5.

Relatively thin lithosphere (70–80 km) is found east and south of the rift system and is in spatial connection with the Khangai-Khuvsgul region of anomalous mantle in Mongolia.

Based on the long-term measurements of GPS monitoring network, the refined estimate obtained for the velocity of the divergence of the Siberian and Transbaikalian blocks, is 3.4 ± 0.7 mm/yr in the southeast direction (130°) (Sankov et al., 2014).

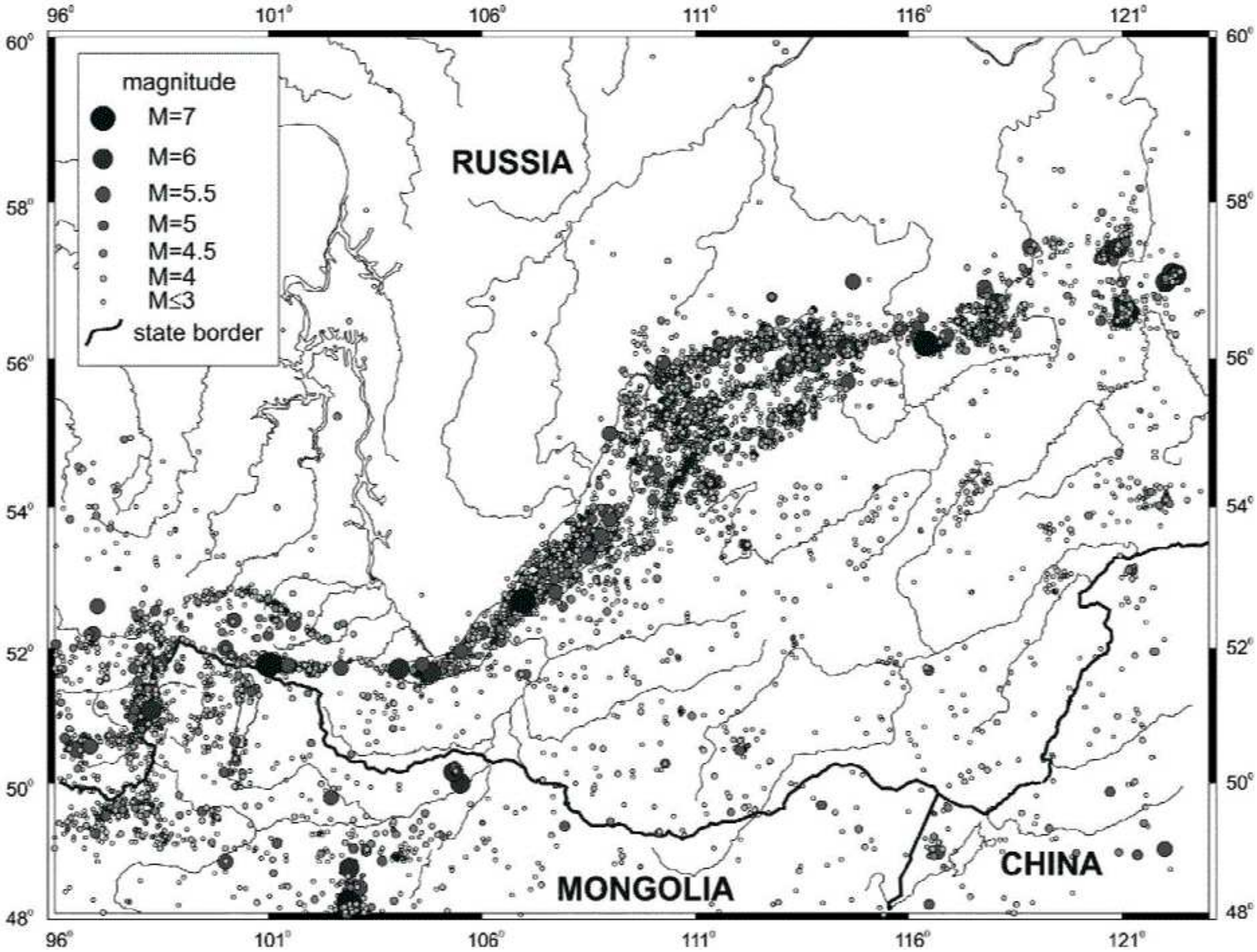

Figure 1.22. Seismicity of the Baikal rift system in the span time 1950–2012 (Data base from Baikal Regional Seismological Center, Geophysical Survey of the Russian Academy of Sciences) (after Dobrynina et al., 2016).

1.2.4 Large active faults in Eastern Mongolia (Ulaanbaatar)

1.2.4.1 The Amurian plate

Researchers find that the deformation in Northeast Asia can be well described by a finite number of rotating blocks, which are independent of the Eurasian plate motion with statistical significance above the 99% confidence level (Jin et al., 2007) (Figure 1.4). They indicate the existence of a plate located to the North East of Asia called Amurian plate.

Its northern limit follows a clear geographical boundary between the Kuril–Japan trench and the Baikal rift zone. The Baikal Rift between the Amurian and Eurasian plates is opening at about 3.0 mm/yr. But its border becomes less clear and diffuse throughout continental Northeast Asia to the south of the Baikal rift (Calais et al., 2003; Petit and Fournier., 2005; Jin et al., 2007).

For its southern boundary, Jin et al (2007) proposed that the tectonic boundary between North China and Amuria follows the Yin Shan–Yan Shan Mountain belts and they described its relative motion with other plates. This Mountain belts is associated with about 2.4 mm/yr extension (Jin et al., 2007).

To first order, Wei and Seno (1998) and Bird (2003) proposed already a similar southern limit except for its eastern part (Figure 1.4). But Heki et al. (1999) proposed a southern boundary more to the south, between the south China and north China blocks along the Qinling–Dabie fault, which is moving, left laterally at about 3.1 mm/yr. It means that they include the north China block into the Amurian plate.

Unfortunately, the western boundary of the Amurian plate, when it is crossing Mongolia, is much less clear and understood because the deformation in the area is very slow, the seismicity low and there is no clear NS structure in that area. The observations that could enhance this boundary are still weak: east of Khangai dome, the topography is smother, the altitude lower, and the seismic activity much lower. The only known structure with a more or less NS direction is the NS Mogod fault segment, a part of which broke during the 1967 large earthquake with a metric right-lateral slip and with a length of less than 100 km (Figure 1.18). The region east of Khangai is, in term of active tectonics, poorly studied, mainly because it is a region of low strain and no large earthquakes are known in that area, considered by some as a quite and aseismic region.

The region of Ulaanbaatar is situated in the Amurian plate, so a better knowledge of its western limit will help to better understand the relation between the deformation in the capital area and western Mongolia.

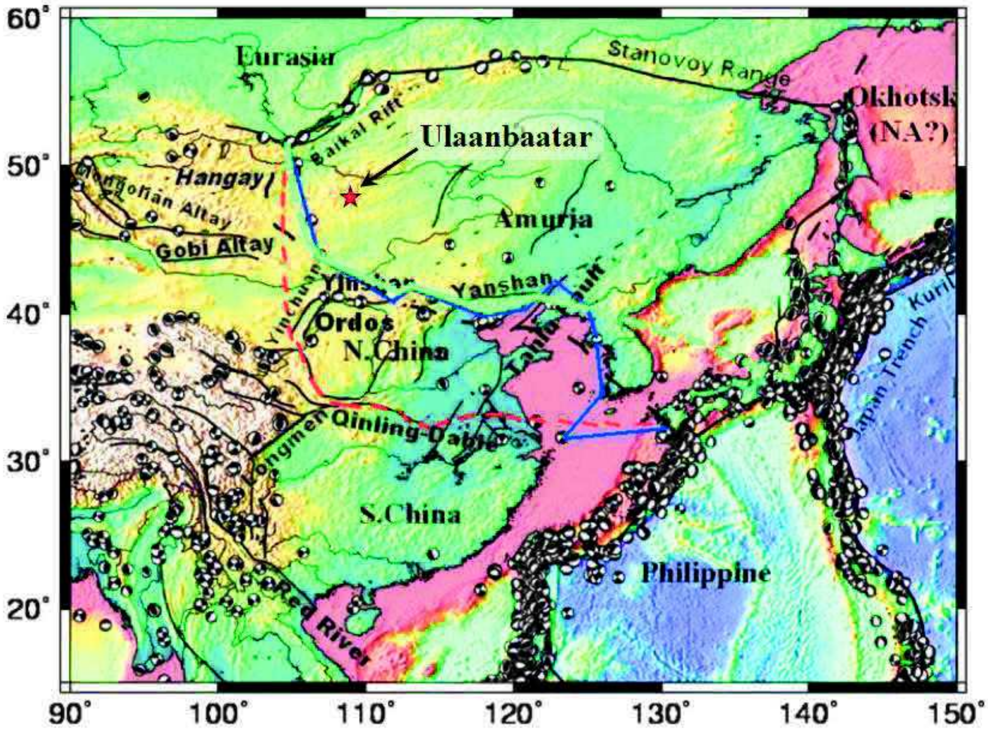

Figure 1.23. Tectonic map of Northeast Asia superimposed on topography. Focal mechanisms are from Harvard CMT catalogue (1976–2005, Mw>5.0). The continuous lines in various colour are the limits of the Amurian plate depending on the authors: upper blue solid line is from Bird (2003), middle black dashed line is from Wei and Seno (1998), bottom red dashed line is from Heki et al., (1999), and the upper green solid and dashed lines is from Jin et al. (2007) (after Jin et al., 2007).

1.2.4.2 Geological and tectonic context of Ulaanbaatar region

The Ulaanbaatar area sits in the northern Mongolian tectonic domain and belongs to Haraa Terrane and Khangai-Hentey group (red square in Figure 1.2). The area of Ulaanbaatar is geologically included in the northern domain of Khangai-Hentey basin (Eenjin et al., 2009 and Figure 1.24). The Haraa group occurs in the west to northwest part of the city and the Khangai-Hentey basin extends widely in Ulaanbaatar. The Haraa Terrane consists of Cambrian to Lower Ordovician metasedimentary rocks originated from back-arc or fore-arc basin. The Khangai-Hentey basin consists of metasedimentary rocks (such as sandstone and mudstone) including ophiolites (Badarch et al., 2002).

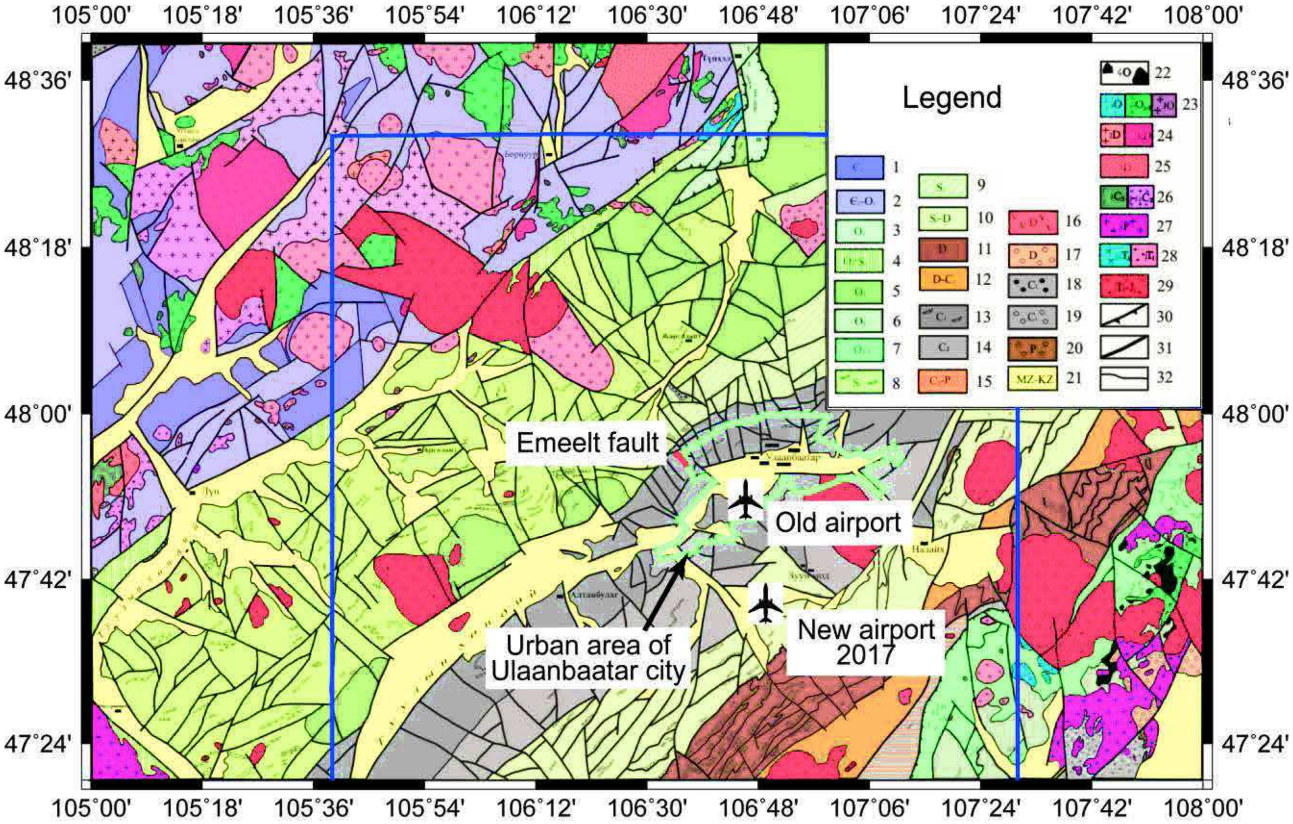

Figure 1.24. Simplified geological map around Ulaanbaatar (modified after Tomurtogoo, 2009). Blue square is study area (area of 140kmx140km) 1-15- Overlapping & trust – folded complexes: 1-2-Haraa turbidite complex ($\dot{E}_2$-O_1): 1- Dorgont formation, 2- Shiguu formation, 3-4-Brown-upper formation accretionary complex (O-S_1); 3-volcanogenic massive, 4-quartzite-schist flysch massive, 5-6- Unegt group methaform complex ($O_{1\text{-}2}$); 5-sulfide-volcanogenic- grapholite massive (O_1), 6- quartzite-grapholite massive (O_2), 7-9-Mandal group accretionary complex (O_2-S_2); 7-Khushuut formation ($O_{2\text{-}3}$); 8-Khuingol formation (S_1); 9- Sugnugur formation (S_2); 10-15-Hentey group accretionary complex (S_p-P); 10-Gorhi formation (S_2-D), 11-Sergelen formation (D), 12-Maanit formation (D-C_1), 13-Altan-Ovoo formation (C_1), Orgiochuul formation (C_2), 14-15-Shine us formation (C_2-P); 16-21- Methamorphosed structural complexes: 16- devonian volcanigenic massive, 17-devonian ocean molasses, 18- early carboniferous ocean molasses, 19-late carboniferous ocean molasses, 20-Permian ocean molasses, 21-mesozoic-cenozoic grabine complex (continental coal molasses, molasoide); 22-31-Intrusive & subvolcanic complexes: 22-Ordovician ultrabasite-gabbro complex, 23-Ordovician gabbro's(a), diorite-granodiorite's(b) & granite-leucogranite's(b) complexes, 24- Devonian alkali granite's (a) & syenite Montserrat's (b) complexes, 25- Devonian subvolcanic porphyry complex, 26-carbonian gabbro's(a) & granodiorite-granite's(b) complexes, 27-Permian granite- leucogranite's complex, 28- Triassic tonalite's(a) & granite-leucogranite's(b) complexes, 29- Late Triassic-early Ura's rare metallic granite complex; 30 – Reverse fault, 31- other type's fault, 32-geological boundary.

Ulaanbaatar region is considered a low seismic hazard region because of the absence of strong earthquakes, based on the known historical seismicity and the very limited known active faults.

The deformation of the region appears low. GPS observations and analysis show that the capital Ulaanbaatar is moving in the southeast direction relative to Irkutsk on the northern side of the Baikal Rift or stable Eurasia (Calais et al., 2003) (Figure 1.25). A large part of this motion is taken by the opening of the Baikal rift. Nevertheless, the remaining deformation, of about 2.3mm/yr between station UDUN to the south of the Baikal rift and station ULA1 is distributed across several structures between Baikal Rift and the capital (Figure 1.25). It is enough to generate moderate to strong earthquakes in central Mongolia, though not frequent. Unfortunately, we do not have enough GPS stations between Baikal and Ulaanbaatar to measure if the deformation is concentrated in some areas or not, thus we do not know the rate of deformation in the area of Ulaanbaatar.

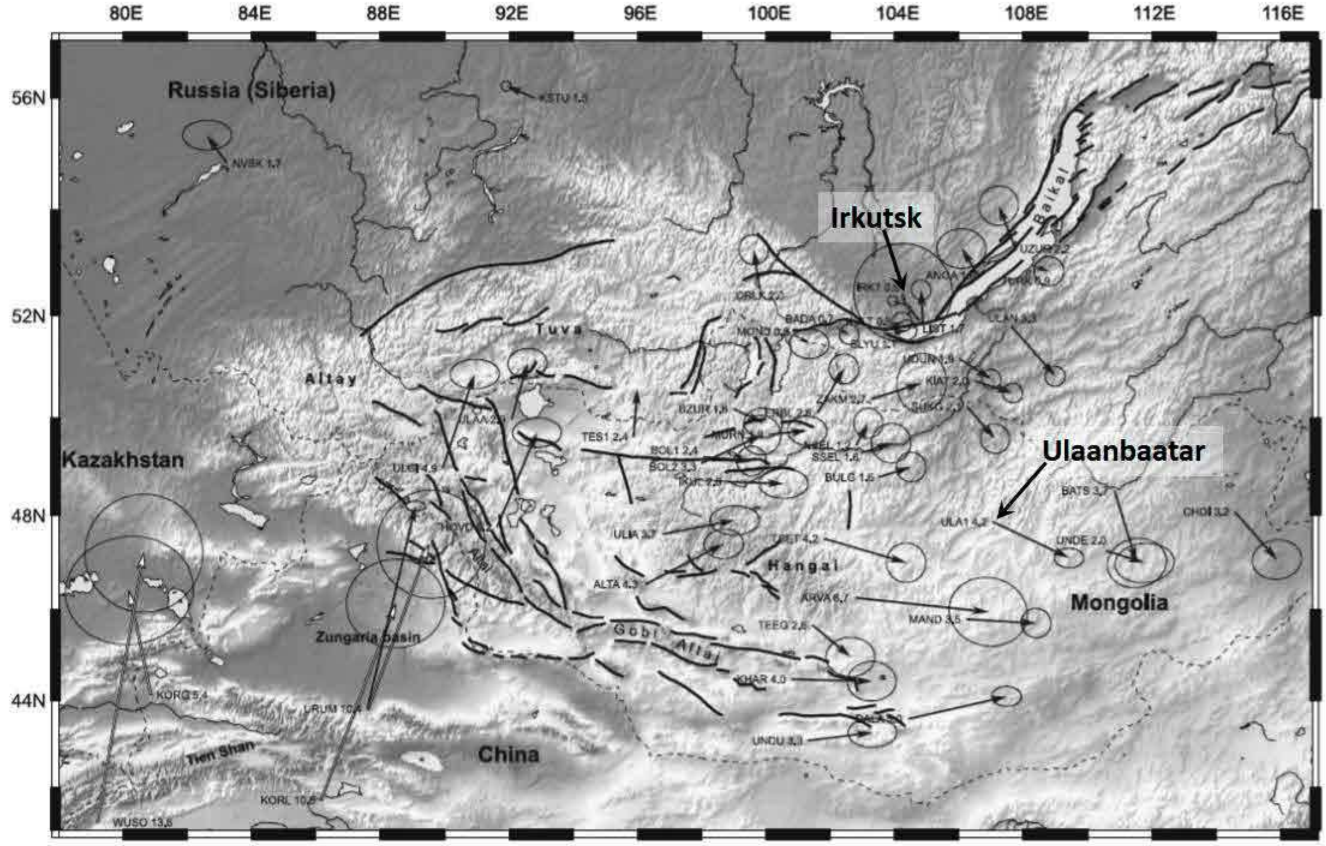

Figure 1.25. GPS-derived velocities with respect to Eurasia. Ellipses are 95% confidence. Numbers on the side of station names are velocities with respect to Eurasia in mm/year (after Calais et al., 2003).

Eleven years after the installation of high sensitive digital seismic stations (operational since 1994, see chapter 2.1.2), we detected an increase in the seismic activity including several moderate size earthquakes, with magnitude 3.5-5, which were felt in Ulaanbaatar by citizens. Therefore, a new interest in the area started and new studies have shown the presence of several active faults that were unknown before (Fleury et al., 2012; Dujardin et al., 2014; Schlupp et al., 2013; Al-Ashkar., 2015). Despite low seismicity and low deformation in the east part of the country in comparison with active deformations in Western Mongolia, the Ulaanbaatar area is more active than what was considered up to now. Here below, I will summarize the main known characteristics of these active faults.

Historicaly, three moderate sized earthquakes (Mw 5.4, 4.9 and 5.2) occurred in the same place within two years, at about 140 km to the west of the city (see chapter 2.1.3). On 3rd of December of 2005, one earthquake occurred in that place with magnitude 5.1.

1.2.4.3 Known active faults less than 100 km from Ulaanbaatar

The territory of Ulaanbaatar is located in a seismic stable area where only one important active fault, the Khustai fault, has been observed in the Khustai range. Another one, smaller, has been identified in the past to the NE of the city, the Gunj fault.

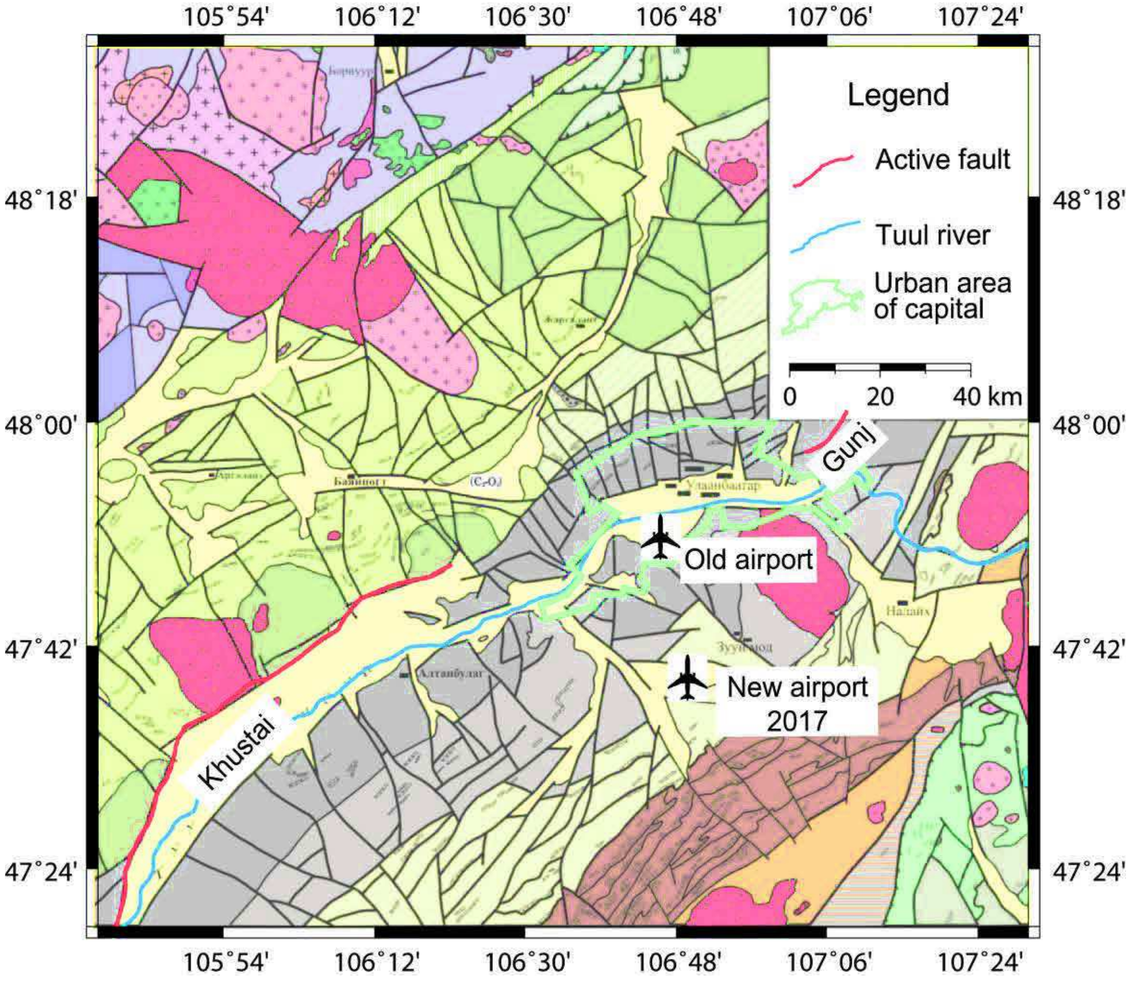

Figure 1.26. Simplified tectonic and geological map of study area (for geological map legend, see Figure 1.24), (modified after Tomurtogoo, 2009). Red lines are active faults around Ulaanbaatar.

1.2.4.3.1 Khustai fault:

The Khustai fault runs along the foot of the Khustai range on the right bank of the Tuul river between 50 to 100 km WSW of Ulaanbaatar (Figure 1.26). It has been studied in details by Ferry et al. (2010, 2012). The recent tectonic activity of the Khustai fault zone is reflected as a scarp affecting the piedmont plain and thalweg of valleys crossing the fault. It shows mixed normal and strike slip faulting geometries. Recent results of Ferry et al. (2010, 2012) suggest that the Khustai fault is presently active under a transtentional regime that reflects its intermediate location between large left lateral strike-slip faults of the Gobi-Altai in the southwest and major normal faults of the Baikal Rift in the north. The vertical amplitude of deformation measured here varies from 6 to 12 m. The Khustai Fault, with a total length of 111 km, can be devided in 2 main segments, of 80 and 31 km length based on ASTER image, SRTM digital elevation model and field observations. At some particular sites there are evidences of displacement produced by the latest events. Zones of fresh outcrops in bedrock show that the amplitudes of vertical displacement might be as high as 2-3 m. The scarps of the Khustai fault were probably produced by several earthquakes, but the dates of these events are unknown yet. If we consider that the whole 111 km of the fault could break in a single event, then it would be associated to an earthquake with magnitude 7.5 (Wells and Coppersmith, 1994). The latest moderate size earthquake that occurred on this fault was on May 06, 2008, with a magnitude M_L=3.5.

1.2.4.3.2 Gunj fault:

The Gunj fault was first investigated by Russian geologists in the framework of water supply research in 1980 but without detailed field survey in the fault area. This fault is located in a place named the “Gunjiin Am,” 18 km from the center of Ulaanbaatar city, and is oriented N45^0 (Figure 1.26). Russian and IAG team made a detailed field survey in 2010 associated with image interpretation (“SPOT-5” with 10 m resolution and “Google Earth” satellite images). A fragment of this fault, exposed by two paleoearthquakes, is traced northeastward for ~25 km from the northern urban area of Ulaanbaatar (Figure 1.26).

The first comprehensive seismogeological studies here were aimed at determining the seismic potential of seismogenic structures on the basis of the dislocation parameters. Judging by the strain amplitudes and length, the authors (Imaev et al., 2012) indicate that an earthquake with a magnitude of > 7.0 might be generated here but it seems to be overestimated when we use Wells and Coppersmith (1994) relations, that gives a magnitude of about 6.7. The paleoearthquake was dated by the radiocarbon method at 7800–4667 B.C. (Imaev et al., 2012). Right lateral strike-slip faults were observed here among active NE-trending faults, suggesting the presence of E–W compression (Imaev et al., 2012). Nevertheless, the authors did not clearly show the observations that bring them to consider a right lateral slip despite, considering the orientation of the fault, we expected a left lateral slip. This point has to be clarified in the future.

1.2.4.4 Recently discovered active structures (since 2008)

During the last 10 years, we (IAG, Mongolia with EOST and Geoscience Montpellier, France) strongly focused our research on active faults in the vicinity of Ulaanbaatar. This increasing interest for the area was triggered by the detection of a new and high seismic activity, since 2005, in the Songino-Sonsgolon area, which is located about 10 km west of Ulaanbaatar. We decided to make several detailed field surveys between 2008 and 2012 in targeted regions preliminary identified for some of them after satellite image analysis with a morphotectonic approach on newly available high resolution data (“SPOT-5” (10 to 5m), “Google Earth” and Pleiades satellite images) (Schlupp et al., 2012). In the field we did morphotectonic analysis followed by geophysical survey and paleoseismological investigations at precise targets along the active faults (Fleury et al., 2012; Dujardin et al., 2014; Schlupp et al., 2013; Al-Ashkar., 2015). We discovered 3 important active structures around Ulaanbaatar, the faults of Emeelt, Avdar and Sharkhai (Figure 1.27). Their main characteristics are summarized in the next sections.

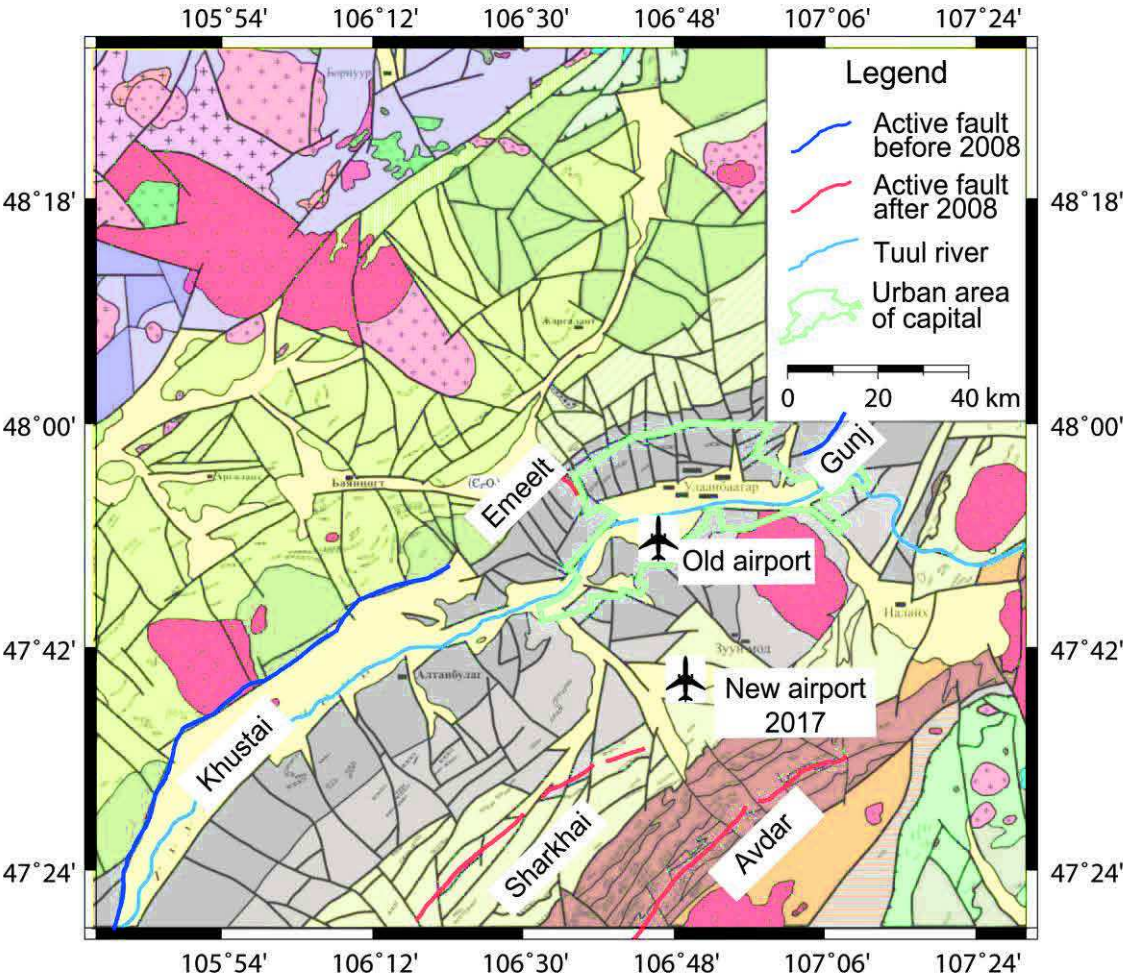

Figure 1.27. Simplified tectonic and geological map of study area (for geological map legend, see Figure 1.24), (modified after Tomurtogoo, 2009). Blue line is active fault known before 2008 and red lines are active faults discovered since 2008 around Ulaanbaatar.

1.2.4.4.1 Sharkhai fault:

The Sharkhai fault, located about 35 km SSW from the capital city, is oriented on average between N42 and N72 for a length of about 46 km (Figure 1.27). The northern end of this fault is located only 10 km away from the new International airport of Mongolia. The fault has been studied in details by Al-Ashkar (2015). The main characteristics are a linear and simple geometry. The fault is moslty left-lateral with meter scale cumulative offset. It can be divided into two segments of similar length. The paleoseismological investigations show evidences for three earthquakes, EQ3 before 3850 ± 120 yr calBP, EQ2 between 2400 ± 70 and 2030 ± 40 yr calBP, and the most recent earthquake (MRE) between 1090 ± 84 yr calBP and the age of modern soil. The return period of strong earthquakes on the fault Sharkhai is between 900 and 2400 yrs. The recurrence time for large earthquakes is 1195±157 yrs. The maximum slip rates vary from 0.6±0.2 to 2.14±0.5 mm/yr. Several segmentation scenarios of the fault are proposed indicating that the fault is capable to produce earthquakes of magnitude ranging from 5.8 up to 7. The cumulative offsets observed could show up to 23 earthquakes (Al-Ashkar, 2015) (Figure 1.28).

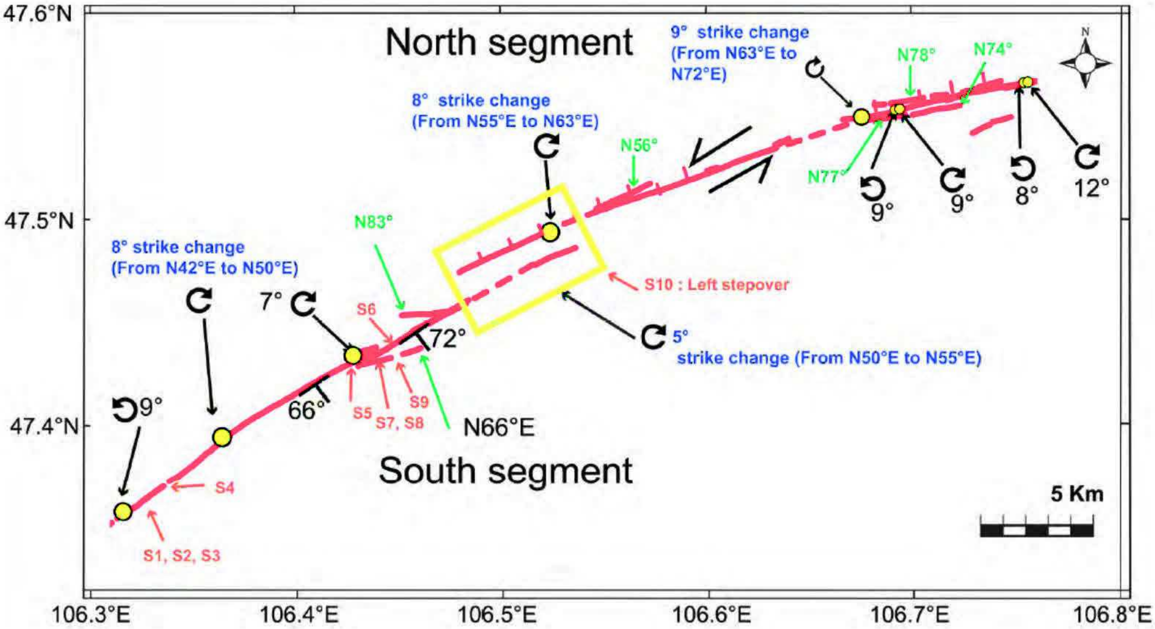

Figure 1.28. Major strike changes relative to the average direction of every segment along the Sharkhai fault (after Al Ashkar, 2015).

1.2.4.4.2 Avdar fault:

Al-Ashkar (2015) studied this fault in detail in the frame of her PhD (EOST, France) using geophysical survey, satellite images, field observations and paleoseismology. It is the first multidisciplinary study carried on this fault. It is located at about 43 km SSE from the capital and oriented on average $N40^0$ for a length of about 47 km (Figure 1.27). It is a left lateral strike slip fault that can be divided into several segments suggesting earthquakes of M=6.6-7. Paleoseismic investigations allowed to estimate the last earthquake as young as 5665 ± 85 yr calBP (Al-Ashkar, 2015) (Figure 1.29). The latest moderate size earthquake, recorded at NDC, occurred along this fault on March 22, 2009, with magnitude ML=4.2 (Figure 2.11). Several residents of Ulaanbaatar and Tuv province felt this event (Al-Ashkar, 2015) (Figure 1.29).

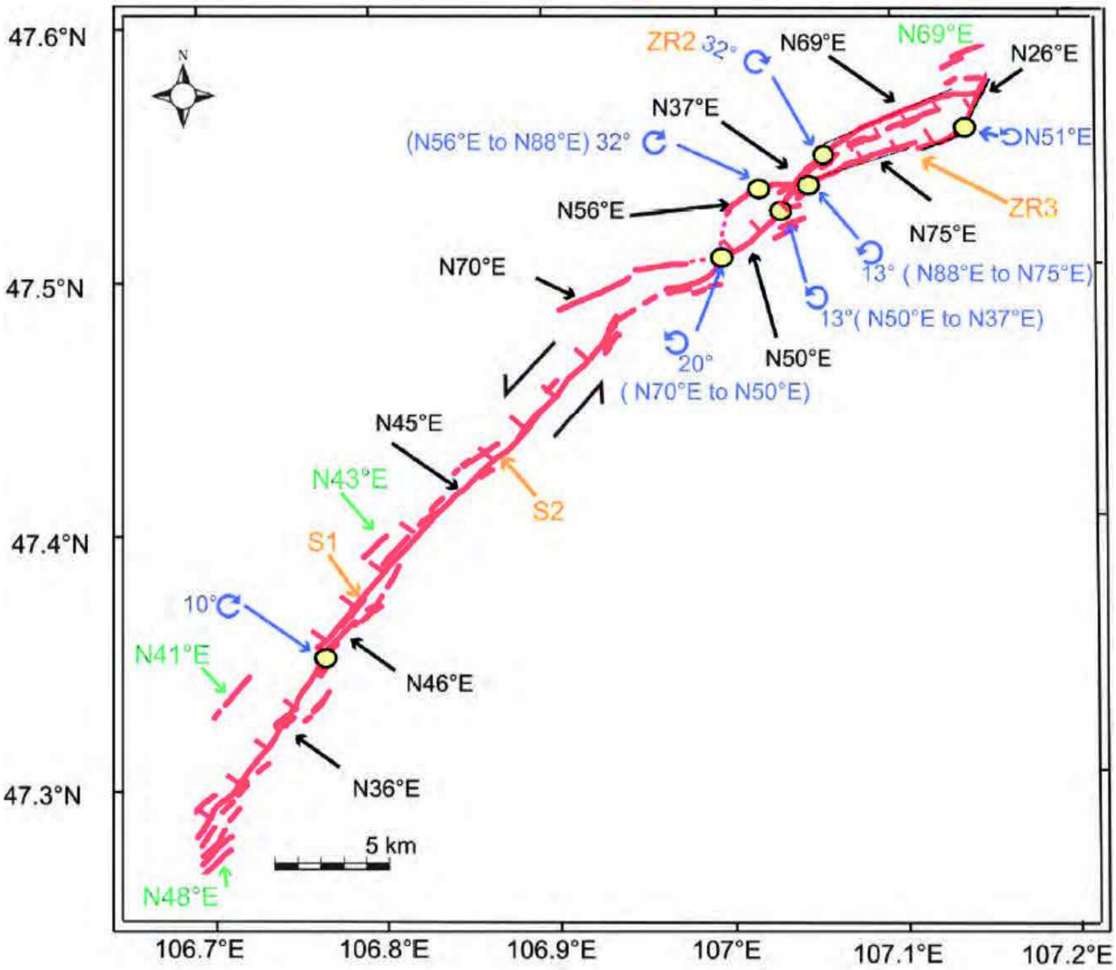

Figure 1.29. Detailed map of fault surface trace along the Avdar fault (after Al Ashkar, 2015).

1.2.4.4.3 Emeelt fault - **Study area**

The Emeelt fault (named after the nearest small town) is located between the capital and Emeelt town at an altitude of about 1500m. The Emeelt area lies in Devonien - Carboniferous formation mainly made of mudstone with interbedded sandstone (Kurihara et al., 2009; Minjin et al., 2006; Takeuchi et al., 2012).

Starting in the middle of 2005, a high seismic activity was detected, with low magnitude events, at 10 to 40 km west from Ulaanbaatar. The IAG and French teams did a morphotectonic field survey in the area of the seismic activity. They discovered eroded surface paleo-ruptures consistent with the characteristics of a new active fault, thus called the Emeelt fault (Figure 1.30) (Schlupp, 2007; Schlupp et al., 2010, 2012).

Figure 1.30. View to north of the Emeelt fault. Observed surface fault trace is marked by red line. Trenches in middle of the picture were made in 2010. Photo towards the north.

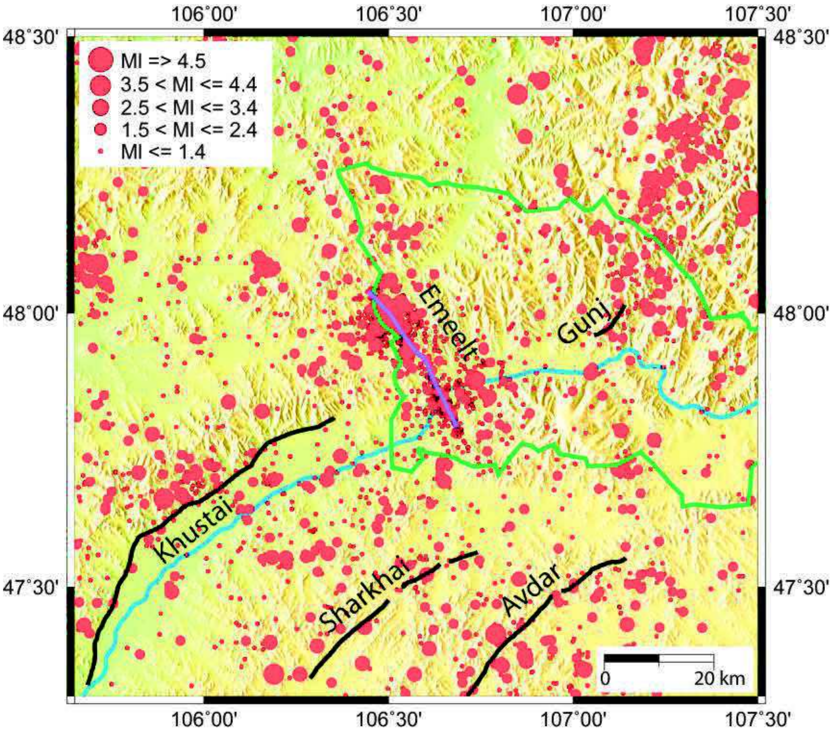

Figure 1.31. Epicentral map of earthquakes occurring between 1995 and 2013.01 around Emeelt fault (study area). Black lines represent active faults. Purple line is approximate Emeelt fault extension based on the distribution of seismic activity. Blue line is Tuul river and green line is asministrative border of Ulaanbaatar city.

At the site, only ~ 4-5 km long surface ruptures were observed (Figure 1.26), but the detected seismic activity occurred also more to the north and south in the same orientation as the surface ruptures. The estimated fault length is about ~ 35 km with a mean strike of N147N^0 considering the seismicity distribution based on National data center (NDC at IAG) catalogue (purple line in Figure 1.31). No clear surface ruptures were identified in the northern and southern part of the seismic activity zone.

The Emeelt fault was studied with satellite image interpretation, geophysical field survey such as high-resolution geomagnetic mapping, seismic survey, ground penetrating radar (GPR) and paleoseismology.

Field observations revealed the presence of a smoothed fault morphology (Figure 1.30) that we could clearly follow along the central branch of the present seismicity (Figure 1.31). The east side of the fault is uplifted and the morphology indicates that the fault is dipping toward the north-east. This geometry indicates a thrust component along the Emeelt fault.

Paleoseismological investigations, in trenches perpendicular and parallel to the fault, show that the recent sedimentary deposits have been cut and displaced by a rupture dipping to the east and associated to a large earthquake. This observation corresponds to the last event, as the deposits , of a thickness of about 1.5m, covering the top of the rupture are not affected. A reverse component (compression) is observed but the main component is horizontal slip.

In the trench we observed clear paleo-river crossing the fault that we followed using pseudo three dimensional GPR profiles. We imaged then a right lateral offset of the stream right bank of about 2m (Figure 1.32) (Dujardin et al., 2014).

Dating (using OSL technique) of the fault displacement gives an age of the last earthquake of about 11000 yrs. This age is consistent with the smoothed morphology, the erosion-deposit process, the fault scarp and the thickness of the deposits covering the last observable break (Schlupp et al., 2010, 2012).

One of the main results of Dujardin et al., (2014) is a strong reflector dipping from 27^0 to 35^0 towards the NNE, which corresponds to the Emeelt fault plane at depth. In addition, the observations done at the bottom of the trench at depth between 1.5m and 2.5m show several ruptures but with steeper angles, mainly from 30^0 to 45^0.

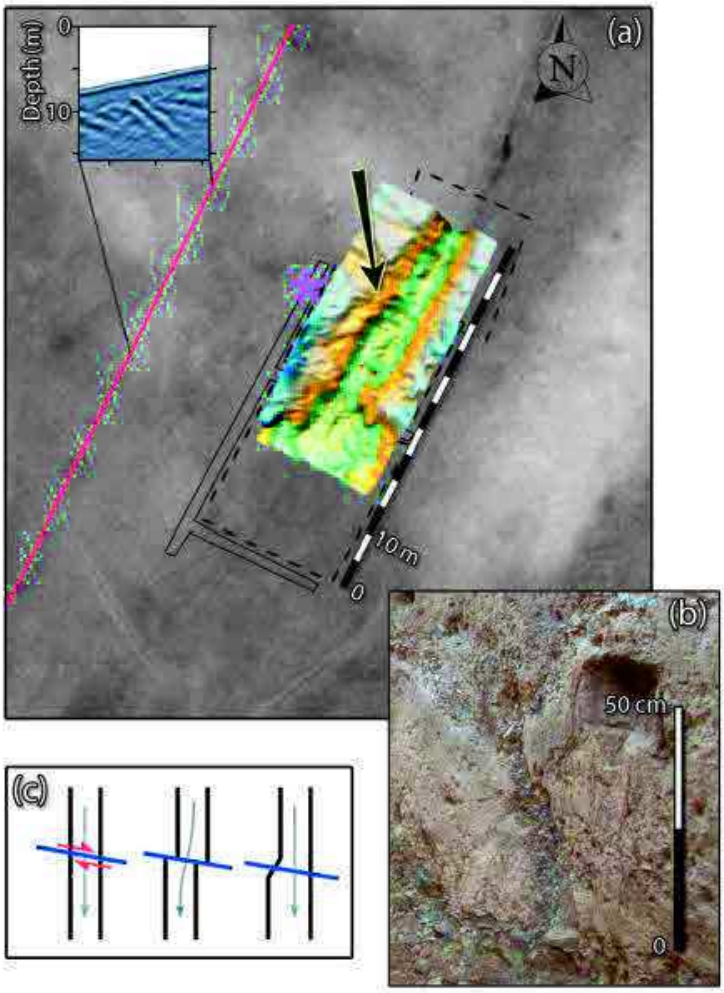

Figure 1.32. Interpretative map of trench area. The interpolated 3-D surface of the channel (after subtraction of its main slope) is superimposed on the satellite image. A horizontal offset of 2 m is observed on the NW riser of the channel (see black arrow), which is consistent with right lateral strike-slip. Pink asterisk shows location of picture (b) in trench where faulting is observed. Closest GPR profile (upper left corner) shows record and location of fault-plane at depth. (c) Evolution sketch of channel banks due to right lateral strike-slip. Downstream right bank is preserved while downstream left bank is eroded after shifting. Sedimentaion in the palaeochannel fossilizes the paleomorphology (after Dujardin et al., 2014).

Seismic profile and radon observations in the area of the Emeelt fault:

To better identify the structures in the last undreds meters under the surface, a seismic profile has been done in 2013 across the area of the main seismic activity for a length of about 7km (Figure 1.33). The data of the profile has been analysed in the frame of a Master diploma by Bolaty (2015) and supervised by Guy Senechal (France, Pau University). I do not describe theses observations alone at this step but I propose to see the discussion in the chapter 5 for a comparison with the relocated seismicity.

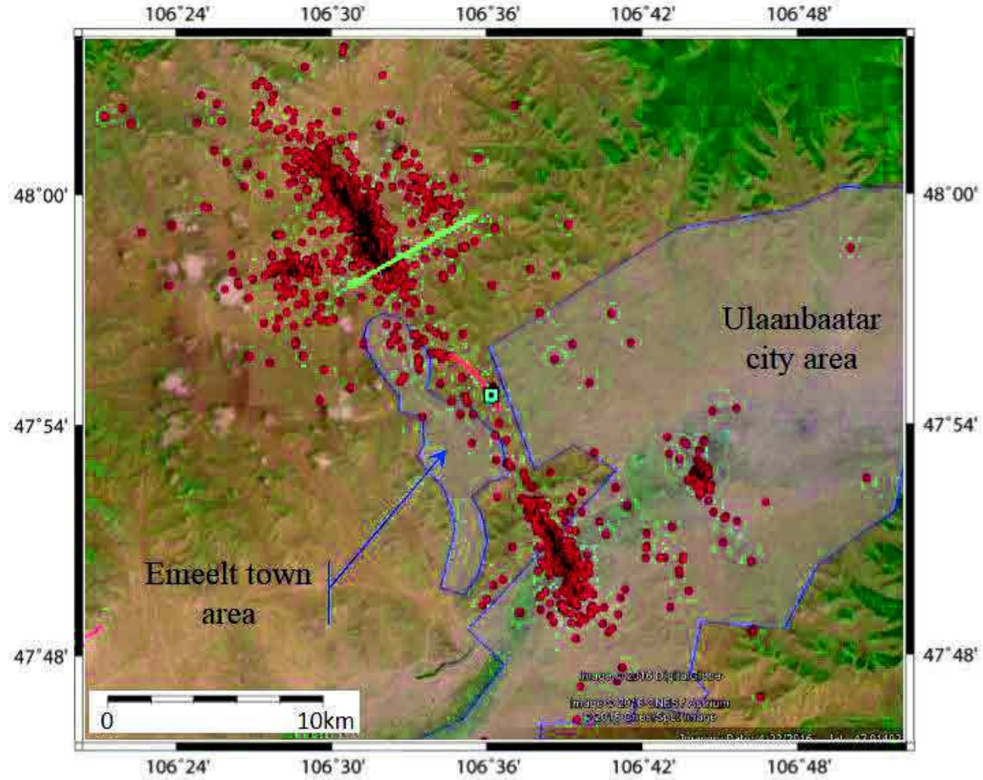

Figure 1.33. Seismicity map in Emeelt fault area (NDC catalog). Red line is surface rupture of Emeelt fault. Aqua square is position of trench site. Green line is extension of seismic profile.

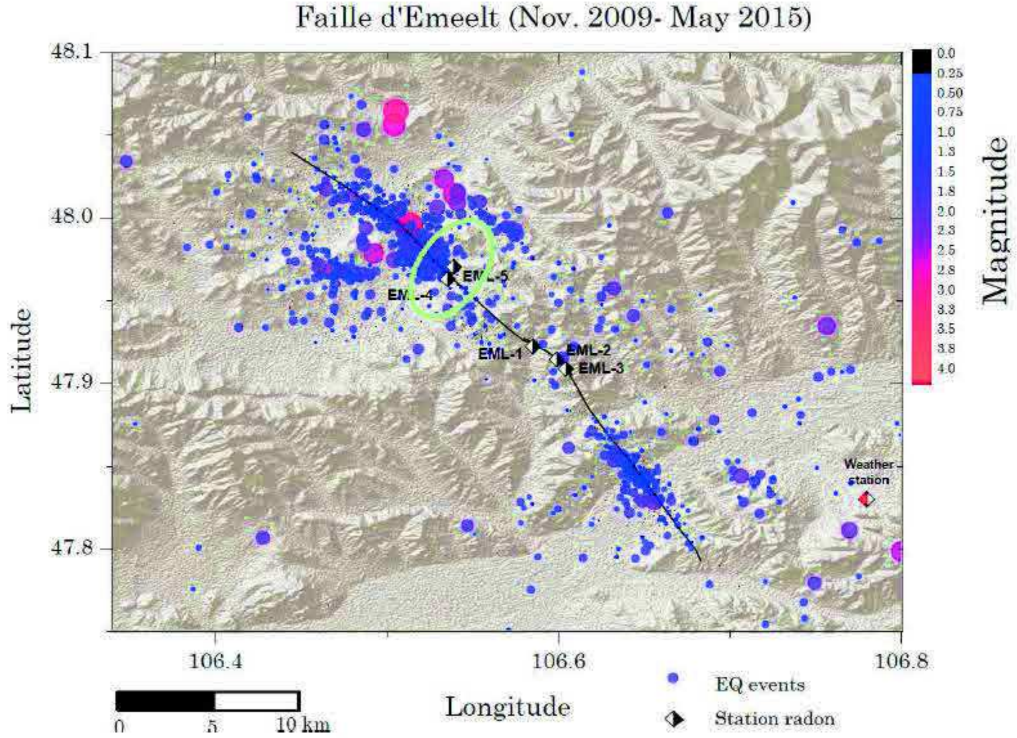

Figure 1.34. Event location (NDC result) map with position of radon stations (after Richon et al., 2015).

Three radon stations (EML-1, EML-2, EML-3) have been installed (IAG and DASE) in December 2009 in the Emeelt fault zone where surface ruptures were observed and one in the Khustai fault area (Hust-4) (Figure 1.34). Additionally in July 2015, we (IAG and DASE) have added two more stations northward (EML-4 and EML-5) in the southern part of the main seismic active area. All this work has been implemented through a collaboration with DASE. The relation of Radon anomalies with the seismicity will be discussed in chapter 5.

1.2.4.5 Summary of main characteristics of active faults around Ulaanbaatar

The discovered active structures and paleo-earthquakes show that the region near Ulaanbaatar, within 150 km, is active with active faults reaching several tens of kilometers. Their surface rupture, despite being eroded, are the result of large earthquakes as observed during paleoseismological investigations (Schlupp et al., 2007, 2010, 2012, 2013; Ferry er al., 2010, 2012; Fleury et al., 2012; Imaev et al., 2012; Dujardin et al., 2014; Al-Ashkar, 2015).

Table 1.1. Known characteristics of active faults in the vicinity of Ulaanbaatar.

Fault name	Distance from center of Ulaanbaatar[1] to closest point of fault	Fault type	Fault total length	Estimated magnitude (Mw)	Age of last event yr BP
Khustai	~40 km (N254^0)	Left lateral strike slip	~ 111 km	7.5	1000
Gunj	~12 km (N64^0)	Right lateral strike slip (?)	~ 25 km	> 7	5577-9321
Sharkhai	~42 km (N198^0)	Left lateral strike slip	~ 46 km	5.8-7	1195±157
Avdar	~42 km (N159^0)	Left lateral strike slip	~ 47 km	6.6-7	< 5665±85
Emeelt	~25 km (N273^0)	Right lateral strike slip + reverse	~ 35 km [2]	6.5-7	~ 11000±2000

These new structures are very important for our seismic hazard estimation, because of their proximity to Ulaanbaatar and because we have still a weak knowledge on these intermediate size structures.

---

[1] Center of Ulaanbaatar city is: Latitude 47.918799; Longitude 106.917605.

[2] Length estimated based on epicentral distribution of microseismicity.

2 Chapter 2: Seismicity around Ulaanbaatar and Emeelt fault area

2.1 Seismic networks and their recent development near Ulaanbaatar.

2.1.1 Overview of the national networks

The first national seismic station was installed in 1957 as the first three components analog SKM-3 seismic station in Ulaanbaatar. Then we, RCAG (now called IAG), developed the network over the whole country and we were able since 1964 to detect and locate all events of $M_L > 3.5$ in Mongolia. The network increased until middle of 1988 with 10 analog seismic stations distributed over Mongolia, mostly in its western part that is characterized by a high seismic activity, particularly due to numerous aftershocks of the four earthquakes of magnitude 8 of 1905, 1931 and 1957.

Nevertheless, it was still difficult to detect and locate small magnitude events near Ulaanbaatar. Until 1994, we had only one analog seismic station running in Ulaanbaatar and the next nearest seismic station was far to the NW, 290 km from Ulaanbaatar in Bulgan Aimag (BLG station) (Figure 2.1). Thanks to the collaboration with CEA/DASE (France) starting in 1994, we installed a new digital, high sensitive, telemetrered seismic network around the capital.

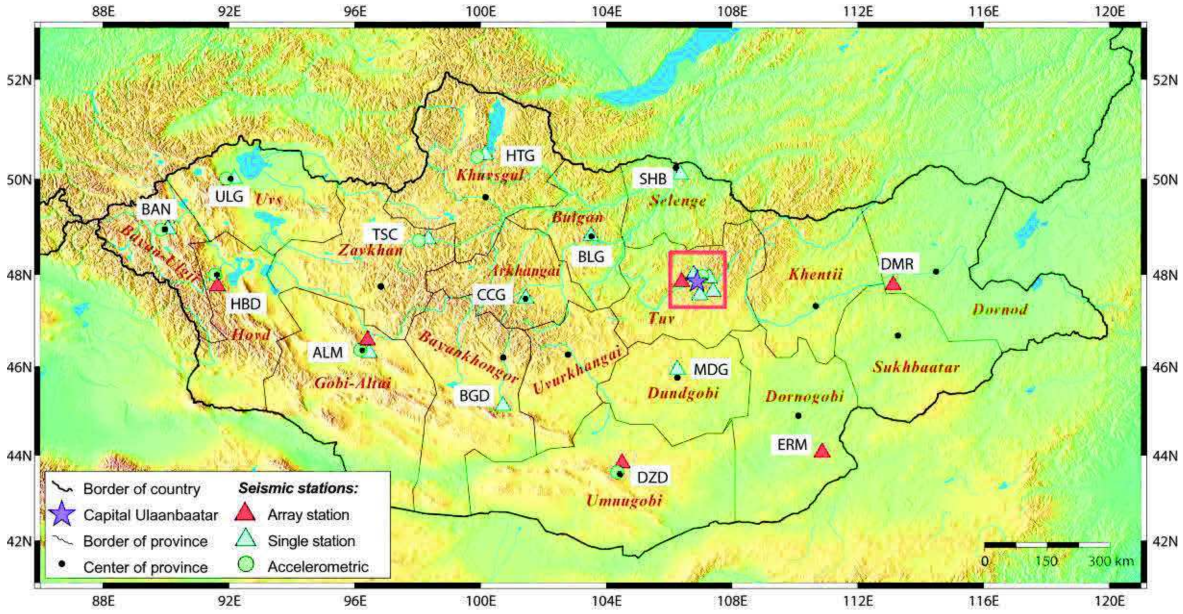

Figure 2.1. Permanent seismic stations network of Mongolia (2015). The area delineated by a red square corresponds to Figure 2.2.

The stations around Ulaanbaatar, at less than 150 km from the city, are now distributed into four networks, three of them are permanent, and all the data are combined at the National Data Centre (NDC):

- “UB array”, the initial permanent seismic stations network developed since 1994 around Ulaanbaatar city (Figure 2.1 and Figure 2.2)
- “CTBT Songino-array” a permanent network installed at about 40 km west of Ulaanbaatar centre in 2000 in the frame of the Comprehensive Nuclear-Test-Ban Treaty
- “UB-mobile”, a temporary network installed between December 2008 until beginning of 2013 to the west of Ulaanbaatar, near the city of Emeelt where an important seismicity is observed and studied in this PhD
- “UB-guralp”, a permanent network installed since October 2012, a multi-sensor geophysical network distributed in a radius of about 150 km from the capital, with 16 broadband seismic stations (Figure 2.2), 7 GPS stations, 5 tiltmeter stations and 3 geomagnetic stations.

These four networks around Ulaanbaatar will be detailed in the next paragraphs.

Since 1994 and outside Ulaanbaatar area, we have also increased progressively the number of seismic stations in whole Mongolia and upgraded existing stations by high sensibility, digital, telemetry seismic stations (Figure 2.1). This includes several mini-arrays, three in collaboration with DASE (CEA-France) in 1997, 2000 (CTBT-array) and 2012 (each with one broad band and 6 to 7 short period Z component), and three in collaboration with Air Force Technical Applications Centre (USA) in 2006 (each with 9 short period Z component and one broad band station, all in borehole at 40 to 60m depth) (Figure 2.1). The last upgrade was at the end of May of 2014, when we installed two new stations, SHB and MDG located respectively at 270 km north and 260 km south (at the Deren’s seismic activity area) from Ulaanbaatar (Figure 2.1).

Today, the Mongolian seismic networks are widespread over 15 sites (Ulaanbaatar region is considered here as one site) that have, all together, over 70 high sensibility digital seismic stations. Data are all transmitted in near real time to the NDC of IAG where the waveforms are integrated into a database and the interpretations are done (hypocentral location, magnitude, etc).

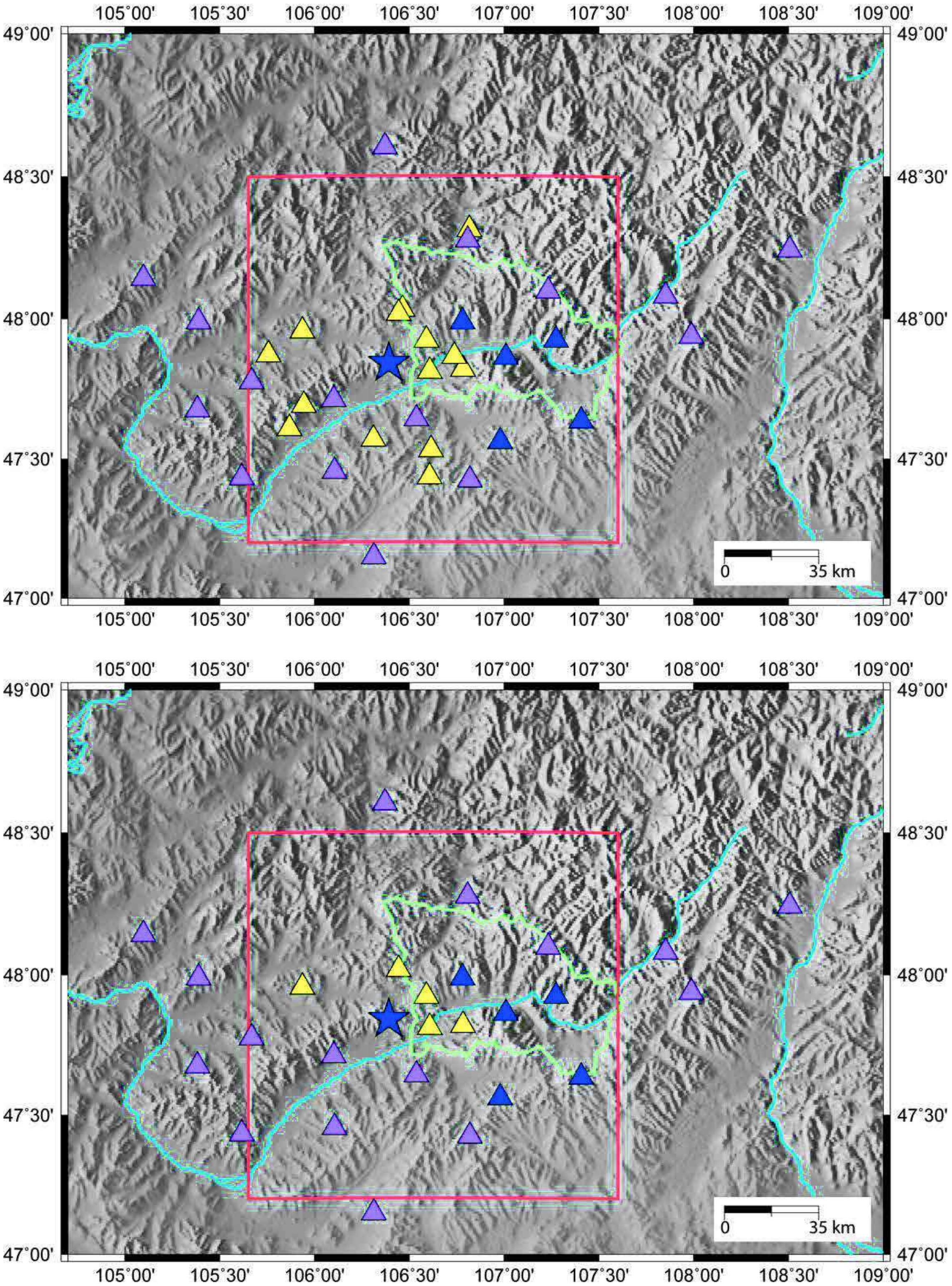

Figure 2.2. Seismic network around Ulaanbaatar: Top figure: All stations that were operational in the area. Bottom figure: Stations operational today (situation in November 2015). The area delineated by a red square corresponds to Figure 2.3. Blue line is Tuul river and green line is asministrative border of Ulaanbaatar city. Blue: permanent network "UB-array", yellow: temporary network "UB-mobile" and purple: new seismic network "UB-guralp". For details of working period see table 2.1.

2.1.2 Permanent networks around Ulaanbaatar: "UB array", "CTBT Songino-array" and "UB-guralp"

The first three components and analog seismic station SKM-3 has been running in the underground part of the building of IAG in Ulaanbaatar (installed on the rock) from 1957 until October 1994. In 1994, the first digital stations array "UB-array", with telemetric transmission, was installed around Ulaanbaatar up to a distance of 70km in collaboration with DASE (CEA, France). This network consists of one 6 components station (3 long period and 3 short period components-ALFM), and 5 vertical short period stations (ARTM, SEMM IVGM, TSAM, UGDM) but 2 stations are stopped now: IVGM and TSAM (blue triangle in Figure 2.3 and Table 2.1). Moreover, also in 1994, a broadband seismic station (ULN) was installed 20 km to the east of Ulaanbaatar in cooperation with the Incorporated Research Institutions for Seismology (IRIS) and data are available through IRIS. It is included into the "UB-array" network. Continuous records are sent in real time to the Mongolian National Data Centre of IAG (NDC) by radio frequency (UHF). The aperture of this network was calculated to allow consistent region monitoring in real time. This first improvement of the seismic network around Ulaanbaatar has allowed to increase the detection level in this area and to better characterize the earthquakes.

Later in 2000, we have installed a "primary CTBTO technology", "CTBT-Songino-array" including a seismic mini-array PS25, infrasound mini-array IS34, radionuclide-RN45 and SPALAX stations, all at about 40 km WSW from Ulaanbaatar (blue star in Figure 2.3). The PS25 array is spread on a 4 x 4 km area, the minimum distance between two stations is 500 m and the maximum distance is 5 km. This array is included into the 50 primary stations network of the International Monitoring System to verify the future CTBTO and therefore must be operational continuously with strict quality criteria. The data are sent continuously and in near real time to the International Data Centre through the French National Data Centre using VSAT facilities.

Since October 2012, we are developing a multisensor geophysical stations network, which consist of 16 broadband seismic stations (named "UB-guralp") (Figure 2.2), 7 GPS stations, 5 tiltmeter stations and 3 geomagnetic stations distributed up to about 150 km from the capital.

2.1.3 Temporary network around Ulaanbaatar – "UB mobile"

From the middle of 2005, a high seismic activity is observed, with low magnitude, 10 to 40 km west of Ulaanbaatar with the "UB-array" and "CTBT-Songino-array". Therefore, starting end of

2008, we installed 10 temporary seismic stations (CMG3 and LE-3D sensors), covering an area of 80 x 100 km west of Ulaanbaatar (yellow triangles and UB9, now replaced by an accelerometer, in Figure 2.3). The aim of this network was to precisely locate the events and understand their origin, in relation with faults and study the possible impact on the seismic hazard of the Ulaanbaatar region. During the seismic swarm of 2013, we installed in addition 4 stations in the Emeelt area (aqua colour in Figure 2.3) to increase the number of station at south and north of the seismic activity and improve their location. Unfortunately, these stations were running only 14 days beginning of 2013 due to priority projects and insufficient mobile stations at IAG. Now, we stopped some stations of the "UB-mobile" network as we developed the "UB-guralp" permanent network in the area (Figure 2.2). The "UB-guralp" stations are used for daily interpratation since February of 2013.

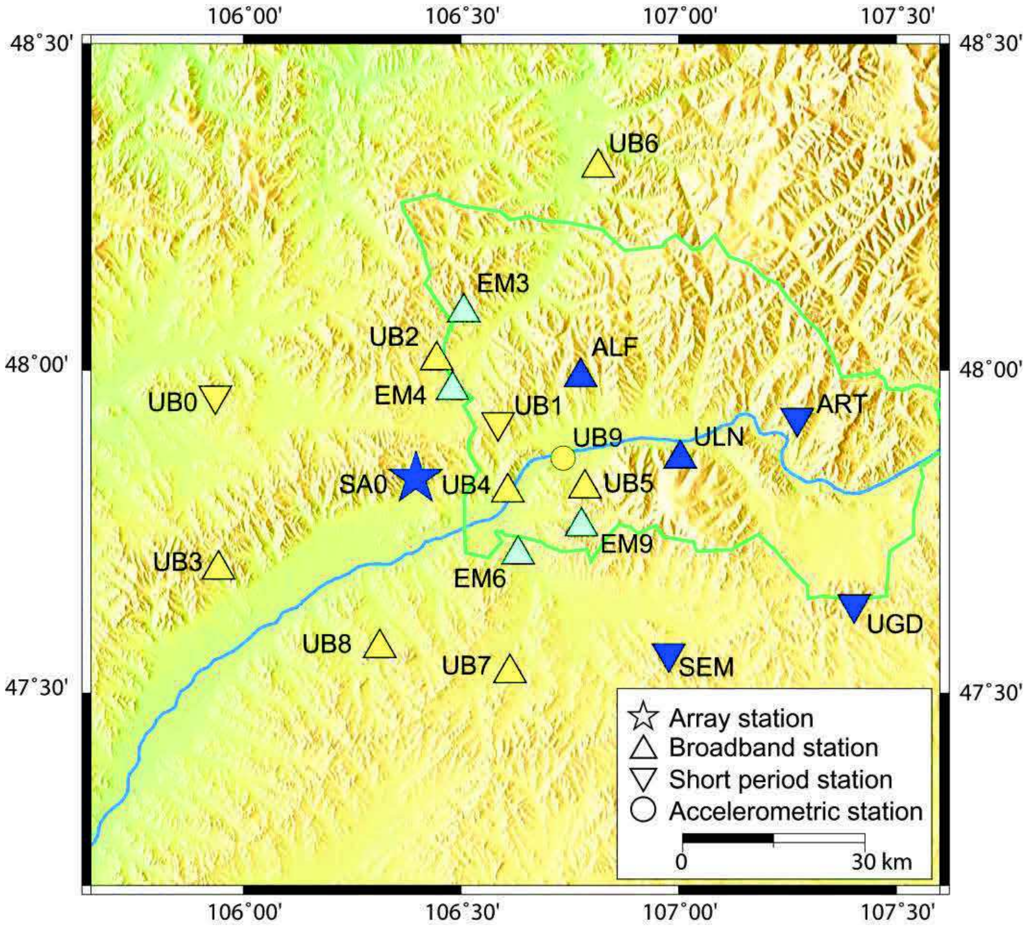

Figure 2.3. Seismic network around Ulaanbaatar area (in January 2013) used in this PhD work. Blue line is Tuul river and green line is asministrative border of Ulaanbaatar city. Blue: "UB-array", yellow triangles: "UB-mobile", and aqua: additional mobile stations active during 2 weeks in 2013.

Table 2.1. Time history of the development of the seismic networks around Ulaanbaatar (2013.01).

Station name	Geographical coordinates		Altitude of station (m)	Station recording time		Station type	Comments
	Lat (N)	Long (E)		Start	Stop		
UBR	47.920	106.955	1330	1957.07	1994.10	Short period_3 com	The first analog seismic station
UBR	47.920	106.955	1330	1994.10	2006	Short period_Z com	UB array
ARTM	47.927	107.270	1916	1994.10	-	Short period_Z com	UB array
SEMM	47.563	106.976	1700	1996.11	-	Short period_Z com	UB array
UGDM	47.638	107.401	1869	1995.09	-	Short period_Z com	UB array
IVGM	47.400	106.571	1900	1994.09	2005.12	Short period_Z com	UB array
JAVM	47.988	106.774	1860	1994.09	1997.11	Short period_Z com	UB array
TSAM	47.714	107.111	1963	1994.09	1998.05	Short period_Z com	UB array
ULN	47.865	107.053	1610	1994.12	-	Broad band_3 com	IRIS station, UB array
ALFM	48.004	106.772	1590	1995.09	-	Short period_3 com Long period_3 com	UB array
SA0*	47.835	106.395	1416	2000.10	-	Short period_3 com Long period_3 com	UB array
UB1M	47.923	106.587	1376	2008.12	2009.05	Broad band_3 com	UB mobile
UB1M	47.923	106.587	1376	2009.05	-	Short period_3 com	UB mobile
UB2M	48.036	106.464	1436	2009.03	2009.08	Broad band_3 com	UB mobile
UB2S	48.019	106.443	1455	2009.08	-	Broad band_3 com	UB mobile
UB3M	47.872	106.757	1235	2008.12	2009.06	Broad band_3 com	UB mobile
UB3S	47.693	105.941	1311	2009.07	-	Broad band_3 com	UB mobile
UB4M	47.815	106.608	1209	2008.12	-	Broad band_3 com	UB mobile
MO5M	47.610	105.868	1259	2008.12	2009.05	Short period_3 com	UB mobile
UB5M	47.819	106.782	1389	2009.06	-	Broad band_3 com	UB mobile
UB6M	48.315	106.814	1233	2009.03	-	Broad band_3 com	UB mobile
MO7M	47.438	106.603	1543	2008.12	2009.04	Short period_3 com	UB mobile
UB7M	47.533	106.611	1474	2010.04	-	Broad band_3 com	UB mobile
MO8M	47.570	106.312	1331	2008.12	2009.05	Short period_3 com	UB mobile
UB8M	47.570	106.312	1331	2009.05	-	Broad band_3 com	UB mobile
UB9M	47.867	106.737	1250	2009.05	2009.06	Short period_3 com	UB mobile
UB9M	47.867	106.737	1250	2009.06	2010.02	Broad band_3 com	UB mobile
UB0M	47.960	105.936	1360	2010.05	-	Short period_3 com	UB mobile
EM3M	48.092	106.505	1391	2012.12	2013.01	Broad band_3 com	UB mobile
EM4M	47.972	106.481	1383	2012.12	2013.01	Broad band_3 com	UB mobile
EM6M	47.728	106.630	1244	2012.12	2013.01	Broad band_3 com	UB mobile
EM9M	47.762	106.778	1399	2012.12	2013.01	Broad band_3 com	UB mobile

SA0* - “CTBT-Songino-array” is a mini-array with ten stations. SA0 is one of these stations.

2.2 Earthquake location procedure of NDC

Before 1994, all earthquakes were analysed manually in Ulaanbaatar. As the events were recorded on photopaper, they were sent from the station to Ulaanbaatar for their analysis. For large events, the phases were picked at the stations by local employers, and arrival times transmitted by phone to Ulaanbaatar. The events were localized using the “EPIC” software, developed by IAG, giving event origin times, location of epicentres, magnitude and associated errors. The estimation of the depth was very difficult because of the large distance between permanent seismic stations (a mean distance of about 250 km) and most of the time, the depth of the events was not determined.

Since 1994 and the installation of the first digital stations telemetric array around Ulaanbaatar, “UB-array”, all data are daily interpreted and the main events are localized in short real time at the NDC where there is a 24h/24h duty. Only after about 2 weeks the informations of analog stations is send by regular post. A that time, the event parameters, located preliminary only with the “UB-array”, are upgraded.

Nowadays, all data from all seismic stations are collected in the NDC in near real time using either VSAT facilities or Internet connections. The “ONYX” location software developed by DASE (CEA, France) is used to analyse the events in near real time. Unfortunately, aside few events in specific areas, it is still difficult to determine the focal depth of earthquakes.

2.3 Seismicity around Ulaanbaatar

2.3.1 Overview of the seismicity in the vicinity of Ulaanbaatar (area of 400x400 km)

The seismic activity observed in the vicinity of Ulaanbaatar is relatively low compared to the activity observed in western Mongolia.

The histogram of detected events in the vicinity of Ulaanbaatar shows several increases of earthquakes number. The first and largest is in 1994, and then others occur in 1995, 2001, 2005, 2010 and 2012 (Figure 2.4). The increased number of observed events in 1994 is explained by the important network improvement that happened in September 1994. It changed drastically the detection capacity as shown in the histogram, without specific change in the seismicity level (only small events). The “CTBT-Songino Array” installed in October 2000 contributes to the quality of the location but did not improve much the detection level in the Ulaanbaatar area as it is used as a single station. The other increases of earthquakes observed in 2005, 2010 and 2012 are related to the recording of new seismic activity (swarms) along the Emeelt faults, which are the focus of this study. Notice that at the end of 2008 a local upgrade of the seismic network occurred that could explain partially the small increase of observed seismicity in 2009.

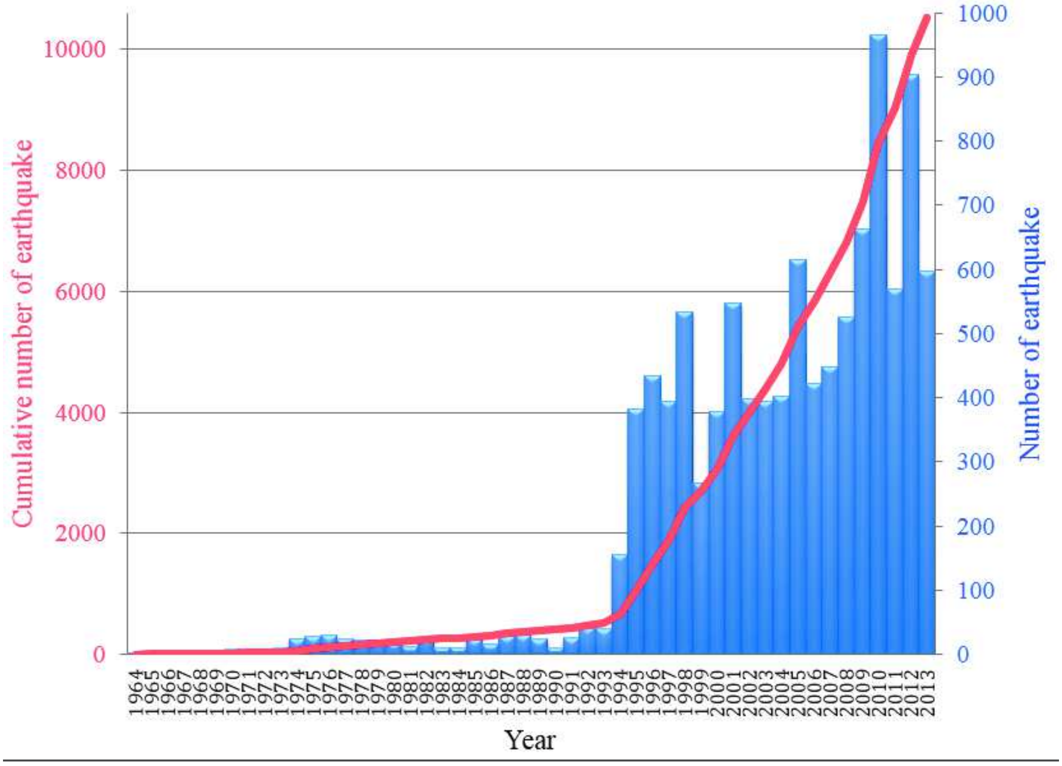

Figure 2.4. Histogram of events detected in the vicinity of Ulaanbaatar between 1964 and January 2013 (area of 400x400 km).

We can consider three periods of observation for the seismicity in the vicinity of Ulaanbaatar: ***historical*** (until 1964), ***early instrumental*** (1964-1994) and ***recent instrumental*** (1995-2014) observation periods, based on the detection level of the seismic stations in the area of Ulaanbaatar.

2.3.1.1 Seismicity of the historical period (before 1964)

There are only few events noted in this area in the earthquake bulletins at NDC of IAG (Table 2.2 and Figure 2.5).

The moderate sized earthquakes (M= 4.7 to 5.4), which occurred in 1925 and 1927 are also reported in the bulletin of the International Seismological Centre (ISC).

The location of the 7th Dec 1947 event, using macroseismic data, was first estimated between 70 to 80 km to the northeast of Ulaanbaatar (Natsag-Yum et al., 1971). But later on, using the same macroseismic data, other authors estimated that this earthquake occurred inside the Ulaanbaatar basin in the area of “Sonsoglon and Songino” (Khilko et al., 1985), which is located to the west of Ulaanbaatar, in the area where we observe today a high seismic activity. The authors mention that it is one of the biggest events, which occurred in this area. They estimate a magnitude of 4.7 deduced from macroseismic data. However, due to the lack of detailed macroseismic data (Khilko et al. 1985) location of this earthquake is still poorly constrained and the uncertainty are difficult to estimate.

Table 2.2. Known historical earthquakes in the vicinity of Ulaanbaatar (after Khilko et al., 1985). Notice that the distance from the central point of the city is poorly constrained as the event location are themselves poorly contrained (uncertainty are not available)

	Date	Origin time (UTC)	Location		Magnitude	Distance from central point of city [km]
			Latitude (N)	Longitude (E)		
1	1925-02-07	17:23:50	48.00	105.00	5.4	143
2	1925-06-24	16:11:24	48.00	105.00	4.9	143
3	1927-02-27	03:20:00	48.00	105.00	5.2	143
4	1927-10-20	20:21:56	49.60	104.30	4.7	267
5	1947-12-07	17:36:00	47.80	106.70	4.7	21
6	1957-09-06	12:52:50	47.60	104.50	4.1	184
7	1961-03-27	15:28:40	49.40	106.00	4.3	178
8	1962-04-06	07:46:11	49.00	105.90	4.0	142

There are two other earthquakes noted in this area by Natsag-Yum (1971), but both of them have no any information about the magnitude and very poor locations.

The first one was recorded 10 November 1960 (Natsag-Yum et al., 1971) in the Sonsoglon and Songino active area. Its epicentre was located ~5 km to the south of the Chinggis Khan airport (International airport of Ulaanbaatar). The epicentre location is very poorly constrained as it was recorded only by the three components seismic station of Ulaanbaatar (UBR). However, residents of Ulaanbaatar felt this event widely with intensity III (MSK64).

The second one occurred 2 December 1961 and was recorded at several Mongolian and Russian seismic stations. The epicentre was estimated 20 km to the north of Ulaanbaatar. There is no any information about its magnitude, but it could be around 4-5, because it was recorded at Russian stations more than 600 km away.

2.3.1.2 Seismicity of the instrumental period

The "***early instrumental***" (1964-1994) period corresponds to a low number of seismic stations characterized by low sensitivity. It induces a poorly constrained location of the seismic activity in the vicinity of Ulaanbaatar especially for the small events. There are only 672 earthquakes localized in this area between 1964 and 1994 (Figure 2.5) in comparison to more than 10 000 between 1995 and 2013.1.

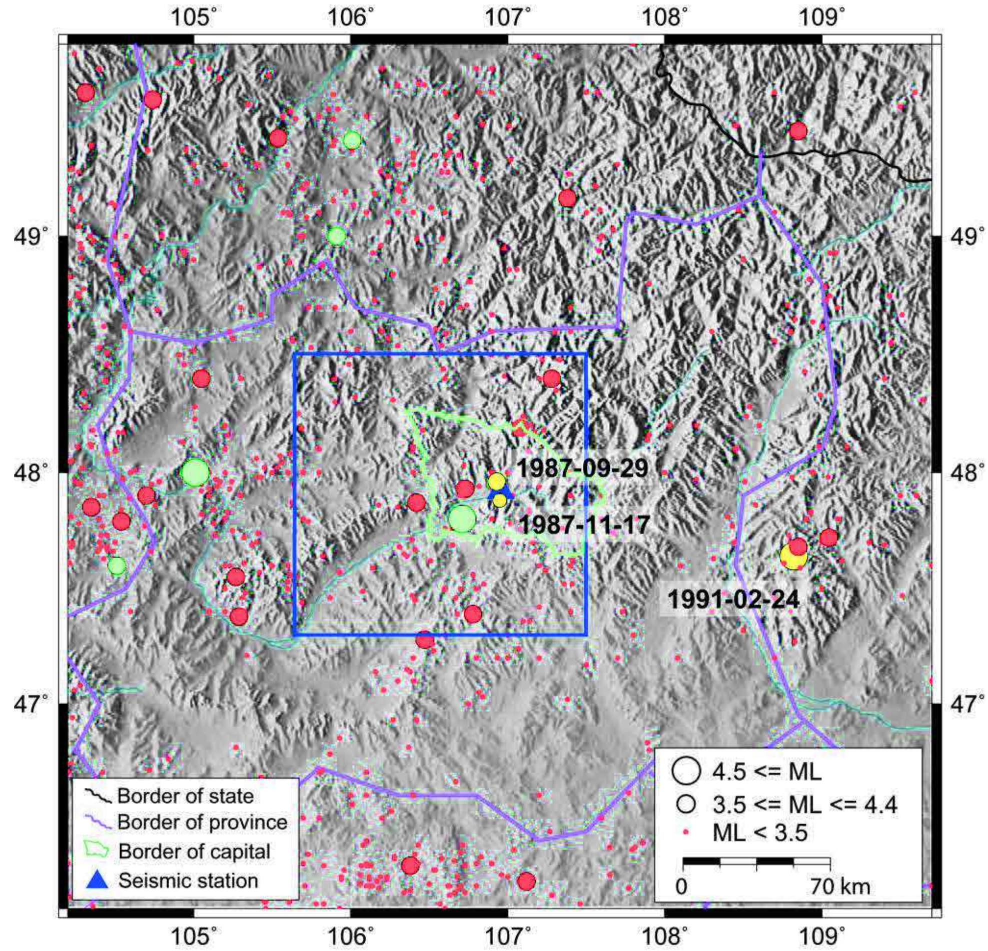

Figure 2.5. Map of seismicity and seismic stations in the vicinity of Ulaanbaatar (area of 400x400km) between 1925 and 1994. Green: historical events (between 1925 and 1963, (see Table 2.2) and yellow color show felted events (see Table 2.3). Green line is asministrative border of Ulaanbaatar city. Blue square is Figure 2.11.

The "***recent instrumental***" period covers the end of 1994 to the present time. Since October 1994 the installation of new high sensitive digital stations, with continuous recording, increased the detection capacity and allowed to localize more precisely the seismic activity of the Ulaanbaatar region, even for very small earthquakes. Using these data, it was possible to start to constrain the depth of the events. During this time, 9843 earthquakes were detected and located with a magnitude up to 5.6, but about 90% of them are very small events with local magnitude of less than 2.5. Nevertheless, these events are important to characterize the active zones. Among the largest events recorded, 978 have magnitude between 2.5 to 3.4, 108 between 3.5 to 4.4, 11 between 4.5 to 5.4 and one with magnitude 5.6, which corresponds to the Deren earthquake that occurred 24 September 1998 (Figure 2.6).

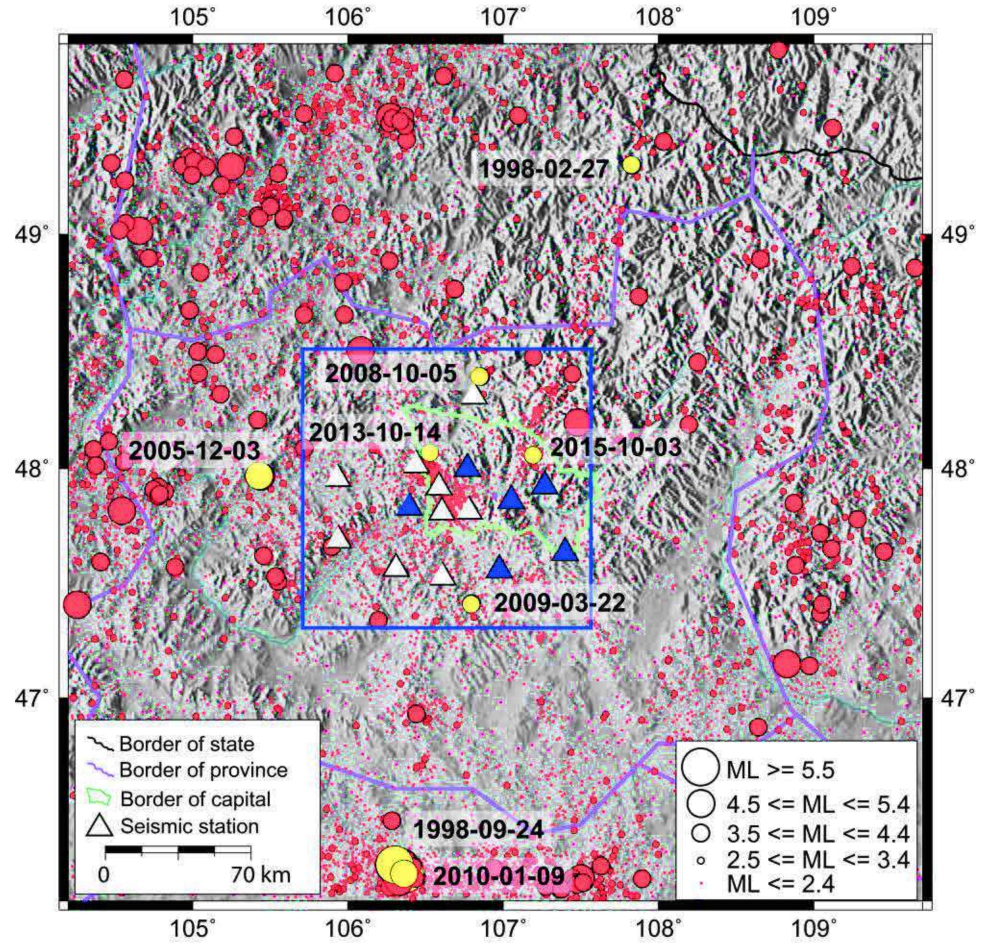

Figure 2.6. Map of seismicity and seismic stations around Ulaanbaatar (area of 400x400km) between 1995 and 2013. Yellow show felted events (see Table 2.3). Triangles are seismic stations, white="UB mobile" that worked more than six months and blue="UB array". Green line is asministrative border of Ulaanbaatar city. Blue square is Figure 2.12.

Although no strong earthquake occurred in the area during the recent period, several were largely felt by residents of Ulaanbaatar (Table 2.3 and Figure 2.6). The biggest event occurred the 1998-09-24 in the Deren active area with magnitude 5.6 about 190 km south of Ulaanbaatar (Appendix 1) and was felt by residents with a shaking level (Intensity MSK) estimated between III and V. The city was also shaken by smaller events (magnitude less than 4) at very short distance (less than 5km from the city centre). Nevertheless, these small events may be associated with active faults that may induce bigger events. Even with moderate sizes (Mw≈5), these events would increase the previoulsy observed Intensities at Ulaanbaatar, which could then produce damage at least on the weakest constructions. Therefore, we need to consider also moderate events at short distances, and not only the largests, for the seismic hazard assessment for Ulaanbaatar.

Table 2.3. Earthquakes felt by residents in Ulaanbaatar (UB) between 1987 and 2016.06. (area of 400x400km)

Date	Origin time (UTC)	Epicentral location		Magnitude (M_L)	Distance from center of city (km)	Observed Intensity (MSK64) at UB
		Latitude (N)	Longitude (E)			
1987-09-29	10:04:18	47.96	106.93	3.5	4.7	
1987-11-17	13:24:12	47.88	106.95	2.8	4.9	
1991-02-24	10:22:17	47.70	108.92	4.2	152	
1998-02-27	05:22:25	49.34	107.89	4.1	174	
1998-09-24	18:53:41	46.26	106.30	5.6	190	III to V
2005-12-03	00:50:05	47.97	105.36	5.0	116	II to III
2008-10-05	01:45:43	48.32	106.75	3.9	46	
2009-03-22	20:36:02	47.42	106.87	4.2	56	II to III
2010-01-09	07:15:36	46.22	106.37	5.1	193	III to V
2013-10-14	14:08:45	48.07	106.57	3.7	31	II to III
2015-10-03	09:30:59	48.06	107.14	4.4	23	II to IV

Estimation of the magnitude for the smallest events

The attenuation law for events recorded only less than 100 km was considered as not constrained in the NDC procedure, therefore no local magnitude have been estimated for 2767 events (Figure 2.7). After working on the improvement of the duration magnitude Md (Appendix 2), and its relation with local magnitude, we could finally associate a magnitude value to 91.4% of these events (Figure 2.8). Their magnitudes are low, always less than 3.4 with about 97% of them with a magnitude of less than 2.5.

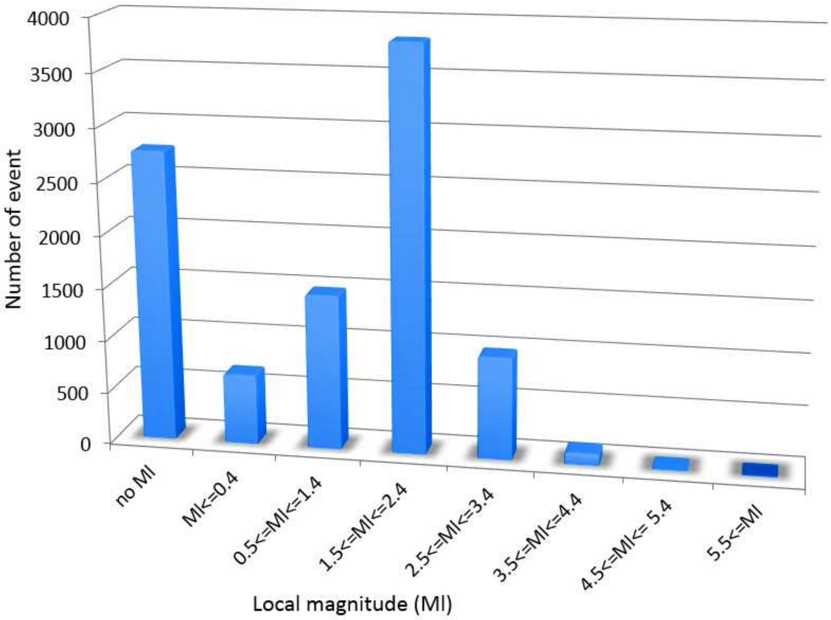

Figure 2.7. Local magnitude histogram of events occurring during the 1995-2013.01 period in the area shown in Figure 2.6 (area 400km x 400km).

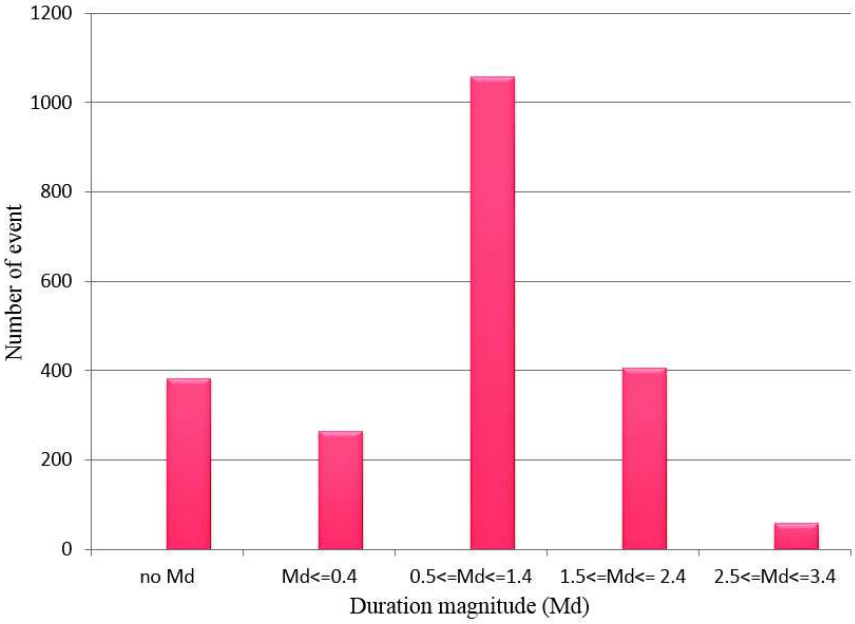

Figure 2.8. Duration magnitude histogram of the events without local magnitude (see Figure 2.7) that occurred in the area shown in Figure 2.6.

Figure 2.9 shows the frequency-magnitude relationship for Ulaanbaatar (area of 400 x 400 km) using the least square method. I used all data with magnitude more than one recorded during 1964 – 2012. Magnitude completeness is Mc=2.5.

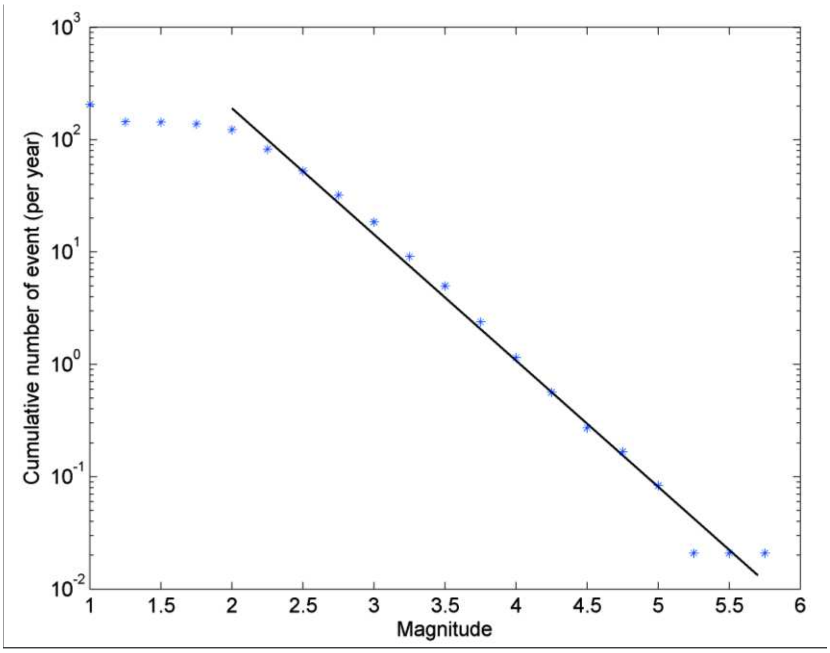

Figure 2.9. Frequency-magnitude distribution of Ulaanbaatar (area of 400x400 km) (1964-2012).

This area is characterized by moderate seismicity (seismic activity rate $a = 4.5$, seismic regime $b = 1.1$). In comparison, at the scale of whole Mongolia, we estimated a rather low $b = 0.8$ value and higher seismic activity $a = 6.1$ (Figure 2.10).

Mongolia is about 10 times (1.500.000 km^2) larger than the Ulaanbaatar region (400x400km=160.000 km^2). If the seismicity rate would be the same, the "a" value for the Ulaanbaatar region should be about 1 value less (6.1-1=5.1) considering a similar "b" value. We observe an "a" value of 4.5 that shows that the Ulaanbaatar area is much less active than the average whole Mongolia.

For the b value, it is lower for whole Mongolia. It shows that there are larger events versus the number of small events in Mongolia than in the region of Ulaanbaatar. Nevertheless, for Mongolia, the activity is due, for a large part, to aftershocks along the faults that broke during the 20th century large events. For Ulaanbaatar, it is more related to events independent of large events (known large events). The comparison is therefore not straightforward.

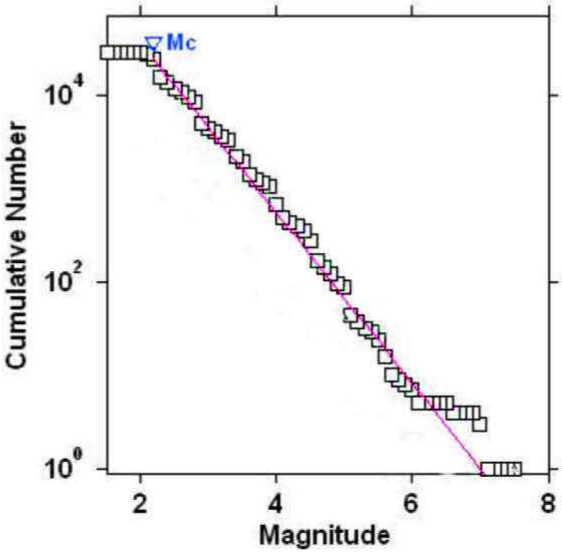

Figure 2.10. Frequency-magnitude distribution of Mongolia from 1964 to 2002 (after Munkhuu, 2006).

2.4 Detailed seismic activity around the Emeelt fault (area of 140x140km): study area

Historical overview: before 1964, based on macroseismic data, we know only one event in this area that occurred in 1947 with M_L= 4.7 (Khilko et al., 1985) (Figure 2.11).

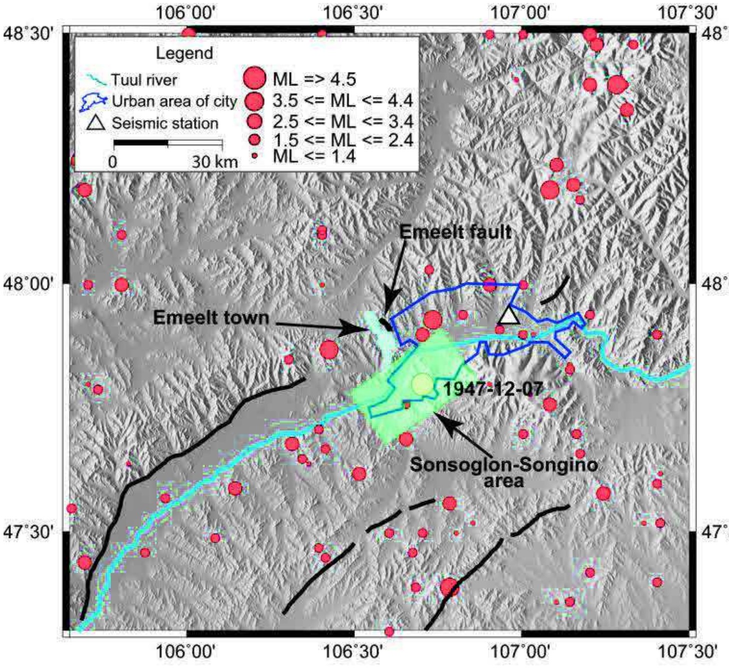

Figure 2.11. Map of seismicity and seismic stations around the Emeelt fault (area of 140x140 km) between 1964 and 1994. Black lines are active faults. The Emeelt fault is limited on the length of the fault observed at the surface (north to 1947 event)

Early instrumental period: between 1964 and 1994, our knowledge of the seismicity is poor, although 5 events with magnitude more than 3.5 were observed in the study area, less than 70 km from the Emeelt active fault (Figure 2.11).

Two of them, with a with magnitude of 3.5, are located near the Emeelt fault surface ruptures:

- 18 December 1974, located about 14 km to the west of the Emeelt fault.
- 29 September 1987, located about 10 km to the ENE of the Emeelt fault.

Two events are located near the Gunj fault area:

- 25 November 1987, located 23 km to the north of Gunj fault with a magnitude 4.4 (also 48 km to the NE from the Emeelt fault).
- 6 April 1985, an earthquake located 75 km NE of the Emeelt fault with magnitude 3.6.

The last one is located near the Avdar fault:

- 16 February 1980, located 58 km to the SSE from the Emeelt Fault with magnitude 4.2. Note that we observed in 2009 an event with magnitude 4.2 at the same location (~2.7 km) despite the much less precise of 1980 .

Recent instrumental period: From 1995 until 2013.01, we localized about 3400 events in the study area (based only on data collected by the NDC of IAG) (Figure 2.12).

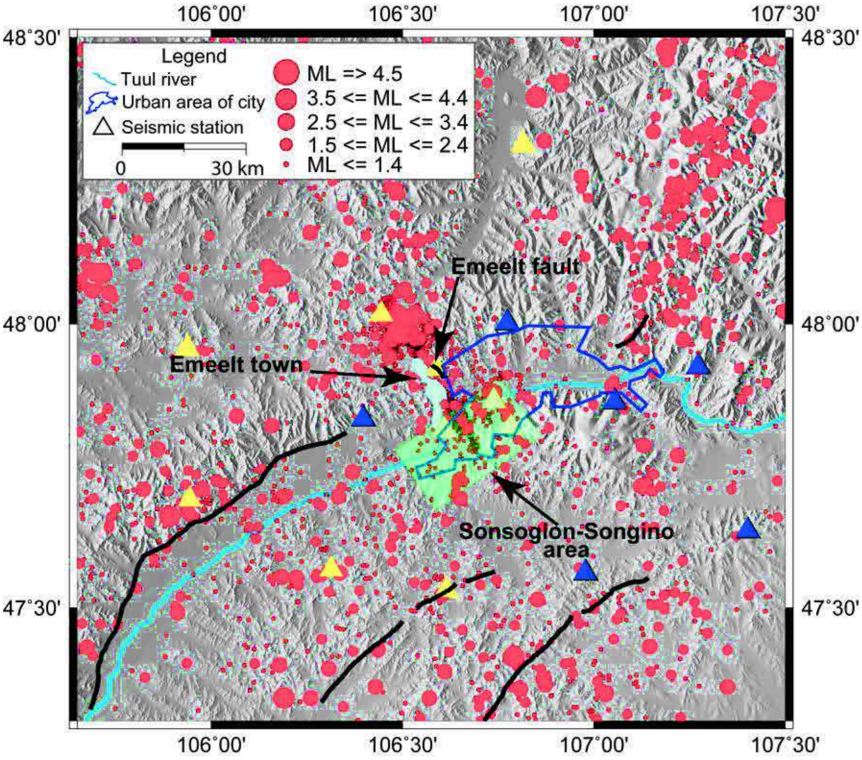

Figure 2.12. Map of seismicity and seismic stations around Emeelt (area of 140x140 km) between 1995 and 2013.01. Trianlge is seismic station: blue=UB array and yellow=UB mobile. Black lines are active faults.

From 1995 until 2005, about 70 earthquakes/yr were recorded. In April 2005 an increase of the earthquake activity started in “Sonsoglon and Songino” area and north of it near Emeelt city, about 14 km to the WSW from the urban area of Ulaanbaatar (Munkhuu et al., 2010) with more than 250 earthquakes recorded during only a few months (Figure 2.12). This seismic activity, with “a swarm characteristics”, drew the interest from scientists and public, but also because the 1947 earthquake of M_L=4.7 could have occurred in this area (Khilko et al., 1985). Based on the distribution of these earthquakes and the evidence of surface ruptures (Emeelt fault) discovered after field investigations, the question raised of the relation between this seismicity and the fault and the maximum magnitude that occurred in the past on it. Due to its proximity with the capital, the authorities requested to characterize at best this activity and the potential impact of that discovery on the seismic hazard for Ulaanbaatar and nearby cities. Because small earthquakes occurring in this area were undetectable and the other events were poorly located by the network at that time, new stations were installed in 2008 (see “UB-mobile” network chapter for details).

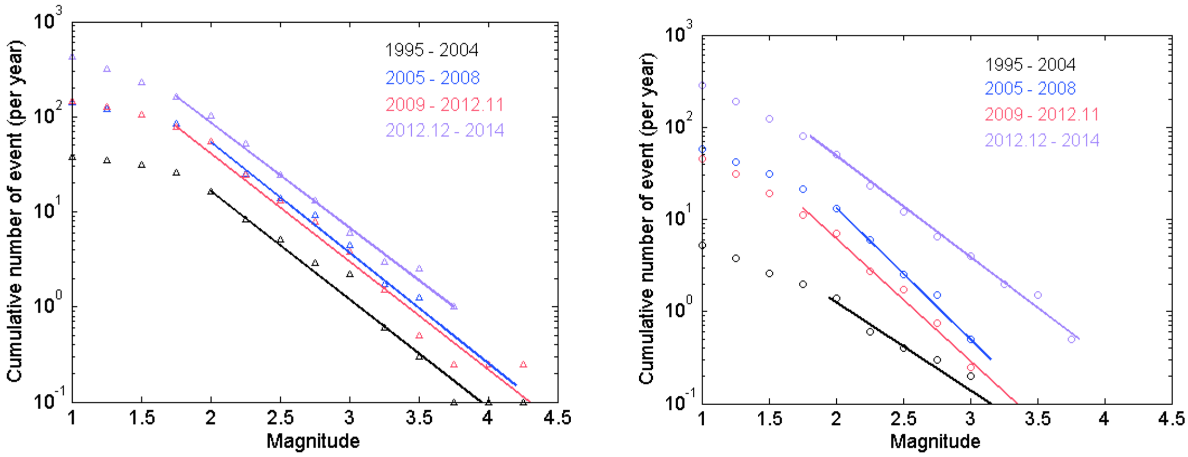

Figure 2.13. Frequency-magnitude distributions (GR) of Emeelt region for two different areas (140x140 km = top figure and 60x60 km = bottom figure) centered on the Emeelt fault and for 4 time periods.

I represent 4 time periods based on the seismic stations upgrade (2008) and swarms periods (2005, 2012.11) from 1995 until 2014 (Figure 2.13 and Figure 2.14 and Table 2.4). The various swarms will be detailed in the part 2.4.1, here we consider 4 large periods as following:

- The first period, 1995-2004 (black colour in figures) is before the first detected swarm in the Emeelt area.
- The second period is from 2005 (blue colour in figures), beginning of activity along the Emeelt fault, to 2008 when mobile stations have been installed.
- The third period corresponds to several swarms until the end of November 2012 (red colour in figures).

- The last period has been chosen to represent the change in the swarm activity (magenta colour in figures), a period with a very high number of seismic events.

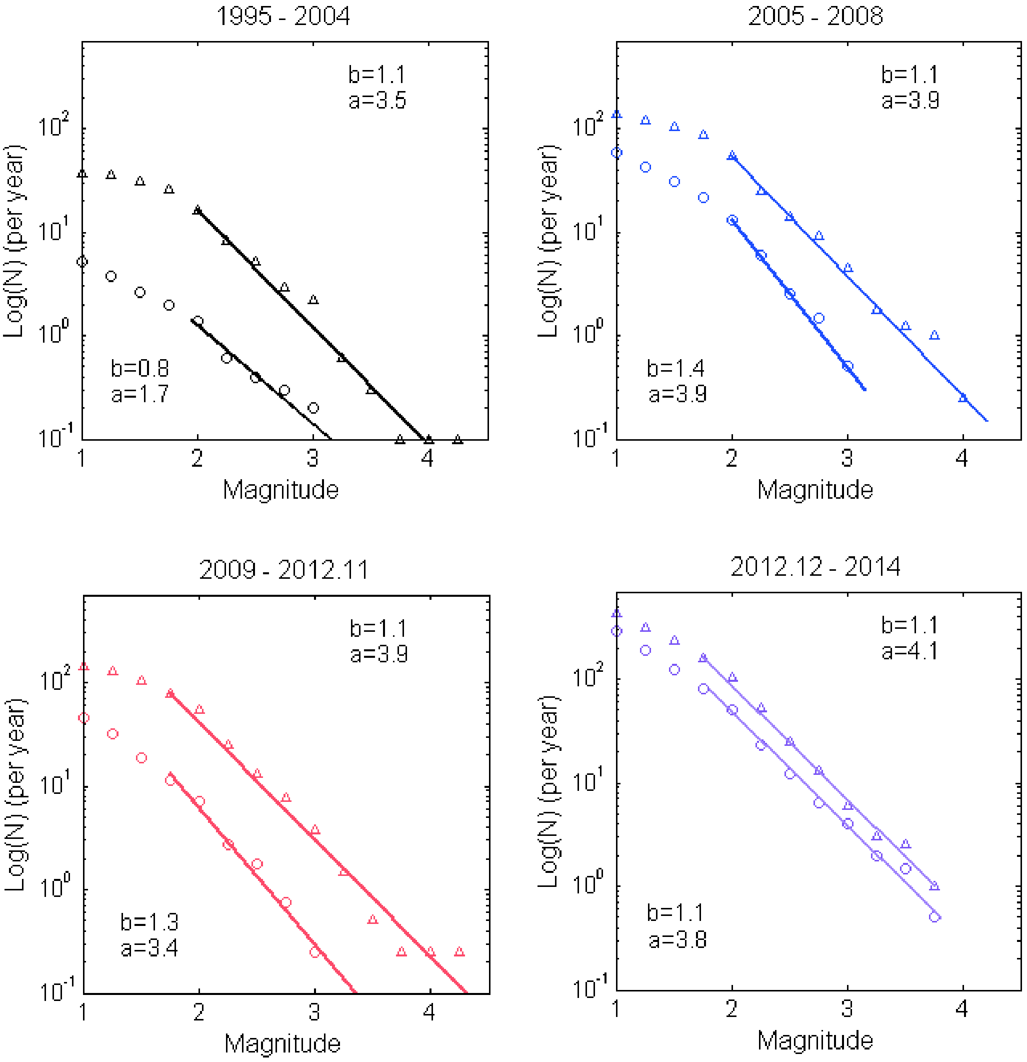

Figure 2.14. Comparison between frequency-magnitude distributions (GR) in the Emeelt region for two different areas (140x140 km = triangle and 60x60 km = circle) centered on Emeelt fault and for 4 time periods (a, b value are summarized in Table 2.4). The “a” and “b” values noted in the upper right and lower left corner correspond to the 140x140 km and 60x60km area, respectively.

We observe a variation in “b” value between the large (140X140 km) and small (60 X 60 km) areas for a given period except for the last period (2012.12-2014) (Figure 2.14). The “b” value for the larger area is stable over the whole period (b=1.1). But for the small area, more centred around the activity of the Emeelt fault zone, the “b” value moves from 0.8 to 1.4 with the first swarm activity, and then it decreases progressively until a value of 1.1 for the last period. It shows that, first, the number of small events increased rapidly (2005-2008), then, it is the number of “larger” events that are increasing rapidly. The relation between small and larger events changes with time for the swarm activity.

The rate of seismicity "a" is lower for the small region, due to its smaller size (5.5 times smaller) , but is quite similar for the last period for the two regions. It means that during this last period almost all the seismicity is concentrated in the Emeelt fault area.

Another observation is that the rate of seismicity increases with time since the swarm activity starts (2005), from 2.8 to 3.9 for the large area and from 1.7 to 3.9 for the small area, the last period corresponds to the highest.

Table 2.4. Seismic regime and seismic activity value of the Emeelt zone

Duration period	Area of 140x140km		Area of 60x60 km	
	b value	a value	b value	a value
1995 – 2004	1.1	3.5	0.8	1.7
2005 – 2008	1.1	3.9	1.4	3.9
2009 – 2012.11	1.1	3.9	1.3	3.4
2012.12 – 2014	1.1	4.1	1.1	3.8

2.4.1 Emeelt earthquake swarms as observed with the stations and procedure of the NDC

2.4.1.1 Changes in the seismicity between 1994 and 2014

Between 1995 and 2014, we have located more than 5700 events in the area of 140x140 km around the Emeelt fault (based only on data from NDC of IAG). About 77% are localized near the Emeelt fault (area of 70x70 km shown by a black square in Figures 2.17-19). The cumulative number of these events shows clear increases in 2005, 2010 and between end of 2012 and 2015, that are related directly to the Emeelt activity and with a swarm characteristics (Figure 2.15).

An earthquake swarm consists of a sequence of earthquakes closely grouped in space and time without a clear mainshock, that can also be defined as an increase of the seismicity rate (Mogi, 1963; Sykes, 1970). Until 2015, the highest swarm activity occurred between December 2012 and January 2013, with more than 2075 events detected including the strongest recorded event with a magnitude 3.4 (M_L). In particular, we observed 2 swarms “crisis” with more than 200 events/day: the 26 December 2012 and the 14 October 2013.

Figure 2.15 shows the cumulative number of detected events with time around the Emeelt fault. The annual number of events is mostly constant until the first quarter of 2005. The installation time of new seismic stations (shown by green lines, in 2000 and 2008, see network chapter for details) may have changed the detection capability, but the observed changes in the seismicity (based on NDC procedure) are independent from the seismic stations installation time. The changes observed are clearly associated with the activity near the Emeelt fault as we can see on Figure 2.15 (before 2005) and Figure 2.17 (between 2005 and 2008).

Figure 2.15. Cumulative number of earthquakes between 1995 and 2014 (area of 140x140 km). Green line is starting time of new station installation, in 2000 installation of "CTBT Songino array" and in 2008 installation of "UB-mobile".

Note that the depth of all events were not well constrained in our NDC catalogue, most of event depths are fixed at 2 km, 15 km or 30 km (from Figure 2.16 to Figure 2.19). The permanent network does not allow getting a well-determined depth. This will be one challenge of my work using "UB-mobile" stations. Also, the location quality of events with magnitude under 3.5 or 3 outside the "UB-array" permanent stations can be poor. Nevertheless, we see that the epicentres have a linear distribution.

Since December 2008, we installed 10 mobile stations in and around Ulaanbaatar to better characterize the seismicity and increase the detection level (Figure 2.18). We changed the position of some of them after a few months, to improve their safety, and I included all these positions on the Figure 2.18.

At the end of 2012, we developed a complex geophysical stations network including seismic, tiltmeter, GPS and geomagnetic stations in and around Ulaanbaatar. In Figure 2.19, I plotted earthquakes localized between 2013.01 and 2014 and seismic stations including UB-guralp.

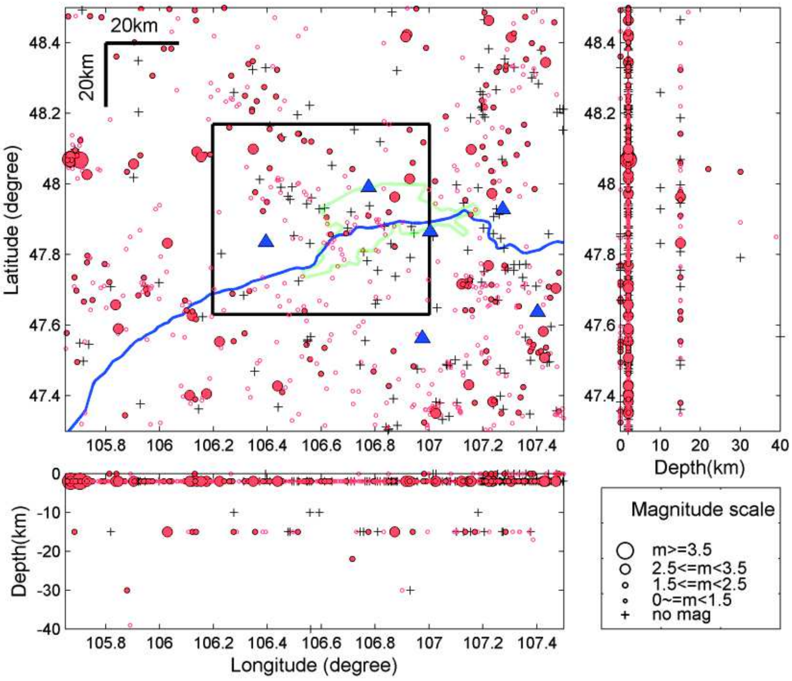

Figure 2.16. Hypocenters in the study area between 1995 and 2004 (based on NDC results). Green line is urban area of Ulaanbaatar city, blue line is Tuul river and black square represents Emeelt fault area of 60x60 km of Figure 2.21. Triangles in blue colour are permanent seismic stations of "UB-array".

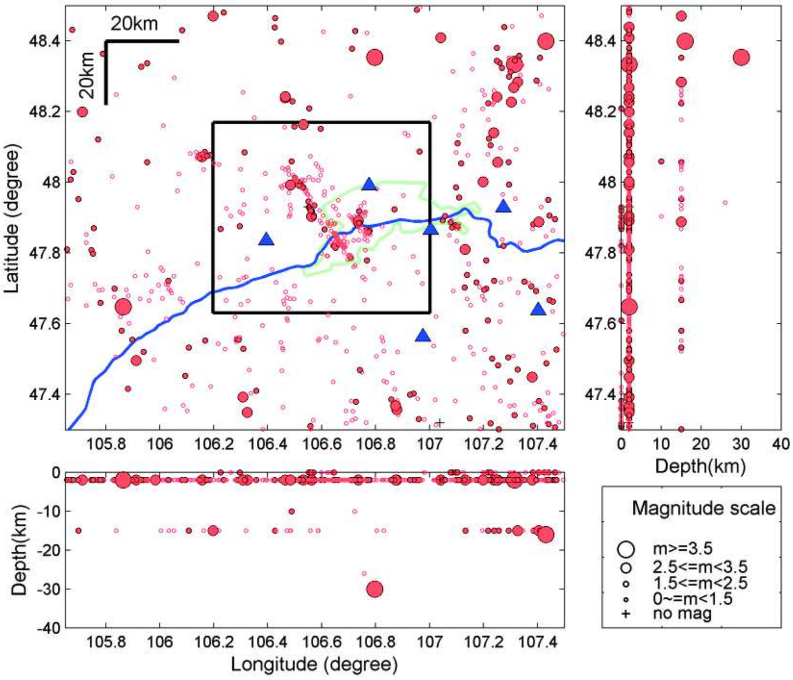

Figure 2.17. Hypocenters in the study area between 2005 and 2008.11 (based on NDC results). Green line is urban area of Ulaanbaatar city, blue line is Tuul river and black square represents Emeelt fault area of 60x60 km of Figure 2.21 Triangles in blue colour are permanent seismic stations of "UB-array".

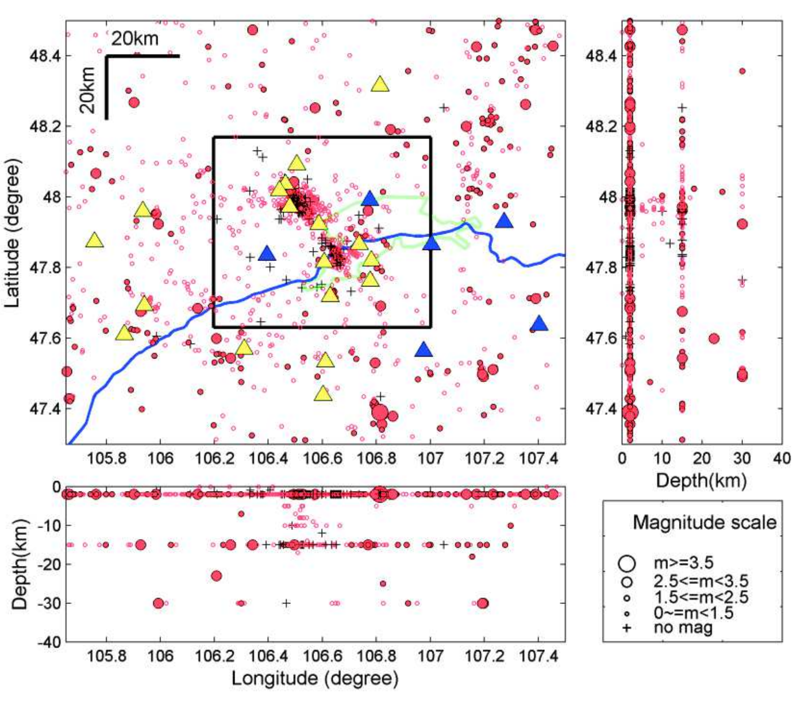

Figure 2.18. Hypocentres in the study area between 2008.12 and 2013.01 (based on NDC results). Green line is urban area of Ulaanbaatar city, blue line is Tuul river and black square represents Emeelt fault area of 60x60 km of Figure 2.21. Triangles in blue colour are permanent seismic stations of "UB-array" and in yellow colour are "UB-mobile" stations (10 mobile stations but with a change of position during the period, the figure shows the cumulative locations).

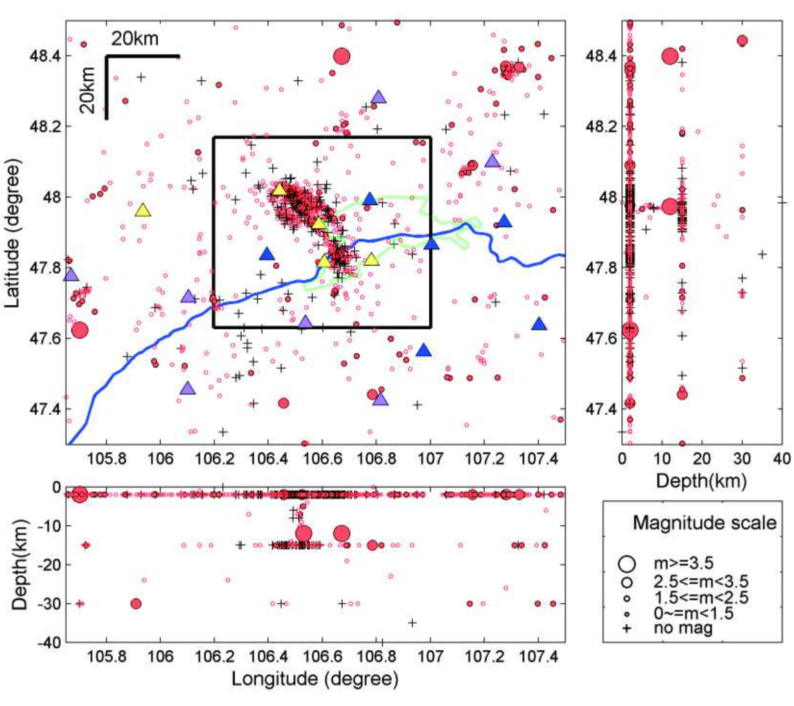

Figure 2.19. Hypocenters in the study area between 2013.02 and 2014 (based on NDC results). Green line is urban area of Ulaanbaatar city, blue line is Tuul river and black square represents Emeelt fault area of 60x60 km of Figure 2.21. Triangles in blue colour are permanent seismic stations of "UB-array", in yellow colour are "UB-mobile" and in purple colours are "UB-guralp" stations.

Since 2005, at the beginning of the detected seismic swarm around the Emeelt fault, we observe sometimes series of events with similar locations and magnitudes, but without any mainshock.

2.4.1.2 Swarm identification and characteristics around the Emeelt fault (area of 60x60 km)

Earthquakes swarm typically refers to an earthquake cluster, which is empirically defined as an increase in seismicity rate above the background rate without a clear mainshock (Mogi, 1963). Mogi (1963) introduced a classification of earthquake sequences into three types, depending on their time-frequency relation (Gutenberg and Richter, 1944). Types 1 and 2 comprise mainshock-aftershock and foreshock-mainshock-aftershock patterns, while seismic swarms are assigned to type 3 that describes a gradual increase and decay of seismicity in time, without a distinct mainshock. Based on this definition, these earthquakes in the Emeelt fault zone belong up to now to type 3.

The empirical definition of a seismic swarm by Mogi (1963) is the following:

- the minimum number of events in one swarm sequence is more than 10

- the daily number of events is greater than twice the square-root of the swarm duration in days: $Nd > 2\sqrt{T}$

When the structure on which the swarms occur is unknown, we apply this formula, or test that condition, on an area (window) of a given radius. When Nd>2√T in the area, we consider the events as a swarm. Then to cover the full region studied, we move that window by steps. I did not use this procedure, because the Emeelt fault zone studied here is considered as a structure on which the swarms occur.

Based on this definition, I looked for swarms with durations between 2 and 20 days. I identified twenty swarms in this area (Table 2.5).

I grouped successive swarms, up to a few days between them and located at the same place (called “Subswarms” in Table 2.5) in a unique swarm sequence (called “Swarm” in Table 2.5). For example Swarm 5: I combined the subswarms 5-1-1 and 5-1-2, as they are continuous in time, in subswarm 5-1, and the subswarms 5-2-1, 5-2-2 and 5-2-3 in subswarm 5-2. Then I grouped the subswarms 5-1, 5-2 and 5-3 as they are separated by only 11 and 3 days, respectively, in swarm 5.

Table 2.5. Identified swarms in the Emeelt fault area of 60x60 km.

Identified swarm			Subswarms ID		Combined swarm		
ID	Start date	Duration day			Swarm ID	Start date	Duration day
1	2005 – 04 – 06	4	-	-	Swarm 1	2005 – 04 – 06	5
2	2010 – 01 – 28	2	-	2-1	Swarm 2	2010 – 01 – 28	4
3	2010 – 01 – 29	3	-	2-2			
4	2010 – 03 – 07	2	-	-	Swarm 3	2010 – 03 – 07	2
5	2010 – 08 – 29	2	-	-	Swarm 4	2010 – 08 – 29	2
6	2012 – 12 – 25	9	5-1-1	5-1	Swarm 5	2012 – 12 – 25	50
7	2013 – 01 – 02	4	5-1-2				
8	2013 – 01 – 17	6	5-2-1	5-2			
9	2013 – 01 – 23	6	5-2-2				
10	2013 – 01 – 24	12	5-2-3				
11	2013 – 02 – 04	3	5-2-4				
12	2013 – 02 – 10	3	-	5-3			
13	2013 – 04 – 04	2	-	6-1	Swarm 6	2013 – 04 – 04	7
14	2013 – 04 – 09	2	-	6-2			
15	2013 – 10 – 14	9	-	7-1	Swarm 7	2013 – 10 – 14	29
16	2013 – 10 – 23	3	-	7-2			
17	2013 – 11 – 08	4	-	7-3			
18	2014 – 01 – 06	9	-	-	Swarm 8	2014 – 01 – 06	9
19	2014 – 03 – 27	3	-	-	Swarm 9	2014 – 03 – 27	3
20	2014 – 12 – 20	4	-	-	Swarm 10	2014 – 12 – 20	4

Finally, based on the earthquakes catalogue of the NDC, which contains 3796 events localized between 2005 and 2014 in the Emeelt fault area, I defined 10 swarms: one in 2005, three in 2010, one in 2012, two in 2013 and three in 2014 (Figure 2.20 and Figure 2.21 and Table 2.6). These swarms are along the Emeelt fault zone. The swarms of 2012 and 2013 represent 46.8 % of the total number of events. Also, 77.3% of events of these 10 swarms occurred during Swarm-5 (2012-2013) and Swarm-7 (2013). Among these 3796 events, a Md magnitude is estimated for about 600 of them and about 400 of them have still neither a M_L nor a Md magnitude.

Table 2.6. Information about seismic swarms in the Emeelt fault zone (area of 60x60 km).

Swarm ID	Started date	Continuous days	Number of events	% of events since 2005	% of events of all swarms	Maximum magnitude (ML)
1	2005.04.06	5	29	0.8	1.3	2.4 – Apr 09
2	2010.01.28	4	79	2.1	3.6	1.6 – Jan 29
3	2010.03.07	2	56	1.5	2.6	1.1 – Mar 07
4	2010.08.29	2	20	0.5	0.9	1.1 – Aug 30
5	2012.12.25	50	1123	29.6	51.2	3.4 – Jan 25
6	2013.04.04	7	80	2.1	3.6	2.1 – Apr 04
7	2013.10.14	29	572	15.1	26.1	3.7 – Oct 14
8	2014.01.06	9	79	2.1	3.6	2.3 – Jan 09
9	2014.03.27	3	121	3.2	5.5	1.9 – Mar 28
10	2014.12.20	4	33	0.9	1.5	2.2 – Dec 20

The periods 2010 and 2012 to 2014 are characterized by high seismic activity with 9 swarms, which include particular clusters: the 25.12.2012 (combined 7 subswarms) with 1123 events and the 14.10.2013 (combined 3 subswarms) with 572 events and a maximum local magnitude of 3.7. The epicentre distribution of the seismic swarms using the NDC catalogue shows a displacement of the seismic activity with time, especially in 2010, between the 3 swarms in January, March and August. I will discuss it later in chapter 5 after the re-location and checking of the events. Note that the largest event occured in the middle of the swarm 5 but for the swarm 7 it occured at the begining.

Seismic activity from 2006 to 2009 and during 2011 was much less important than the other years, without clear swarms and with about 58-136 events/yr. However, this number is still 4-9 times higher than the average number of earthquake occurring before 2005, about 6-30 events/yr in this region.

Evolution of the time delay between consecutive events:

Before 2005, the delay time between two events is most of the time larger than 1 day (0.86×10^5 seconds) with very few delay of less than 1 hour (Figure 2.20). At the beginning of the swarm crisis in 2005, this delay decreased until about 1 minute. After each crisis, we see that the minimum delay decreases, down to 4 seconds for example during the 2014 crisis. The maximum delay also decreased from about 10 days (8.6×10^5 seconds) in 1995 down to about one day in 2005 and only about 12 hours in 2014.

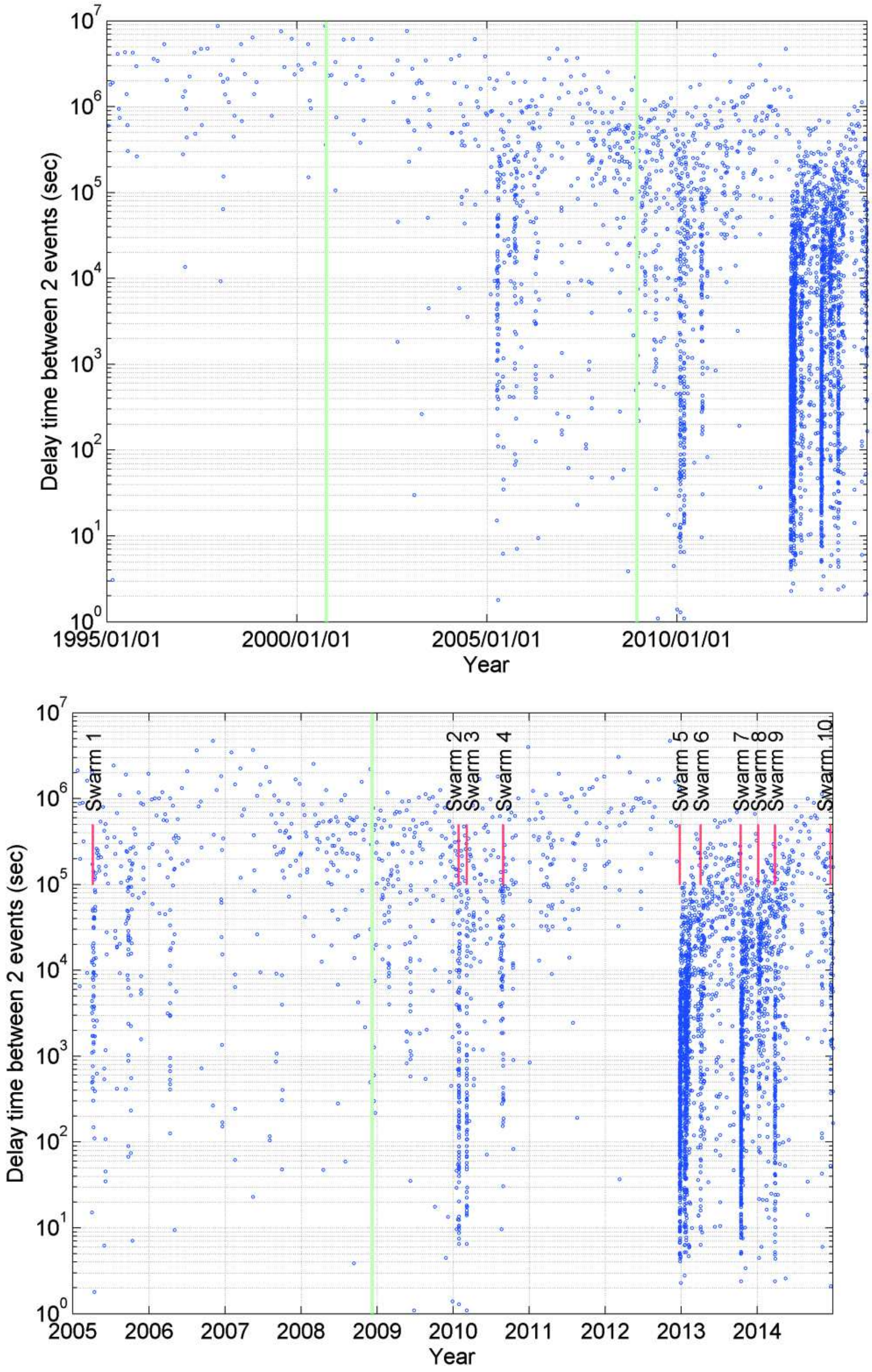

Figure 2.20. Delay time (in seconds) between two consecutive events in the Emeelt fault area of 60x60 km. Top figure is between 1995 and 2014 and bottom figure is zoomed between 2005 and 2014. Green line is upgrade time of seismic network (Songino array in 2001 and UB-mobile in 2008). Red line is starting date of swarm (bottom figure).

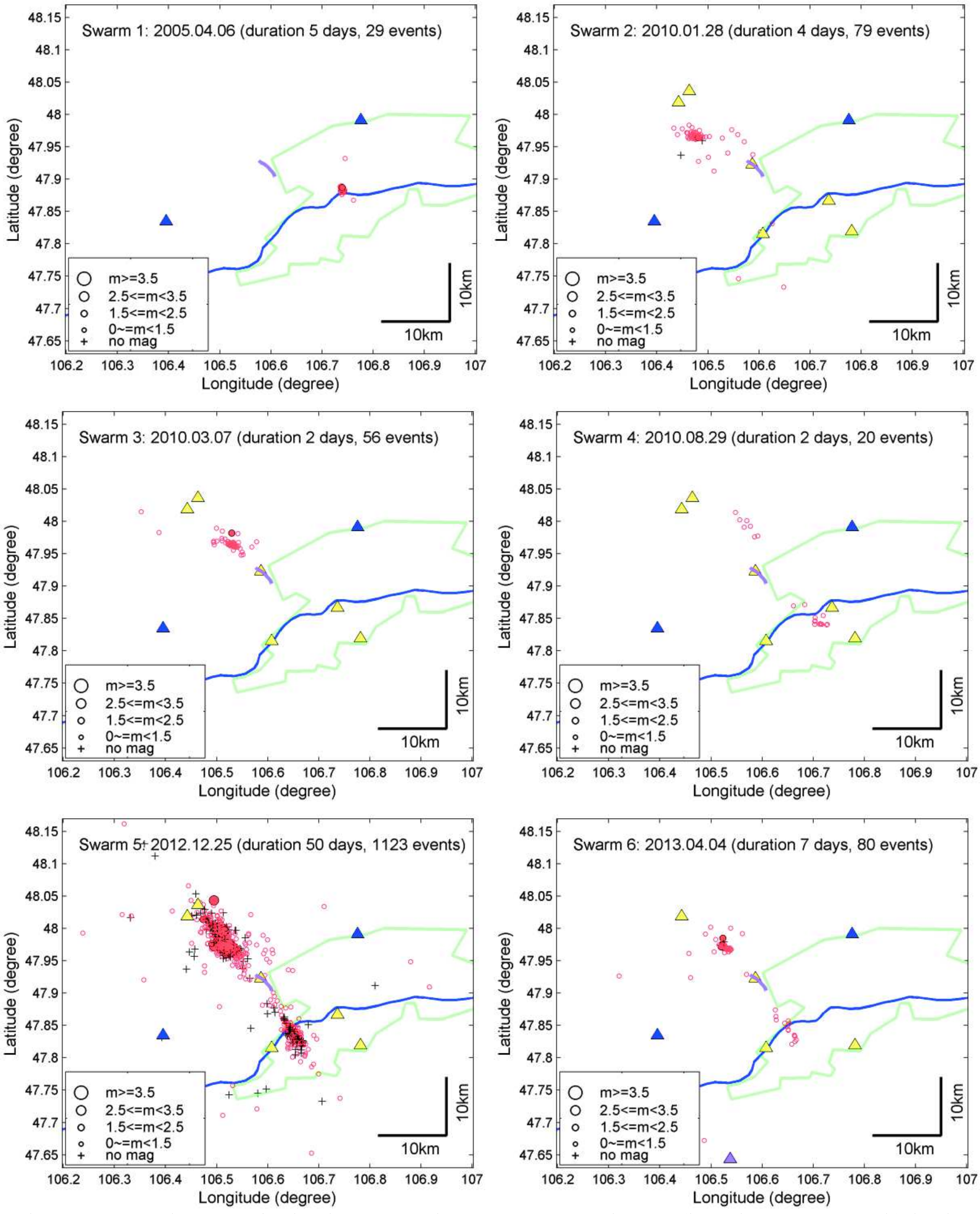

Figure 2.21. Epicenter of seismic swarms between 2005 and 2014 (based on NDC result) in the Emeelt fault area of 60x60 km. Green line is urban area of Ulaanbaatar city, blue line is Tuul river and purple line represents observed surface rupture of the Emeelt fault. Triangle are seismic stations that were operating during the swarm time, blue colour = UB-array and yellow colour = UB-mobile.

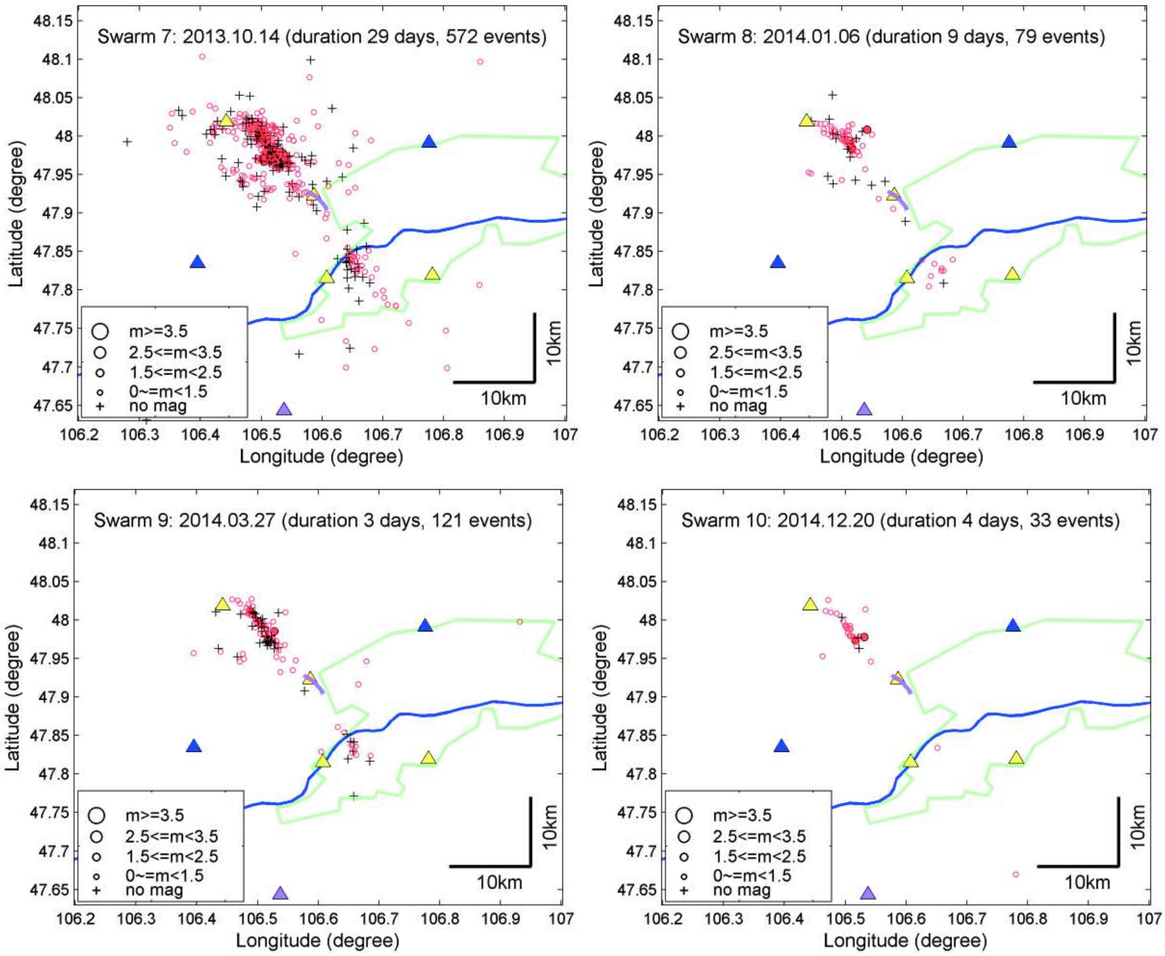

Figure 2.21 continued.

Average background seismic rate in the Emeelt fault area of 60x60 km is 0.04 event/day based on detected and localized events between 1995-2004. Figure 2.22 shows the seismic rate of events localized between 2005 and 2014. Average number of daily events increases from April 2005 (Figure 2.22) by 50 times more. Maximum seismic rate reached 15-17 events/day during the period of Swarm_5 and Swarm_7.

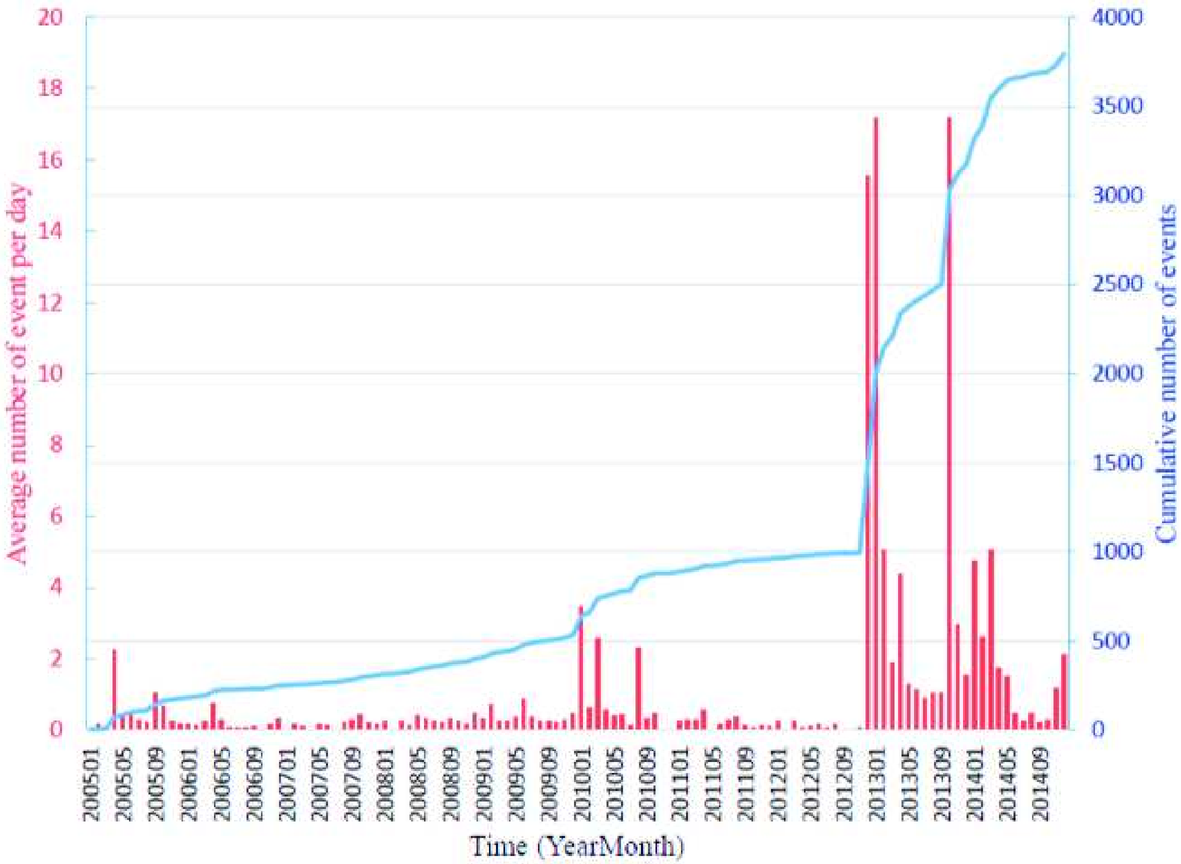

Figure 2.22. Cumulative number of seismic events and average number of events/day during specific month in Emeelt fault area of 60x60km for 2005 and 2014.

2.4.1.3 Characteristics of the swarms based on the NDC catalog.

Swarm of 2005 (Swarm 1: Apr06-Apr10): In April, 67 earthquakes occurred, which is 3 times more than the annual average. During the swarm, 29 events with maximum magnitude 2.4 occurred. The NDC epicentres of this first swarm are shown in Figure 2.23. Interestingly, epicentres are very near to the epicentre of events that occurred in 1987 and 1947, with estimated magnitude of 3.5 and 4.7, respectively, in the “Sonsgolon and Songino” area mentioned by Khilko (1985). Notice also that the seismic activity of April 2005 is not located along the Emeelt fault surface rupture, but at its SE, and it is only at the end of 2005 that it moved in the area of the fault (respectively blue and orange-red colours in the Figure 2.23).

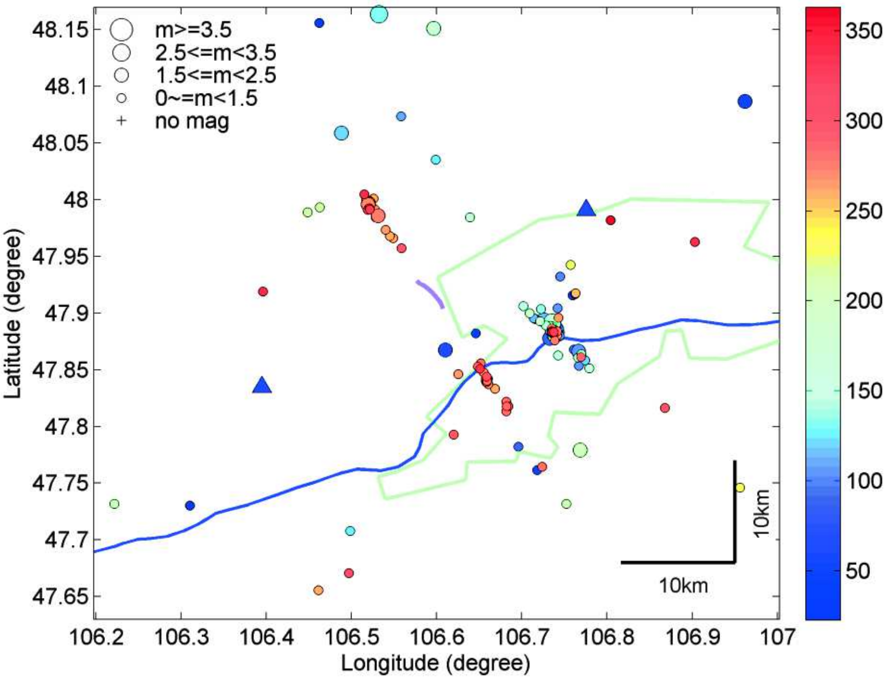

Figure 2.23. Hypocenters in the Emeelt fault area of 60x60 km in 2005 (based on NDC results). Magenta line = Emeelt fault; triangles = seismic stations. Colour legend indicates days since 2005.01.01.

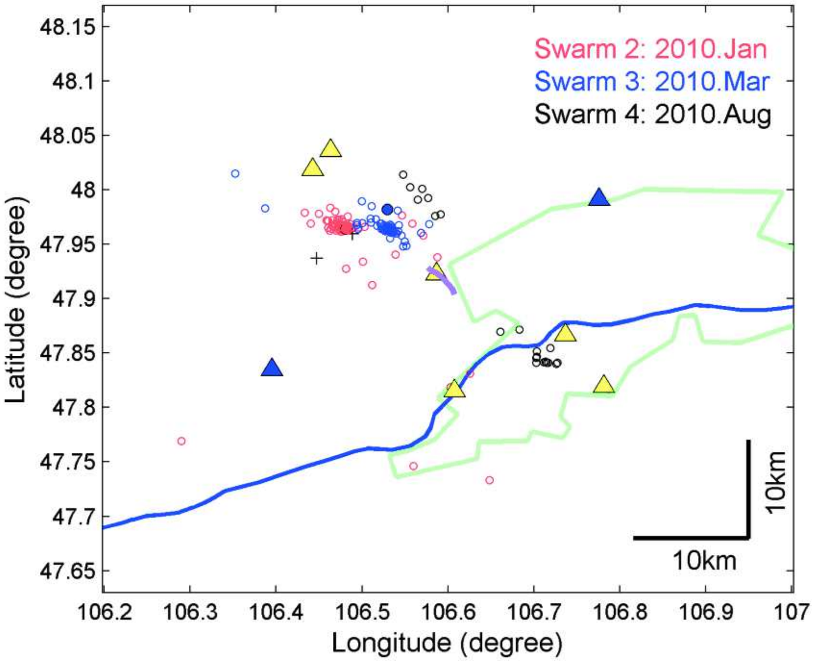

Figure 2.24. Epicenter of three seismic swarms in 2010 (based on NDC results). Green line is urban area of Ulaanbaatar city, blue line = Tuul river and purple line = observed surface rupture of Emeelt fault. Triangles are seismic stations, blue colour = UB-array and yellow colour = UB-mobile.

The 3 swarms (2, 3 and 4) appears concentrated along three lines parallel with the Emeelt fault segment observed in the field but more to the north of it (Figure 2.24). The swarm of January is located in the west (about 3.5 km W of the main fault), the swarm of March in the center (northern extension of the fault) and the swarm of August in the east (about 4 km to the NE from the main fault). There is a migration shows from SW to NE with time based on the NDC catalogue. Unfortunately we can not follow the depth migration due to poorly constrained depths and the location has to be verified to confirm these preliminary observations (I discuss this issue in chapter 5).

Swarms of 2012 (Swarm 5: Dec25-Feb12): During this swarm, between 25 Dec 2012 and 12 Feb 2013, we localized 1123 events (Figure 2.21). The biggest event, with a maximum magnitude of 3.4 (M_L), occurred 25 January 2013. Since 2005, it is the most important swarm and it represents alone 29.6% of all events observed in this area and 51.2% of swarm events between 2005 and 2014. The distribution of this swarm is concentrated along the main fault and appears also toward the SE using the NDC catalogue.

During this swam, a particular important activity started 17 January with 104 events followed by 462 events until 31 January; 3 events had magnitudes greater than 2.0 (M_L), the biggest occurred 25 January (M_L=3.4).

Swarms of 2013 (Swarm 6: Apr04-Apr10 and Swarm 7: Oct14-Nov11): We observed two swarms in 2013, in April and October, with, respectively, 80 and 572 events (Figure 2.21). The epicentre distributions of the 2 swarms are similar and are concentrated along the main segment of the Emeelt fault. The biggest event, on 14 October, has a magnitude of 3.7. This event corresponds to the largest one of the seismic activity observed around the Emeelt fault since 2005.

Swarm of 2014 (Swarm 8: Jan06-Jan14, Swarm 9: Mar27-Mar29 and Swarm 10: Dec20-Dec23): We observed, respectively, 79, 121 and 33 events during the January, March and December swarms (Figure 2.21) with a maximum magnitude of 2.3 (M_L) on 9 January. These swarms are distributed along the main segment of the fault, similarly to all the swarms since 2012.

2.5 Conclusion

Since April 2005, we observe a high seismic activity near Emeelt town and just west of Ulaanbaatar. Due to this activity we (IAG) deployed temporary seismic stations since December of 2008 and some of them, progressively, have been included in the NDC procedure.

Based on the earthquake catalogue of NDC, I identified 10 swarms near the Emeelt fault (area of 70x70km) with a duration of between 2 and 50 days and a number of events between 20 and 1123. These swarms are all oriented along the surface rupture of the Emeelt fault (Figure 2.21).

We can summarize the activity and observations:

- The “b” value changes between large and small areas for a given period (Figure 2.14) except for the last period (2012.12-2014). The level of seismicity is lower for the small region, due to its smaller size, but is very similar for the last period for the two regions sizes. It means that during this period quite all the seismicity is concentrated in the Emeelt fault area.
- The rate of seismicity increases when the swarm activity starts (2005), from 2.8 to 3.9 for the large area and from 1.7 to 3.9 for the small area, and stays more or less stable after.
- The “b” value for the larger area of 140x140km is stable over the whole period (b=1.1). But for the small area of 70x70km, more centred on the activity near the Emeelt fault, the “b” value moves from 0.8 to 1.4 with the first swarm activity, from 2005 to 2008, and then it decreases progressively until a value of 1.1 for the last period. It shows that, first, the number of small events increased more rapidly (2005-2008), then, it is the number of “larger” events that is increasing more rapidly. The relation between small and larger events changes with time for the swarm activity.
- The swarm of 2005 is located very near the epicentre area of 1947 with M_L= 4.7 (Khilko et al., 1985) (Figure 2.11).
- The Emeelt fault area started to be more active with the swarms of 2010. Three occurred in 2010, January, March and August. These swarms are very typical and the distribution of the events appears concentrated along three lines, parallel with each other and with the Emeelt fault segment observed in the field but more to the north of it (Figure 2.24). The swarm of January is located to the west (about 3.5 km West of the main fault), the swarm of March in the centrer (northern extension of the fault) and the swarm of August to the east (about 4 km NE from the main fault). A migration from SW to NE with time is observed based on the NDC catalogue. Unfortunately, we can not follow the depth migration due to poorly constrained depths and the location has to be verified to confirm these preliminary observations (Figure 2.16-Figure 2.19) (see next chapters).
- Most of the events tha occurred during swarm_5 (end of 2012 - beginning 2013) and swarm_7 (end of 2013) represent 46.8 % of the total number of events detected between 2005 and 2014 and 77.3% of events of all swarms. The biggest events of these 2 swarms have, respectively, magnitudes M_L 3.4 and 3.7.
- Before the beginning of the seismic swarms, the delay time between two consecutive events is mostly larger than 1 day with very few delay of less than 1 hour (Figure 2.20). At the beginning of the swarm crisis in 2005, this delay decreased until about 1.5 min.

> After each crisis, the minimum delay decreases down to 4s (for example during the 2012 and 2014 crisis), and the maximum delay decreases from about 1000 days in 1995 down to about 231 days in 2005 and only about 11 days in 2014.

One of the aim of my study is to well constrain the depths distribution of seismic events in the Emeelt fault area. I will do this by systematic studies presented in chapters 3 and 4. In chapter 3, I will constrain a 1D velocity model for this area and relocate the events. In chapter 4, I will produce a 3D velocity model of the study area and estimate precise locations of events. After this procedure, I will be able to discuss the hypocentre migration of these swarms and their characteristics.

3 Chapter 3: 1D inversion for the study area and new location of seismicity around the Emeelt fault

Inversions based on 1D velocity models can provide accurate earthquake locations when more complex 3D models are not available. Moreover, these 1D velocity models provide also a computational stable initial model for 3D local earthquake tomography and relative earthquake relocation (Kissling et al., 1994, Kissling 1988). Nevertheless, in the area of Ulaanbaatar we do not have any precise 1D velocity model. Therefore, I have to constrain a 1D velocity model, which is the first purpose of this chapter.

The second one is co compute a high-resolution location of the seismic activity using the Hypoinverse procedure. This step is very important, as the input locations that will be used in the TomoDD procedure (next chapter) must have reduced uncertainties.

3.1 Introduction and previous study of 1D model

Earthquake location can be improved using a reference model close to the real earth model and station corrections that mitigate the effects of the structure close to the receiver and deviations from the simple laterally homogeneous model. Eberhart-Phillips (1990) and Kissling et al. (1994) proposed that the natural solution to this problem is the 1D model that itself represents the least square solution to the coupled hypocentre-velocity model parameter relation. This part of the chapter presents the study to produce a minimum 1D velocity model using arrival times recorded by UB-array and UB-mobile stations between 1994 and January 2013.

I used the VELEST algorithm that allows variable Vp/Vs with depth and solves for the minimum 1D velocity model and station corrections for a local region (Kissling et al., 1995, Kissling, 1988). I simultaneously inverted P-and S-wave arrival times. The resulting 1D velocity model, with associated station's correction, is used to relocate all seismicity recorded by the UB networks (UB-array and UB-mobile).

Previous studies: In general, the velocity models are poorly constrained beneath Mongolia, not only in the study area. In the past, few works have documented the detailed deep structure of Mongolia, mainly along specific transects, on the basis of the interpretation of seismic data, such as, Zorin (1993), Zorin et al. (1994, 2002), Mordvinova et al. (1996, 2007), Petit et al. (2008) and Tiberi et al. (2008) (Figure 3.1). They used seismic data recorded by temporary seismic networks, like the PASSCAL-1992 transect (Mordvinova et al., 1996; Zorin et al., 2002) and MOBAL-2003 transect

(Mordvinova et al., 2007; Petit et al., 2008; Tiberi et al., 2008) (Figure 3.1). Unfortunately, it will be impossible to compare our results with the results of Mordvinova et al. (2007), Petit et al. (2008) and Tiberi et al. (2008) because their studies are mostly concentrated on deep lithospheric structures. Also, their works were based on the MOBAL-2003 transect, which is located at about 400 km from the study area.

PASSCAL-1992 transect, with 29 seismic stations, was located along a profile of 820 km between (52.168N, 104.385E) and south Mongolia (45.262N, 108.260E) that crossed the east part of my study area. Zorin et al. (2002) used a transect implemented in 1994, which runs approximately along the PASSCAL-1992 transect, to study geological and geophysical structures along Baikal-Mongolia. One of the 86 stations of the PASSCAL-1992 transect was located to the east of the capital. Zorin et al., (2002) used the receiver function method, P-to-S converted waves at crustal and mantle interfaces beneath the seismic stations and compared them with gravity and geological study. We will mainly compare our work with the results of Zorin et al. (2002).

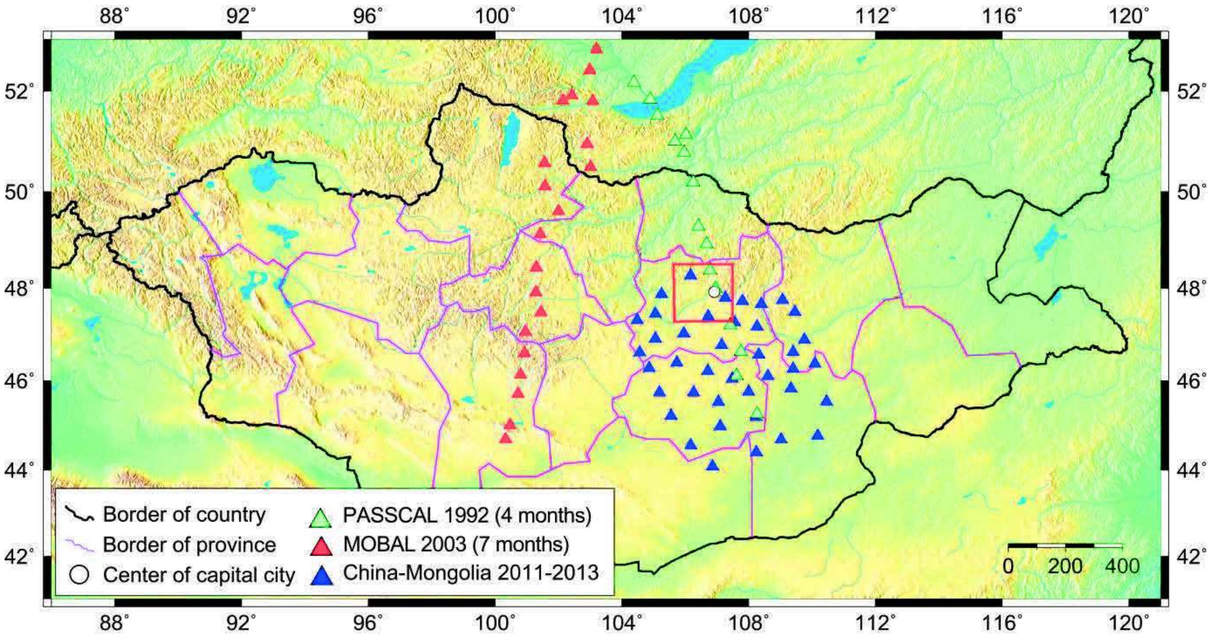

Figure 3.1. Location of the temporary seismic stations. The study area is delineated by a red square.

Up to now, the results based on of the analysis of 2 years of recorded data (from August 2011 to July 2013) with the temporary seismic array deployed through an international science and technology cooperation project between China (Institute of Geophysics, CEA) and Mongolia (IAG) is limited to the Moho depth and geometry (from 39 to 45 km) (He et al., 2014) (Figure 3.1).

Nevertheless, the distance between the stations in these projects are quite important (several tens of kilometres) and will give only an average 1D velocity model for the area. I will nevertheless compare those results with my 1D model.

In the NDC, we use only two models for the location procedure that differ only for the crustal depth, which is 45 km in the west and 35 km for central and eastern Mongolia. These models are based on the average travel timetable in Mongolia (Baljinnyam et al., 1975). They are constrained with the aftershocks of the Mogod earthquake (1967-01-05, Ms=7.4[3]), with the aftershocks of the Tsagaan-Shuvuut's earthquake (1970-05-15, Ms=6.6) and with the earthquakes localized by the national seismic network of Mongolia between 1968 and 1973. However, these models give only an average simple model for Mongolia, due to the poor stations coverage and detection level during that period.

3.2 Procedure applied for the 1D inversion

The working procedure of the 1D inversion (called "Procedure A") is summarized in Figure 3.2. Each step will be detailed in the next parts.

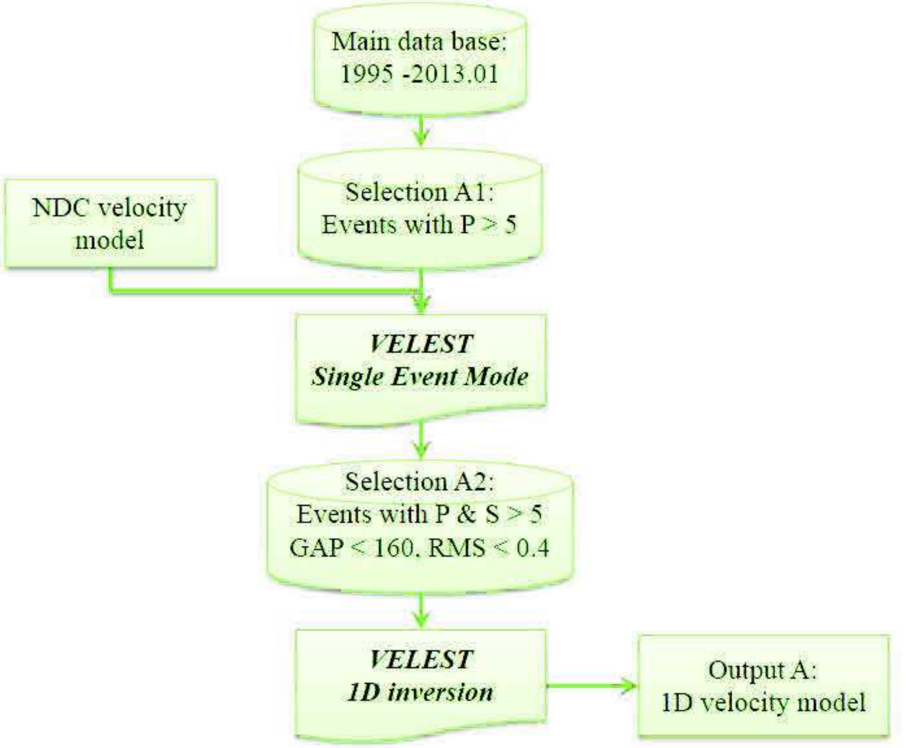

Figure 3.2. Working procedure of the 1D inversion (Procedure A).

---

[3] Energy class determined based on the Rautian nomogram (1964). This nomogram calibrated for SKM seismometers.

3.2.1 Input data for the 1D inversion

This part details the “Main data base”, the “Selection A1” , the NDC velocity model and the “Selection A2” (Figure 3.2).

3.2.1.1 Main data base

The next part concerns the way the “Main data base” was built. It is summarized in Figure 3.3 and each step is explained in details below.

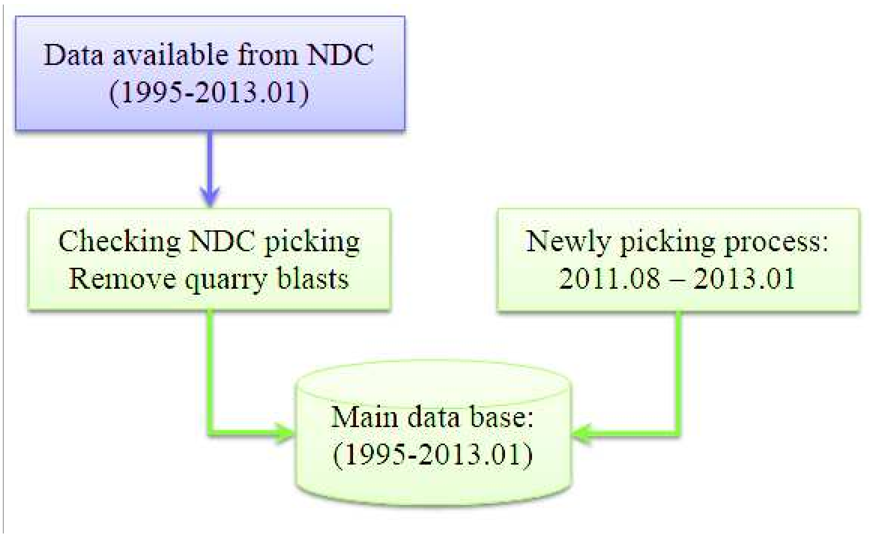

Figure 3.3. Flow chart for the construction of the “Main data base”.

3.2.1.1.1 Data available from NDC and checking NDC picking.

At the beginning of my work, I took earthquakes data from the NDC of IAG and selected the events located within an area of 400x400km centred on the Emeelt fault between 1st January 1964 and 31 January 2013. The selected distance is chosen to consider only the region that can have an impact on the Ulaanbaatar seismic hazard. The selected period corresponds to the available data when I performed this work. With this space and time selection I obtained 10515 seismic events (plotted in Figure 2.6).

Nevertheless, it appeared rapidly that this large area and the widely spread seismic network made it difficult to compute a precise crustal velocity model and hypocentre location from those data. Therefore, I decreased the size of the study area down to an area of 140x140km centred on the Emeelt fault where the seismic network is denser (Figure 2.12). I decreased also the period of observation from 1995 until 2013, when the network around Ulaanbaatar was operating. In addition, I checked all arrivals on the recorded signals and removed 109 quarry blasts from this database. I obtained 3490 events, which I named *"Main data base"* (plotted in Figure 3.4).

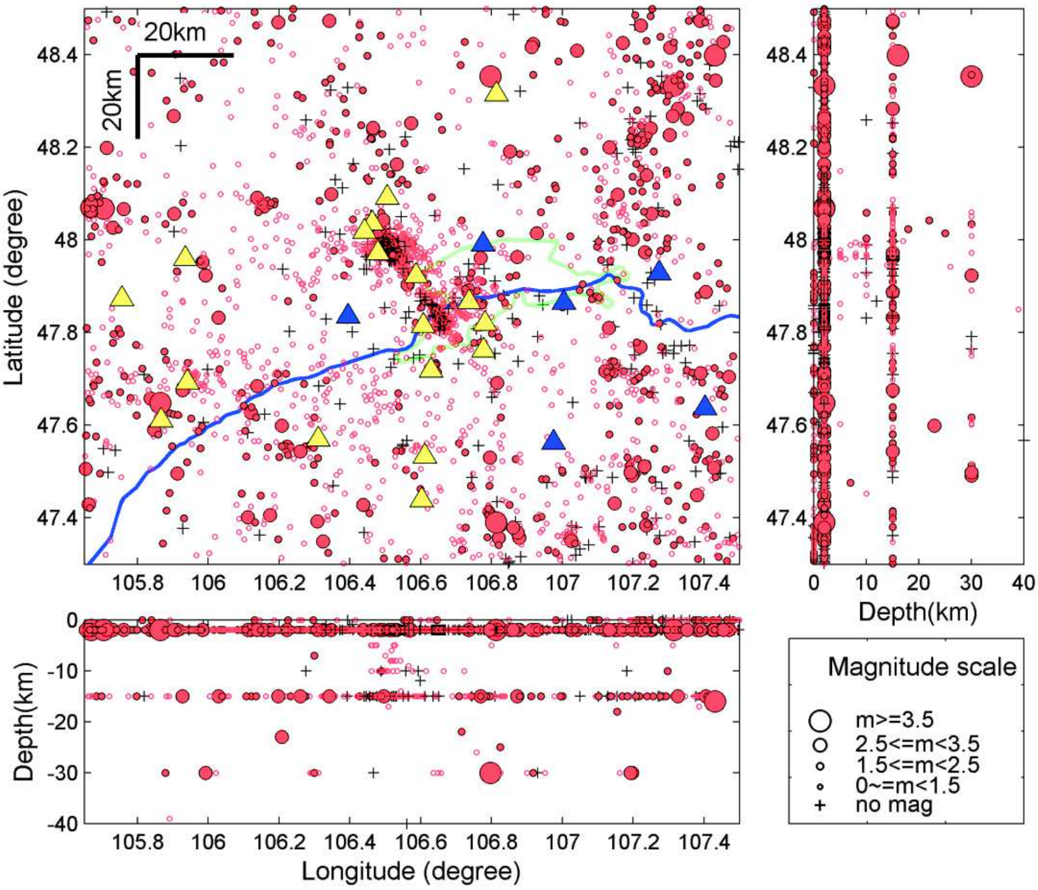

Figure 3.4. Hypocenter of events selected into *"Main data base"* based on NDC results (1995-2013.01). Blue line is Tuul river and green line is urban area of Ulaanbaatar city. Blue (UB array) and yellow (UB mobile) triangles show seismic station locations.

All of my study is based on this database until I obtain the 3D velocity model. These events were detected and located based on UB-array and UB-mobile records. For the localization, we use the ONYX software program that was developed by DASE (CEA) based on non-linear inversion by least square method, to build the regular earthquake catalogue of NDC. I participated in this procedure and associated duty from 1997 to 2009. Notice that I have used only SA0 station data of "CTBT-Songino-array".

3.2.1.1.2 New complementary picking process

The second step was to add complementary pickings for the selected events in the *"Main data base"*. This process was an important step to improve earthquakes location because the phase picking done at NDC for the localization did not include all phases of all UB-mobile stations. The reason is that we only collected the mobile station's data each 30 days directly at the stations (local record, no data transmission), and then we can include them in the localization process. Unfortunately, mobile station's data were not included since the end of 2011. Thus I had to read the continuous data of all available UB-mobile station's, to pick manually, according to the quality of their onsets, all available P and S arrival times between August 2011 and January 2013. Unfortunately, I could not measure all phases that I wanted because sometimes no signal was recorded in the mobile stations (station problem or shutdown). As mentioned above, because we collect mobile station's data once a month, we do not know if the station was working normally or not during the period until we extract the data from the station and read them.

I could also observe from my reading of continuous recordings several quality problems in the NDC bulletin that I had to correct:

- Several arrival times were not precisely picked or even not picked at all at some stations.

- Six mobile stations were not included in the duty process (EM3M, EM4M, EM6M, EM9M, UB2S, UB3S) and some picking were missing at the other stations.

- Many small events have been missed. In my thesis work, I did not add new events outside those identified by the NDC; therefore I did not pick the arrivals of these small events observed during the seismic crisis. Nevertheless, in the near future, it would be useful to include all of them by using, for example, wave cross correlation methods.

Also, I discovered that the coordinates of two mobile stations were wrong in the database of NDC (high residuals), UB2 and UB7, and we corrected them.

After this procedure, the number of phases picked increased up to 38.54% from the mobile stations.

Figure 3.5 shows the percentage of phases picked in mobile stations by the duty procedure and the newly picked between 2011.08 and 2013.01. Starting with 2881 arrivals (by duty), I added 1807 new arrivals from the UB mobile stations.

	UB1	UB4	UB9	EM4	UB5	UB2S	EM6	EM9	EM3	UB7	UB8	UB6	UB0	UB3S
🟥 Newly picked	325	219	2	203	2	403	47	103	149	43	15	208	4	99
🟦 Picked by duty	591	458	73	0	302	0	0	0	0	82	130	250	68	0

Figure 3.5. The phase picking percentage of events between 2011.08 and 2013.01 per station. All these stations are mobile stations. Blue colour represents phase picking by the duty at NDC and red colour represents my newly picked phases. The order of the stations, from left to right, is by increasing distance from the central point of the study area (47.9N, 106.6E)

3.2.1.2 Event selection A1 for Single Event Mode (VELEST)

The aim of the first selection (*Selection A1*) is to restrict the “Main Data Base” to the events that could be located with an “enough good accuracy” before the *Selection A2*. The criteria are:

Firstly, between 1996 and 2011.08, I selected 284 events, which are associated with P and S phases at least at 5 stations and with an azimuthal GAP of less than 180^0.

Secondly, between August 2011 and January 2013, I did not consider the azimuthal GAP for the selection. The reason is that the azimuthal GAP provided by the NDC database did not include the UB-mobile stations and was therefore not representative for the data I used (I included the mobile stations with new picking). In this period, I got then 343 events with P and S phases at least at 5 stations.

At the end, I obtained 627 earthquakes (*Selection A1*) located in the study area (Figure 3.6). Regarding depth distribution, the events are separated in two classes at NDC, with 477 evens (76% of those events) localized at 2 km and 101 (16% of those events) events localized at 5 km depth, which does not represent the reality.

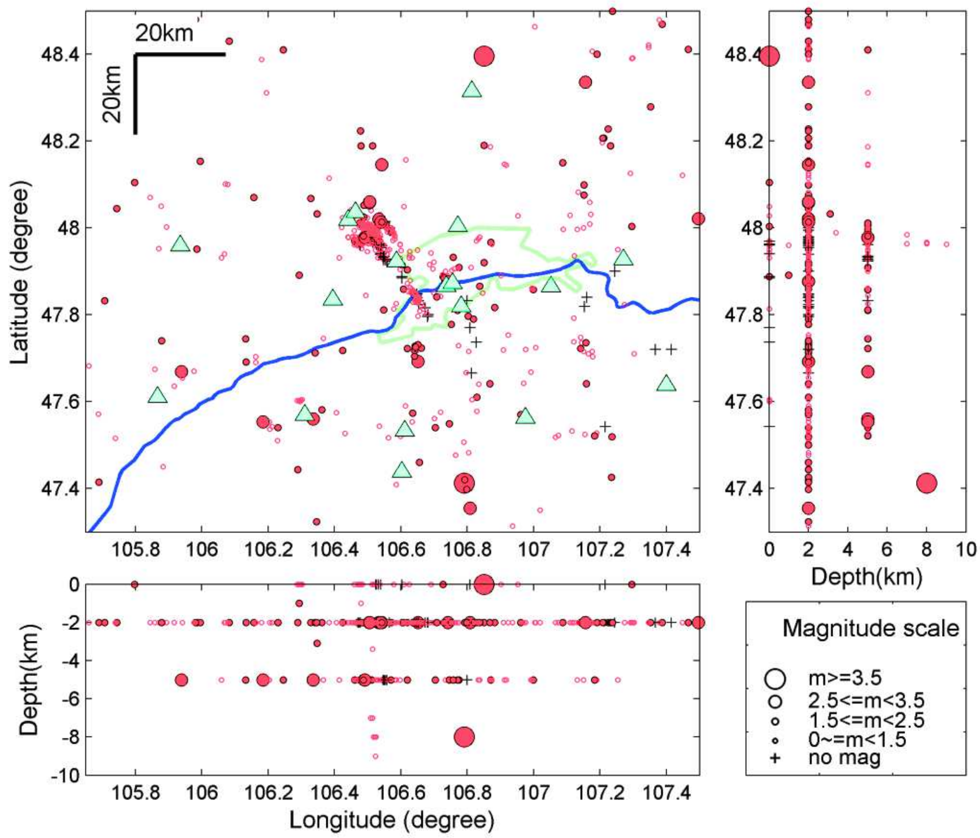

Figure 3.6. Hypocenters (based on NDC database) around Emeelt fault area (140x140km) of the Selection A1. Green line = urban area of Ulaanbaatar, blue line = Tuul river and aqua triangles = seismic stations.

3.2.1.3 Single Event Mode (VELEST) location

Then I did an initial localization of these 627 events by VELEST single-event-mode (SEM) using the NDC velocity model to improve the poorly constrained depth with the NDC catalogue and to include all newly picked phases from UB-mobile stations (Figure 3.7and Figure 3.8). Earthquakes relocated by SEM are presented with low rms values, 0.28 (Figure 3.9), and average values of errors estimate in longitude, latitude and depth, are 3.56, 2.79 and 10.76 km, respectively.

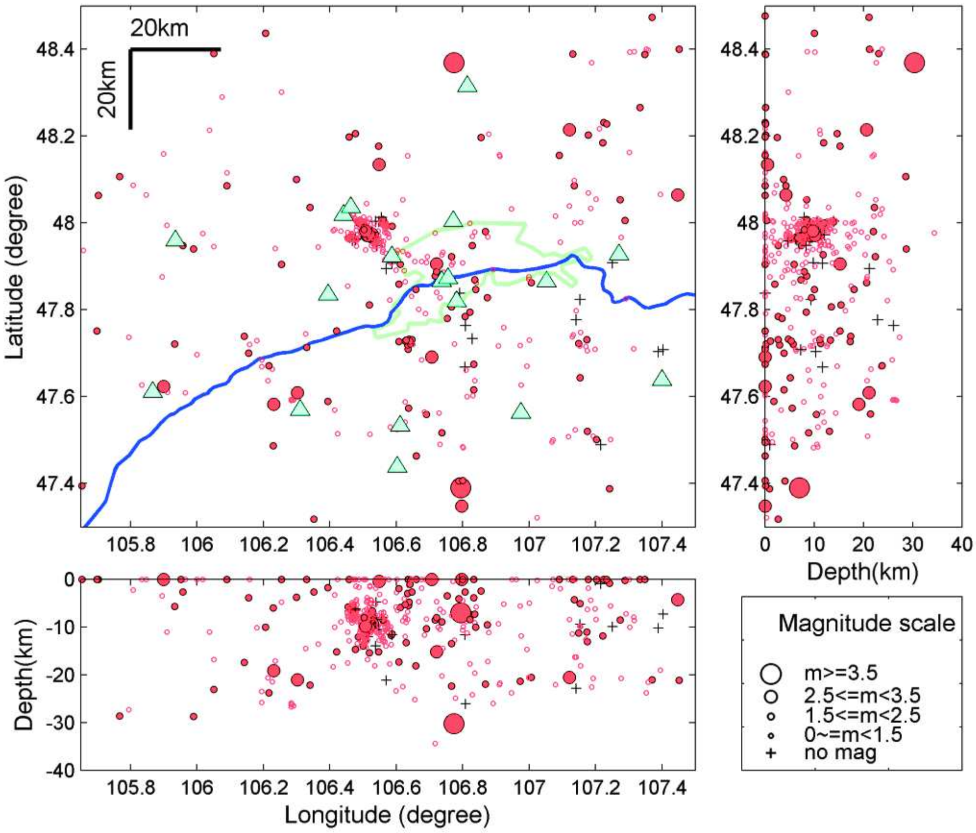

Figure 3.7. Hypocenters of Selection A1 earthquakes after relocation by SEM of VELEST. Green line = urban area of Ulaanbaatar, blue line = Tuul river and aqua triangles = seismic stations.

Hypocentres of earthquakes shown in Figure 3.7 and depth histogram shown in Figure 3.8. The location result gives a mean rms of 0.28 for the hypocentral location (Figure 3.9).

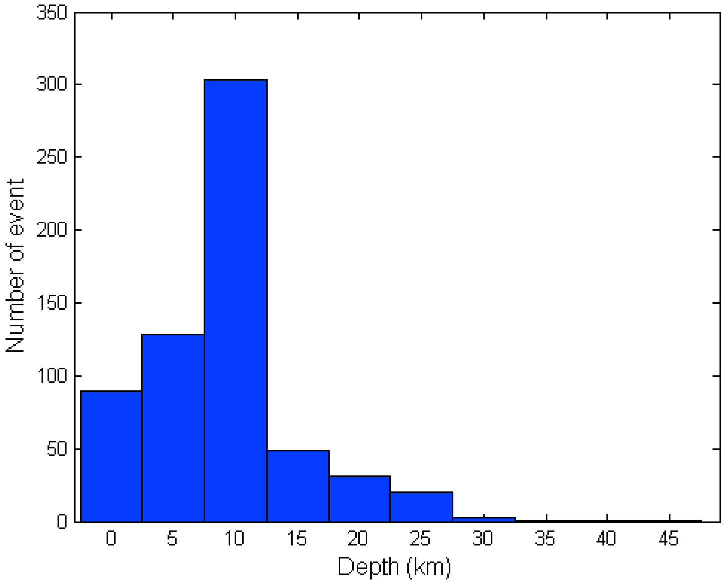

Figure 3.8. Histogram of depths of relocated events selected into Selection A1.

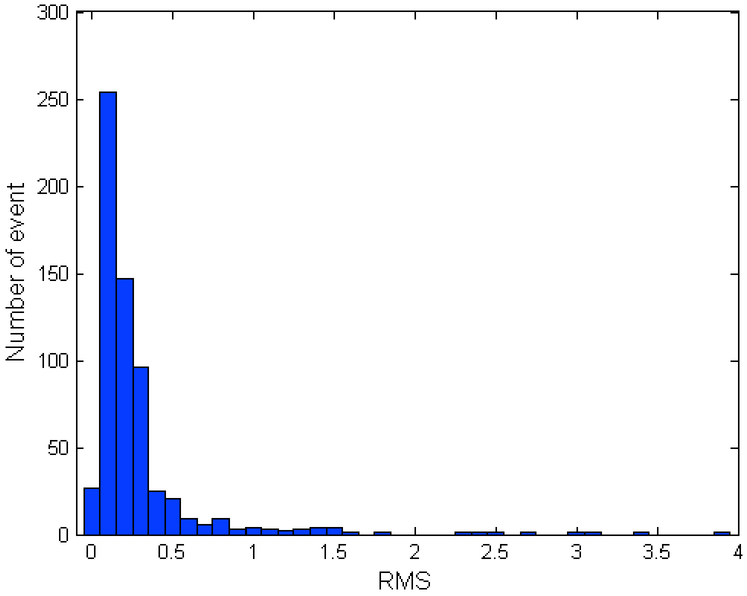

Figure 3.9. Histogram of rms of relocated events of Selection A1.

Most of the times, the main change in hypocentre location between NDC and SEM results is related to depth improvement (comparison between Figure 3.6, Figure 3.7 and Figure 3.11), the NDC depths were most of the time blocked at 2 and 5 km (Figure 3.6).

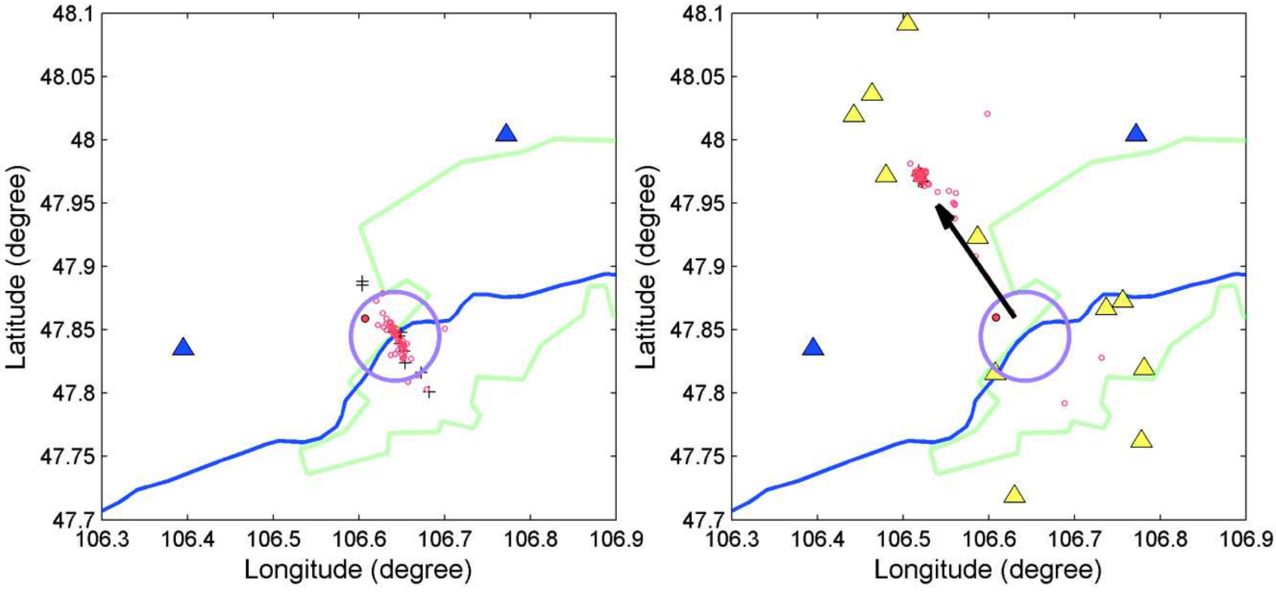

Figure 3.10. Initial misslocation and correction of seismic events near the Emeelt fault. Left figure is events located by NDC (national data center) using only 2 stations and right figure is location with SEM (single event mode) including UB-mobile stations. Triangles indicate seismic stations of UB-array (blue) and UB-mobile (yellow). Green line = urban area of Ulaanbaatar and blue line = Tuul river.

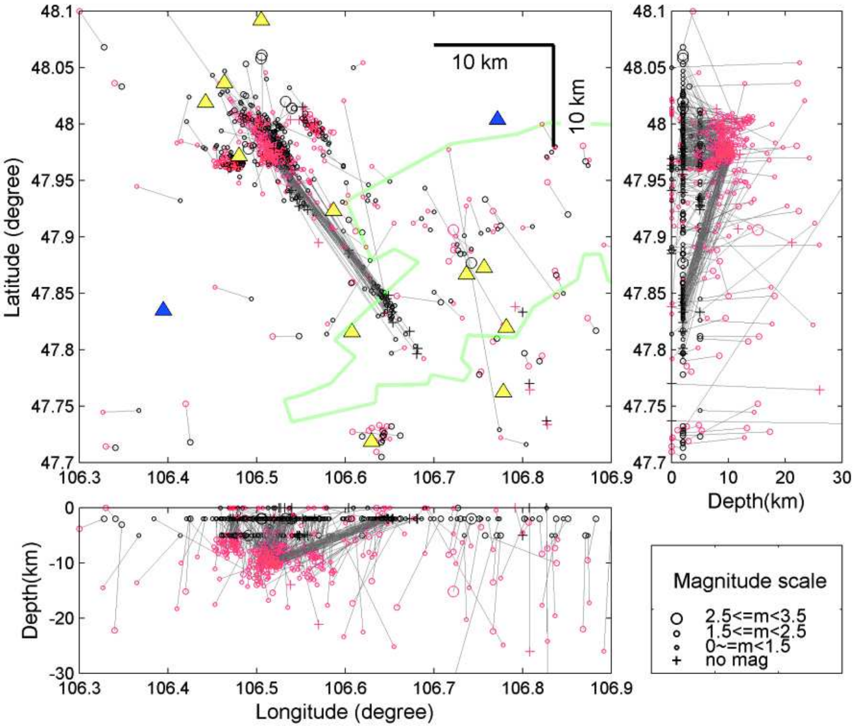

Figure 3.11. Epicentral and hypocentral view of events localized by NDC (black) and SEM (blue). Triangles indicate seismic stations of UB-array (blue) and UB-mobile (yellow). Gray line is movement trajectory of events between NDC and SEM hypocenter location. Green line = urban area of Ulaanbaatar and blue line = Tuul river.

After relocation procedure, there are interesting epicentre movements observed in the Emeelt fault area. Almost all events that were located to the south (left side of Figure 3.10) of the Emeelt fault moved to the north of this fault (right side of Figure 3.10). This was related to the fact that two permanent stations were located perpendicularly to the direction of the fault (ALFM station and SA0 station from CTBT-Songino-mini-array) giving a strong location uncertainty when they were used alone (blue triangle in Figure 3.10 and Figure 3.11). Adding new picking from other stations (UB-mobile denoted in yellow triangle in Figure 3.10) allowed correcting this “mirror artefact” in the NDC locations (Figure 3.10 and Figure 3.12).

I show one example (Figure 3.12) of an event that occurred in 2013/01/09 with 0.2 magnitude (M_L). The Table 3.1 shows two localization results of this event, from NDC (2 stations) and from relocated SEM (7 stations) with very low RMS=0.11. This event moved by 19 km to the NW direction from NDC location.

Table 3.1. Location results of event occurring 2013/01/09.

	Origin time	Latitude	Longitude	Depth	Gap	Number of stations
NDC	09:03:55.70	47.8319	106.6420	2.0	243	2
SEM	09:03:55.93	47.9736	106.5133	9.4	83	7

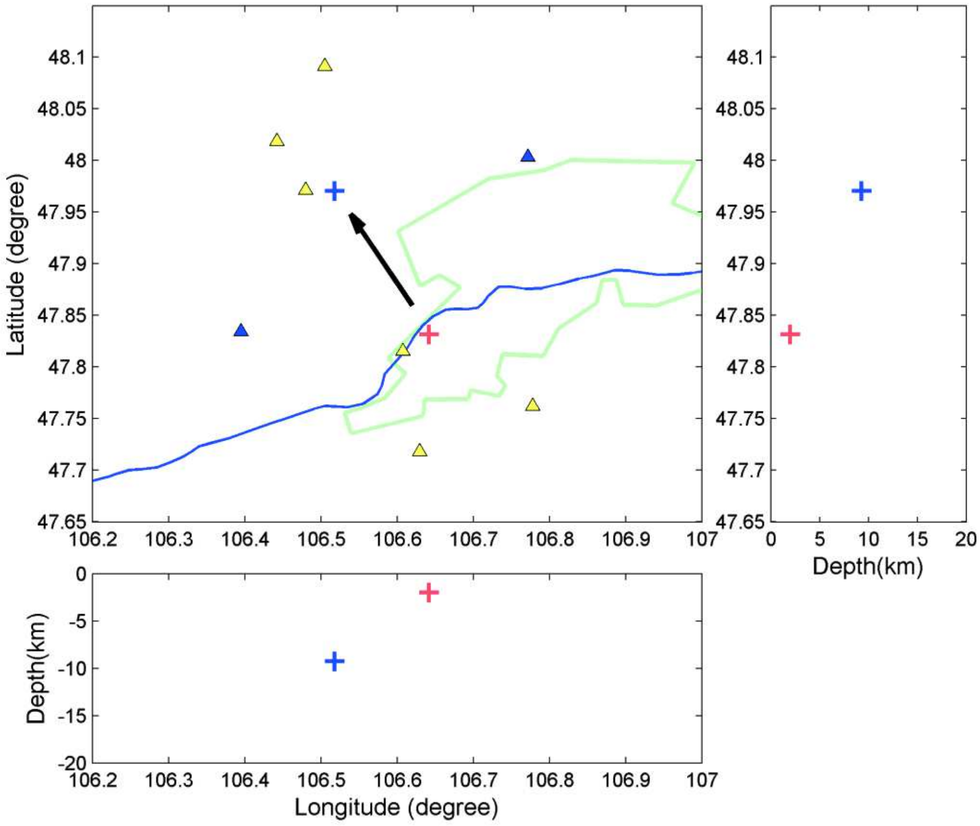

Figure 3.12. Hypocenters of earthquake occurring on 9 January 2013 (M_L=0.2). Red cross is the location determined by the NDC with 2 stations and the blue cross is the new location of this event after adding all arrival times from 7 UB-mobile stations. Blue triangles are the permanent UB-array stations and yellow triangles are UB-mobile stations. Blue line is Tuul river and green line is urban area of Ulaanbaatar city.

Table 3.2. Arrival times of event shown in Figure 3.12.

Station	Arrival time of P phase	Arrival time of S phase
EM4	09:03:57.81	09:03:58.99
UB2	09:03:58.15	09:03:59.63
EM3	09:03:58.76	09:04:00.63
SA0	**09:03:59.18**	**09:04:01.60**
UB4	09:03:59.53	09:04:01.94
ALF	**09:03:59.55**	**09:04:01.99**
EM6	09:04:01.26	09:04:04.98
EM9	09:04:01.29	09:04:05.24

The arrival times of this event shown in Table 3.2 are, in red, the permanent stations (very similar arrival times giving strong uncertainty on the location) and, in black, the added stations that allow correcting and constraining the event location. This event is detected first at the EM4, then at the UB2 and finally detected at the EM9; it means this event is located near the EM4 and UB2 stations.

3.2.1.4 Event selection A2 for the 1D inversion (VELEST).

After the “single event mode” location, I did the second selection (*Selection A2*) based on the relocated result of Selection A1. The aim is to use only the events with the best observations to build the 1D velocity model. These events will be also relocated using this 1D new model.

The criteria are: azimuthal GAP of less than 160^0 and location RMS of less than 0.4s. Then, I obtained 271 events, named *Selection A2.* Their epicentre location (single event mode) is shown in Figure 3.13. When we compare “selection A1” (Figure 3.7) and “selection A2” (Figure 3.13), we see that the events of selection A2, are more precisely located, and start to describe some vertical structures. We can see that in Figure 3.14 and Figure 3.15 the depth improvement of the Selection A2 between the NDC location (with a distribution of the depths mainly between 5 and 11 km) and the “single event mode” location. The minimum depth difference is 0.5 km and the maximum is 26.8 km (Figure 3.15).

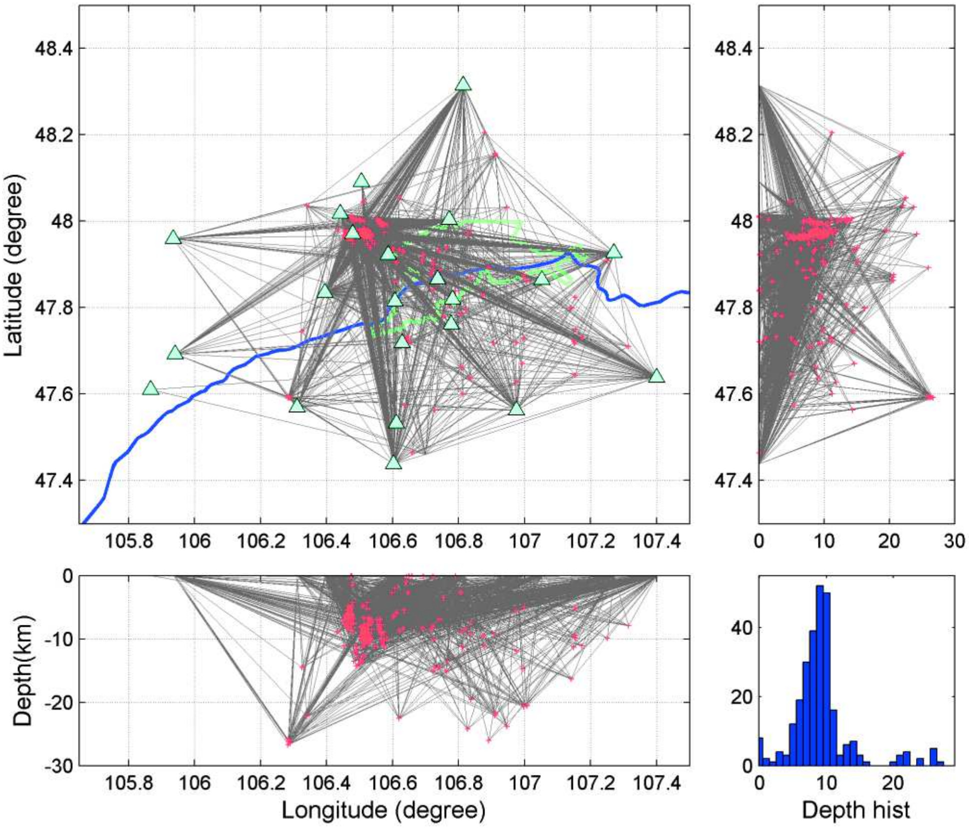

Figure 3.13. Hypocenters of events selected into the *Selection A2*. Gray lines show direct ray paths between event location (red cross) and picked stations (blue triangle).

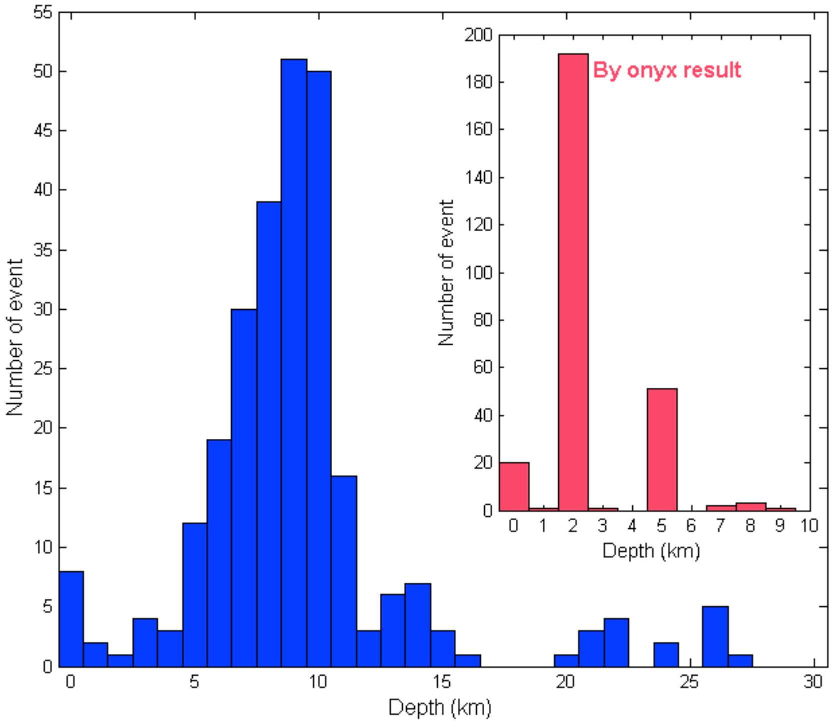

Figure 3.14. Depth histogram of the *Selection A2*. Blue colour shows single event mode location and red colour indicates NDC location.

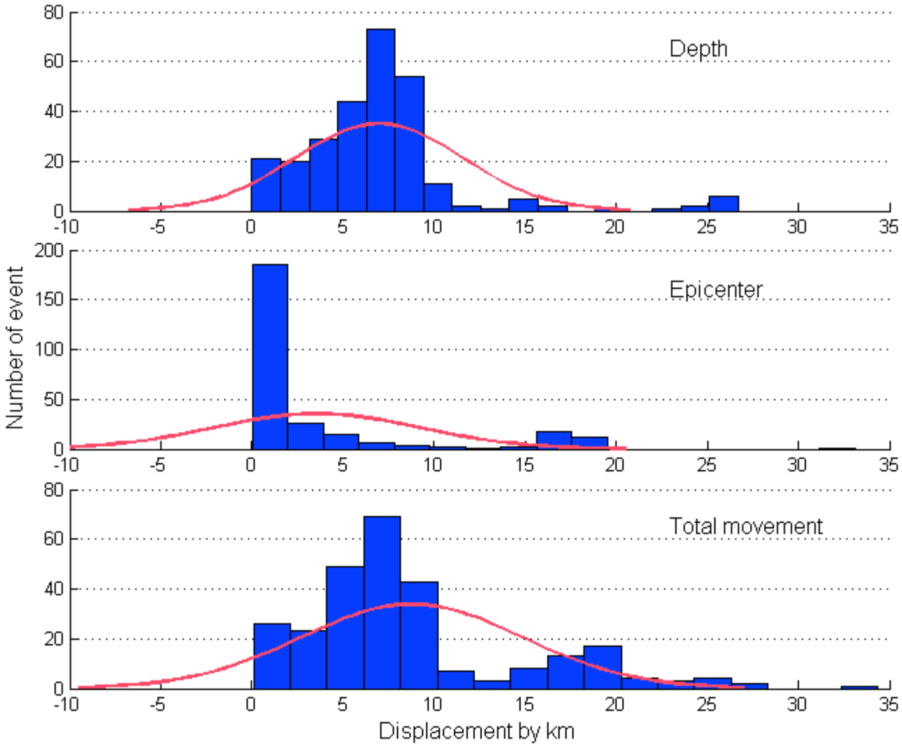

Figure 3.15. Depth changes (top), epicentral changes (middle) and total displacement (bottom) of events between NDC location and "SEM" location for the Selection A2.

3.2.1.5 *Initial 1D velocity model*

3.2.1.5.1 Initial velocity model for Vp

In this study, I used the NDC velocity model as the base to build the "initial velocity model" for the 1D inversion. The velocity model of NDC is characterized by two layers, 6.11 km/s from surface to 35 km depth and 8.1 km/s between 35 and 50 km with a Vp/Vs of 1.73. This model is based on the average travel-time table of Mongolia (Baljinnyam et al., 1975) calculated using the main seismic phases of earthquakes occurring between 1968 and 1973 (blue coloured in Figure 3.16). It is the velocity model still used today at the NDC.

For the "initial velocity model", I used another crustal thickness, 45 km, based on more recent studies done near Ulaanbaatar by Mordvinova et al., (1996) and Zorin et al., (2002). They used the receiver function method, P-to-S converted waves at crustal and mantle interfaces, beneath each seismic station of the PASSCAL-1992 transect (Figure 3.1 and Figure 3.17).

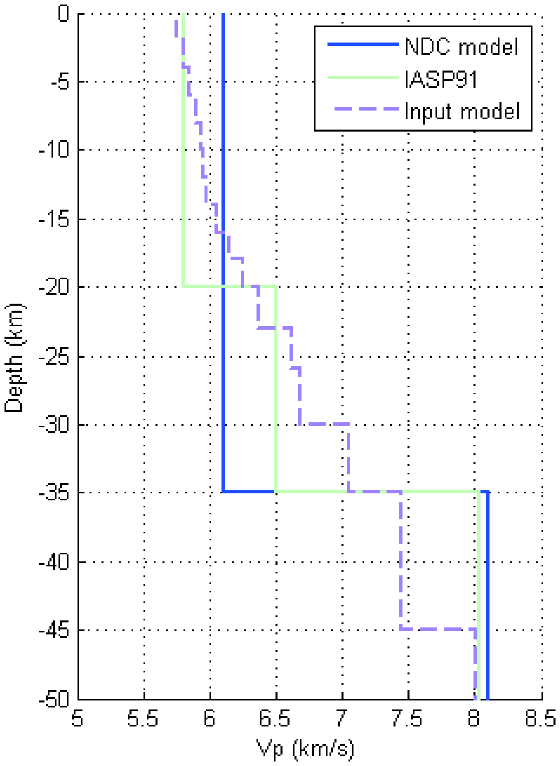

Figure 3.16. Initial 1D velocity model (NDC model after Baljinnyam et al., 1975)

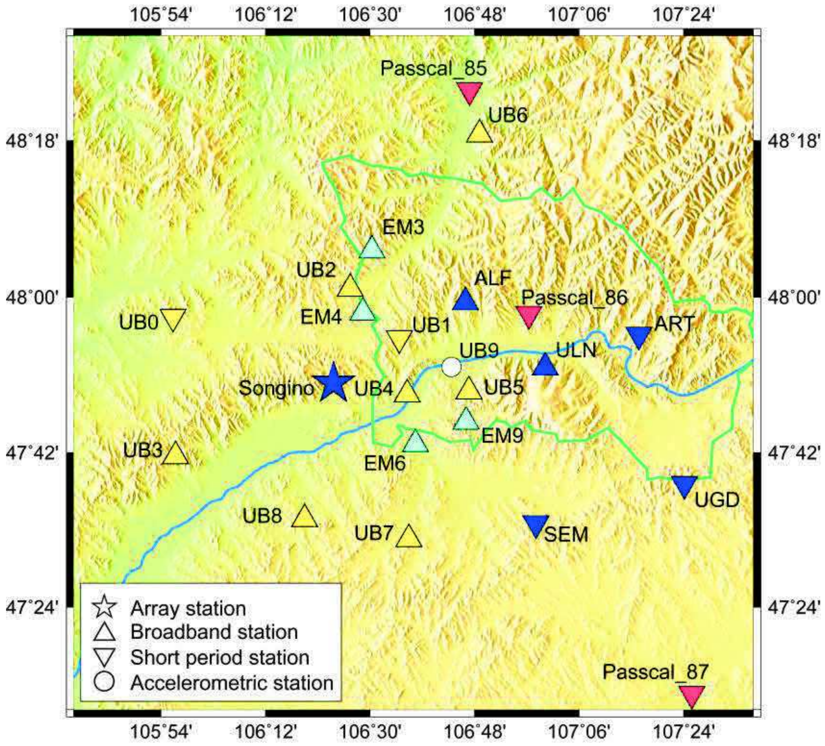

Figure 3.17. Seismic network around Ulaanbaatar (as in January of 2013). Triangles are location of seismic stations, blue is UB array, yellow is UB-mobile and aqua is additional mobile stations active during 2 weeks in 2013. Blue star is "CTBT Songino array". The red triangles are location of seismic stations from PASSCAL transect. Blue line is Tuul river and green line is administrative limit of Ulaanbaatar city.

Moreover, I have to smooth the "initial velocity model" before using it for the "1D velocity model inversion". I did that manually with in my case 2 km steps down to 20 km, then 3 km down to 26 km and below 5 km, with Vp values chosen close to the NDC velocity model (Figure 3.16).

3.2.1.5.2 Velocity ratio (Vp/Vs)

I determined the velocity ratio by the Wadati method (Wadati, 1933), which produces a fairly accurate estimate of Vp/Vs without the knowledge of source parameters. This technique was originally suggested to estimate the origin time of an earthquake and is used by many researchers for velocity-ratio estimates. I calculated the velocity ratio using the "selection A2" data set. I obtained a velocity ratio range between 1.63 and 1.78km/s with an average of 1.7 km/s (Figure 3.18) associated with RMS between 0.02 and 0.56. Therefore, the input file for the S velocity model in the 1D inversion was derived from the P velocity model assuming Vp/Vs=1.7.

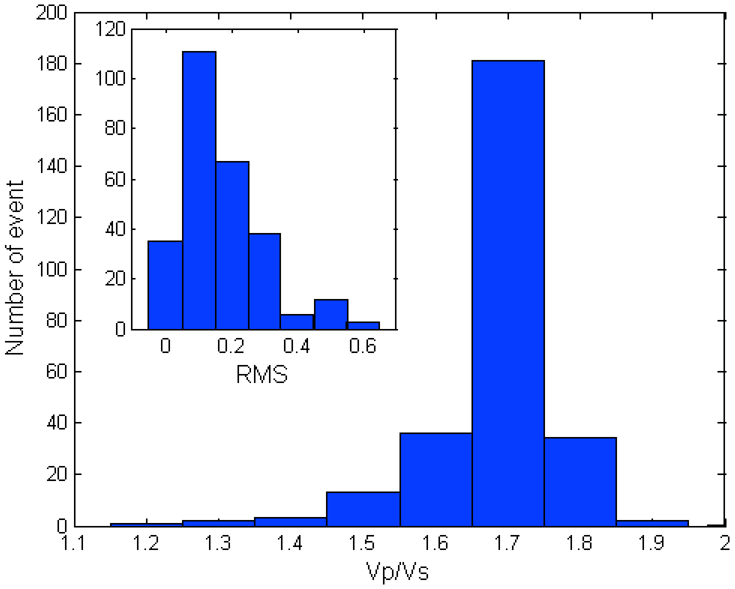

Figure 3.18. Histogram of Vp/Vs ratio and RMS for the events of "Selection A2".

3.3 Velest 1D inversion

I performed the 1D inversion using the 271 earthquakes of the *Selection A2*. The Figure 3.13 shows the hypocentres of *Selection A2* and the ray path up to the stations with available arrival time. For the reference station, I choose the ALF station, which is located inside the UB networks and with continuous recording during the whole period.

As there is no any study based on controlled seismic sources for identifying deep layers in the study area, I followed the recommendations of Kissling (1994). I began with a large number of thin layers (~2 km). Then, between the inversion iterations, I combined layers for which velocities are similar. The inversion process was stopped when the earthquake locations, station delays and velocity values did not vary significantly in subsequent iterations.

A total of 3985 arrivals from 271 selected events were inverted. After iterations, we obtained a final rms of 0.19 s. A value of 6.0km/s is obtained for the upper crust, and values around 6.3 and 6.7km/s are computed for the middle and lower crust, respectively.

The computed 1D model is shown in Figure 3.19 (Output 1D inversion) and compared with previously available models: NDC, Zorin et al., (2002) and input 1D model.

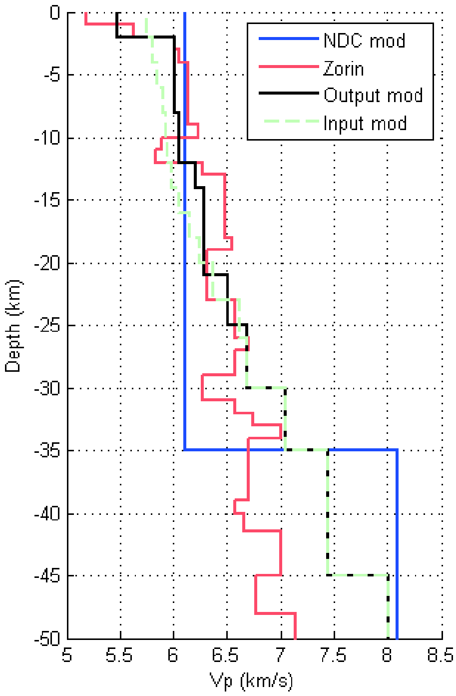

Figure 3.19. New 1D P-velocity model = black line. The NDC model = blue line and Zorin et al., (2002) model = red line. The input 1D model = green dahsed line

From top until ~27-28 km depth, the obtained 1D velocity model shows similar velocity gradients with the Zorin et al. (2002) velocity model. Below 27-28 km, the input P-velocity remains unchanged as very few illuminating ray-paths were available but it is not constrained because most of the events are shallower and the rays do not travel at these depths.

However, other important parameters to compute minimum 1D velocity model are the station corrections that contain information from near surface velocity heterogeneities and the geometry of the crust. I obtained very low station corrections (Figure 3.20 and Figure 3.21), mainly ±0.05 for P waves and ±0.08 for S waves in reference to the ALF station. The ULN station is associated with high station corrections (+0.28 for P and +0.49 for S). Despite they are only 39 events used (see Figure 3.21 and Table 6.1 of Appendix 3), it cannot be the explanation as they are other stations with lower station correction and even less events used. For ULN station, the reason can be the particlar underlying geology with a large granite body (Bogd Mountain). For the UB3M, a preliminary explanation could be that the station is at the middle of the Ulaanbaatar basin.

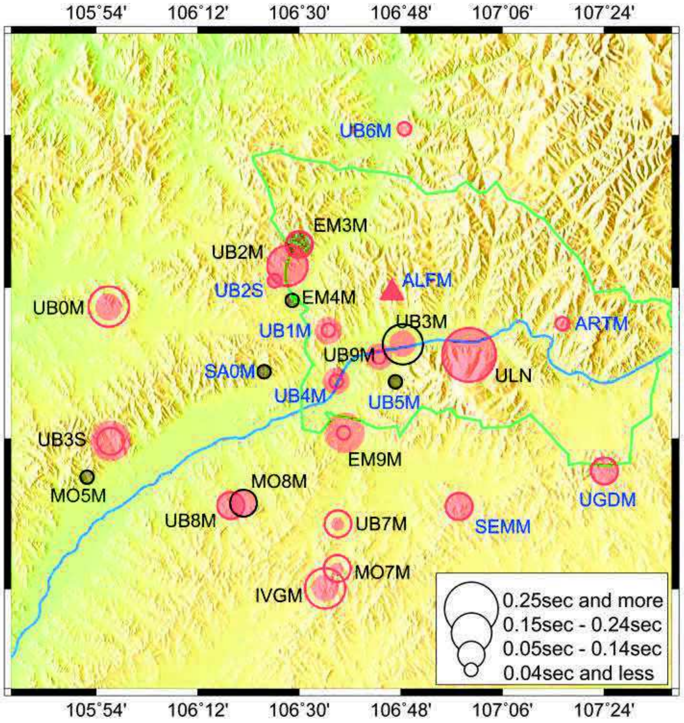

Figure 3.20. Station correction value. Blue colour names are stations at which we used more than 100 events and black colour names are for stations at which we used less than 50 events. Circles in red and black represent, respectively, positive and negative values with respect to the reference station (ALFM = red triangle). Open circles represent corrections for P and filled ones for S waves.

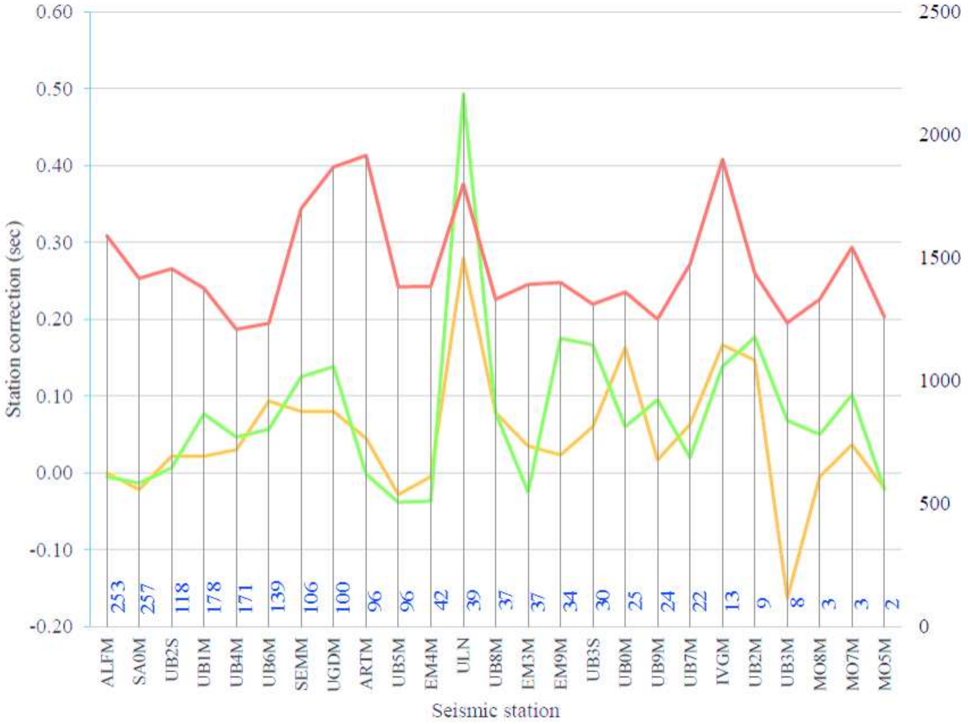

Figure 3.21. Station correction values (yellow = P and green = S) and station elevations (brown line). Numbers in blue are the number of event used at each station .

3.4 Conclusion on 1D model

This is the first study of local 1D velocity model inversion in the area of Emeelt using local earthquake data and a dense seismic network.

The comparison between the new 1D velocity model and Zorin et al. (2002) model shows high similitude down to ~28 km depth. Below this depth, our new 1D velocity model is not well constrained because of poor ray path (Figure 3.13 and Figure 3.19). A value of 6.0km/s is obtained for the upper crust, and values around 6.3 and 6.7km/s are computed for the middle and lower crust, respectively. The 1D velocity model obtained shows that there is no large variation in average P wave velocity of the upper and middle crust.

Regarding the station corrections values, they are very low (average correction is +0.03 sec) when more than 100 events are used (see Appendix 3). The most important station corrections are for ULN station with +0.28s (P) and +0.49s (S) and other two stations, UB3M and EM9M, with respectively, -0.16s (for P) and 0.18s (for S) (Figure 3.20 and Figure 3.21). It is probably related with the very low number of events used for iteration at these stations. For example the UB3M station correction is based on only 8 events.

3.5 New location of seismicity around the Emeelt fault

The quality of the earthquake location by the NDC in the area of the Emeelt fault is poor, mainly for the depth problem. The quality has been improved with my previous work. I added arrivals from mobile stations and sometimes new picking at permanent stations. I also checked and corrected, when necessary, the precision of the picking made during the duty. From the VELEST procedure, I obtained a local 1D velocity. This chapter focuses now on a high-resolution location of this seismic activity using HYPOINVERSE (Kissling, 1978) procedure with event locations and velocity model based on the previous work. This new step is very important, as the input locations that we will be used in the TomoDD procedure (next chapter) must have reduced uncertainties. The procedure is summarized in Figure 3.22 and each step will be detailed hereafter.

Notice that we cannot use the VELEST localization method for that because VELEST includes station corrections, which roughly represent the velocity model under the station.

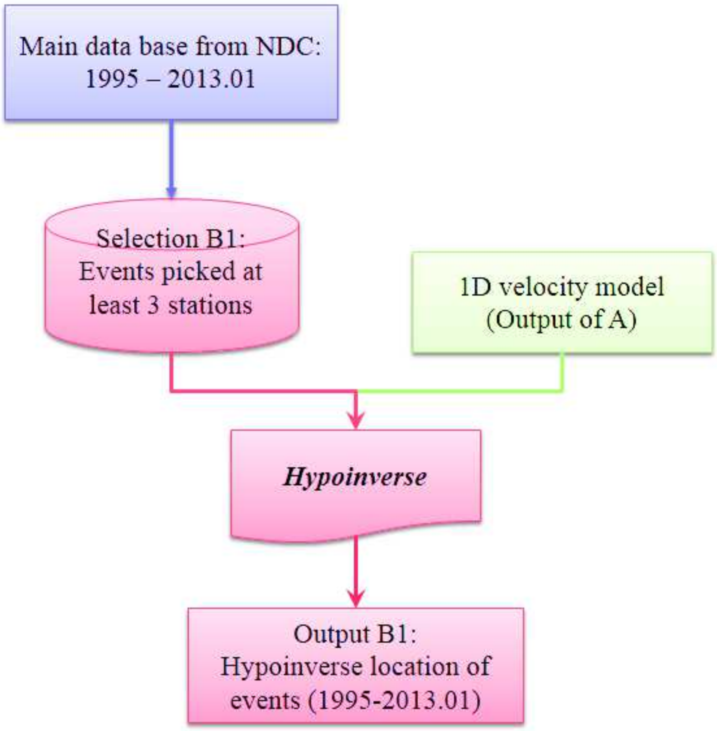

Figure 3.22. Summary of the location process using Hypoinverse (Procedure B1)

For this new location procedure, I selected events, which are picked at least at three stations to build the Selection B1 (Figure 3.22). I obtained 1926 earthquakes from the total 3490 earthquakes detected in the region. Their locations are presented in Figure 3.24 and, magnitude and depth histograms in Figure 3.23. As I mentioned several times before, it shows clearly that the depth is not constrained, 80% of event's depth were fixed at 2 km in the NDC catalogue.

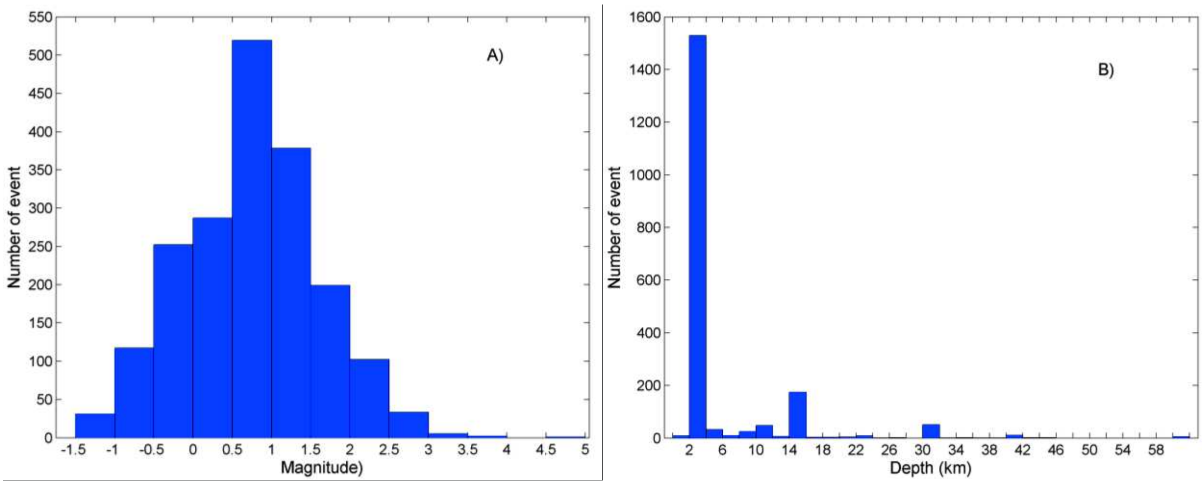

Figure 3.23. NDC magnitude (A) and depth histogram (B) of Selection B1.

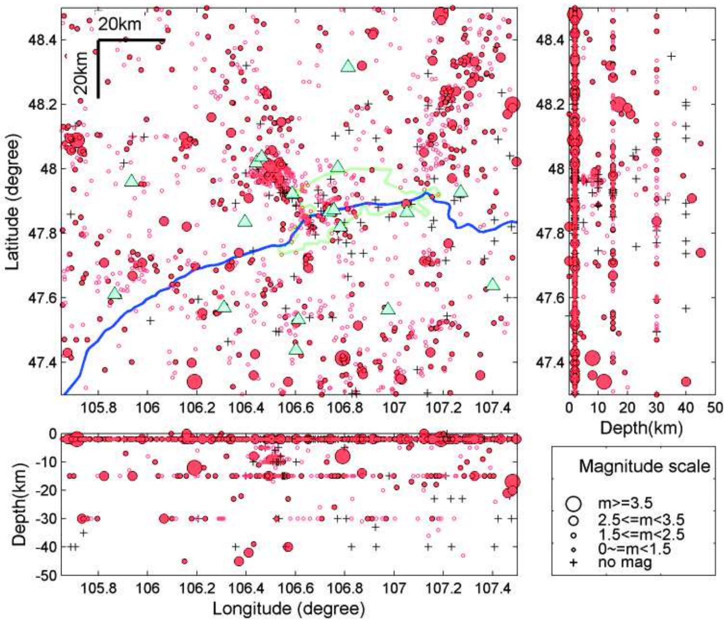

Figure 3.24. NDC hypocenter location of the 1926 events of the Selection B1. Triangles = seismic stations, blue line = Tuul river, green line = urban area of Ulaanbaatar city.

3.5.1 Results of the HYPOINVERSE localization

After the hypoinverse localization procedure, we improved significantly the hypocentres with a considerable reduction of depth uncertainty (Figure 3.25). The distribution of seismicity confirms that the majority of the seismic activity is clustered in space in the Emeelt fault area.

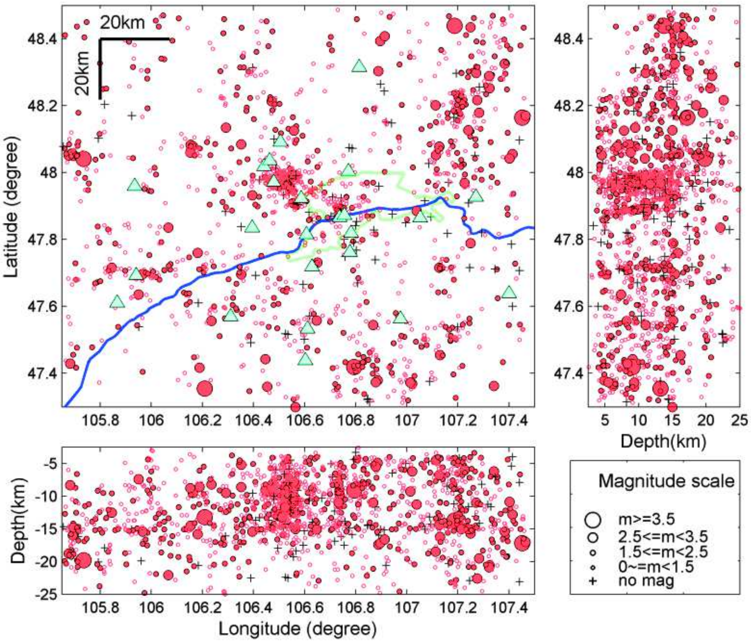

Figure 3.25. Hypoinverse hypocenter locations (selection B1) using the new 1D velocity model. Blue line is Tuul river and green line is urban area of Ulaanbaatar city.

This new data allows us to initiate discussions on the depth of events. Most events are shallower than 16 km, with a large number of hypocentres concentrated in the uppermost part of the crust between 4 and 16 km (Figure 3.25 and Figure 3.26-B). There is an apparent increase of events at about 16 km depth that should be considered with caution at this step. The RMS is between 0.01s and 2.7s with a mean of 0.136s (Table 3.3). The mean RMS is 0.136 second (Figure 3.26-A), the mean horizontal uncertainty (1 sigma) is 3.33 km (Figure 3.26-C) and the mean vertical uncertainty (1 sigma) is 5.99 km (Figure 3.26-D).

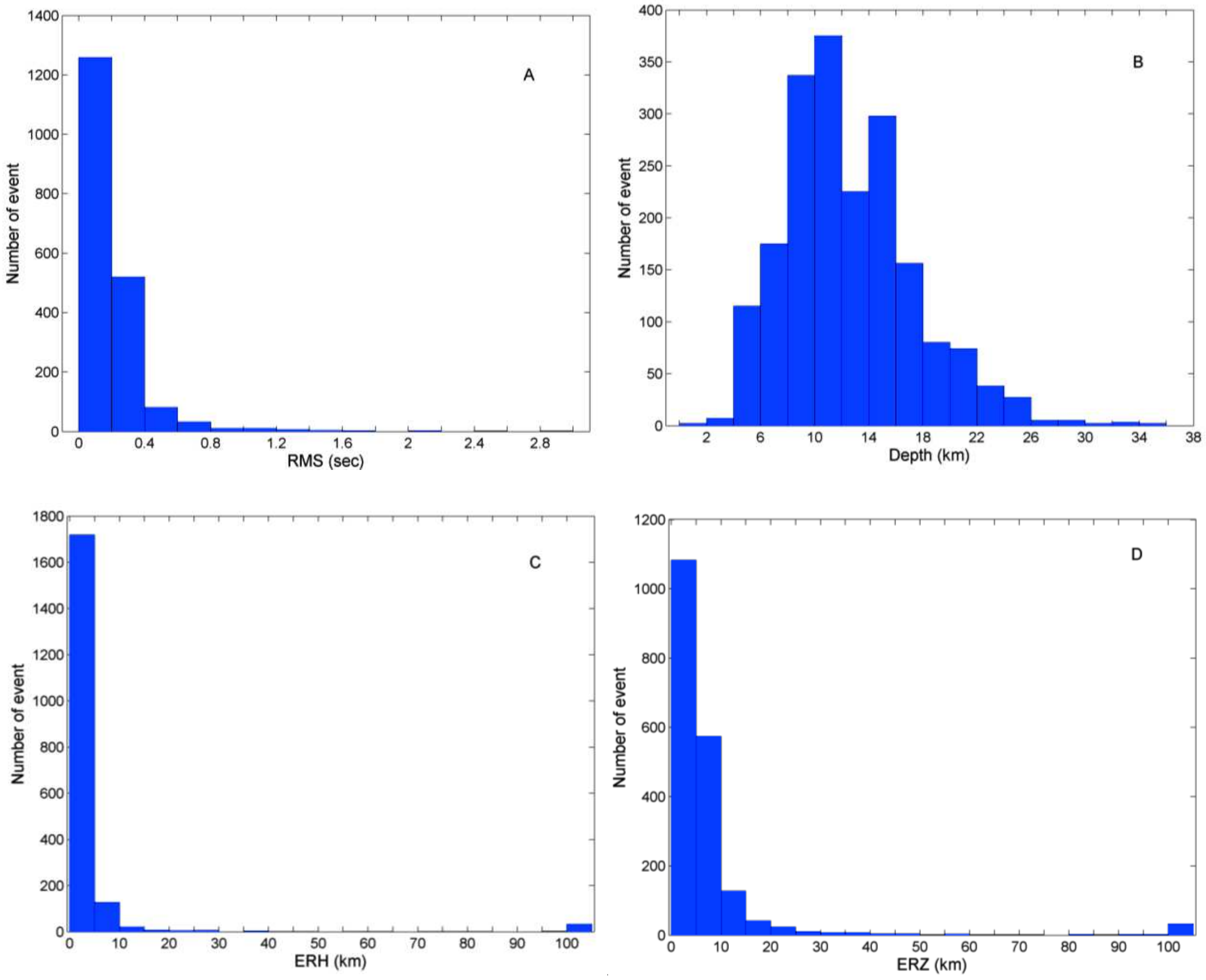

Figure 3.26. Histogram of hypoinverse locations parameters (A) Root mean square (rms), (B) depth, (C) horizontal uncertainty (1 sigma) and (D) vertical uncertainty (1 sigma).

Table 3.3. Mean RMS, ERH and ERZ errors of Selection B1 from Hypoinverse procedure.

Epicentral movement, km	Number of events	Mean errors		
		RMS	ERH	ERZ
All localized events	1926	0.2929	3.3362	5.9917
EpiMov < 1.5	698	0.1045	0.7340	5.5438
1.5 <= EpiMov < 2.5	351	0.1099	1.0368	6.2923
2.5 <= EpiMov < 3.5	232	0.1194	1.7297	4.9341
3.5 <= EpiMov < 4.5	164	0.1136	2.9787	5.9976
4.5 <= EpiMov < 5.5	107	0.1189	1.5757	6.1093
5.5 <= EpiMov < 6.5	75	0.1948	2.2720	5.1920
6.5 <= EpiMov < 7.5	52	0.1760	5.1846	4.5769
7.5 <= EpiMov < 8.5	22	0.1168	10.0136	2.5409
8.5 <= EpiMov < 9.5	16	0.2431	14.1812	5.5313
9.5 <= EpiMov	209	0.2929	17.2426	9.1292

3.5.2 Discussion on depth and epicentral changes between NDC and Hypoinverse localizations

Several figures illustrate the difference between the NDC and the new location by Hypoinverse (with completed arrivals dataset and new 1D velocity model). They are separated according to the increasing epicentre change between NDC locations and Hypoinverse locations (≤1.4km: Figure 3.27, 1.5 to 2.4km: Figure 3.28, 2.5 to 3.4km: Figure 3.29, 3.5 to 4.4km: Figure 3.30, >9.5 km: Figure 3.32 and Table 3.4).

After the relocation procedure, 36.2% of the events of Selection B1 moved (only epicentre displacement) less than 1.5 km (Figure 3.27 and Table 3.4). But the vertical correction of those events is between 1 and 19.5 km. About 75% of the locations moved less than 4.4 km (Figure 3.28, Figure 3.29 and Figure 3.30). We do not see particular location dependence with epicentre correction when it is less than 4.4 km, they are widespread over the whole region.

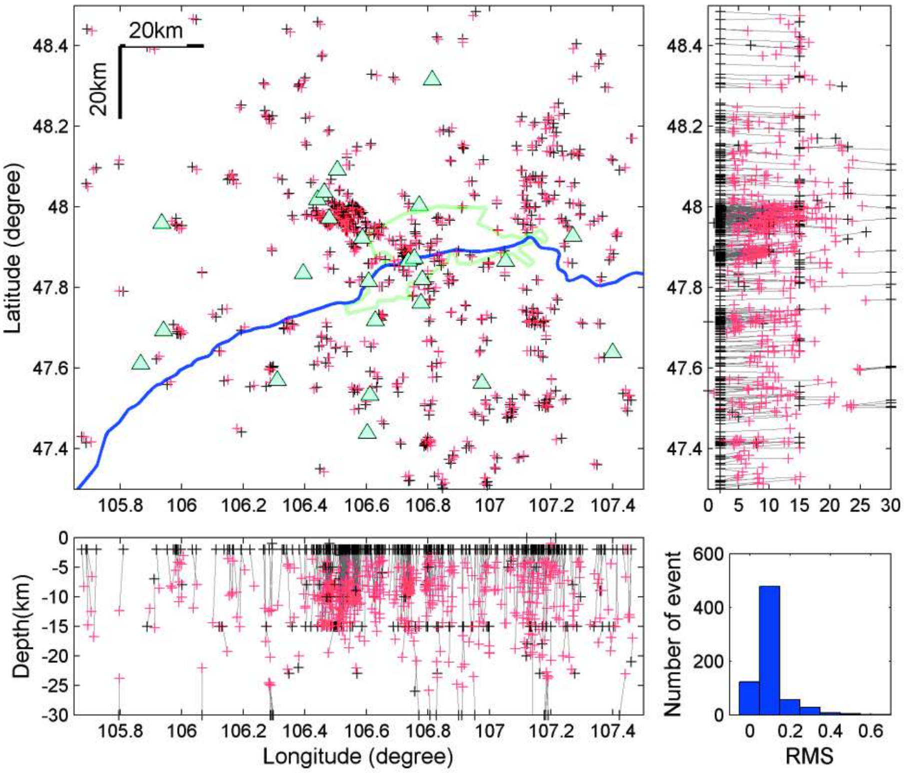

Figure 3.27. Epicentral movement ≤1.4 km (698 events): Red cross is hypoinverse location. Black cross is NDC location. Grayline shows movement of hypocenter between NDC and hypoinverse. Blue line is Tuul river and green line is urban area of Ulaanbaatar city.

Notice that the depth correction is much more important that the epicentre correction and reach locally 45 km and with an average correction of about 8 km (Table 3.4 and Figure 3.31). It means that vertical errors are high even for earthquakes with small epicentre errors.

Table 3.4. Summary of epicentral and vertical corrections on Selection B1 (NDC to hypoinverse location)

Epicentral movement, km	Number of events	Vertical correction ranges, km
EpiMov < 1.5	698	1 – 19.5
1.5 <= EpiMov < 2.5	351	0.6 – 18.8
2.5 <= EpiMov < 3.5	232	2.1 – 26.6
3.5 <= EpiMov < 4.5	164	2.2 – 25
4.5 <= EpiMov < 5.5	107	3 – 44.8
5.5 <= EpiMov < 6.5	75	0.6 – 22.7
6.5 <= EpiMov < 7.5	52	0.2 – 20.6
7.5 <= EpiMov < 8.5	22	0.7 – 23.1
8.5 <= EpiMov < 9.5	16	4.4 – 44.9
9.5 <= EpiMov	209	0.4 – 39.4

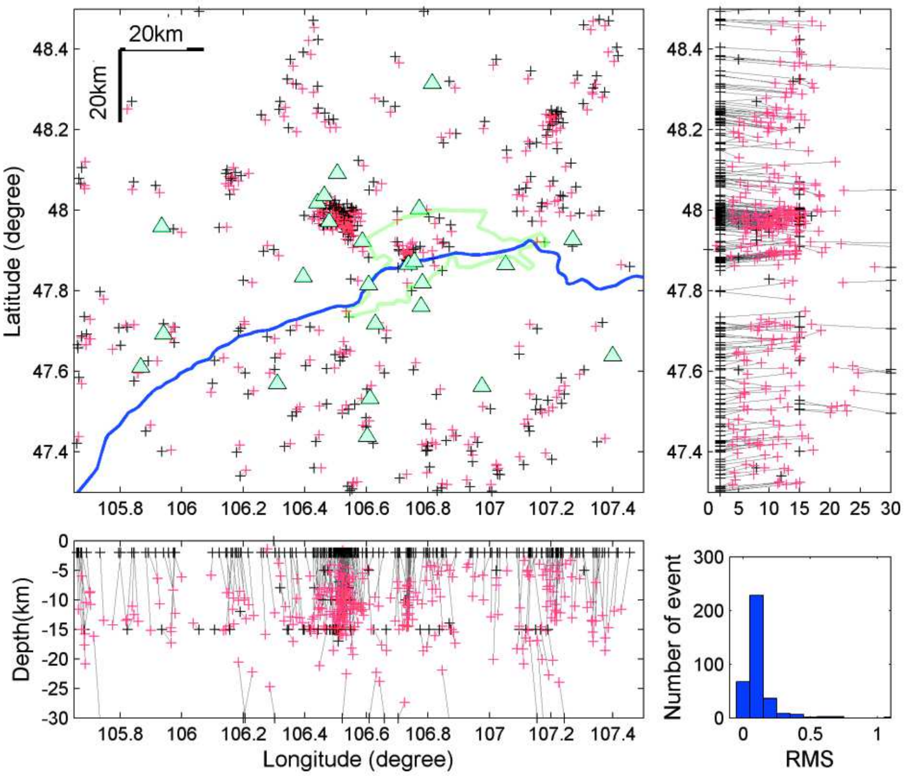

Figure 3.28. Epicentral movement between 1.5 and 2.4 km (351 events). Legend is same as Figure 3.27.

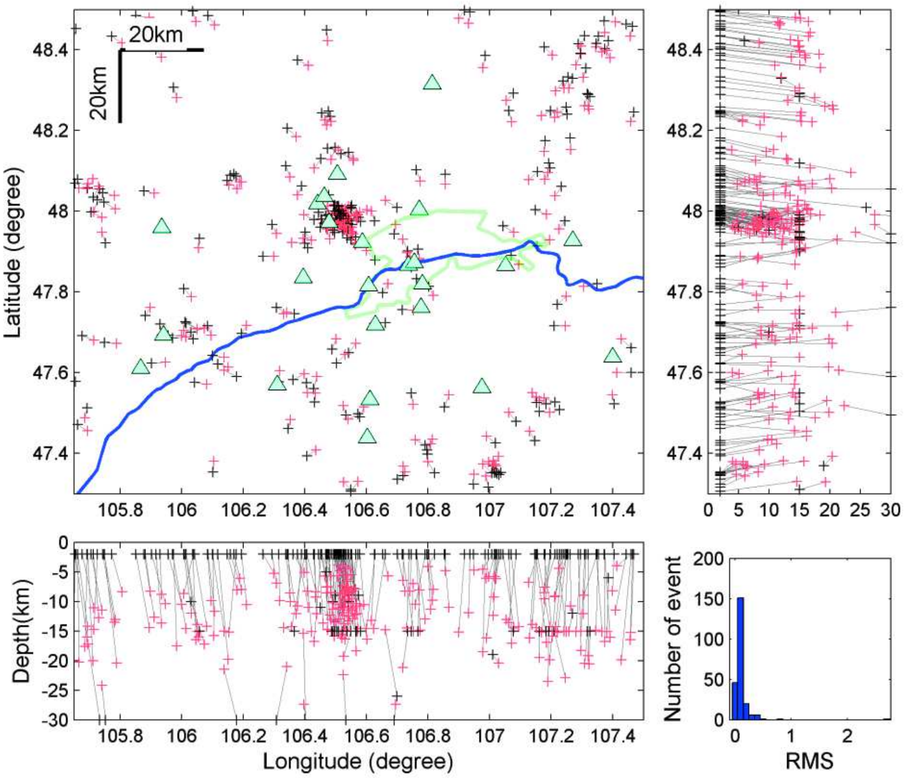

Figure 3.29. Epicentral movement between 2.5 and 3.4 km (232 events). Legend is same as Figure 3.27.

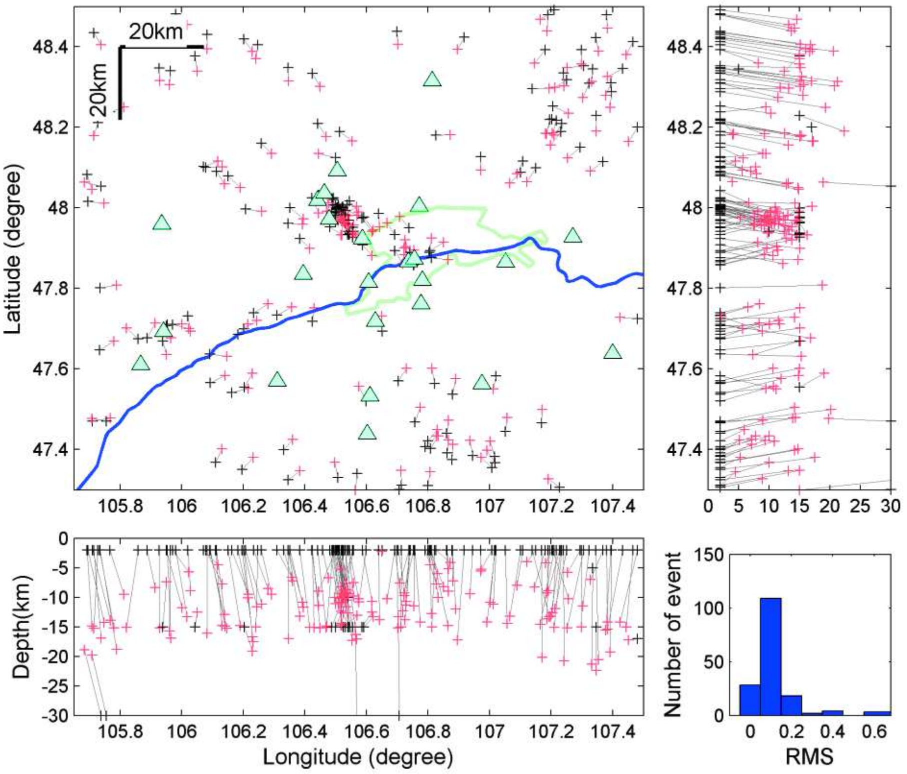

Figure 3.30. Epicentral movement between 3.5 and 4.4 km (164 events). Legend is same as Figure 3.27.

The depth corrections are very large. The new locations are mostly deeper than the NDC locations (Figure 3.31). About 10% are shallower and sometimes with very large corrections. Some events were mislocated at about 60 km depth in the NDC catalogue.

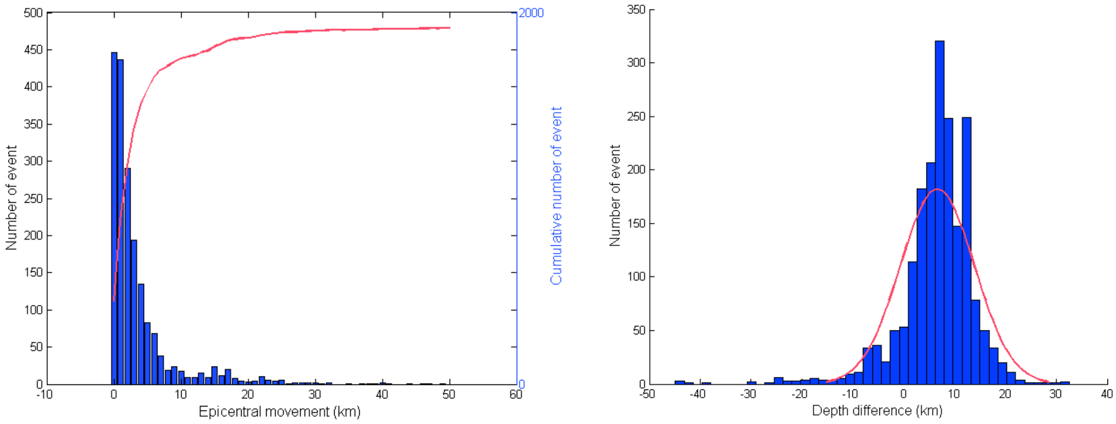

Figure 3.31. Histograms of difference between Hypoinverse and NDC locations. Left: Epicentral shift in km. Right: Depth difference in km (Hypoinverse – NDC).

209 events have important epicentre shift of more than 9.5 km (Figure 3.32) and many of them are located in the Emeelt fault area.

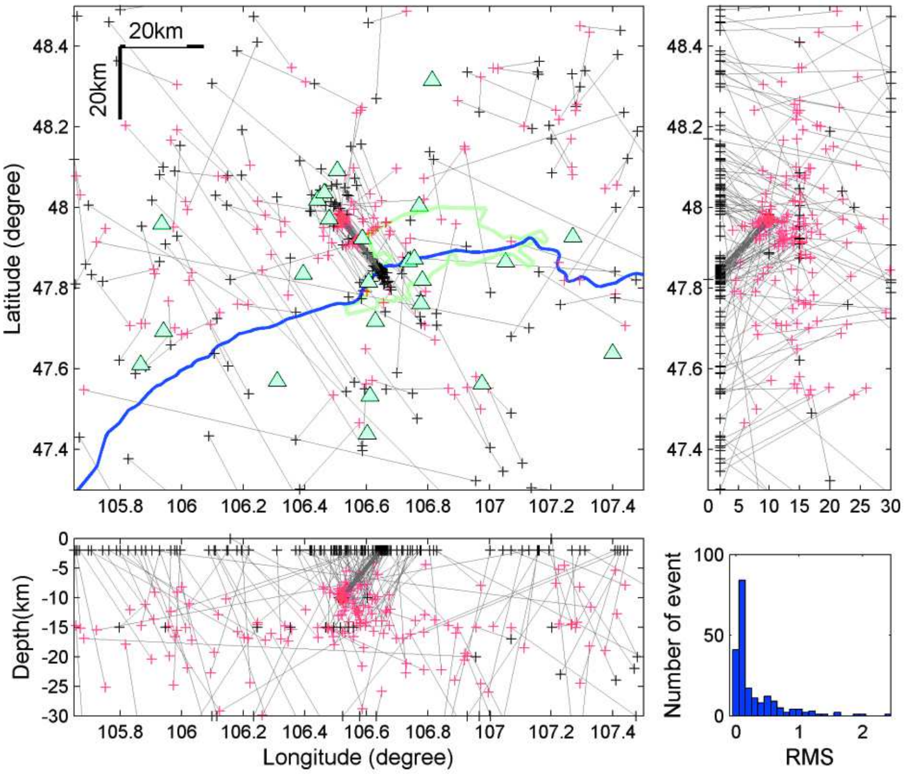

Figure 3.32. Epicentral movement of more than 9.5 km (209 events). Legend is same as Figure 3.27.

Some of theses events are in the south part of the Emeelt fault. If we compare epicentres near the Emeelt fault localized by the NDC and Hypoinverse (Figure 3.33), it appears that some events disappear in the south. In fact, when I included arrival times from the temporary network, these events moved from the south to the north part of the Emeelt fault (see 3.2.1.2). We already observed it with the relocation of few events done with the VELEST procedure and explained it with a mirror effect. Here, with a larger dataset, the impact is very clear. Finally, these events moved near to their right location after Hypoinverse procedure.

Moreover, large location corrections are also observed outside the Emeelt fault area, the improvement is directly due to the larger coverage of the stations network when we include the mobile stations (Figure 3.32).

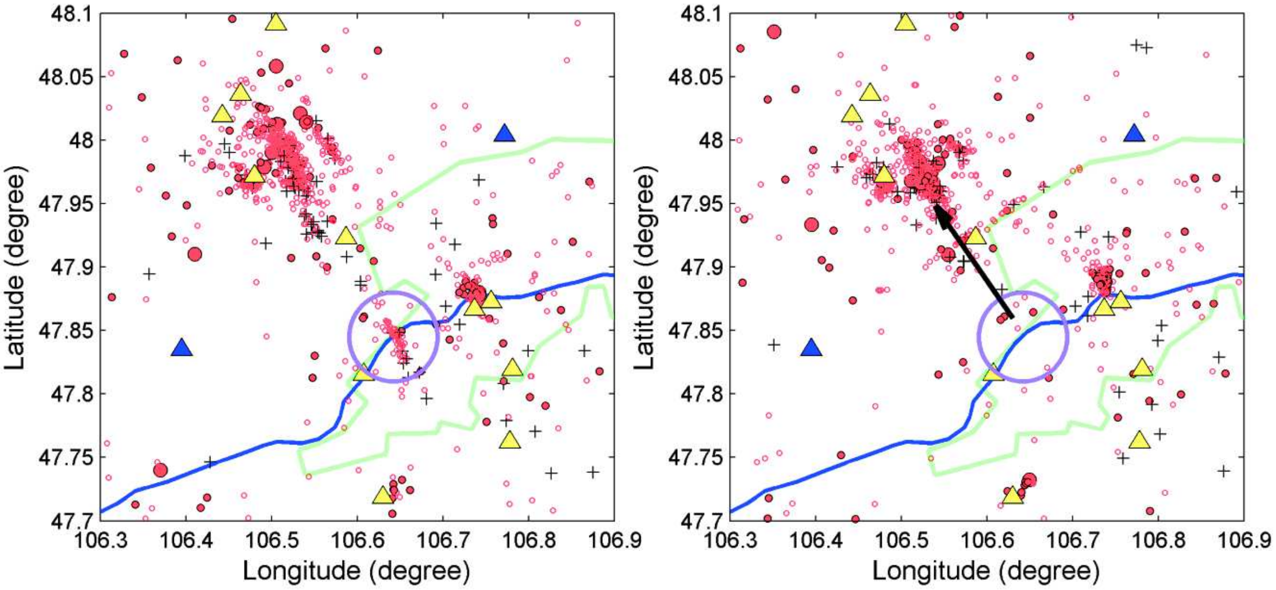

Figure 3.33. Hypocenters of events in the Emeelt fault area by NDC (left) and New location with Hypoinverse (right). Magenta circle shows area with events wrongly located in the NDC catalog (see figure 3.10). Blue line is Tuul river and green line is urban area of Ulaanbaatar city. Blue triangles represent the "UB-array" and yellow triangles represent the UB-mobile.

At the end of this work, we obtain for the dataset, called "Selection B1 dataset", a new location with the Hypoinverse procedure, using the local 1D velocity model. This new location is called "output B1" and will be a part of the input locations of the TomoDD procedure that will be done in the next chapter.

4 Chapter 4: 3D velocity structure and precise relocation of the seismic activity around the Emeelt fault zone

4.1 Introduction

The goal of this chapter is to determine:

- The 3D velocity structure around the Emeelt fault
- The precise hypocentre location of the seismic events based on the 3D velocity model.

It is only with this tomoDD localization that it will be possible to:

- Characterize the real extent of the seismic activity and seismic swarms in the Emeelt fault area
- Identify the seismogenic layer thickness of the Emeelt fault area
- Analyse the relation between the seismicity and the variations in the seismic velocity
- Determine the minimum "fault" area
- Compare the structure highlighted by the seismicity with surface, subsurface and near surface observations (morphotectonic, geological faults, GPR, shallow seismic profile)
- Analyse the spatial evolution of the swarm activity with time.

In this chapter I present the three-dimensional (3D) local earthquake tomography study of the seismicity of the Emeelt fault area. I recall the limits of the studied region: 47.3^{0}E - 48.5^{0}E and 105.65^{0}N - 107.5^{0}N, covering an area of 140 x 140km centred on the Emeelt fault. The selection of this area is related to the seismic stations coverage and the observed seismicity (interest area).

4.2 TomoDD methodology

Pujol (2011) has well summarized the interest of seismic tomography to determine the variations of earth properties in 3D using arrival times or waveforms from seismicity. An important addition of this technique is the high resolution it provides compared to other geophysical methods and most importantly it helps to constrain tectonic and seismic hazard at local scale.

There are various kinds of tomographic techniques. In my case, I used local earthquake tomography. The local earthquake tomography technique minimizes travel times data misfit through simultaneous inversion for hypocenter and seismic velocity parameters, such as Vp, Vs and Vp/Vs (Thurber, 1993; Eberhart-Phillips, 1990; Kissling et al., 1994). One adaptation of the local earthquake tomography is the double-difference tomography (tomoDD) developed by Zhang and Thurber (2003), which provides a highly resolved Vp and Vs model and hypocenter locations. It solves event locations and velocity structure simultaneously by using both absolute and differential data of local events. Errors on hypocenter locations are strongly reduced thanks to the use of the differential arrival times. They developed the code of "TomoDD" based on the location code "hypoDD" of Waldhauser and Ellsworth (2000). Many researchers applied the tomoDD technique allowing a detailed description of the Vp and Vs velocity fields and precise location of events for constraining the complexity of a fault (Zhang et al., 2003; Tomomi et al., 2006; Jeanne et al., 2007; Nakamichi et al., 2007; Dorbath et al., 2008; Moretti et al., 2009; Pei et al., 2010; Nugraha et al., 2013; etc).

In this study, I apply the tomoDD method to image the subsurface structure in the Emeelt fault zone. The seismic swarms near the Emeelt fault are ideal for conducting a local seismic tomography study, as they provide frequent earthquakes and we benefit from a dense stations coverage. I used the data recorded between 1994 and 2013 because this method is adapted for regions where the events are clustered closely together. The advantage is that it can image the velocity structures immediately surrounding the cluster because the algorithm minimizes the modeled and observed travel time difference between two earthquakes recorded at a single station (Waldhauser et al., 2000; Zhang et al., 2003).The inputs for the tomography inversion are from the previous analyses and chapters (1D velocity model, Hypoinverse location). Here, I apply two processes based on the tomoDD code of Zhang and Thurber (2003). First, a 3D inversion is performed to constrain the 3D velocity model of the study area. For that I selected data with strong criteria given by a small number of high-quality events. Second, a TomoDD relocation is performed with a larger dataset, based on the obtained 3D velocity model. For that, the selection criteria are less strong and I added also new data covering 2013 and 2014.

4.3 TomoDD inversion for the 3D velocity model

4.3.1 Event selection

For the first process of the TomoDD inversion, I selected 810 events from "output of B1" (results of the HYPOINVERSE locations, from 1995 to 2013.01) that fit the following conditions: at least 8 phases including at least two S arrivals and RMS lower than 0.5 sec. However, during the beginning of the observation period (1995 to 2000) we had only 4 stations operating in the area. Therefore, for that period, to get 8 phases, I considered only the events recorded at 4 stations with P and S arrivals times on each station. This concerns only 42 events on the 810 used. Therefore, they have a limited influence on the results. Other events, I means since 2000 until 2013.01 I considered events which picked at least 5 stations. The other criteria (distance and RMS) are the same. It is named *Selection C* (Figure 4.1).

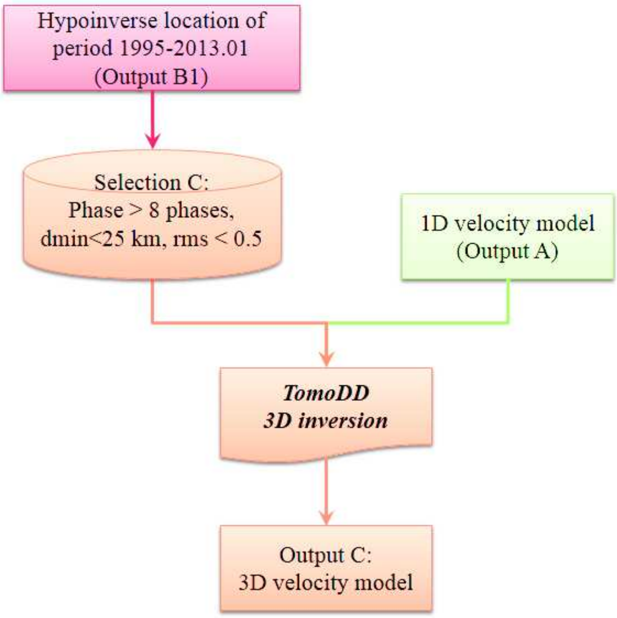

Figure 4.1. Working procedure for the 3D velocity model construction (Procedure C).

Several histograms show the result of selection C like depth, RMS, number of P phases and/or S phases and distance to the nearest station (Figure 4.2). Half of the events are associated with at least 11 phases and about 75% with at least 10 phases. Also, about 80% have at least 5 P or 5 S phases. The distance to the nearest station is less than 12.5 km for half of them. At least 75% of the events are over the minimum requested for the selection C procedure. The locations of the events of the selection C are shown in Figure 4.3. Their depths and RMS histograms are shown in Figure 4.2.

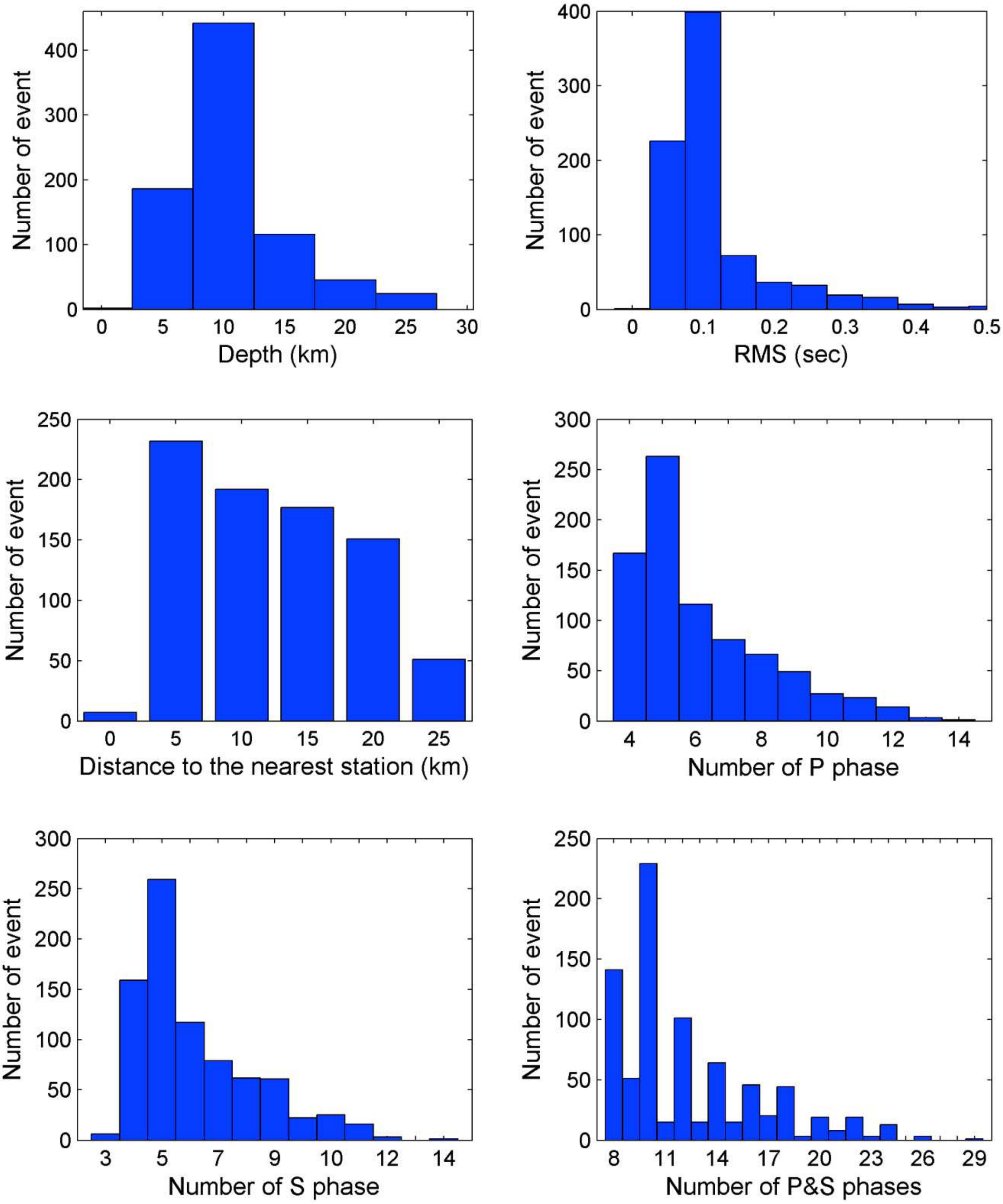

Figure 4.2. Histogram of depth, RMS, distance to the nearest station/event (distance within ± 2.5 km), number of P and/or S phases/event of the *SelectionC*.

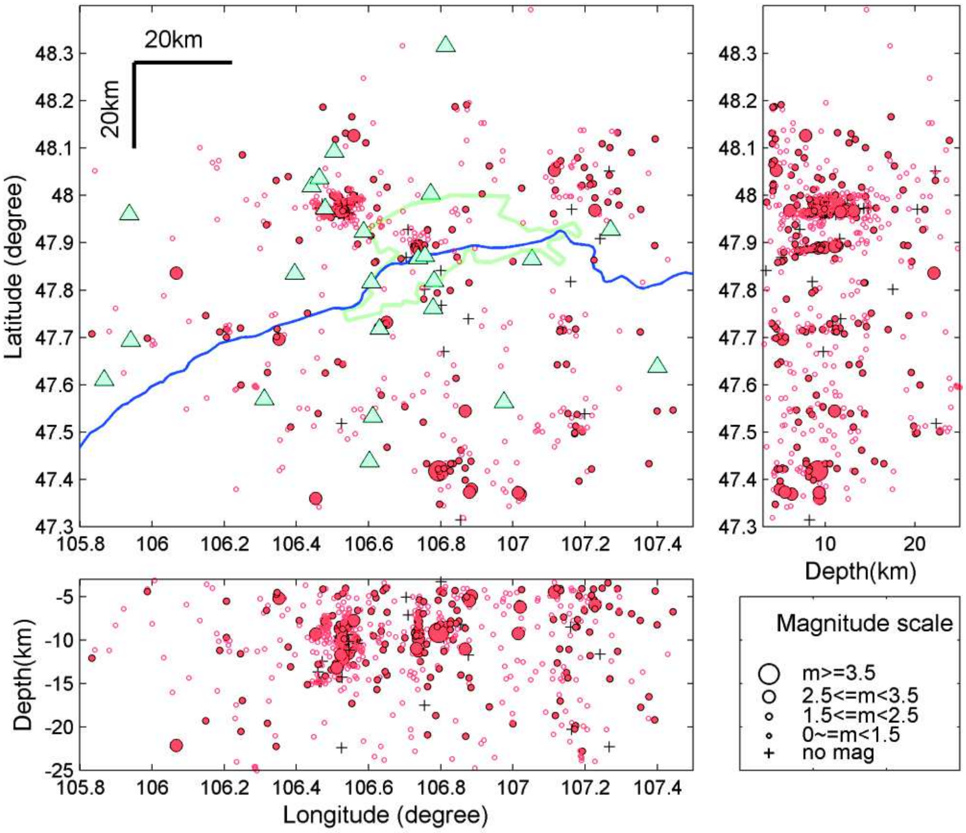

Figure 4.3. Hypocenters of earthquakes selected with *Selection C*. Triangle are seismic stations used for the inversion. Green line is urban area of Ulaanbaatar city and blue line is Tuul River.

4.3.2 Absolute and differential arrival times

In the inversion, I used the absolute arrival times and the catalog of the differential times. In *Selection C* I have 9982 absolute arrival times. I constructed the differential times through directly differencing absolute arrival times at common stations with a maximum hypocentral distance of 10 km between the event pairs. I obtained a total of 148.063 differential times. Since all picking were performed manually I imposed a weight of 1.0 for P phases and 0.7 for the S phases.

4.3.3 Input velocity model construction for inversion

Starting from the obtained “new 1D model” from the VELEST study (Chapter 3), I created an optimized 1D velocity model by a smoothing interpolation between layers (Figure 4.4).

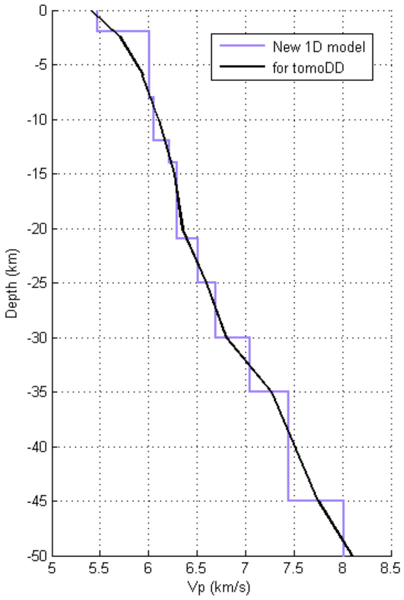

Figure 4.4. 1D optimized model for 3D inversion (black line) and “new 1D velocity model” (magenta line).

The S velocity model was derived from the P velocity model assuming Vp/Vs=1.7.

4.3.4 Inversion grids parameters

4.3.4.1 Reference grid nodes

The 3D grid covers the studied region (47.3^{0}E-48.5^{0}E and 105.65^{0}N-107.5^{0}N) down to 35 km (Figure 4.5). Along latitude, longitude and depth, this 135 km x 136 km x 35 km volume (centered on 47.9N - 106.6E) is divided into 21x21x11 nodes (4851 nodes in total). The grid is 5 km spaced in map view for 100 km in latitude and longitude and is centered on 47.9N - 106.6E, the center of the model. The outside limit of the model is a square with 300 km long sides. The vertical grid is spaced by 5 km from 10 km down to 35 km. Near the surface, the nodes are closer and at depths of Z= 0, 2.4 and 6 km (Figure 4.5). The vertical limits of the model is +5 and -100 km.

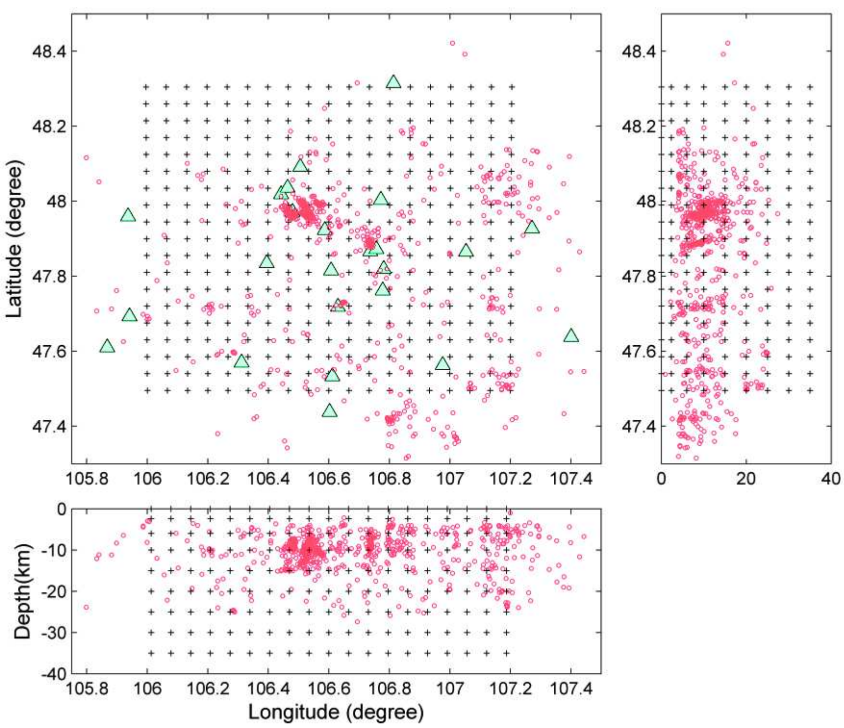

Figure 4.5. Inversion grid used for the study (does not include outside limit). Triangles are seismic stations and red dots are earthquakes hypocenter from selection C used for the 3D velocity model inversion.

4.3.4.2 Construction of grids

To reduce the uncertainty related to the geometric choice of the grid on the calculated 3D velocity model, we define 13 different inversion grids. For that we started from the reference grid node (Figure 4.5) and we produced 12 other grids after various rotations and shifts along X, Y and Z directions (Table 4.1). At the end we combine the 13 obtained 3D velocity model into a unique model, called WAM (Weighted average model) (Calo, 2009, Calo et al., 2012).

Table 4.1. Models grid nodes information (excluding the boundary nodes)

Model-1	Reference grid node (rotation angle is 0)
Model-2	Rotated 15 degrees clockwise
Model-3	Rotated 30 degrees clockwise
Model-4	Rotated 45 degrees clockwise
Model-5	Rotated 60 degrees clockwise
Model-6	Rotated 75 degrees clockwise
Model-7	Rotated 90 degrees clockwise
Model-8	Shifted along X direction
Model-9	Shifted along Y direction
Model-10	Shifted along Z direction
Model-11	Shifted along Z direction and velocity changed with depth
Model-12	Shifted along X,Y and Z direction
Model-13	Shifted along X, Y, Z direction and velocity changed with depth

4.3.4.3 Test of the dependency of the velocity model on the inversion grids

To evaluate the dependency of the final velocity model on each inversion grid, we made the inversions using 13 different grid nodes (Table 4.1). The main low and high velocities are observed at the same place so the velocity structure does not change drastically when the positions of nodes change. Few examples of these tests are shown in Figure 4.6 along horizontal slices at 10 km depth.

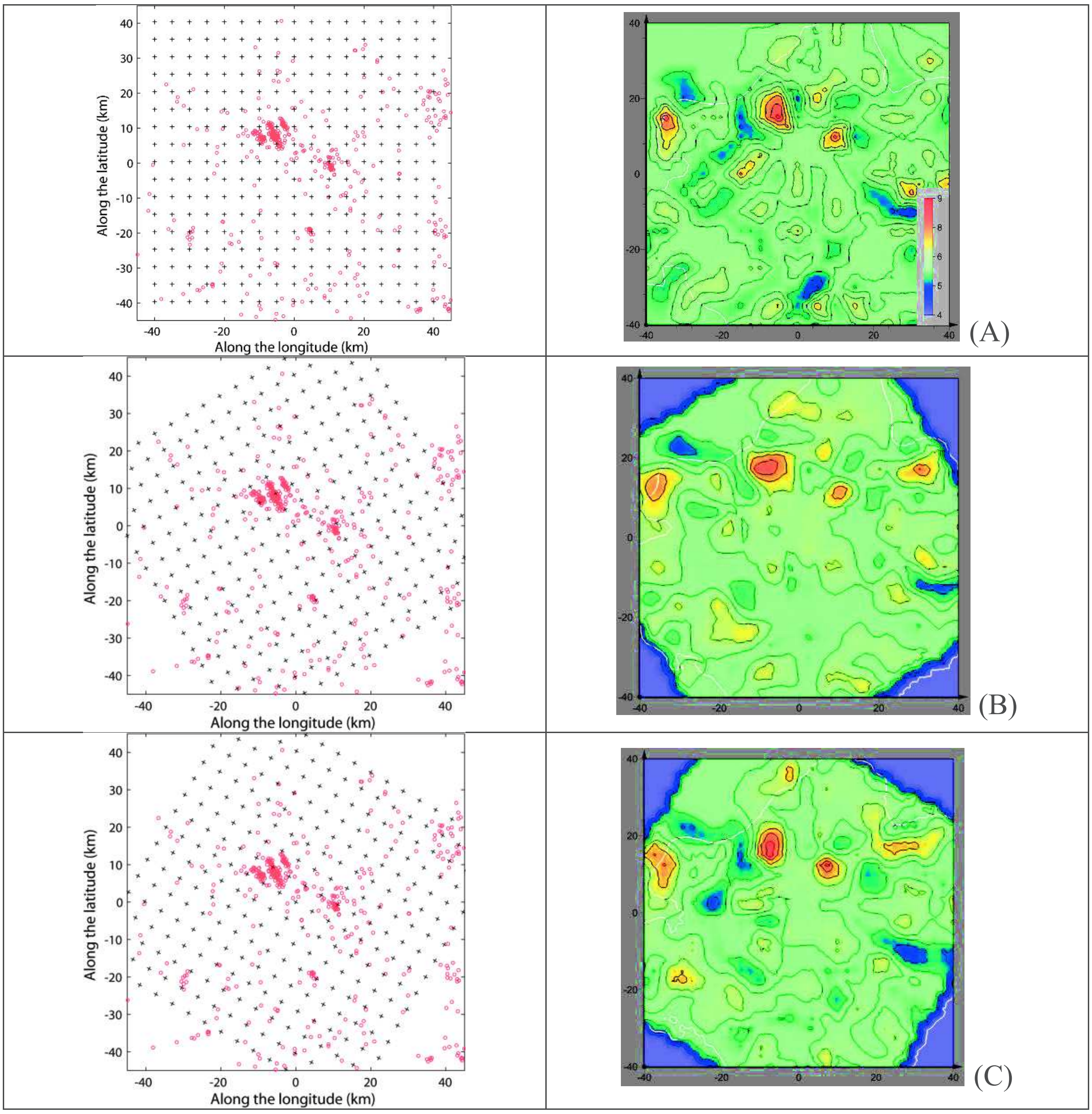

Figure 4.6. Dependency of Vp velocity models on inversion grids (see Table 4.1). Cross sections are at 10 km depth. A = model 1 reference, B = model 4 and C = model 6.

4.3.4.4 Checkerboard resolution test

To assess the reliability of the recovered 3D velocity model, I applied a checkerboard test described in Zelt (1998). This is a useful alternative, which gives a general picture of the resolving power of the data/method.

I build a checkerboard model characterized by alternating positive and negative anomalies of ± 10% with respect to the initial 1D velocity model. The cells size is 10km. Based on this checkerboard model, I generate synthetic arrival times using for the event hypocenter location the “selection C” (810 events with location from Hypoinverse) and the actual stations position. Then these synthetic arrival times (absolute and differential times) are inverted (tomographic inversion) in the hope of recovering the checkerboard pattern.

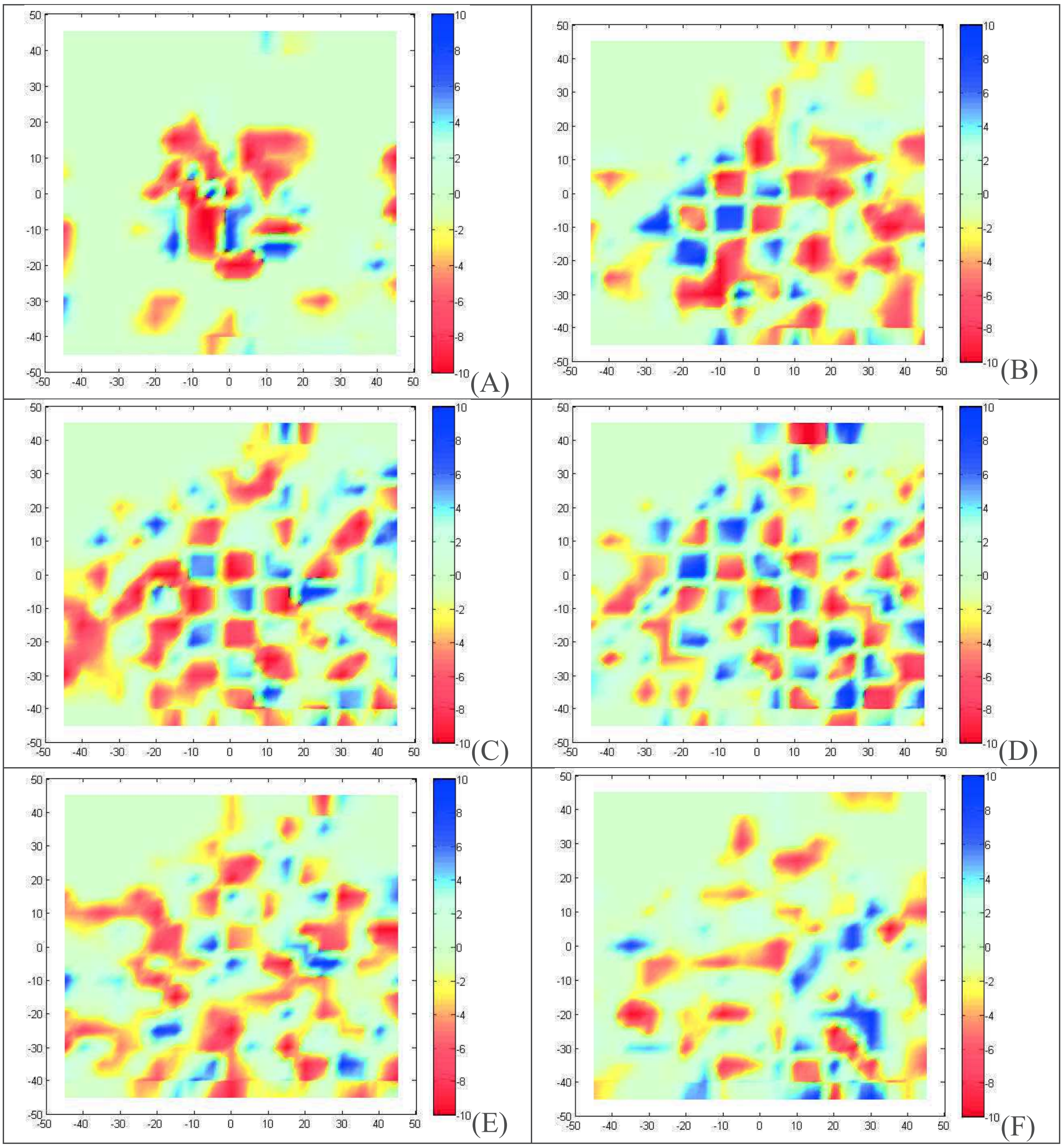

Figure 4.7. Result of checkerboard resolution test with a model sized of 90X90 km and cells size of 10 km. Map views of recovered models are shown at six different depths: at 0 km depth (A), at 4 km depth (B), at 7 km depth (C), at 11 km depth (D), at 15 km depth (E) and at 20 km depth (F).

If the recovery of perturbation is perfect, the result should be an exact sinusoidal pattern in 3D with maximum values in the center of each cell. With no recovery of perturbations (null resolution), the values in center of each cell are nul. In our case, the 3D velocity model parameters at various depths are finely recovered over the Emeelt fault area except below 15 km and above 4 km (Figure 4.7).

The 3D velocity model is well constrained between 4 and 15 km, and in some parts until 20 km in depth. Notice that the NW part of study area is always poorly constrained due to the lack of seismic stations.

4.3.5 Weighted Average Model – WAM

We obtained the 3D velocity model of the study area with relocated events of the *Selection C* (mean RMS is 0.012).

To improve the 3D velocity model in and around the Emeelt fault, we applied the Weighted Average Model (WAM) method (Calo 2009 and Calo et al., 2012). The WAM is a post-processing technique that produces an average model to reduce the spread of the set of the possible models and to synthesize a new model, which avoids to find the best model or to define a probability density of the class of the models. In my case, we resampled the space of velocity models 13 times (Table 4.1): 5 rotations, 2 shifts with velocity perturbation, 4 shifts without velocity perturbation with respect to the inversion model.

The WAM velocity is composed of the weighted mean of velocities obtained from each iteration. The velocity values for which we obtained DWS>50 were considered in the construction of the average model. This 3D WAM velocity model (called the "Output C") covers approximately a 90x90x30 km area.

I present in Figures 4.8 - 4.10 several horizontal sections of the 3D WAM velocity model respectively at 5 km, 10 km and 15 km depth.

Due to the station coverage and event distribution, we could not well constrain the 3D velocity model for the north-west part of the study area as shown in Figure 4.7.

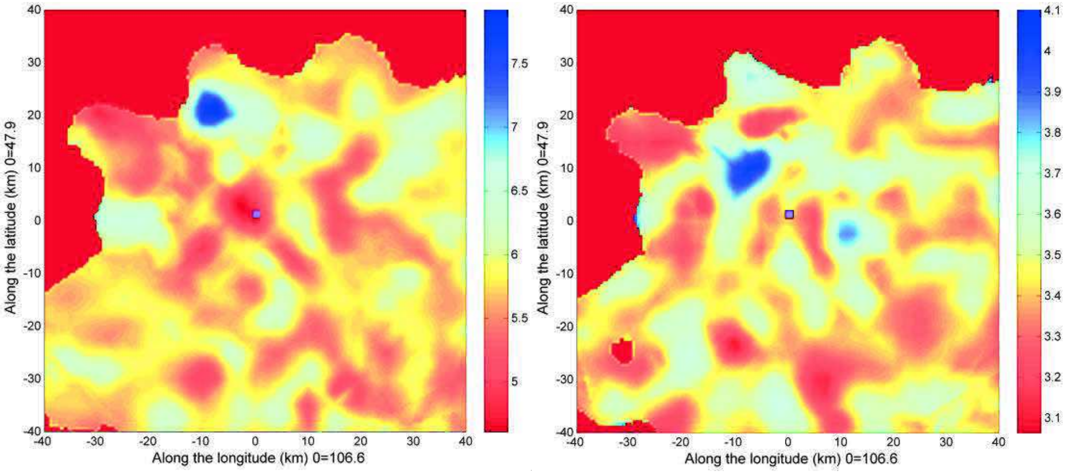

Figure 4.8. Horizontal section of WAM_P (left) and WAM_S (right) velocity model at 5km depth (uniform coloured area is DWS < 50). Purple square is trench site of Emeelt fault.

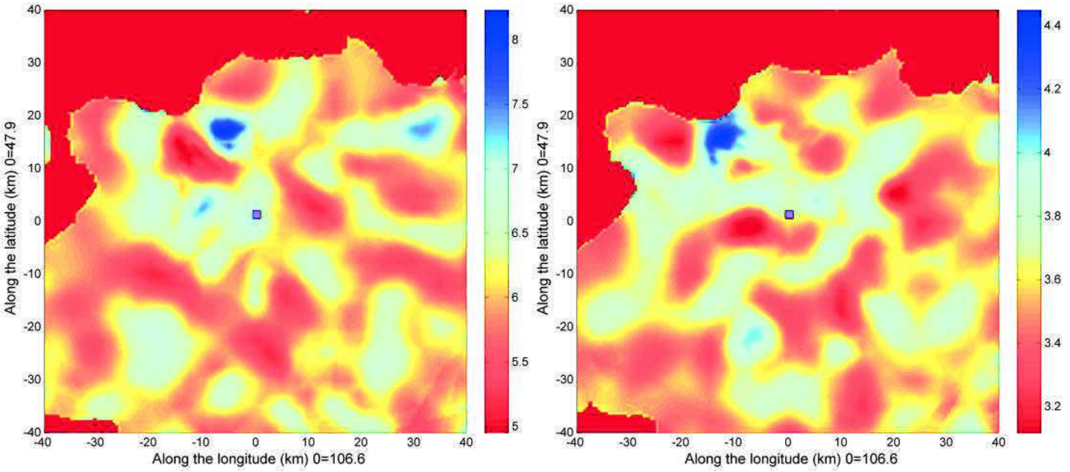

Figure 4.9. Horizontal section of WAM_P (left) and WAM_S (right) velocity models at 10km depth (uniform coloured area is DWS < 50). Purple square is trench site of Emeelt fault.

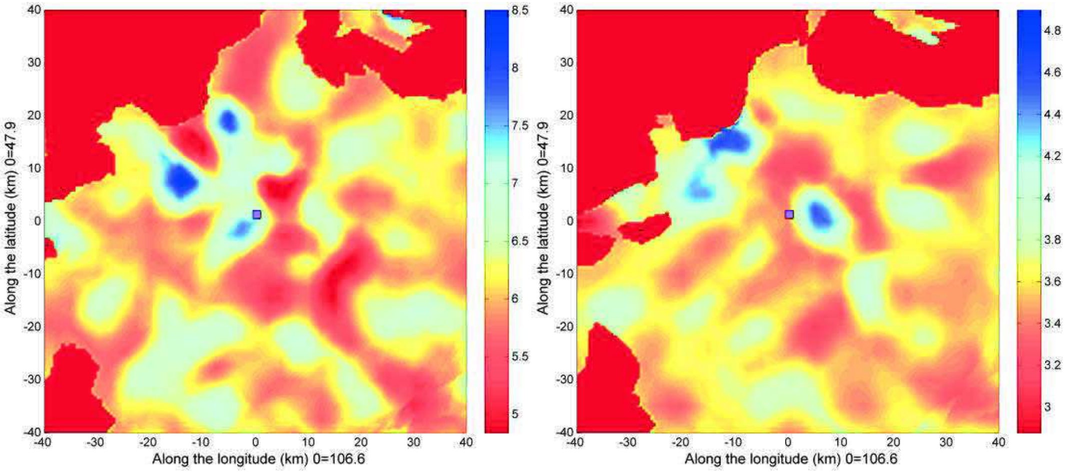

Figure 4.10. Horizontal section of WAM_P (left) and WAM_S (right) velocity model at 15km depth (uniform coloured area is DWS < 50). Purple square is trench site of Emeelt fault.

4.4 Precise localization by tomoDD using the 3D WAM velocity model

In this part I present the relocation of the earthquakes using the 3D WAM velocity model (Output C). When I calculated the 3D velocity model, I used earthquakes until end of January 2013 (2013-01). But between January 2013 and the end of 2014, the swarm activity increased by more than 2000 events that represent about 50% of the whole seismicity since the beginning of the crisis in 2005. Therefore, I will include this period into the TomoDD relocation despite they were not used to define the 3D velocity model. This will allow us to better follow the recent time and space evolution of the seismic swarms in the Emeelt fault area.

4.4.1 Event selection during the period 1995-2014 for the TomoDD relocation

4.4.1.1 Two periods of data: 1995 to 2013-01 and 2013-02 to 2014

Period 1995 to 2013-01: Previously (chapter 3.5), I relocated with hypoinverse the “Selection B1”, which contains a selection of events for the period from 1995 until 2013.01. The result was the “Output B1” that contains 1925 events. It will be the input for the TomoDD relocation procedure for the period 1995 to 2013-01 (Figure 4.14 (b)).

Period 2013-02 to 2014: I extended the period ***1995 to 2013-01*** by considering all events (2113) localized by the NDC, which occurred between 2013.02 and 2014.

The stations used by the NDC are the UB-array. Analysts of duty (of NDC) also used some of the UB-mobile until mid of 2013 (yellow triangle in Figure 2.12) and after mid-2013 they used also some of the UB-guralp stations (see chapter 2.1). But, from the 2113 events localized around the Emeelt fault by the NDC, half of them were localized using less than three stations. Therefore I selected only the 1033 events (*Selection B2)* localized with at least three seismic stations (black in Figure 4.12).

Notice that I could not do the extensive work as I did for the period 1995 to 2013-01. I used only arrival times available in the NDC bulletin. Therefore, I did not check and correct if necessary the NDC picking, did not add missed arrival times or missed stations.

4.4.1.2 Hypoinverse location of the selected events for the period 2013-02 to 2014.

As well as for the period 1995 to 2013-01, to get a better depth location than that of the NDC for the input of the TomoDD relocation, I located all the 1033 events by the Hypoinverse procedure with the new 1D velocity model (Figure 4.11). The Hypoinverse location for the period 2013-02 to 2014 is called “Output B2”. It will be the input for the TomoDD relocation procedure for the period 2013-02 to 2014 (Figure 4.15).

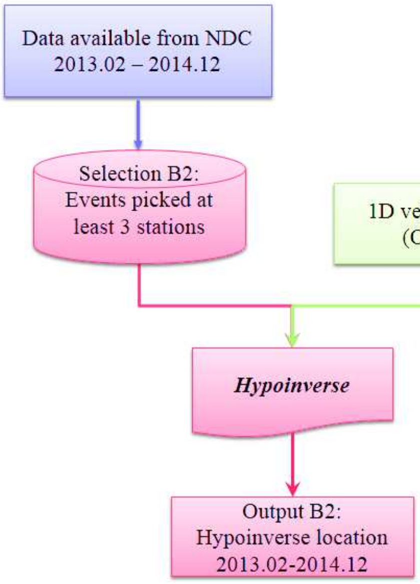

Figure 4.11. Procedure of database preparation for events between 2013.02 and 2014 (Procedure B2).

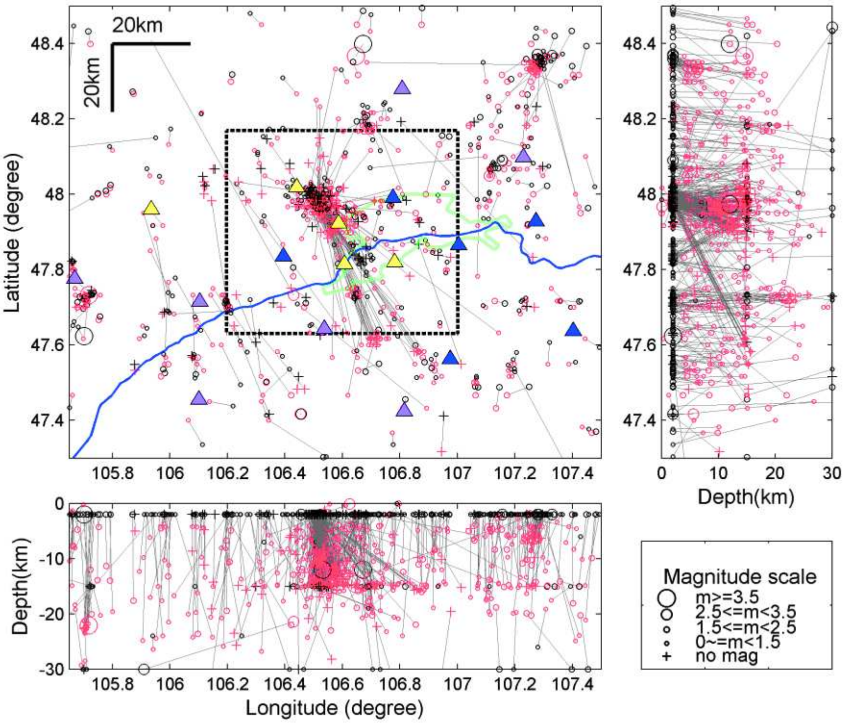

Figure 4.12. Hypocenter of events selected for the ***Period 2013-02 to 2014”***. Black colour indicates the NDC locations and red colour indicates the hypoinverse location (Output B2). Gray lines show the change in location betwwen NDC and Hypoinverse. Blue line is the Tuul river and green line is urban area of Ulaanbaatar city. Triangles show seismic stations location (yellow-UBmobile; blue=UBarray; purple=UBguralp).

The results of the Hypoinverse location for the selected events of the period 2013.02 to 2014 is associated with a mean RMS of 0.12 second, a mean vertical uncertainty (ERZ) of 3.35 km and a mean horizontal uncertainty (ERH) of 13.36 km. It is quite big, but most of them are related with the wrong epicentre determination of NDC).

The hypoinvese locations are most of the time deeper than the NDC location. Outside a depth histogram (Figure 4.13) that shows a depth between 5 and 20 km with the most frequent at about 10km depth, I will not discuss now in more details the change in location or depth, as it will be improved by the TomoDD relocation.

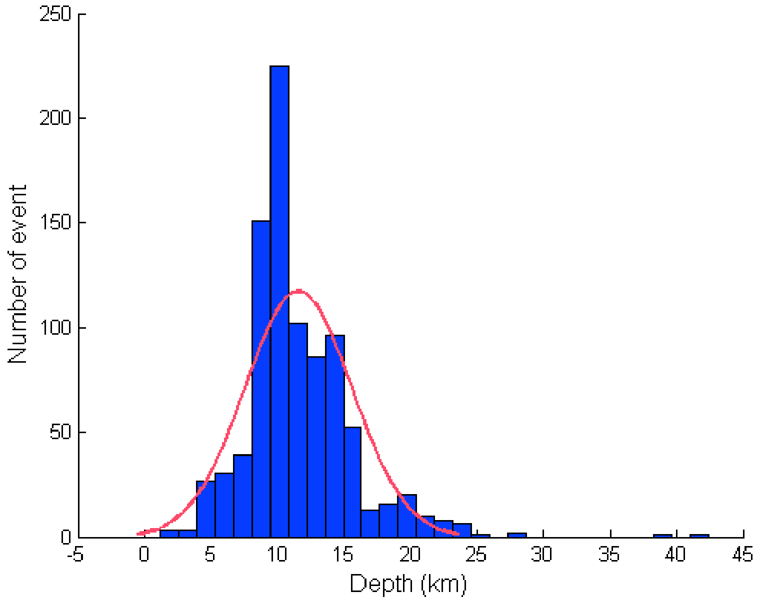

Figure 4.13. Depth histogram of location (Selection B2) after relocation (Output B2).

4.4.1.3 *Event selection for the TomoDD inversion (period 1995-2014)*

From the 2817 events (Output B1=1925 events + Output B2=892 events) located with hypoinverse (Figure 4.14a), I selected 1986 earthquakes with the following criteria (*Selection D*): an RMS lower than 0.5 seconds, stations with epicentre distance less than 25 km, at least 3 stations, at least 6 arrival times, at least 2 S wave arrival times (procedure summarized in Figure 4.15 and for Selction D see Figure 4.14b). There are 1410 events for the period 1995 to 2013-01 and 558 events for the period 2013-02 to 2014. This *Selection D* is relocated by TomoDD using the 3D WAM velocity model produced previously.

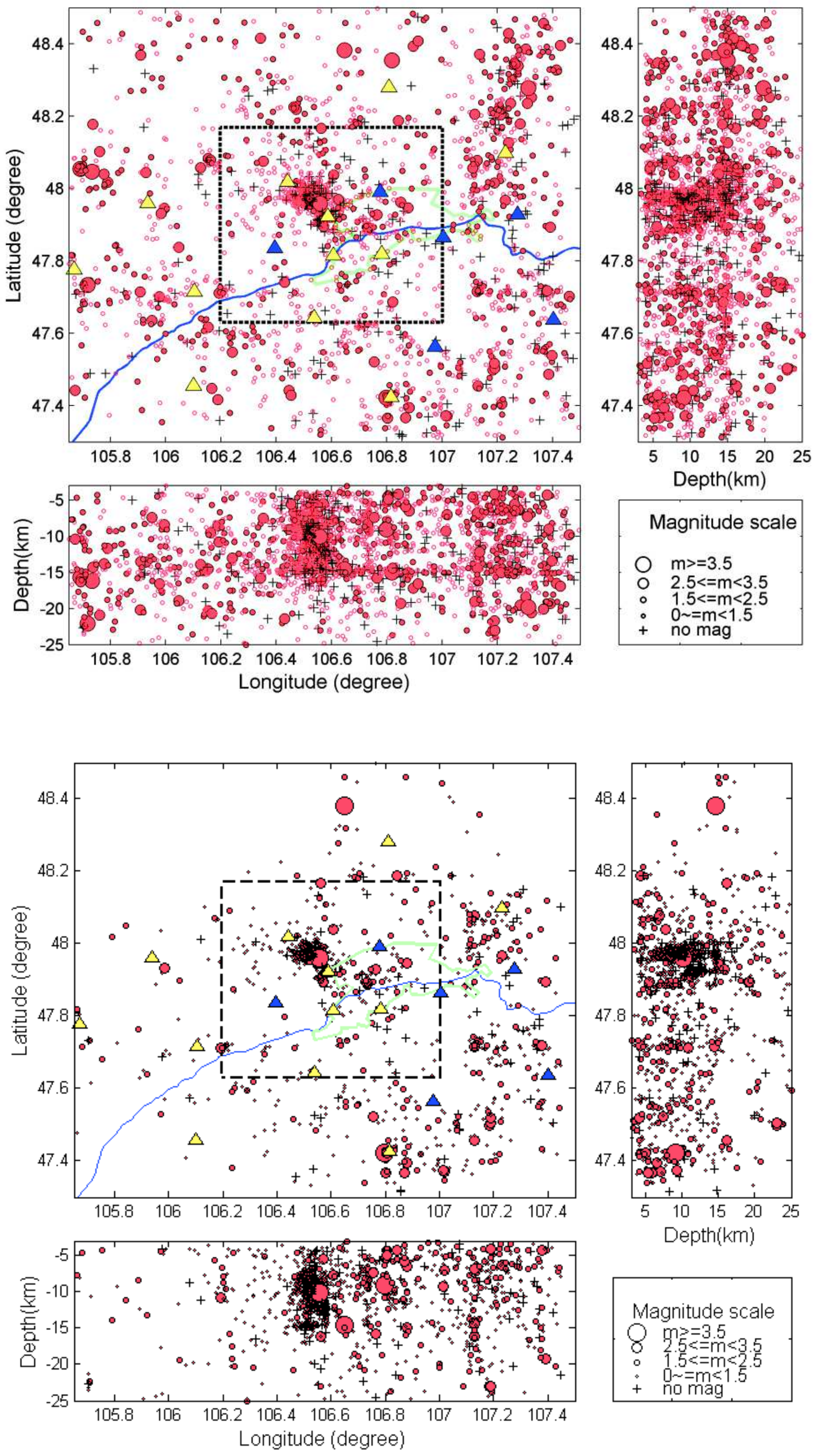

Figure 4.14. Top = Figure 4.14a : Hypoinverse hypocenter locations for the period 1995-2014 (Output B1 and Output B2). Bottom = Figure 4.14b: selected events (Selection D) for the TomoDD relocation = part of the event shown on the figure 4.14a. (Blue line is Tuul river and green line is urban area of Ulaanbaatar city and triangle is seismic station).

For the total period, the relocated events represent about 56% of the total activity detected in the area (1968 relocated events with TomoDD for 3504 detected events by the NDC).

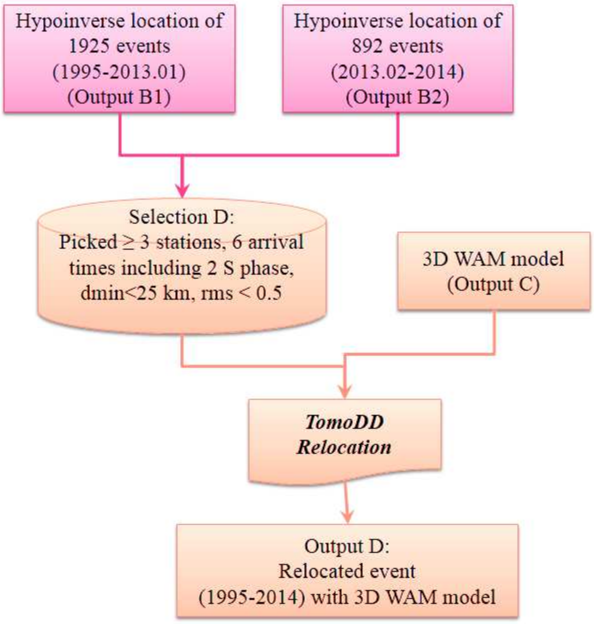

Figure 4.15. Procedure of TomoDD relocation, from event selection until output of TomoDD (Procedure D).

As the processing of the data for the two periods (1995 to 2013-01 and 2013-02 to 2014) is different (see previous chapters) and as the network changed locally, I present some statistics on the number of P phases and/or S phases and distance to the nearest station for each period (Figure 4.16). We see that the distance to the nearest station is better for the second period with a lower proportion of distances of more that 12.5 km (classe 15 km and more on Figure 4.16). Nevertheless, the number of phases per event is more important for the first period thanks to the work done on the data for that period (new picking of all available stations). We have about 20% of events with only 6 phases during the first period when the proportion increases to about 30% during the second period. Nevertheless, the number of events localized with 10 phases and more are about 50% and 45% for the fisrt and second periods, respectively,.

On the other hand, we see that there are mostly about 9 stations used (Figure 5.17) that concentrate most of the phases used. These are the 5 permanent stations (SAOM, ALFM, SEMM, ARTM, UGDM) and 4 mobile stations (UB1M, UB4M, UB2S, UB6M). Also they are more or less as many P and S phases. Moreover, for the first period, there is only 1.8% of the events localized with 3 stations when they are 2.6 in the second period.

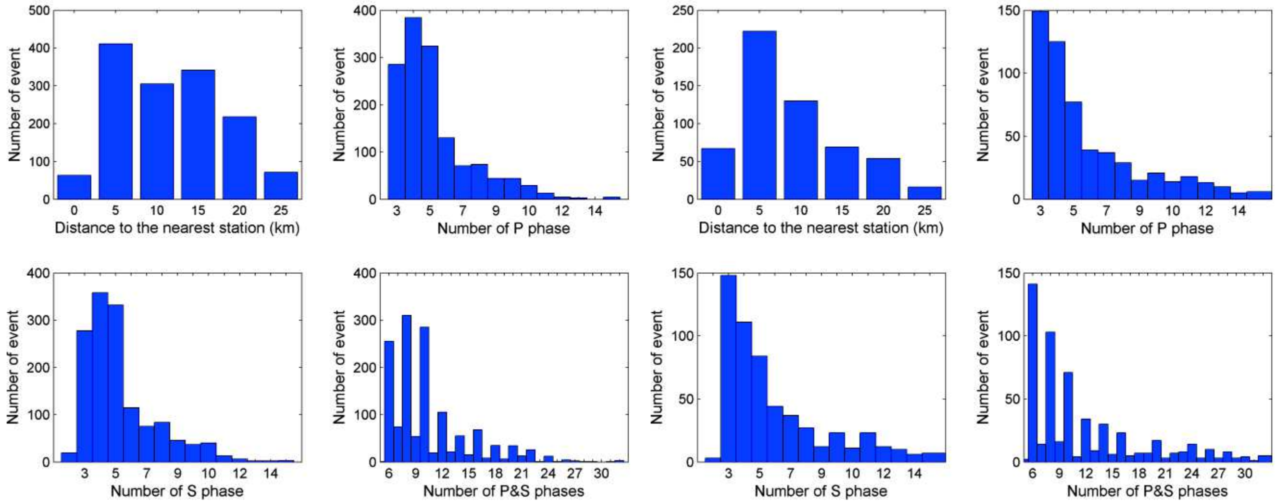

Figure 4.16. Histograms of distance to nearest station/event (distance within ± 2.5 km), number of P and/or S phases/event of *SelectionD* for the two periods (1995 to 2013-01 = left and 2013-02 to 2014= right)

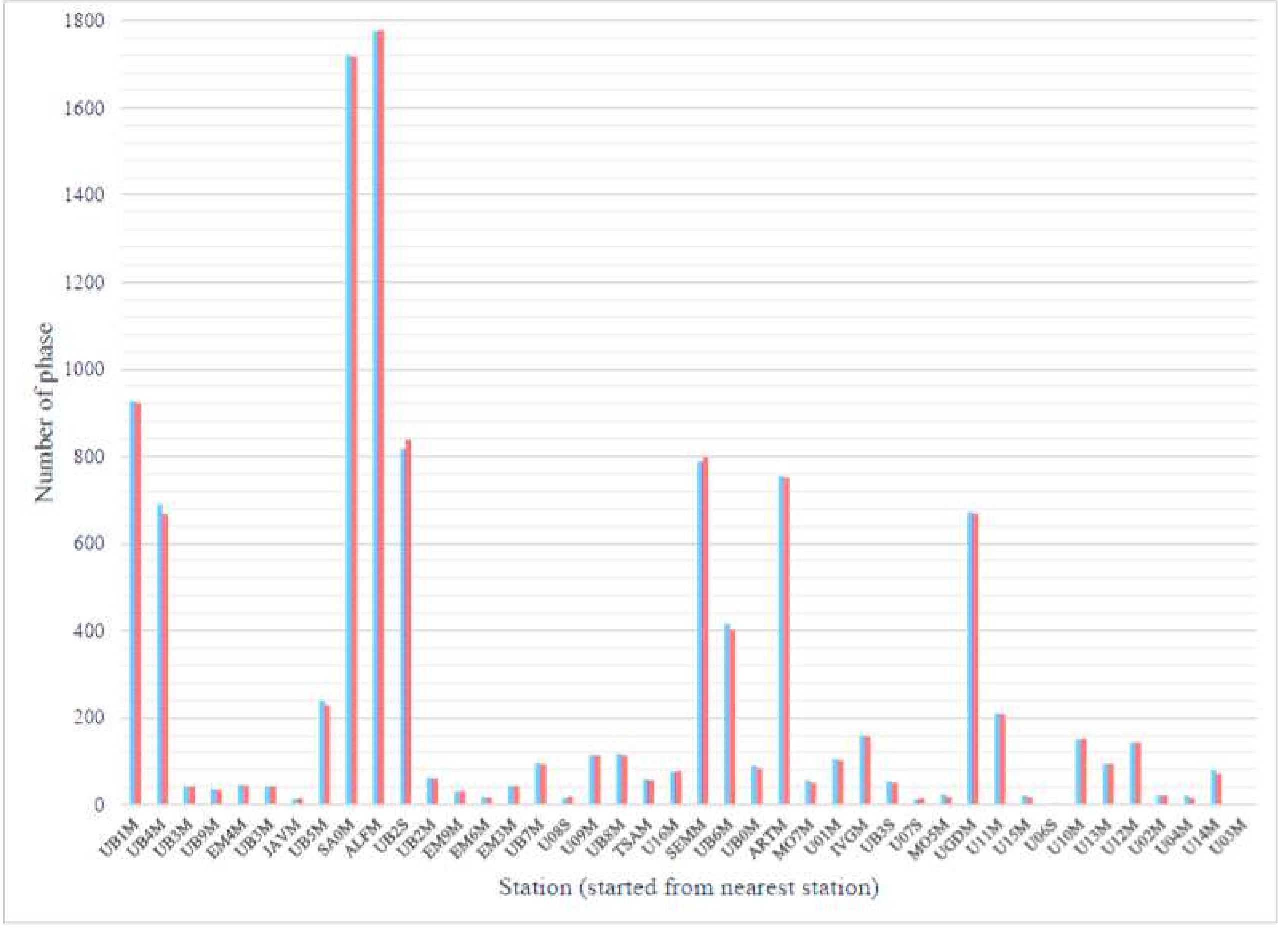

Figure 4.17. Histogram of number of phases per station for *SelectionD*, input for TomoDD relocation (Blue=P phases; Orange = S phases).

4.5 Results of the TomoDD relocation: reference location of the Emeelt seismic activity

4.5.1 Generalities and regional overview

4.5.1.1 General parameters of the seismicity and uncertainties after the TomoDD relocation

The relocated events that occurred between 1995 and 2014, using TomoDD procedure and 3D WAM velocity model, are shown in Figure 4.18.

The RMS of located events is 0.064±0.029 s. The horizontal average errors are 62 and 67m in east-west and north-south directions, respectively. Average depth error is 92m. (Figure 4.19-C). About 22% ot the events are localized with only 3 phases, a same proportion with 4 phases and about 50% with more than 5 phases (Figure 4.16). Unfortunately, the number of events localized with more than 8 phases drops to about 25 %. It shows, that despite the installation of new stations in the area, they were not fully optimized (number and location) over the whole period since 1995.

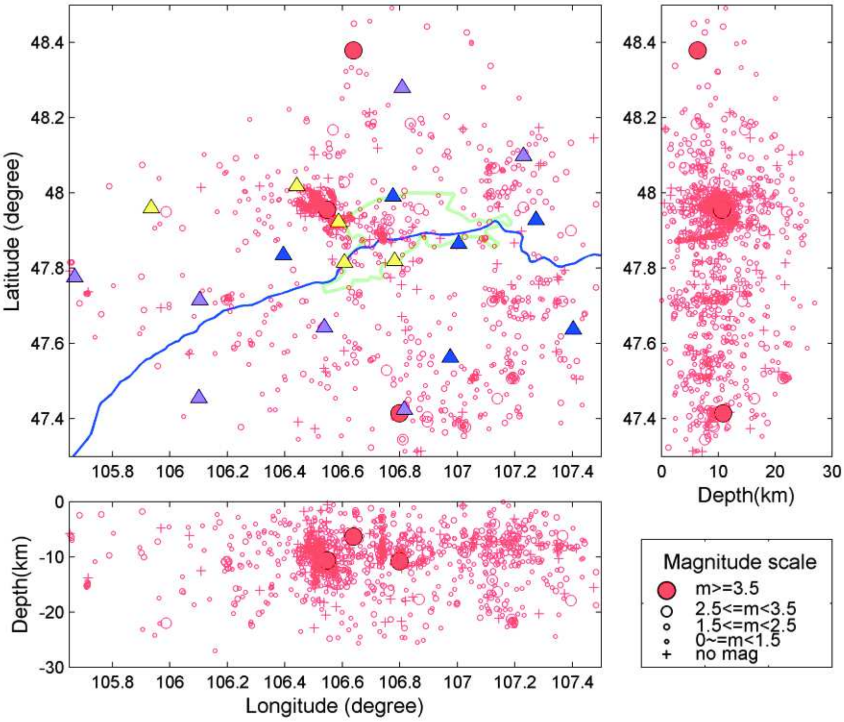

Figure 4.18. Hypocentral view (TomoDD procedure) of seismic activity (1995-2014) for selected events. Blue line is Tuul river and green line is urban area of Ulaanbaatar city. Triangles show seismic station's location (yellow-UBmobile; blue=UBarray; purple=UBguralp (see chapter 2.1). Black squared area zoomed in Figure 4.20.

The event depths are mainly between 0 and 30 km with most of them shallower than 14 km and the most frequent at 10 km. The seismogenic layer appears to be of ≈30 km (Figure 4.19–A). The magnitudes, outside the unknown magnitudes of always very small events (14% of the events), range between -1 and 3 with a distribution centred on magnitude 1. The largest event has M_L=4.2 (Figure 4.19–B).

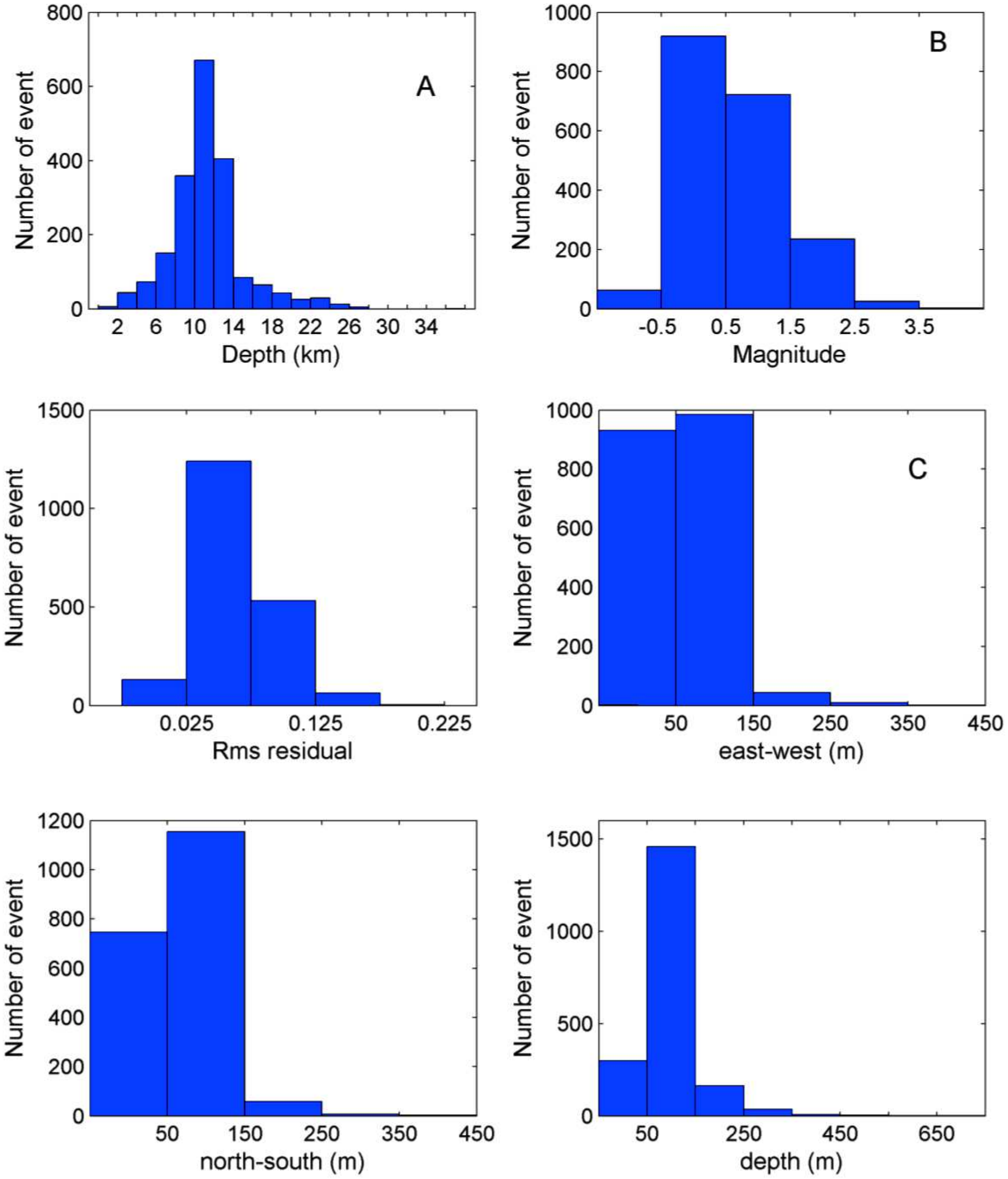

Figure 4.19. Depth (A), Magnitude (B) and RMS (C) distributions.

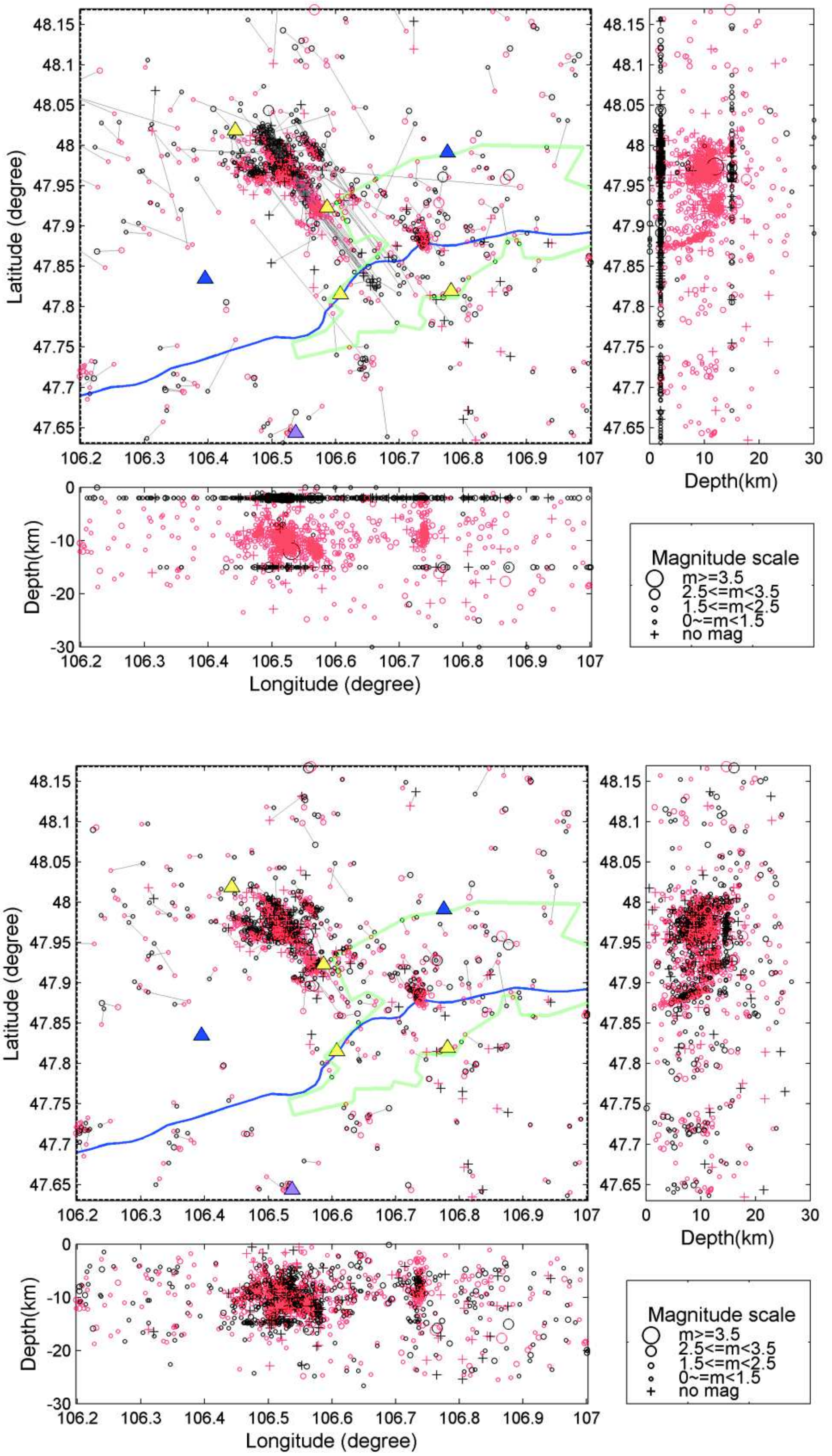

Figure 4.20. Difference in location between the NDC catalog (upper figure) or Hypoinverse hypocenters (bottom) and the TomoDD relocation for the Emeelt fault zone (1995-2014). Black colour indicates NDC or Hypoinverse location and red colour indicates tomoDD location. Blue line is Tuul river and green line is urban area of Ulaanbaatar city. Triangles show seismic station's location.

Upper and bottom figures of Figure 4.20 present, in gray lines, movement of events between NDC or Hypoinverse location and TomoDD relocation.

4.5.1.2 *Few observed concentration of seismic activity outside the Emeelt fault zone*

Due to selection criteria and the geometry of the seismic network used, most of the events outside the network or near its border were not selected and therefore not relocated. Nevertheless we can observe outside of Emeelt few areas with significant activities.

One is to the NE of Ulaanbaatar (about 107.2°E/48.1°N) and corresponds to the Gunj fault area (see chapter 1.2.4.3.2 and Imaev et al., 2012).

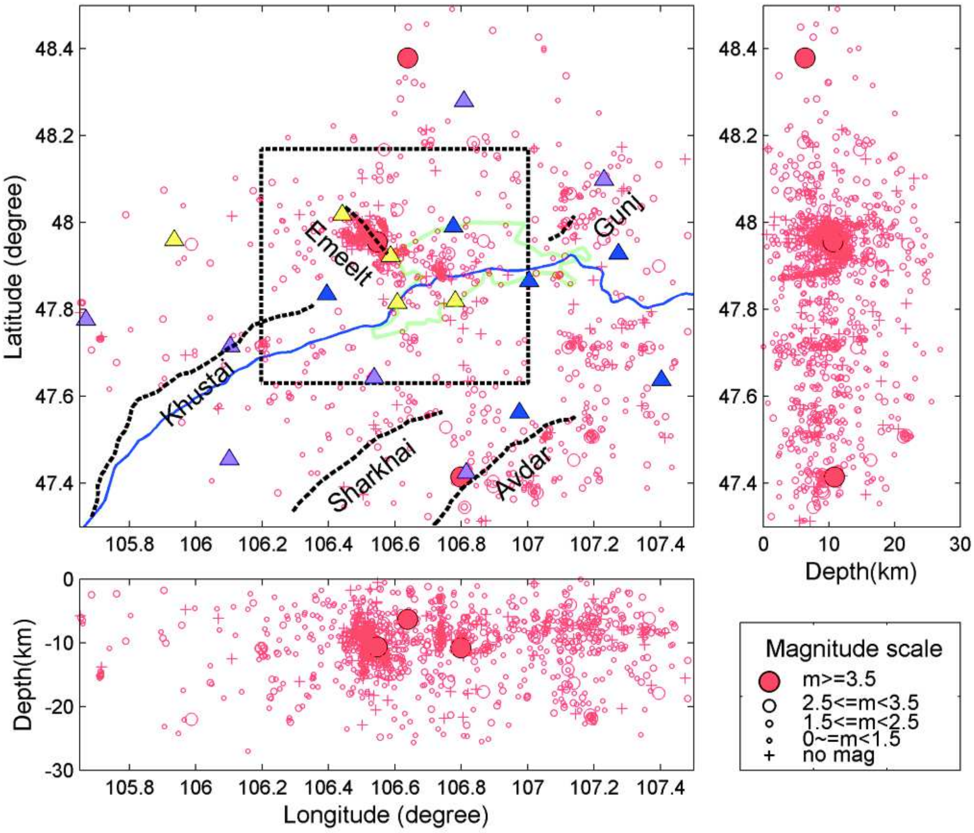

Figure 4.21. Hypocentral view (TomoDD procedure) of seismic activity (1995-2014) for selected events and known active faults (dashed black line). Blue line is Tuul river and green line is urban area of Ulaanbaatar city. Triangles show seismic station's location (yellow-UBmobile; blue=UBarray; purple=UBguralp (see chapter 2.1). Black squared area zoomed in Figure 4.20.

Several "patches" of seismic activity in the southeast quarter of the area, near the faults of Avdar or Sharkhay confirm the seismic activity of this zone. Nevertheless, they are out of the DWS>50 limits of velocity model therefore we have to be cautious about their direct relation or not with faults.

These results suggests that other seismic surveys with dense seismic network could be focused on other targets in the whole region around Ulaanbaatar, until at least 100km from the city center.

4.5.2 Target area around the Emeelt Fault Zone (TEFZ)

From now on, we will concentrate our analysis in a "Target area around the Emeelt Fault Zone" (**TEFZ**) (blue area in Figure 4.23 and following figures), that also corresponds to where the 3D WAM velocity model is the most constrained (Figure 4.22).

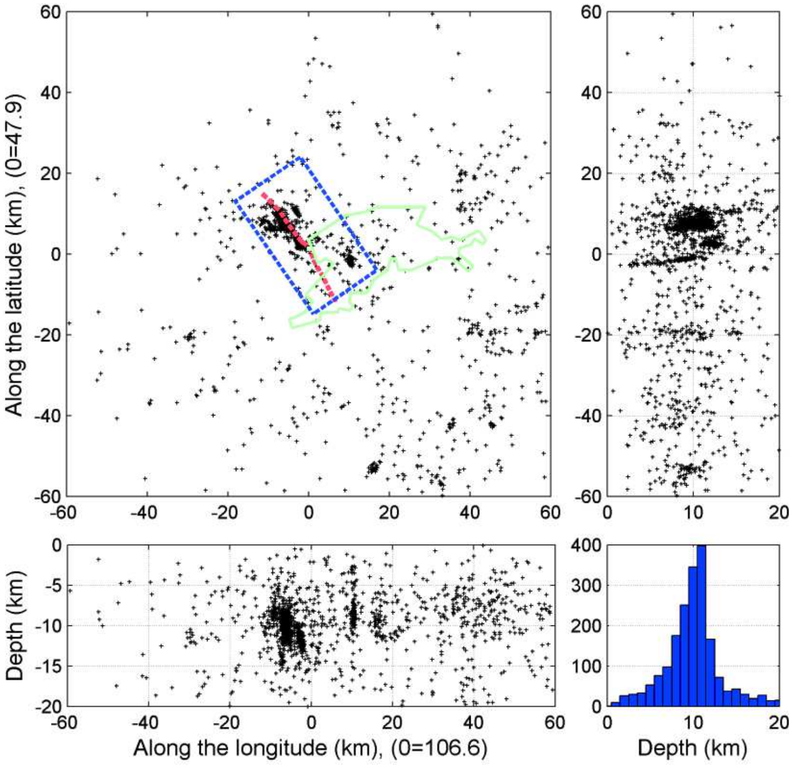

Figure 4.22. Hypocenters obtained from tomoDD relocation (from 1995 to 2014). green line = urban area of city, blue dashed polygon = Emeelt fault area for which results are discussed - Red dashed line = possible Emeelt fault extension. Depth histogram is shown at right down corner of figure.

Before we analyse and interprete the results, it is useful to remind that the relocated events with TomoDD based on a 3D WAM velocity model are just a part of the whole seismicity. They are the result of the selection D made to use data with enough information (number of stations, number of arrival times) and low uncertainties (low RMS, short epicentre distance) to be precisely located. It is better to have a reduced dataset but with a good location precision and low uncertainty. But, in the analysis, we have to keep in mind what is the part of the seismicity that could be well localized. For that, Figure 4.24 presents the number of located events by tomoDD (red) and the total number of observed events by the NDC (blue).

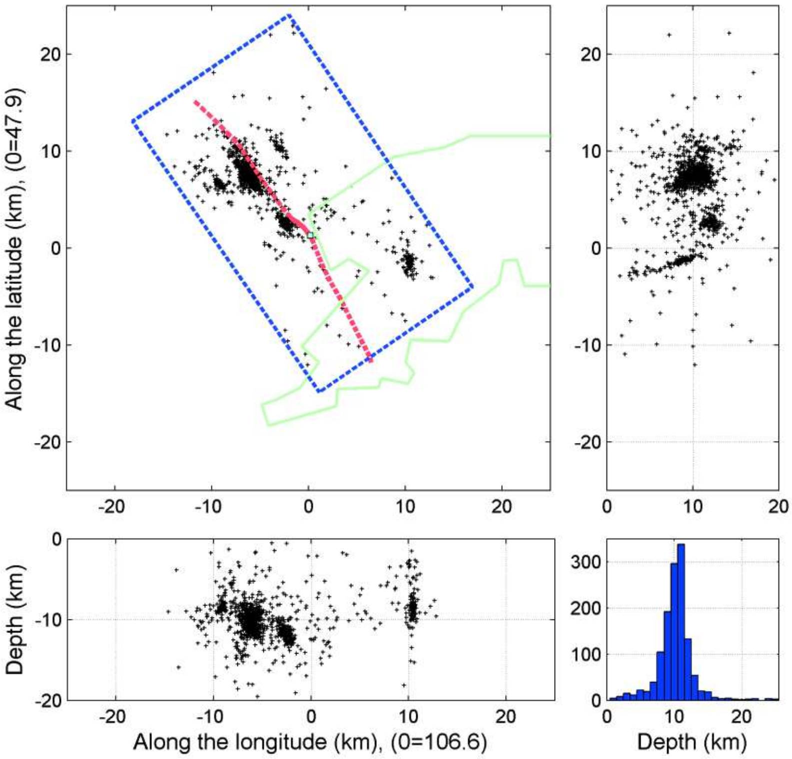

Figure 4.23. Zoom on hypocenters located only in TEFZ (legend same as Figure 4.22).

The number of events increased a lot since 2012 (mainly from December 2012) and also since the end of 2012 only 1/3 of the total number of events could be relocated. This is due to the fact that the data of this period has not been reviewed and completed in a similar way as for the period before December 2012.

The new locations of events are more scattered but clearly cluster in the Emeelt fault area.

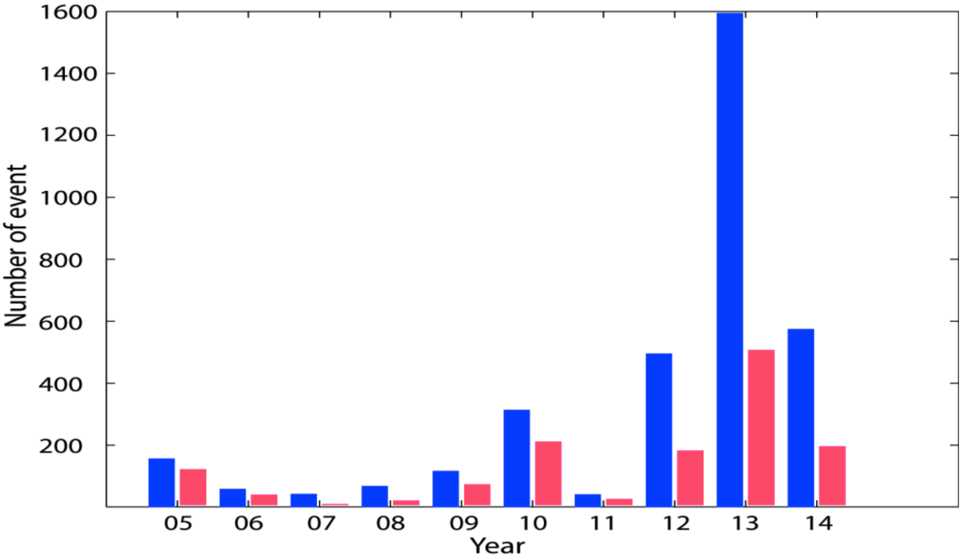

Figure 4.24. Comparison between the total number of event observed by NDC in TEFZ (blue dashed polygon in Figure 4.23) and number of events relocated by TomoDD (red).

4.5.2.1 Comparison of the quality of the TomoDD relocation between the period before and after December 2012

During this work, I did a more precise work on the data of the period 1995 to 2013-01 than for 2013-02 to 2014. The question is then if the changes observed in the seismicity during the second period are related to less precise results or to a real change in the seismicity. During the second period, the seismicity is more widespread along the branches and activates a larger fault surface (Figures 4.25-4.26). Also, the activity propagates deeper (Figure 4.27).

The errors (EW, NS and Z) for the two periods have not important differences (Figure 4.25b). The average errors are, respectively for the first and second period, in EW 64 and 54m, in NS 69 and 62m, and in depth 96 and 78m.

Therefore, we can consider that the quality of the relocations with TomoDD is similar over the whole period (1995-2014) despite they are based on better data for the period 2009-2013.01 when all mobile stations available were used and arrival times careful checked.

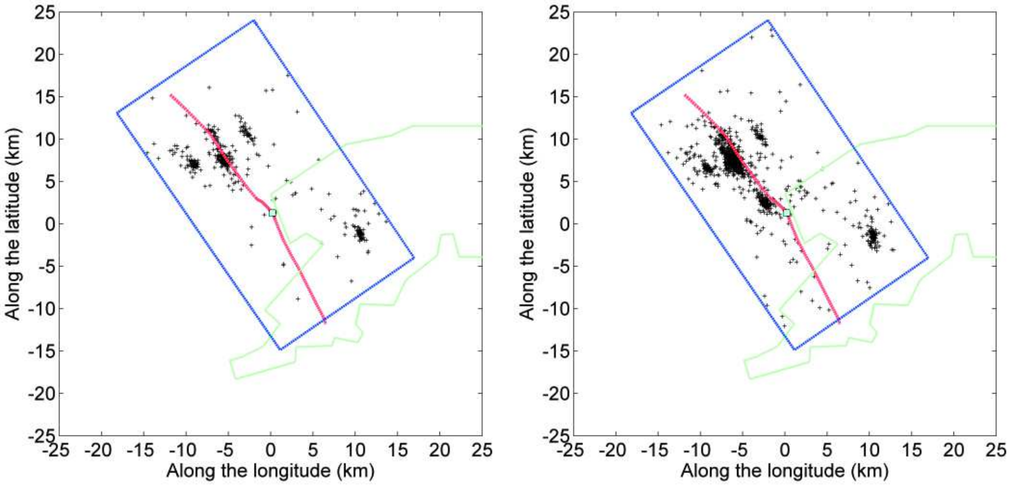

Figure 4.25. Epicentral view of relocated events in TEFZ. Left = 450 events (1995 to 2013-01). Right = 1300 events (1995 – 2014). (Green line = urban area of Ulaanbaatar city, dashed red line = possible Emeelt fault, solid red line = observed surface rupture of Emeelt fault; Aqua square = trench site).

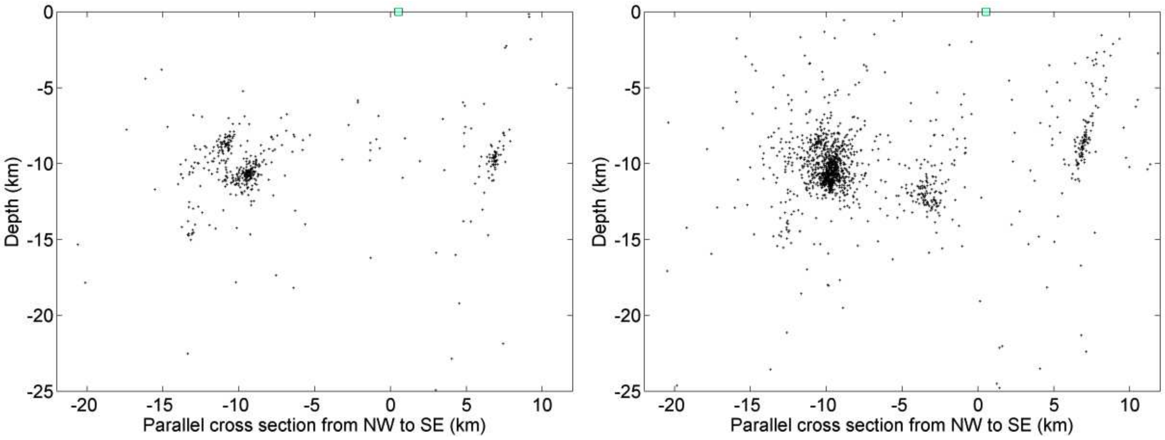

Figure 4.26. Cross section along Emeelt fault (from NW to SE) for the TEFZ. Left = 450 events (1995 to 2013-01). Right = 1300 events (1995 – 2014). Aqua square = trench site (see Figure 4.25).

Most of the events are located in the same area with half of the observed events since 2005 are during the period of 2013-2014 and only few events fall outside the "fault" area. This is also clear in the cross-section parallel (Figure 4.26) and perpendicular to the fault (Figure 4.27). Therefore, we consider that all the events are well located in 3D despite the events before 2014 are still more precisely located.

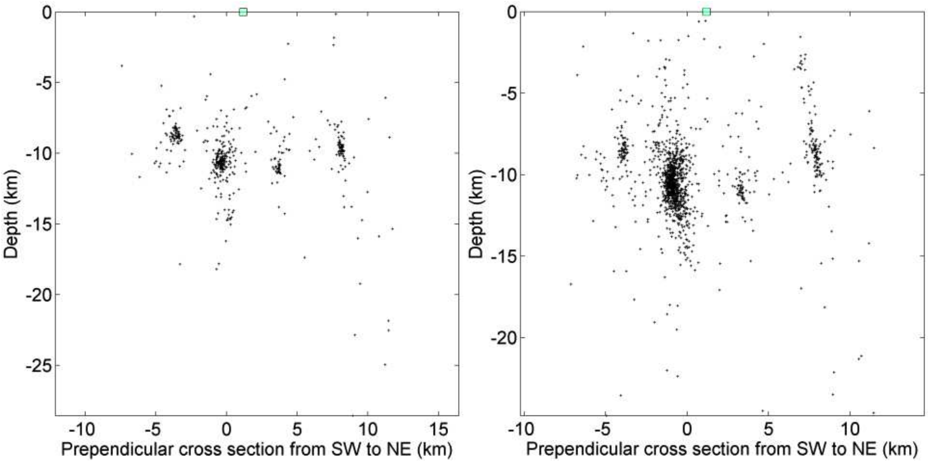

Figure 4.27. Cross section perpendicular to Emeelt fault (from SW to NE) for TEFZ. Left = 450 events (1995 to 2013-01). Right = 1300 events (1995 - 2014). Aqua square = trench site (see Figure 4.25).

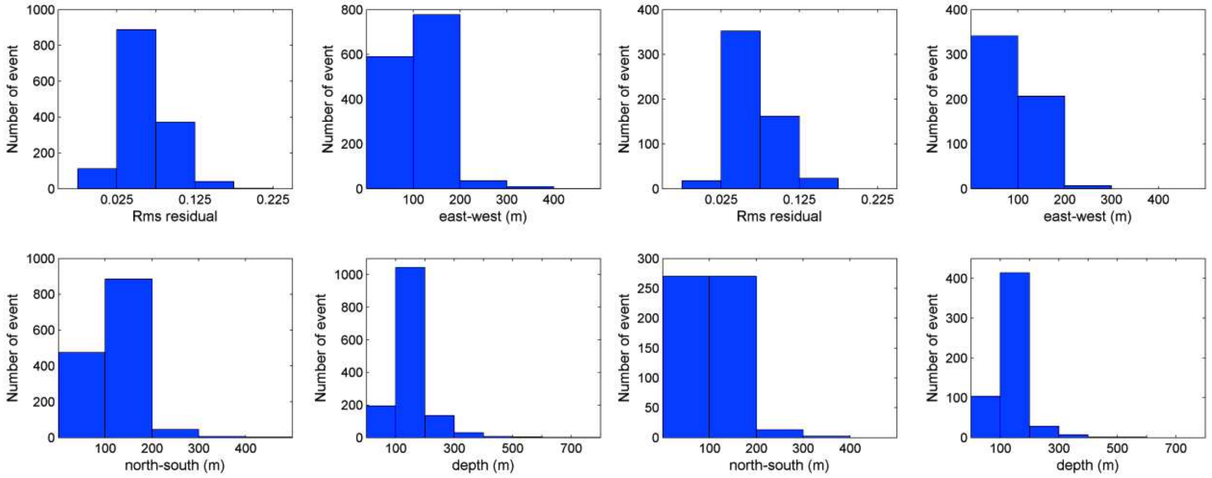

Figure 4.25.b. RMS and errors for the period 1995 to 2013-01 (left) and 2013-02 to 2014.

I discuss in details the 3D velocity structure and precise location of the seismic activity shown in Figure 4.23 in the next sections as well as the relations of the seismicity with active structures.

4.5.3 Seismicity in the Emeelt fault area and velocity structure

I will describe the main characteristics of the seismicity based on the TomoDD relocation and its relation with velocity variations as observed in the 3D WAM velocity model. It will be limited to the TEFZ (Target area of the Emeelt Fault Zone), which is a box, parallel to the Emeelt fault (N147) of 34x9.5 km. It contains 1300 events of the total 1986 events relocated by TomoDD (blue polygon in Figure 4.28).

The epicentre map of the TEFZ shows four parallel "lines" of activity. They underline four parallel active structures oriented in the same direction (N147) as the Main Emeelt Branch (MEB). To discuss each of them, we separated them spatially into 4 polygons (A, B, C and D in Figure 4.28). The observations in each block will be detailed. Also, to compare the 3 active "branches" (polygons A, B and C), we built two other polygons that cover the north part (polygon BAC1) and the south part (polygon BAC2) of this activity.

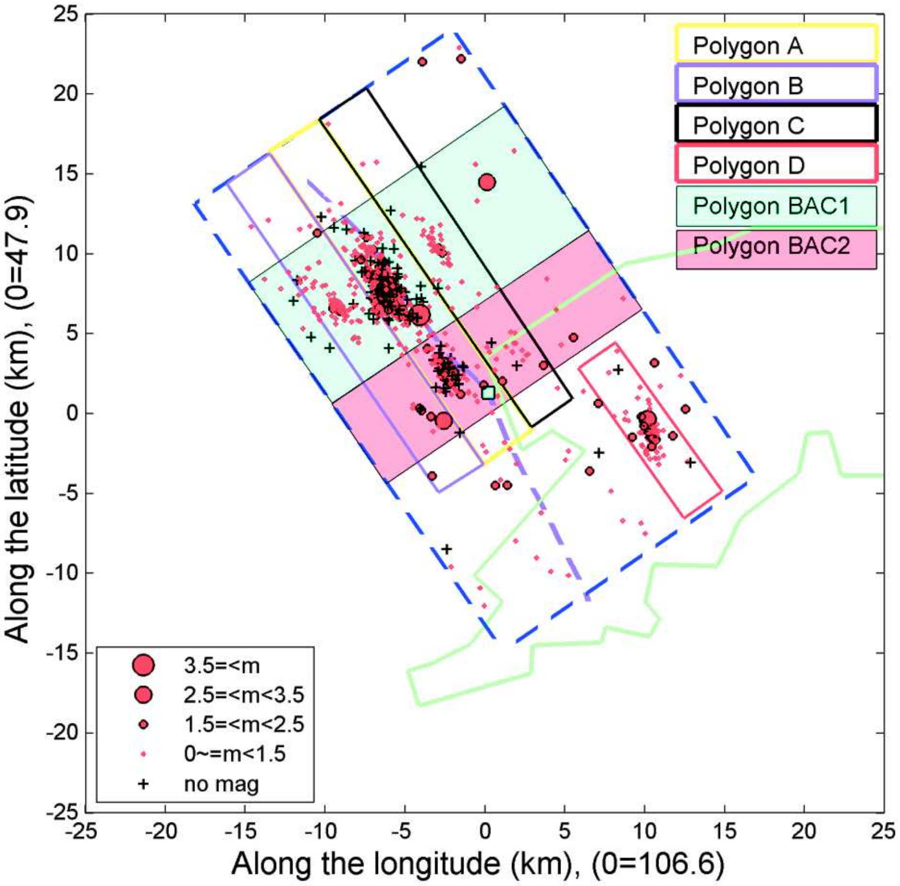

Figure 4.28. Epicentral view of seismic activity in TEFZ between 1995 and 2014. Each polygon corresponds to an area that will be shown in the next figures. Green line = urban area of Ulaanbaatar city; Blue dashed line = border of selected events area (19.5 km X 34 km); Purple line = Emeelt fault (dashed line is supposed Emeelt fault); Aqua square = trench site.

For each polygon, we will show a set of figures: 1) an epicentre map, 2) an epicentre map superposed on a horizontal slice of the Vp velocity model, 3) a cross section parallel and a cross section perpendicular to the seismic activity superposed on the Vp velocity model (from Figure 4.29 to Figure 4.46). The horizontal slice will be always at 10 km depth corresponding to the most frequent observed depth of the seismic activity.

4.5.3.1 Main Emeelt Branch (MEB): Polygon A

The most active area over the period is in the polygon A, which is associated to the Main Emeelt Branch (MEB) identified in the field (Schlupp et al, 2012, 2013; Fleury et al, 2012; Dujardin et al., 2014).

The seismic activity is widespread over 15 km in length (Figure 4.29 and Figure 4.30). The seismic activity is narrow and nearly sub-vertical (about 85° to the NE) and range between ≈ 1 km to

≈18 km depth with the main seismicity between 8 and 14 km (Figure 4.30 and Figure 4.31). It signs a clear active crustal fault.

On the cross section parallel to the fault (A1-A1'), we observe two active areas: 1) one important in the north with weakly elongated shape globally dipping to the NW with some swarms showing a slope of about 55-60° to the NW; 2) the other in the south very local with no particular orientation between 11 to 13 km depth.

This seismic activity "follows" important velocity contrasts, in an area where a high velocity body goes up (red in Figure 4.30). The same observation can be done in map view (Figure 4.29) with the activity located between low and high velocity bodies.

If we interpolate the seismicity activity until the surface, it arrives 4km to the west of the main Emeelt fault trace but the location of the seismicity near the surface is very close to the position of the observed rupture in the field. Notice that the rupture at subsurface (last 5 meters) in the fault area is dipping to the NE but with a much lower angle of 23° to 35° (Dujardin et al., 2014) than the observed seismicity (Figure 1.32 and Figure 5.2). The relation between the seismicity and structures in the area will be discussed in more details in the next chapter.

The seismic activity in the polygon A is from far the most active one, corresponds to the MEB and shows a sub-vertical crustal structure (seismic activity between 1 and 18 km depth) of at least 15km long oriented N147. The shape of the seismic cloud on the fault is weakly elongated and dips to the NW with a slope of ≈55 to 60° for some swarms.

4.5.3.2 West Emeelt Branch (WEB): Polygon B

This branch is less active than the MEB but shows the same direction N147° (Polygon A). The extension of the seismicity on the map is also ≈ 10km, 5km shorter than the MEB and also with much less events (Figure 4.32). The seismic activity is between 3 and 15km depth with the main activity between 7 and 13 km (Figure 4.33 and Figure 4.34).

Along a cross-section parallel to the activity (B1-B1'), the location of the seismicity appears similar to that observed in the north part of MEB (polygon A). The activity "cloud" has an elongated shape dipping to the NW, with a slope of ≈60°, along a velocity contrast (Figure 4.33).

The perpendicular cross-section (B2-B2') shows that the activity describes a narrow sub-vertical structure (Figure 4.34) and that the activity is located between low and high velocity bodies.

The seismic activity in the polygon B shows a subvertical crustal structure (seismic activity between 3 and 15km depth) of at least 15km long oriented along N147 dipping at ≈77° to the NE. The shape of the seismic cloud on the fault is elongated and dips to the NW with a slope of ≈60°.

4.5.3.3 East Emeelt Branch (EEB): Polygon C

This branch is less active than MEB and WEB but shows the same orientation of the seismicity, N147°. The extension of the seismicity on the map is only ≈ 10km (Figure 4.35). The activity is between 6 and 15km depth with the main activity between 8 and 13km (Figure 4.36 and Figure 4.37).

Along a cross section parallel to the activity (C1-C1'), the location of the main seismicity associated with a low number of events is along a cloud with no clear orientation and located in an area where the velocity changes gradually (Figure 4.36). The perpendicular cross-section (C2-C2') shows that the activity describes a sub-vertical structure (Figure 4.37).

The seismic activity in the polygon C shows a sub-vertical crustal structure (seismic activity between 7 and 15km depth) of at least 10km long oriented N147.

Polygon A: Seismic activity along the Main Emeelt Branch (MEB).

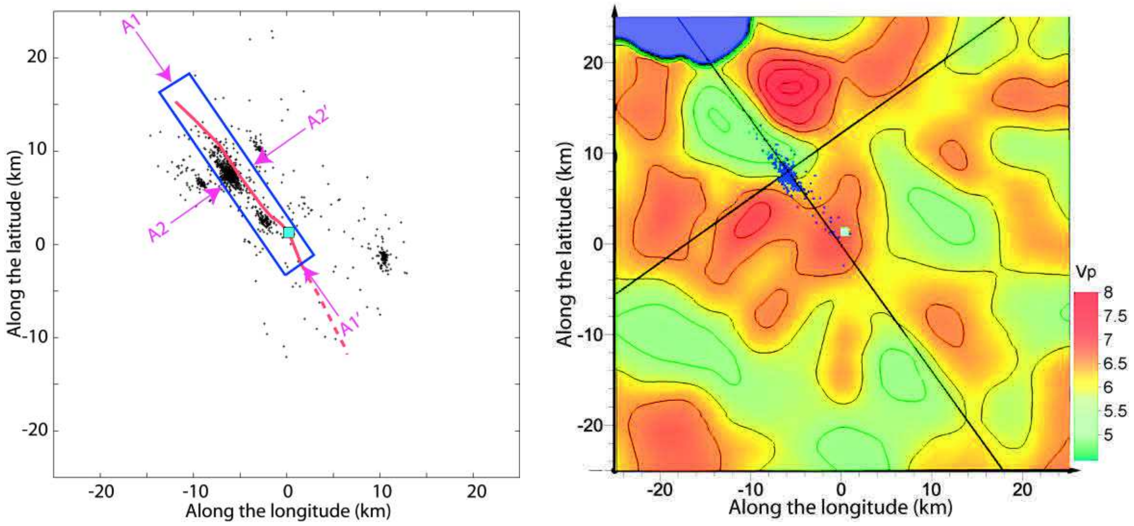

Figure 4.29. Left = Epicentral map and position of polygon A. Red line = Emeelt fault, Aqua square = trench site. Right = Vp velocity model at 10 km depth. Blue dot = epicenter in polygon square illustrated at left. Black lines are positions of NW-SE and SW-NE vertical cross-sections, respectively, in Figure 4.30 and Figure 4.31.

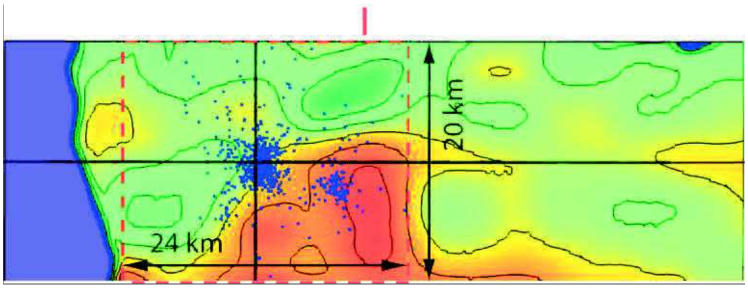

Figure 4.30. Vertical section of Vp model along fault. Vertical black line corresponds to the cross-section across the fault and horizontal black line corresponds to the 10km depth used for the map view. Red line - trench site, red dashed line is border of blue square shown in Figure 4.29. Velocity scale is same as Figure 4.29.

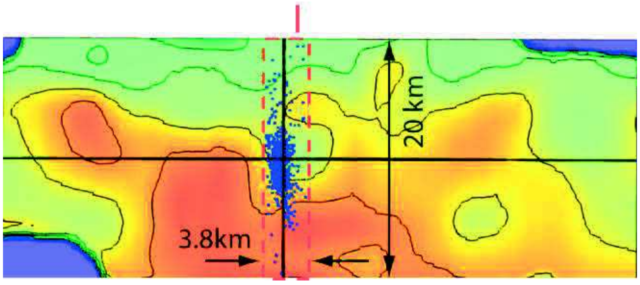

Figure 4.31. Vertical section of Vp model across fault. Vertical black line corresponds to cross-section along fault and horizontal black line corresponds to 10km depth used in map view. Red line - trench site, red dashed line is border of blue square shown in Figure 4.29. Velocity scale is same as Figure 4.29.

Polygon B: Seismic activity of the West Emeelt Branch (WEB)

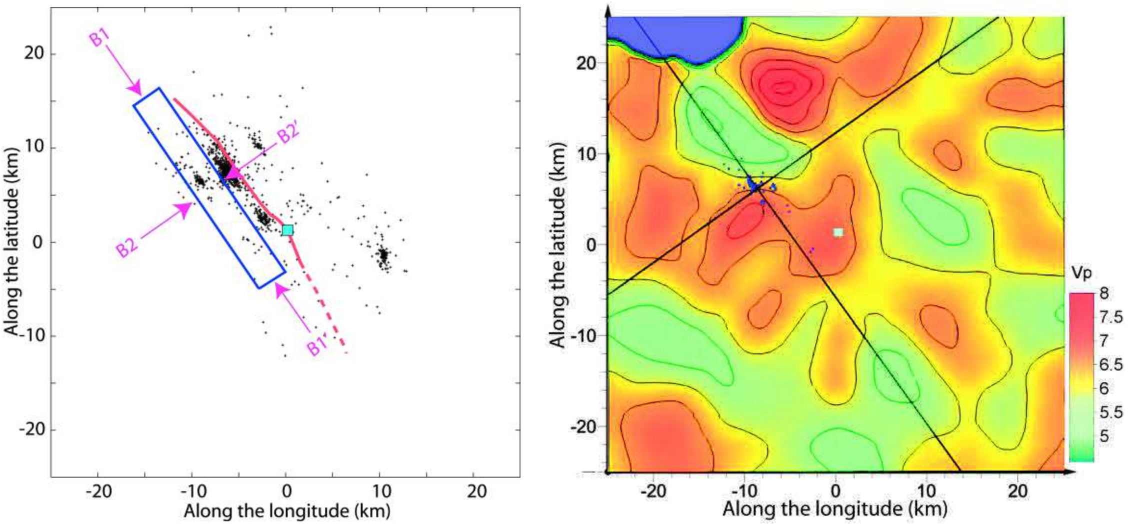

Figure 4.32. Left = Epicentral map and position of polygon B. Red line = Emeelt fault, Aqua square = trench site. Right = Cross section of Vp velocity model at 10 km depth. Blue dot = epicenter in polygon illustrated at left. Black lines are positions of NW-SE and SW-NE vertical cross-sections, respectively, in Figure 4.33 and Figure 4.34.

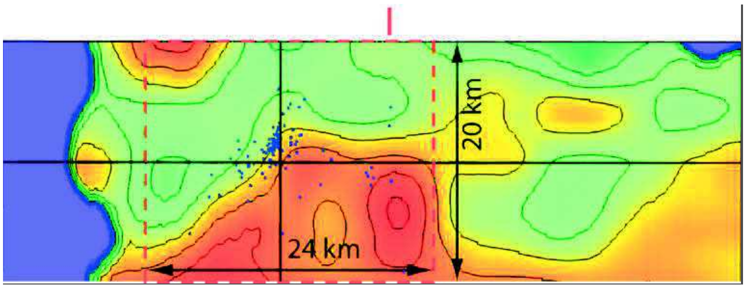

Figure 4.33. Vertical section of Vp model along fault. Vertical black line corresponds to cross-section across fault and horizontal black line corresponds to 10km depth used in map view. Red line - trench site, red dashed line is border of blue square shown in Figure 4.32. Velocity scale is same as Figure 4.32.

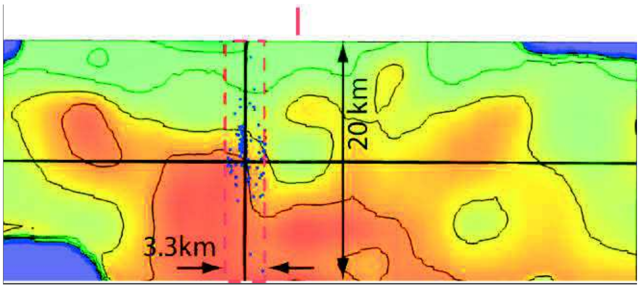

Figure 4.34. Vertical section of Vp model across fault. Vertical black line corresponds to cross-section along fault and horizontal black line corresponds to 10km depth used in map view. Red line - trench site, red dashed line is border of blue square shown in Figure 4.32. Velocity scale is same as Figure 4.32.

Polygon C: Seismic activity of the East Emeelt Branch (EEB)

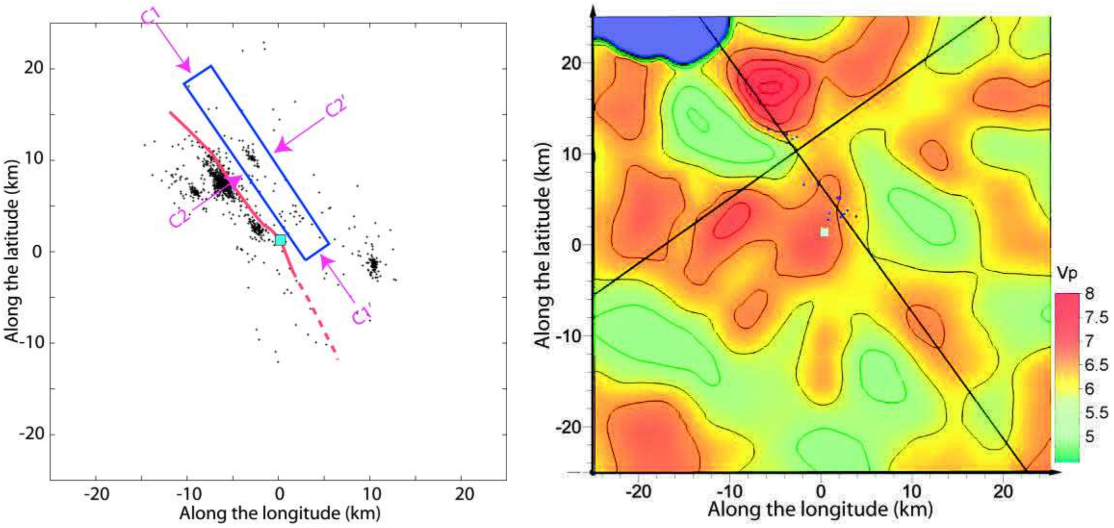

Figure 4.35. Left = Epicentral map and position of polygon C. Red line = Emeelt fault, Aqua square = trench site. Right = Cross section of Vp velocity model at 10 km depth. Blue dot = epicenter in polygon illustrated at left. Black lines are positions of the NW-SE and SW-NE vertical cross-sections, respectively, in Figure 4.36 and Figure 4.37.

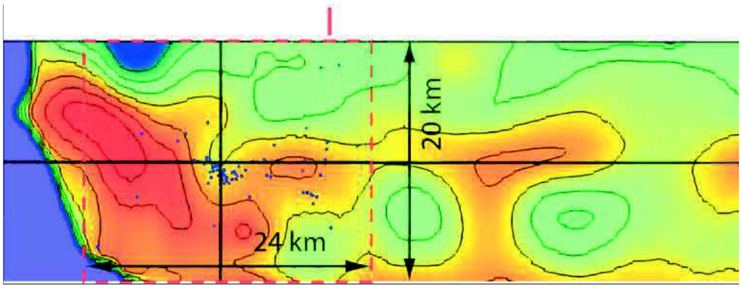

Figure 4.36. Vertical section of Vp model along fault. Vertical black line corresponds to cross-section across fault and horizontal black line corresponds to 10km depth used in map view. Red line - trench site, red dashed line is border of blue square shown in Figure 4.35. Velocity scale is same as Figure 4.35.

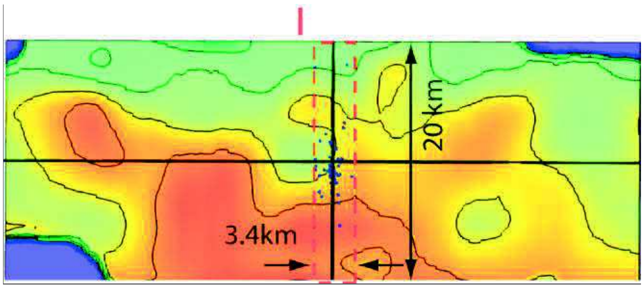

Figure 4.37. Vertical section of Vp model across fault. Vertical black line corresponds to cross-section along fault and horizontal black line corresponds to 10km depth used in map view. Red line - trench site, red dashed line is border of blue square shown in Figure 4.35. Velocity scale is same as Figure 4.35.

4.5.3.4 SE Airport (SEA): Polygon D

This activity is located in the NW corner of the International airport. It corresponds also to the first swarm observed in 2005 in the Emeelt area. It has a clear column shape (Figure 4.38).

This seismic column ranges from 1 to 15km depth with the main part of the activity between 2 and 12km. The diameter of this column of seismicity is about 1.5 to 2.5 km (Figure 4.39 and Figure 4.40).

Therefore, it is difficult to associate it to a specific structure. We suggest it is located on a structure parallel to the three branches of the north, oriented N147°. In that case, after projecting parallel (D1-D1') (Figure 4.39) and perpendicular (D2-D2') (Figure 4.40) to the direction N147, we see that the column is dipping ≈ 75° to the north along the N147 direction and dipping ≈80° to the NE .

There are no obvious relation between the position of the "column shape seismic activity" and the contrast in the 3D WAM velocity model.

The seismic activity in the polygon D shows a seismic column (seismic activity between 2 and 12km depth) that could take place on a structure oriented N147 dipping about 80° to the NE. The diameter of this column of seismicity is about 1.5 to 2.5km.

Polygon D: Seismic column near Ulaanbaatar airport

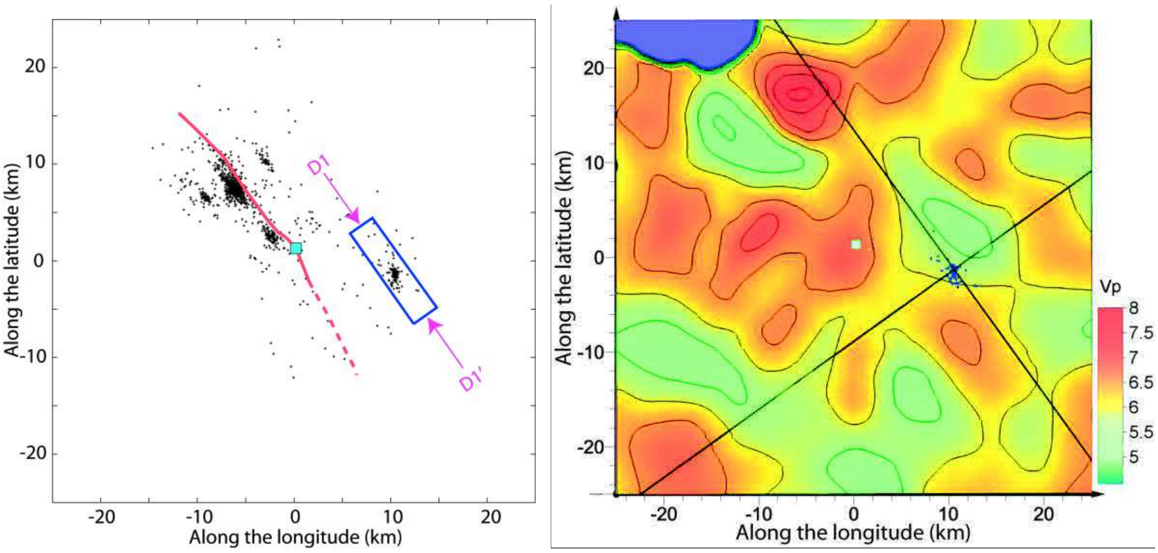

Figure 4.38. Left = Epicentral map and position of polygon D. Red line = Emeelt fault, Aqua square = trench site. Right = Cross section of Vp velocity model at 10 km depth. Blue dot = epicenter in polygon illustrated at left. Black lines are positions of NW-SE and SW-NE vertical cross-sections, respectively, in Figure 4.39 and Figure 4.40.

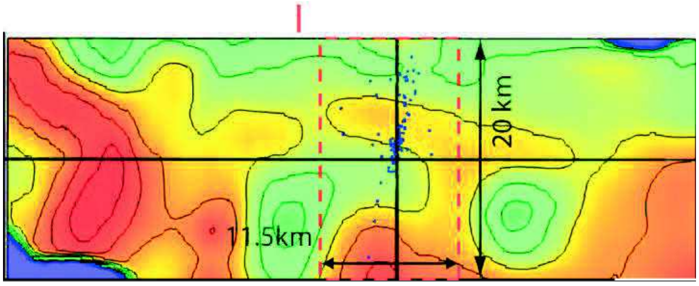

Figure 4.39. Vertical section of Vp model along fault. Vertical black line corresponds to cross-section across fault and horizontal black line corresponds to 10km depth used in map view. Red line - trench site, red dashed line is border of blue square shown in Figure 4.38. Velocity scale is same as Figure 4.38.

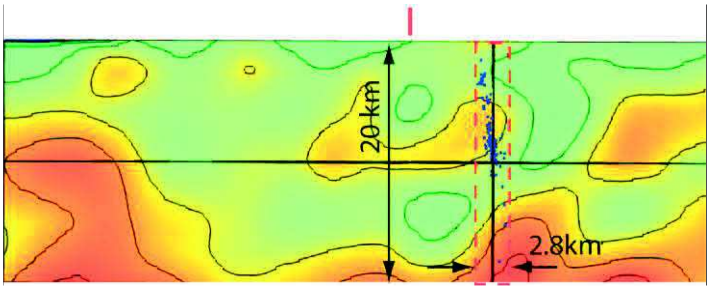

Figure 4.40. Vertical section of Vp model across fault. Vertical black line corresponds to cross-section along fault and horizontal black line corresponds to 10km depth used in map view. Red line - trench site, red dashed line is border of blue square shown in Figure 4.38. Velocity scale is same as Figure 4.38.

4.5.3.5 Relation between West, Main and East Emeelt fault branches: polygons BAC1 and BAC2.

The BAC1 polygon shows the seismic activity of the north part of the three parallel N147 branches (Figure 4.41).

On the N147 cross-section, all the seismicity is in the same area, dipping more or less to the NW. It could indicate a structure perpendicular to the MEB direction dipping at about 60° to the NNW and cutting the three branches (Figure 4.42). We will discuss that point in the next chapter, in the frame of the geological context.

In the cross section perpendicular to the fault, the three branches are not connected, even at depth (Figure 4.43). The three branches are separated by only 3 to 4km and it is possible that they are connected at the depth. Unfortunately, below 15 km, there is quite no seismicity to validate or not this hypothesis.

The seismic activity is concentrated for most of it along the boundary between low and high velocity bodies (Figures 4.41-42-43)

A general observation of the 3D WAM velocity model show a map view shape that looks like an "eggs box" with the velocity going up and down. The orientation of the "eggs box" is along the N147 direction of observed structures. If the direction of the various branches can explain this direction of velocity variation the perpendicular direction, also clear in map view, is not correlated with the seismicity. We will see in the next chapter that it corresponds to some geological features.

The north part of the seismic activity of the Emeelt area shows that the three branches are separated by 2 to 4 km and that they could be associated to one single structure at depth despite the absence of seismicit at that depth. We make the hypothesis that a tectonic structure perpendicular to the MEB direction and dipping between 40° to 60° to the NNW cuts the three branches and that their tectonic activity are inducing the observed seismicity at their intersections.

The BAC2 polygon shows the seismic activity of the south part of the three branches (Figures 4.44-46). Only the MEB branch is associated with a clear activity, which is located near a high velocity body. They are less clear relation between the three branches, due to the limited number of events relocated on the west and east branches, although a possible organization of the three branches as for the BAC1 area can be inferred (Figure 4.43).

Polygon BAC1: Comparison of the three branches of seismic activity (north part)

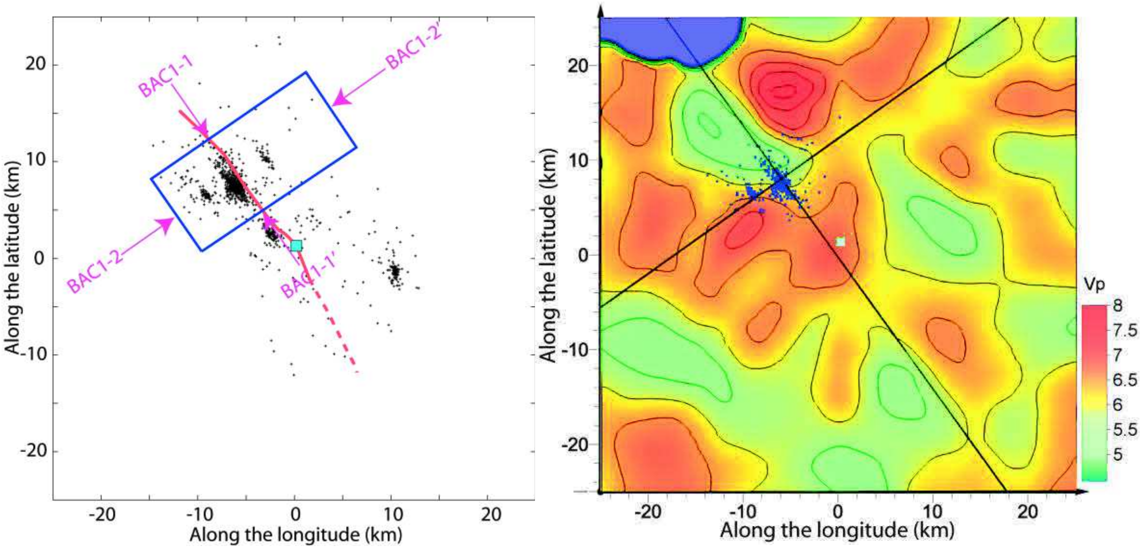

Figure 4.41. Left = Epicentral map and position of polygon BAC1. Red line = Emeelt fault, Aqua square = trench site. Right = Cross section of Vp velocity model at 10 km depth. Blue dot = epicenter in polygon illustrated at left. Black lines are positions of NW-SE and SW-NE vertical cross-sections, respectively, in Figure 4.42 and Figure 4.43.

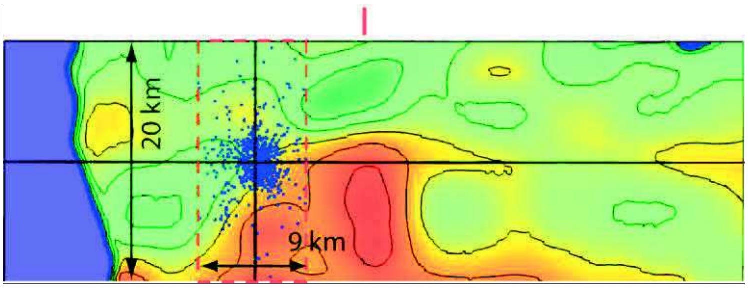

Figure 4.42. Vertical section of Vp model along fault. Vertical black line corresponds to cross-section across fault and horizontal black line corresponds to 10km depth used in map view. Red line - trench site, red dashed line is border of blue square shown in Figure 4.41. Velocity scale is same as Figure 4.41.

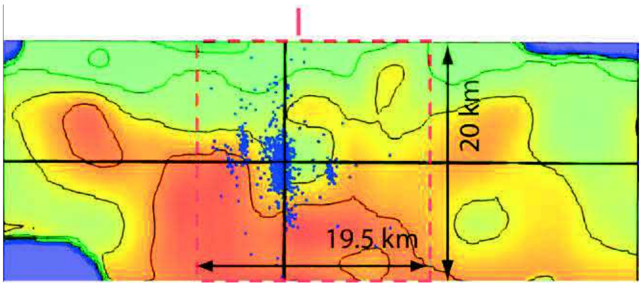

Figure 4.43. Vertical section of Vp model across fault. Vertical black line corresponds to cross-section along fault and horizontal black line corresponds to 10km depth used in map view. Red line - trench site, red dashed line is border of blue square shown in Figure 4.41. Velocity scale is same as Figure 4.41.

Polygon BAC2: Comparison of the three branches of seismic activity (south part)

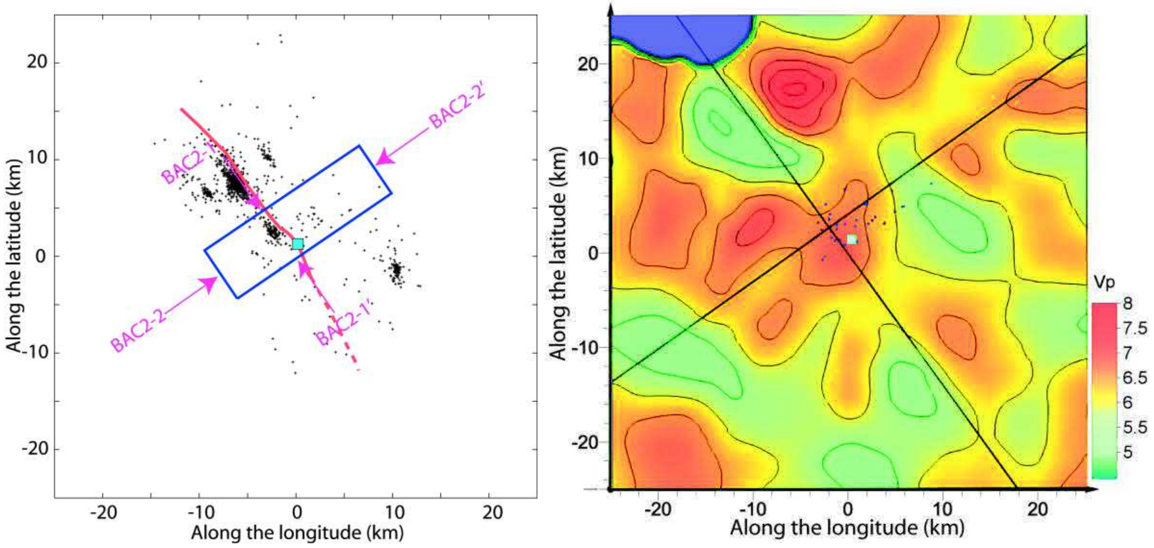

Figure 4.44. Left = Epicentral map and position of polygon BAC2. Red line = Emeelt fault, Aqua square = trench site. Right = Cross section of Vp velocity model at 12 km depth. Blue dot = epicenter in polygon illustrated at left. Black lines are positions of NW-SE and SW-NE vertical cross-sections, respectively, in Figure 4.45 and Figure 4.46.

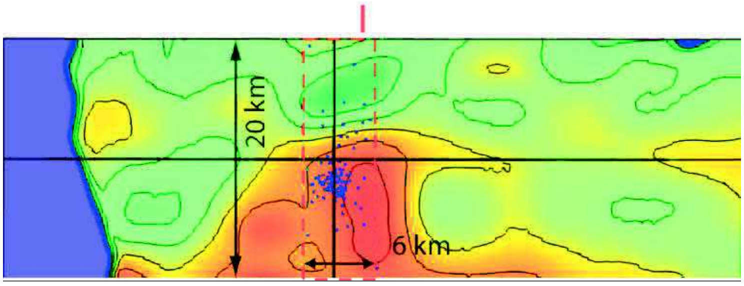

Figure 4.45. Vertical section of Vp model along fault. Vertical black line corresponds to cross-section across fault and horizontal black line corresponds to 10km depth used for the map view. Red line - trench site, red dashed line is border of blue square shown in Figure 4.44. Velocity scale is same as Figure 4.44.

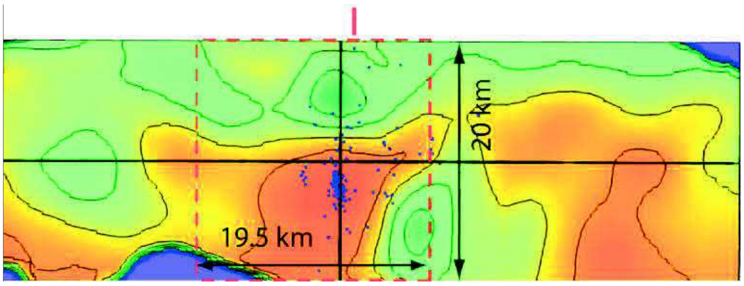

Figure 4.46. Vertical section of Vp model across fault. Vertical black line corresponds to cross-section along fault and horizontal black line corresponds to 10km depth used for the map view. Red line - trench site, red dashed line is border of blue square shown in Figure 4.44. Velocity scale is same as Figure 4.44.

4.6 TomoDD relocation by swarms

Below I present, for each swarm, the map view (top left), a cross section parallel to the fault (bottom left), a cross section perpendicular to the fault (bottom right) and the location, in time, of the swarm for the whole period (top right). The figures in larger scale are presented in Appendix 4. The particularities will be discussed in the next chapter.

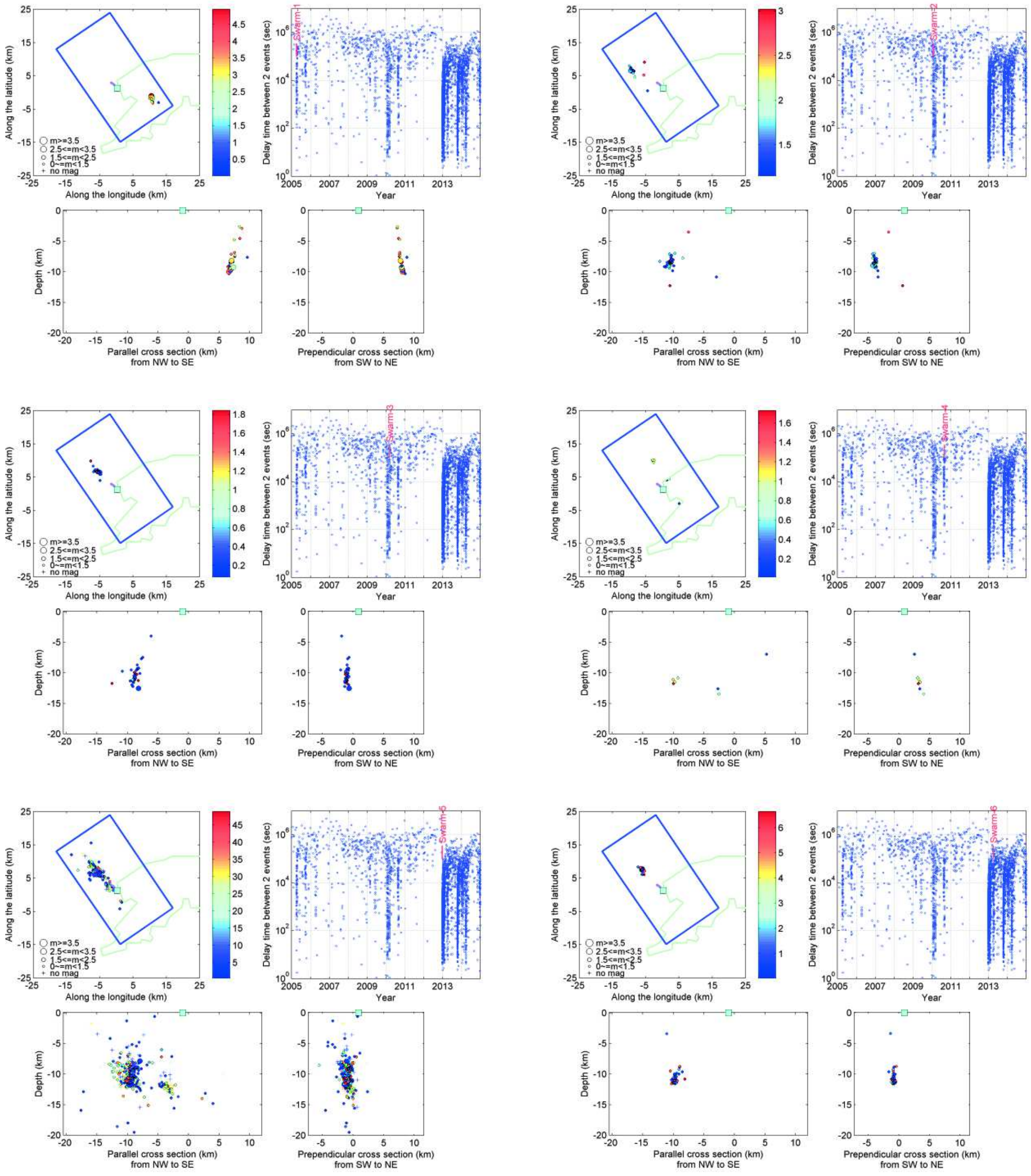

Figure 4.47. Relocated events by swarm

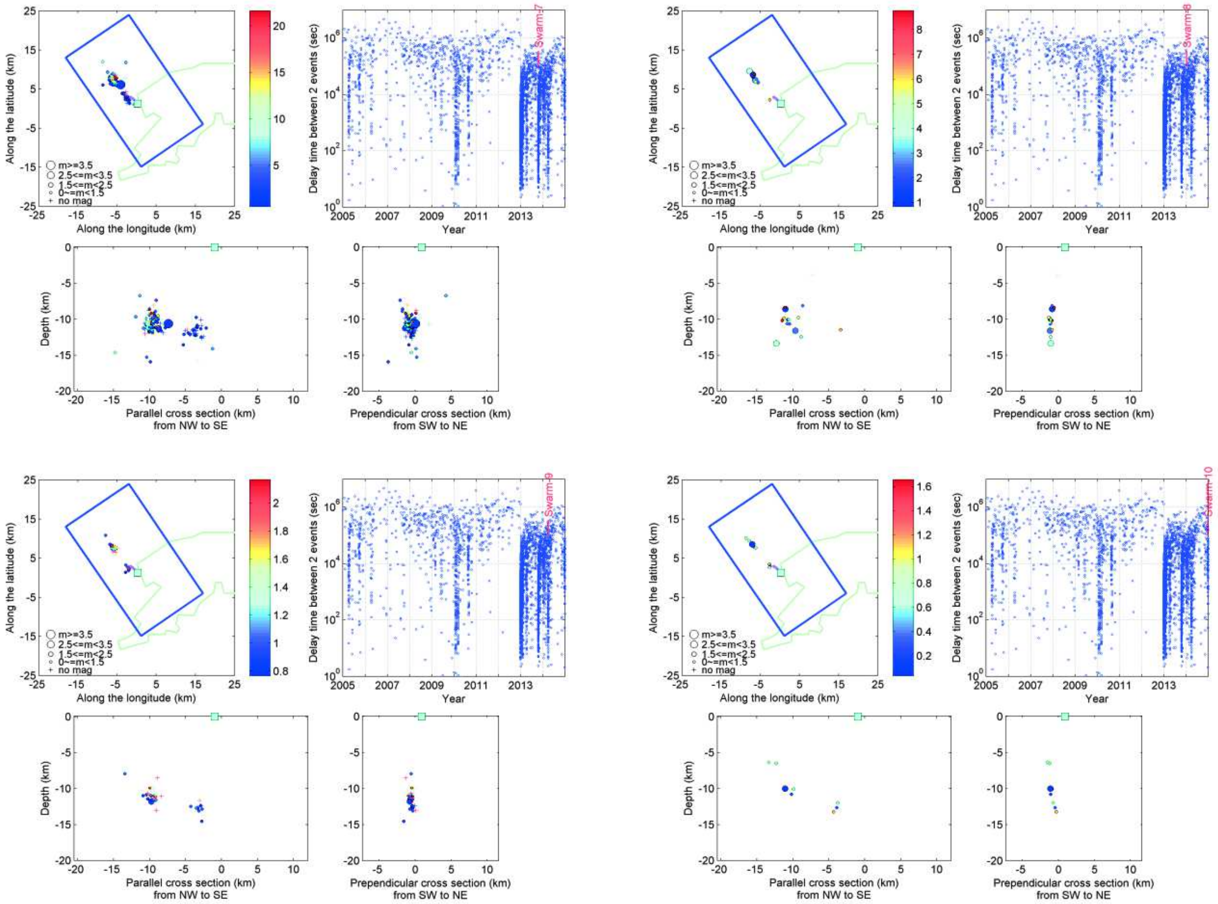

Figure 4.47. Continued.

4.7 Conclusions

The aim of this chapter was to constrain the 3D velocity model and precise locations of the seismic events in the Emeelt active zone. It was the obligatory step before any serious analysis of the space and time evolution of the seismicity and of its relation with known or unknown active structures.

With the precise location of the events by tomoDD, the seismic activity is limited to a length of about 15 km in the north part. But if we consider the distance between the northern active part and the seismic activity located to the north of the airport, the total length is about 30 km.

For the 3D WAM velocity model, we can observe that it has a shape, in map view, looking like an “eggs box” with the velocity going up and down shape. The orientation of the “eggs box” is along about N147, direction of observed structures, and perpendicular. It suggests a structuration of the crust, not only along the Emeelt fault, N147, but also along other, yet unknown, perpendicular structures.

The results of this chapter can be summarized as in the following:

- The three crustal structures (Main, west and east Emeelt active faults) are nearly parallel and strike N147. They and are all more or less sub-vertical (80 to 85° to the NE) and separated by only 2 to 4 km. One hypothesis is that they could be connected at lower crustal depth
- The shape of the north seismic clouds on the three branches are all, more or less clearly, dipping to the NW with a slope between about 55 to 60°.
- For the main branch, the area affected by the seismicity is bigger, with a length of 15km, with a large cloud of seismicity in the north part and a smaller cloud in the south part, and over a depth mainly between 1 and 18km. This branch appears to be connected with the surface ruptures observed in the field.
- The seismic activity of the West Emeelt Branch is much weaker but is widespread over an area similar to the main branches: between 3 and 15km depth and about 15 km in length.
- The seismic activity of the East Emeelt Branch is much shorter with a maximum length of 10 km and depth between 6 and 15 km.
- We make the hypothesis that a structure, perpendicular to the MEB direction and dipping at about 60° to the NNW, cuts the three branches.
- The main activity observed is at about 10-11 km depth, which could be considered as the centre of the seismogenic layer. It indicates an average thickness of the seismogenic layer in the Emeelt fault area of minimum about 20 km.

5 Chapter 5: Relations with other observations, discussions and conclusions

This is the first study to constrain the velocity model and produce a precise location of the seismic activity that started in 2005 in the Emeelt fault area. In addition, an active fault with surface ruptures was discovered in the field in 2008. Thanks to this work, we can now discuss some 3D characteristics of that activity, but also what it tells us about the active structures in the region and what could be the impact of a large seismic event on the capital, Ulaanbaatar.

When we discuss the evolution of the activity in space and time, we have to keep in mind that the relocated seismicity with the 3D velocity model is just part of the observed activity (Figure 5.1). It was necessary to reduce the dataset to be able to get enough precise location and discuss the space and time evolution of the seismicity as well as its relations with active faults.

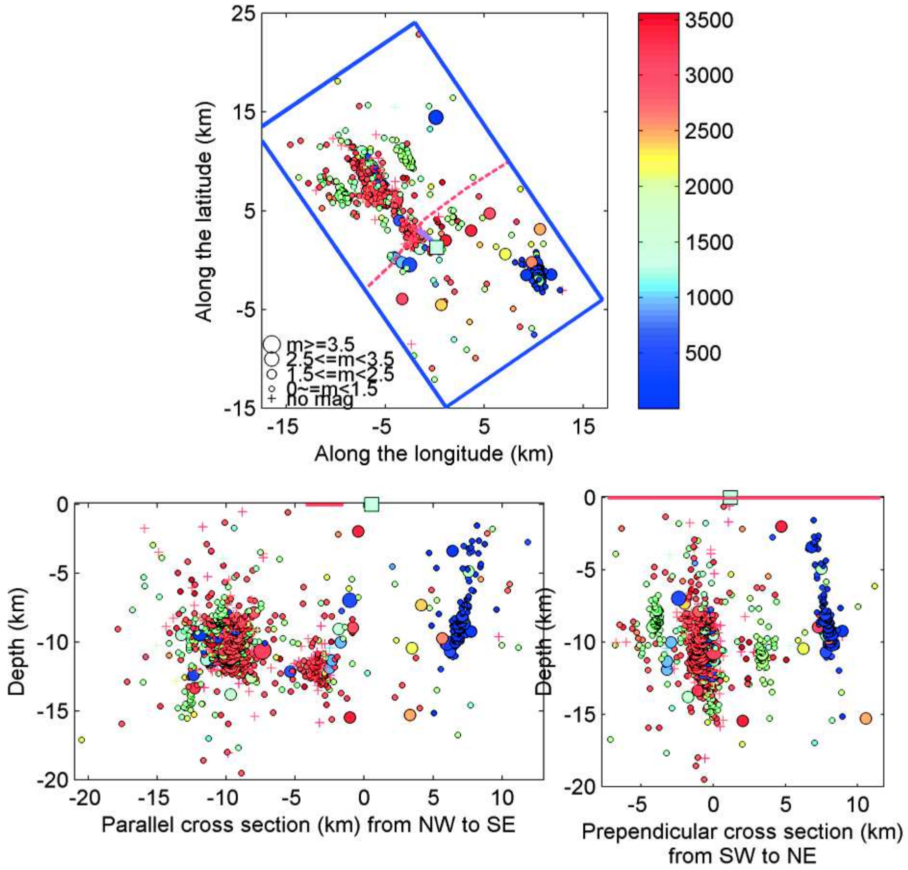

Figure 5.1. Relocated seismicity of Target area of the Emeelt fault zone, TEFZ (between 2005 and 2014). Magenta line = Emeelt fault observed at surface, Aqua square = trench site. Dashed red line= Mesozoic fault. Continuous red line on cross-sections = position of Mesozoic fault at surface. Colour bar indicates number of days since 2005.01.01.

In the area of 140x140km centred on the Emeelt fault, we observe about 5700 events between 1995 and 2014 with local magnitude up to 3.7. I selected 810 events for the 3D WAM velocity model (from 1995 to 2013-01).

The TomoDD relocation is performed for only 1968 events (from 1995 to 2014) representing only about 35% of the total number of detected events (see chapters 3 and 4). This proportion is the same for the TEFZ zone (Target Area of Emeelt Fault), the reduced area around the fault zone that concentrates 60% of the total seismicity and about 65% of the relocated seismicity from the area of 140x140km (see Figure 4.23).

5.1 Fault geometry

5.1.1 Geometry of the fault(s) at the surface (GPR observations), at shallow depth (seismic profile) and at depth (seismicity)

5.1.1.1 Geometry of the fault at the surface (GPR survey)

A field survey of the Emeelt fault zone allowed us identifying 4-5 km-long surface ruptures, oriented about N147^o. A GPR survey has been made at the site where we observed these surface ruptures (Dujardin et al., 2014). The GPR survey shows clear reflections exactly located under the location of surface ruptures, which mean that they are the extension of the rupture at depth. The dip angle near the surface is towards NNE and it ranges from 23^0 in the north to 35^0. The dip varies quite rapidly along the fault with 27^0 in the north (profiles b and c in Figure 5.2), 23^0 in the middle (profile d in Figure 5.2) increasing up to 35^0 in the south (profile e in Figure 5.2). The distance between GPR profiles “a” to the north and “e” to the south is only about 1 km. Dujardin et al. (2014) identified also a right lateral offset of about 2m of a paleo-river, at the trench site, without clear vertical offset (See chapter 1.2).

We observe at the surface a right lateral strike-slip on a fault dipping gently to the NE (23° to 35°) in the first 5 m below the surface.

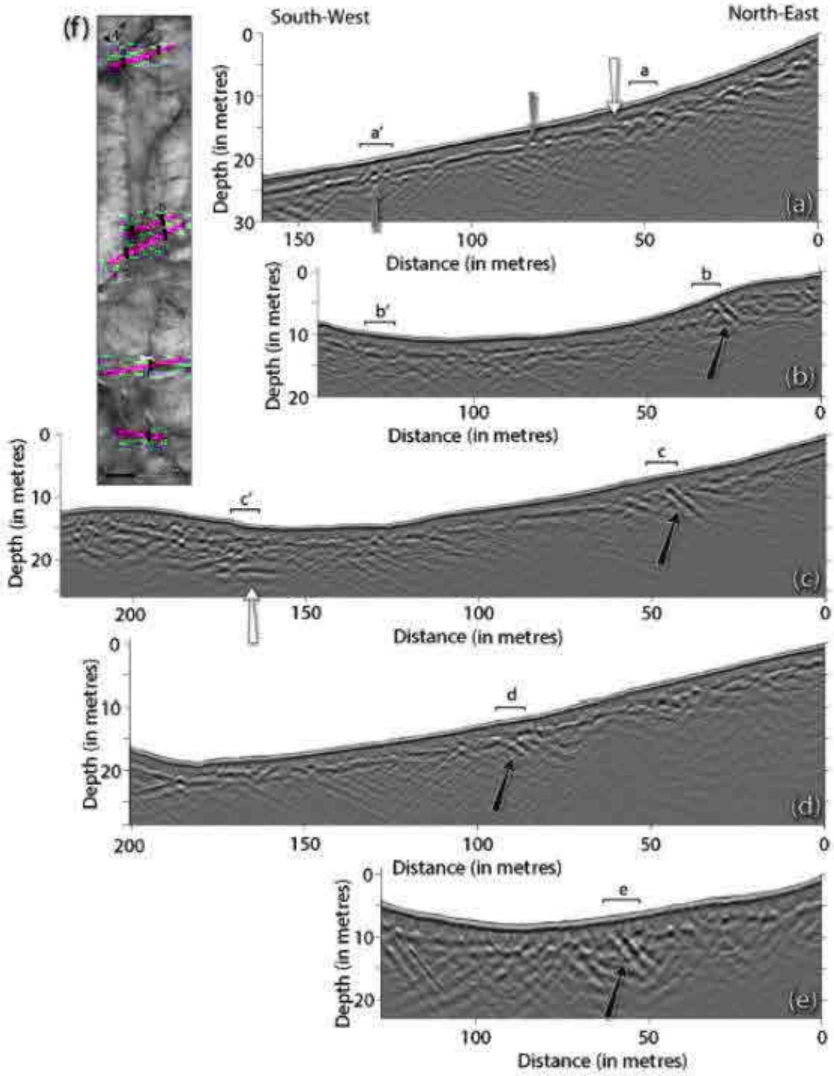

Figure 5.2. All profiles are equally scaled with a vertical exaggeration of 1.8. Location of profiles (from top to bottom) is shown by red lines on map (f). Letters (a)–(e) show places where morphological scarps are observed at the surface. Black arrows show reflections from fault plane and changes in the GPR facies that highlight the fault location and geometry (after Dujardin et al., 2014).

5.1.1.2 Geometry of the faults at shallow depth (seismic profile)

A seismic profile has been recorded in the field in 2012 in the north part of the seismic activity.Figure 5.3 shows the profile location. Only the western part, the first 2500 m, produced a clear image of underneath structures (Bolaty, 2015) near the main seismic activity area (bottom part of Figure 5.3). The seismic profile gives an image of only the first 200 m. Notice that the eastern part of the profile does not show any clear structure but its quality is also lower. The profile shows some horizontal displacements between the coordinates 425 m and 2105 m (coordinate of the profile). At about 425 m there is very strong vertical shift (red arrow in Figure 5.3) that could indicate a fault. Also some vertical breaks are observed (blue dashed lines in Figure 5.3). The structures are nearly vertical with sometimes an important dip of 60° to 80° to the NE.

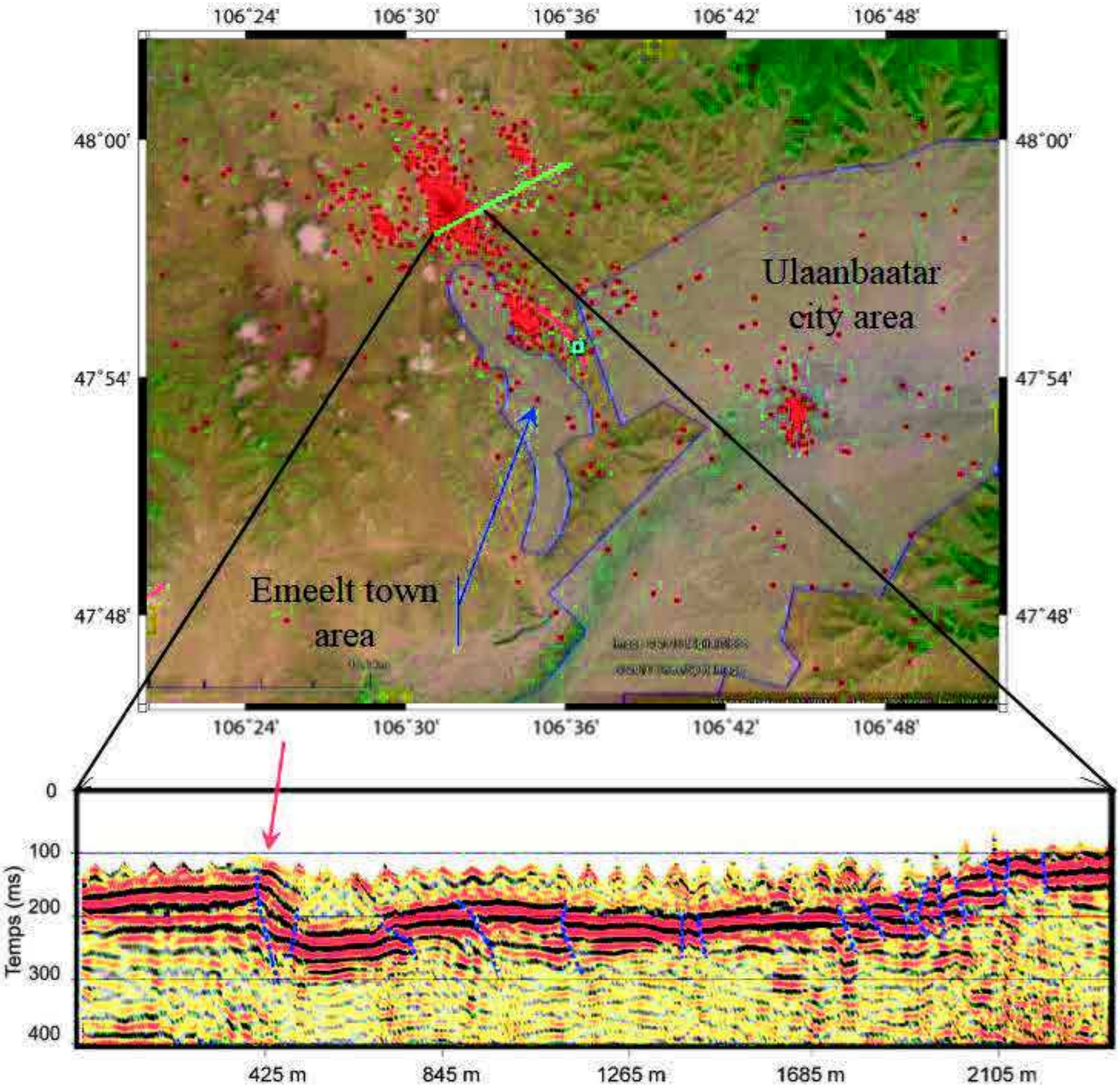

Figure 5.3. Top figure is epicentral map of relocated events and the position of the seismic survey (green line). Aqua square = trench site. Red line = observed surface rupture of Emeelt fault zone. Bottom figure is seismic profile and analysis with, in blue, main faults (modified from Bolaty, 2015).

5.1.1.3 Geometry of the fault branches at depth (seismicity)

Despite no clear surface rupture could be found in the field near the seismic activity except at the trench site, there should be active structures associated with the seismicity because earthquakes are oriented and spatially organized. When precise locations are made, unknown active faults may be identified assuming the seismicity is clearly organized along the fault plane (Courboulex et al., 2003).

The relocated events (Figure 5.5) show that the “swarm” seismic activity of the Emeelt fault zone is located mainly to the NW from the observed surface rupture on the field.

Based on the hypocentral distributions we observe, in map view and cross section perpendicular to the fault, that the Emeelt fault zone includes at least three parallel branches oriented N147°, of the same direction as the observed surface ruptures, and the activity near the airport (SE) suggests even a fourth branch (Figure 5.4-5.5). If the branches appears parallel in map view, in cross section the dip varies from 83°, 85°, 80° to 82° to the NE (respectively, from west to east).

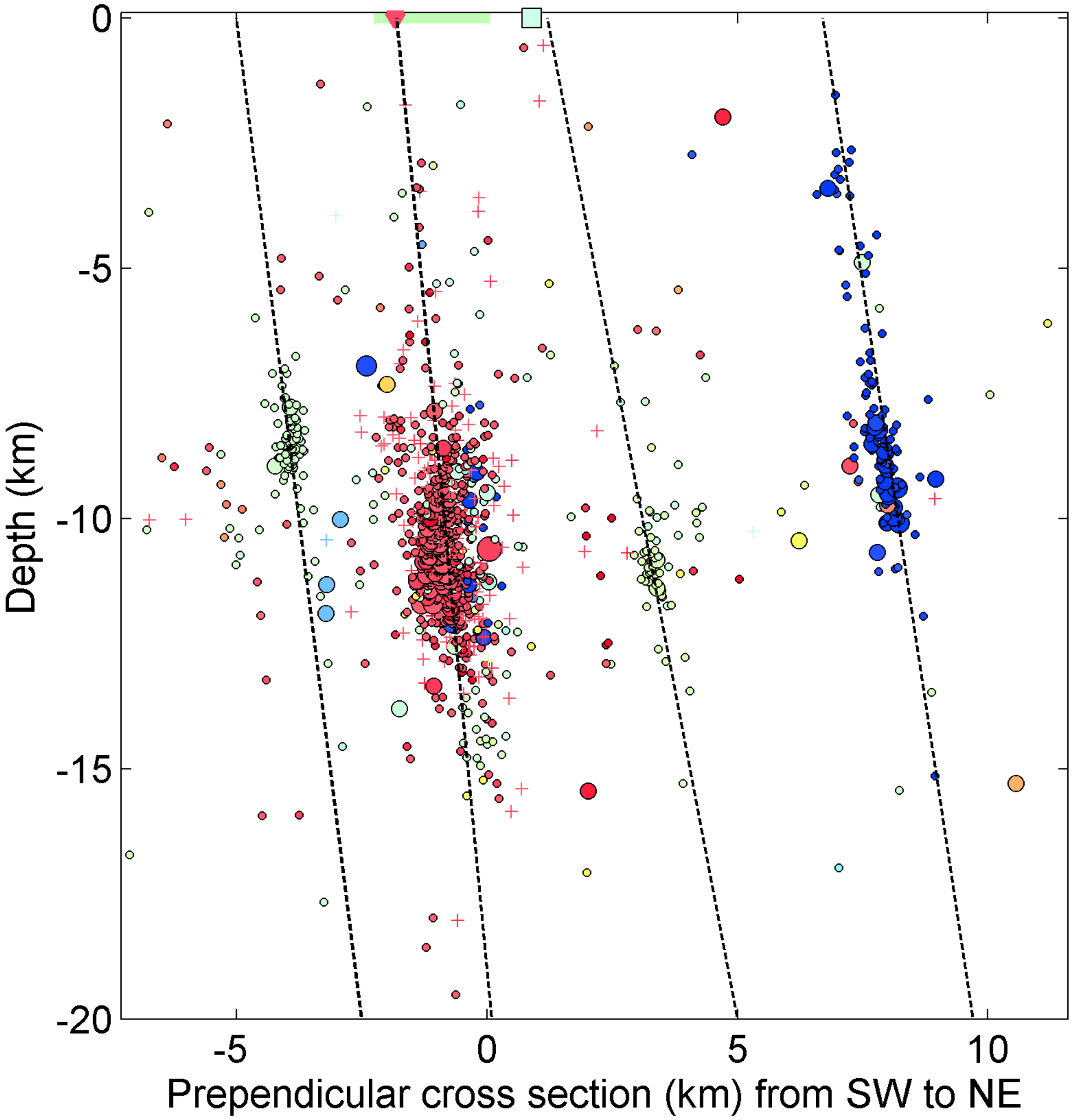

Figure 5.4. Cross section perpendicular to fault (colour legend is same as Figure 5.1). Aqua square = trench site. Green line = position of seismic profile. Red triangle = location of red arrow shown in bottom figure of Figure 5.2. Black dashed lines = extrapolation of seismicity to surface for each branch of the Emeelt fault zone. s

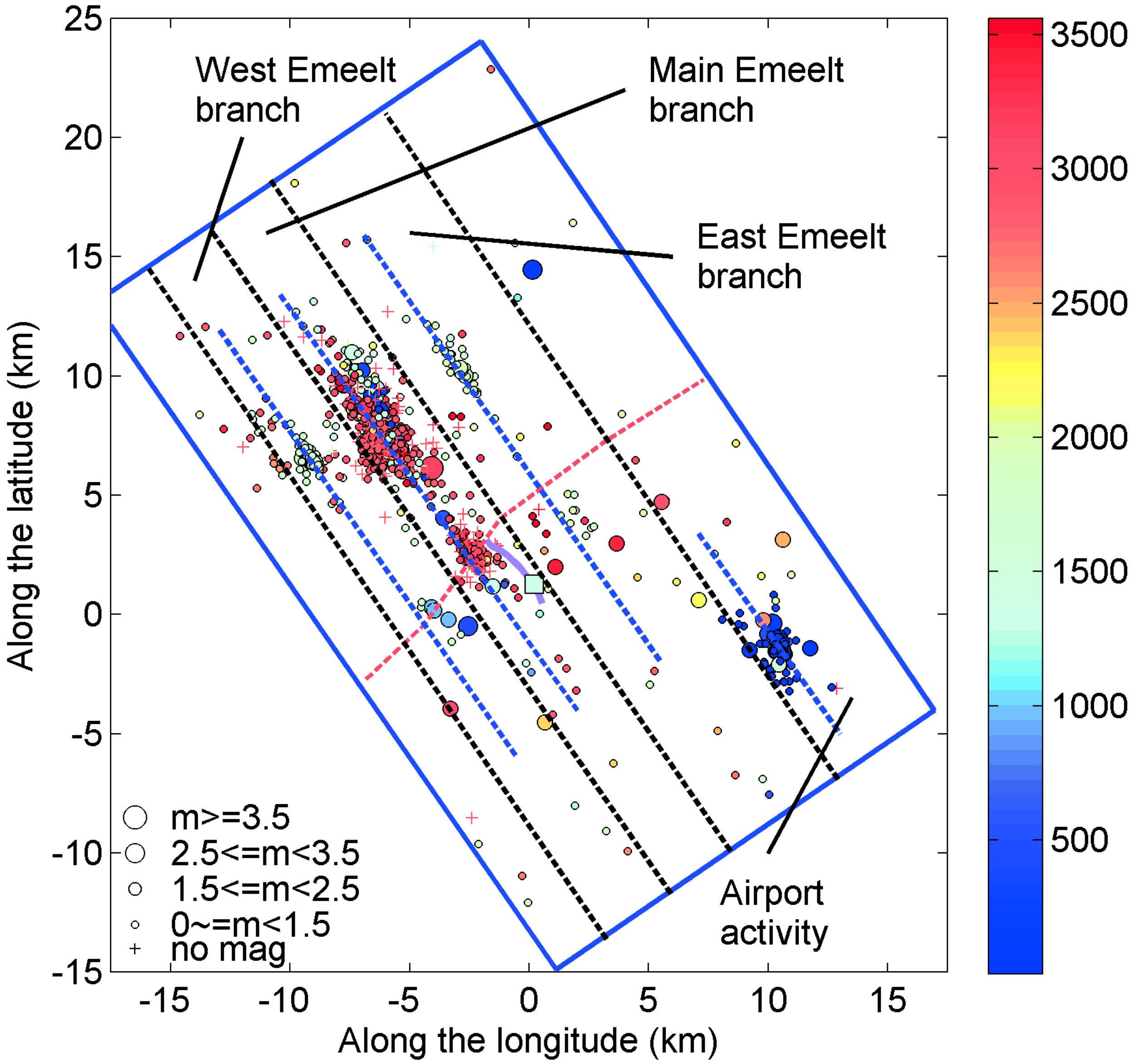

Figure 5.5. Epicentral view of relocated event of Emeelt fault zone (between 2005 and 2014). Magenta line = observed surface rupture of Emeelt fault. Aqua square = trench site. Dashed blue line = middle line of seismic activity for each branch at depth. Dashed black line = possible location of each branch at the surface after extrapolation of the seismicity (see Figure 5.4). Dashed red line = Mesozoic fault (see Figure 5.4). Colour bar indicates number of days since 2005.01.01.

5.1.1.4 Relation between deep and surface observations

The east branch can be connected with the surface ruptures observed in the field (trench position). It is the one with the shallowest dip (but still important, 80°) and this dip could be shallower near the surface to be consistent with the GPR observations (Figure 5.4).

The middle branch (Main Emeelt Branch in terms of activity) cuts the surface exactly at the place of the structures observed in the west part of the seismic profile (Figure 5.4 and red arrow on Figure 5.3).

Until now, no surface or near surface faulting evidence has been found for the airport or the western branches.

On the cross section perpendicular to the fault (Figure 5.4), it appears that the four branches, if we include the seismic activity near the airport, are separated by only 3 to 5km and it could be possible that they are connected at depth. Unfortunately, below 17 km, there is no seismicity to validate or not that hypothesis.

5.1.2 Possible size of the Emeelt fault and associated magnitude

The distribution of the seismic activity helps us to estimate the minimum length of the fault. After relocation, with the selected events, we observe a seismic activity widespread for 15 km in length if we consider the activity on the west, central and east branches, and 25 km if we include the airport area activity (Figure 5.6). The depth of the activated part of the fault is at minimum 15 km. Notice that before the TomoDD relocation, we estimated a length of the active zone of 35 km due to misslocated events.

To estimate the magnitude that could be associated to an event occurring on these branches, I used the common method to estimate the possible earthquake size based on the empirical regression laws relating surface rupture length and magnitude (Wells and Coppersmith, 1994). From the field observations of the surface ruptures of the Emeelt fault, we can clearly observe ~4-5 km long surface rupture at the end of the south part of the seismic activity. Relating this length to one event, it could be associated to a magnitude of about 5.7. If we consider the seismicity along the Main Emeelt Branch (MEB), the 15 km length would produce an earthquake of about magnitude 6.4. If we consider a length of 25 km, by including the seismic activity near the airport and considering that the various branches consist on a wide deformation system working together, it could increase up to 6.7.

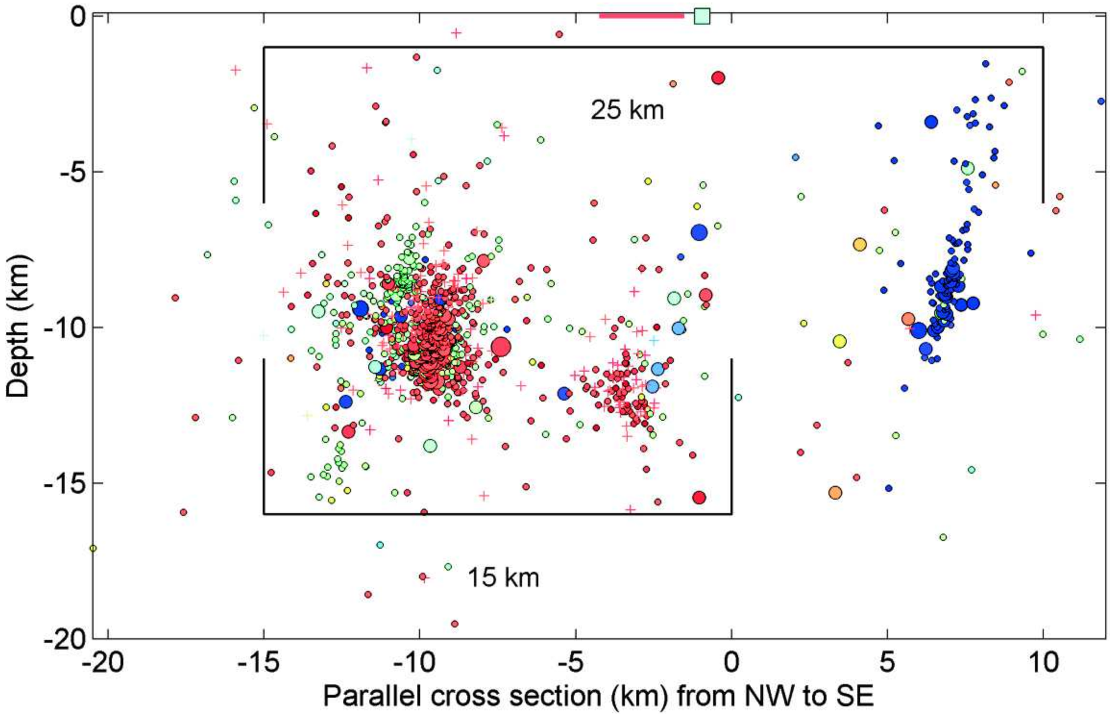

Figure 5.6. Parallel cross section to the fault (colour legend is same as Figure 5.4). Brakets show lengths of active fault considering either 3 branches to the west (15km) or including the Airport activity (25 km)

But we have also to keep in mind that the fault could be longer than these values, which are minimum values based on the area affected by the observed seismic activity.

5.2 Relation-interaction with other structures

5.2.1 Geological structures cutting the fault

The known active structures in the area (Khustai, Avdar, Sharkai) do not show directions similar to the N147° Emeelt fault branches (Figure 5.7). In the geological maps, the area is cut by Mesozoic structures (red in Figure 5.8 and black in Figure 5.9). To the south of the Emeelt activity, there is a Mesozoic structure in the eastern prolongation of the Khustai fault and is oriented in our TEFZ about N60°, perpendicular to the Emeelt branches. This main Mesozoic structure is cut by some small segments perpendicular, which appears to be transfer faults parallel to the Emeelt fault branches. The Emeelt branch characterized by surface ruptures is located on this N60° Mesozoic structure and could thus be also a transfer fault. Notice that this N60° Mesozoic structure follows the northern limit of the urban area of Ulaanbaatar (Figure 5.8).

Most of the Emeelt seismic activity is located more to the north (except the activity near the airport to the SE). Moreover, another Mesozoic structure at the NW end of the seismic activity of the

East Emeelt Branch extend to the NE in a direction of about N30°. Therefore, the Emeelt fault branches could be interpreted as a transfer zone between these N30° and N60° Mesozoic structures (Figure 5.8).

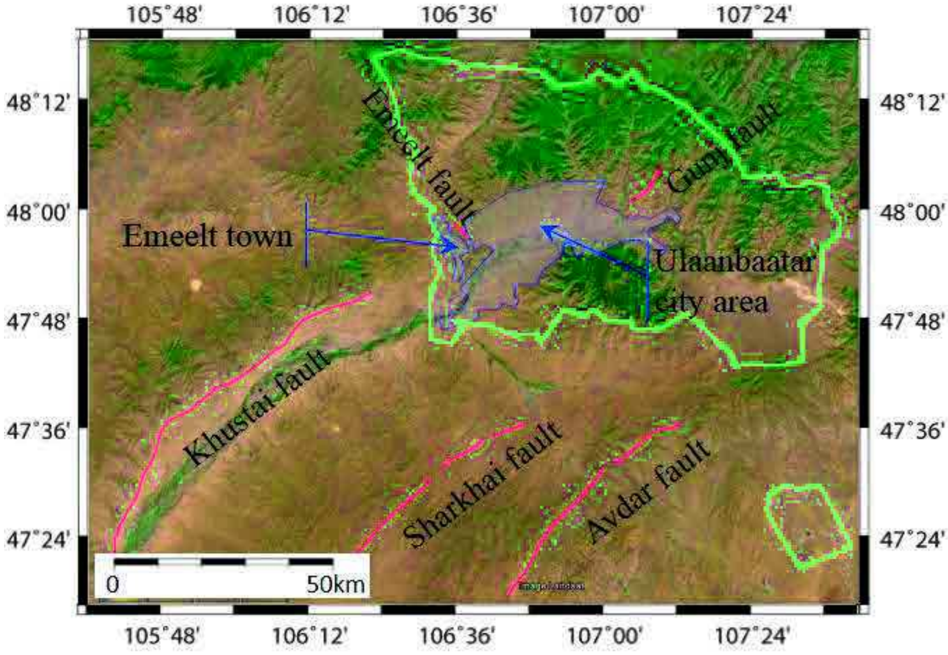

Figure 5.7. Known active faults around Ulaanbaatar: Khustai, Sharkhai, Avdar, Emeelt and Gunj faults.

In a N147° cross section, the prolongation to the surface of only the linear swarms (swarms 2, 3 and 6, Figure 5.10 A) arrives very near the N60° Mesozoic structure. It could suggest that there are several structures, more or less parallel to the N60° Mesozoic structures, and dipping about 60° to the NW. They would cut the Emeelt Branches and the activity would be at their intersection. Unfortunately, the dip of the Mesozoic structures are unknown.

Two focal mechanisms along the main Emeelt branch have been calculated (2012-12-26 with M_L=2.9 and 2013-10-14 with M_L=3.7)(Figure 5.8). Although well constrained, they do not indicate directions near N147°. One nodal plane has in both mechanisms a strike near the EW direction, and the other one is oriented more about N20° to N30°, in a direction close to the NE Mesozoic structures (Table 5.1).

The N30° direction is not favored as the extrapolation of the seismic activity to the surface arrives more south than the N30° Mesozoic structures. To test the EW direction, we plotted a NS cross section (Figure 5.10 B). The three swarms, one occurring on the western branch, the two others on the main branch, are nearly superposed in that case, suggesting an EW structure, totally unknown and dipping about 60° to the north, that would cut the three branches in an EW direction. This dip is nevertheless smaller than the one obtained with the focal mechanism, about 80° to the north.

In conclusion, the seismic activity observed could be, for a large part of it, located at the intersection between N147° Emeelt branches and older structures that cut them, either a Mesozoic structure oriented N60° or and unknown structure oriented EW and dipping to the north.

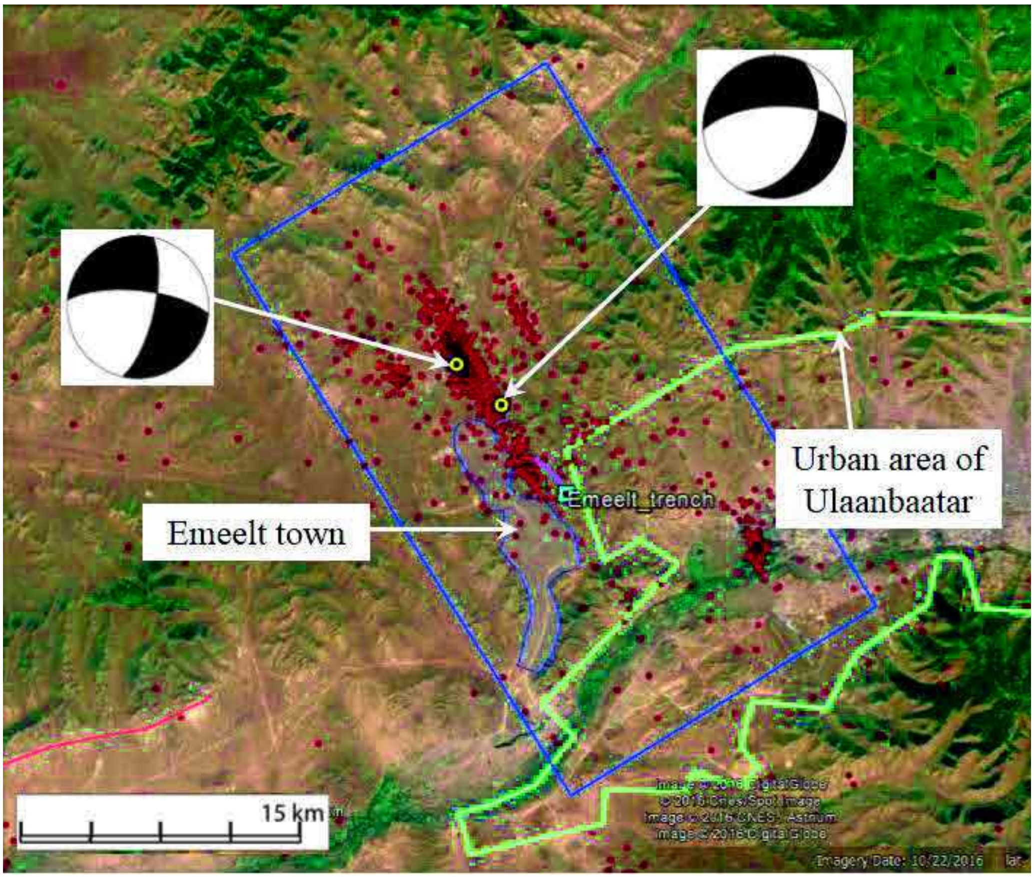

Figure 5.8. Epicentral distribution of Emeelt activity (result of tomoDD). Yellow circles are events (from left) with M_L=2.9 (2012.12.26) and M_L=3.7 (2013.10.14), respectively. Background image = Google Earth. White transparent overlays are urban area of Emeelt west of trench, and green line is urban area of Ulaanbaatar city. Aqua square is trench site and purple line is observed surface rupture of Emeelt fault.

Table 5.1. Fault plane solutions of 2 earthquakes

	Strike 1	Dip 1	Rake 1	Strike 2	Dip 2	Rake 2
2012.12.26	275.6	71.2	-20.3	12.4	70.9	-159.9
2013.10.14	267.5	66.2	-50.7	24.6	45.5	-144.5

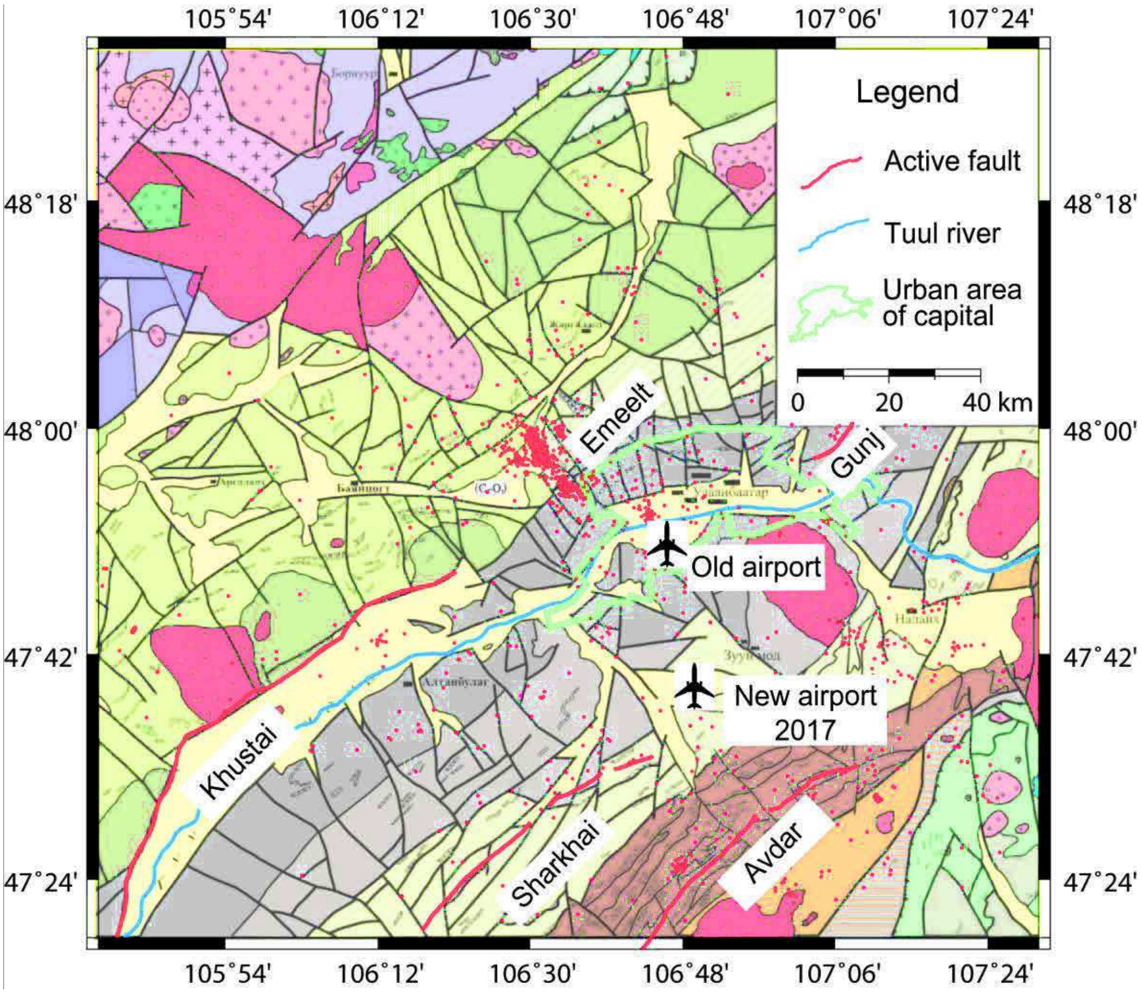

Figure 5.9. Location of relocated seismic events superimposed on simplified geological map (modified after Tomurtogoo, 2009).

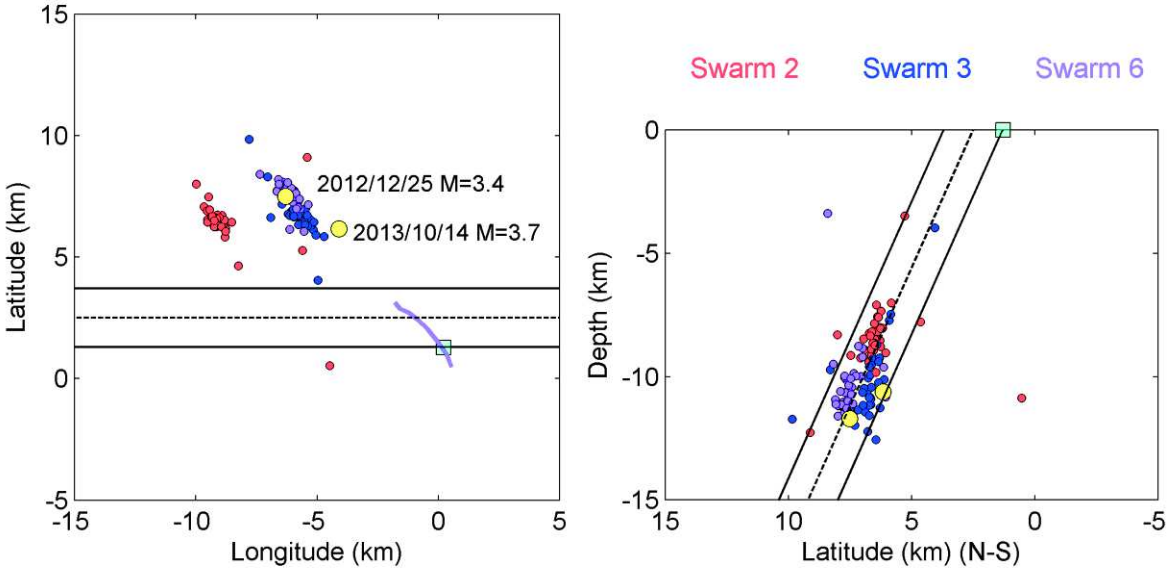

Figure 5.10. Epicentral map of Swarms 2, 3 and 6 in the left (A) and NS cross section in the rigth (B). Aqua square is trench site and purple line is observed surface rupture.

5.2.2 Tentative model of deformation

We propose a tentative deformation model of the area (Figure 5.11). Left picture in Figure 5.11 is a schematic diagram of the active faults around Ulaanbaatar city. The Khustai, Sharkhai and Avdar faults are left-lateral strike slip faults. The Emeelt branches are right-lateral strike slip faults with possible small vertical components. In the area of Emeelt, several Mesozoic structures cut the Emeelt branches and it is not impossible that another EW structure exists. In this scheme, the Emeelt fault zone may be explained as a transition or transfert zone in a "simple" bookshelf model (Figure 5.11, rigth). Interactions between the Khustai fault and the Emeelt fault zone can be imagined. The Emeelt fault activity should be considered in the frame of these two structures. There is no clear relation between the Emeelt fault zone and the Sharkhai and Avdar structures at farther distances.

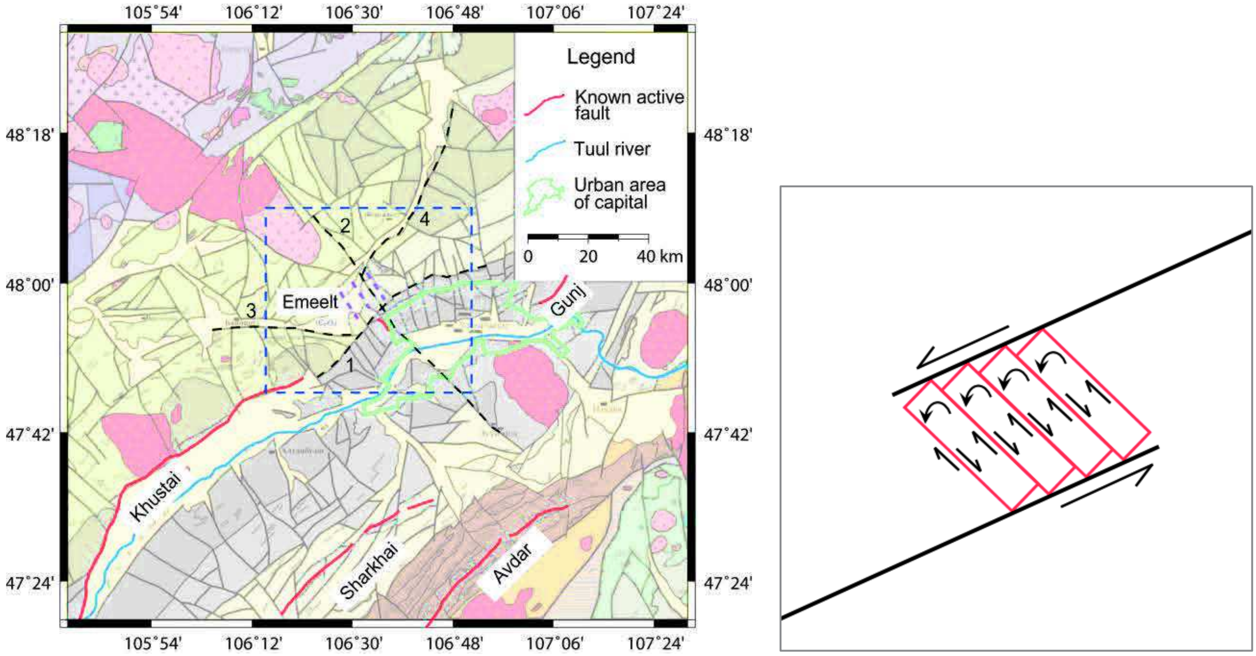

Figure 5.11. Left = Schematic diagram of active faults around Ulaanbaatar. Red line is active fault, purple dashed line is location of observed seismicity in the Emeelt fault area and black line is geological fault: 1=east extension of Khustai fault, 2=south and north extension of Emeelt activity, 3=possible perpendicular fault (see Figure 5.10), 4=possible North fault (possible transfer through Emeelt activity). Blue dashed line area = concerned limits for the right figure showing a bookshelf model that may explain the tectonic process in the Emeelt fault zone.

5.2.3 Relation with focal mechanisms and stress orientation.

The map of focal mechanisms shows (see Appendix 5) that the earthquake focal solutions in the southern and western parts of Mongolia and the neighbouring regions of China and Russia are quite uniform (strike-slip and thrust movements).

According to the stress inversion results, the SHmax is turning from EW in eastern Mongolia to NE-SW in the Gobi-Altai and the central Mongolia, and then to NS in the western part of the region (Figure 5.12) (Radziminovich et al., 2016). The regularity can be explained by the recent geodynamics of this part of Asia.

The SH direction estimated in the region of Ulaanbaatar is very near from the fault orientation of Khustai, Sharkhai and Avdar, on which clear left-lateral strike slip movements have been observed with small normal component. It is nearly perpendicular to the Emeelt structures that have important dips (80 to 85°) and then consistent with the reverse component observed on it. The two focal mechanisms calculated in the Emeelt fault zone show SH direction of about N45-55, nearly perpendicular to the fault oriented N147. Nevertheless, the local stress field is based on only few events and need still to be studied in details.

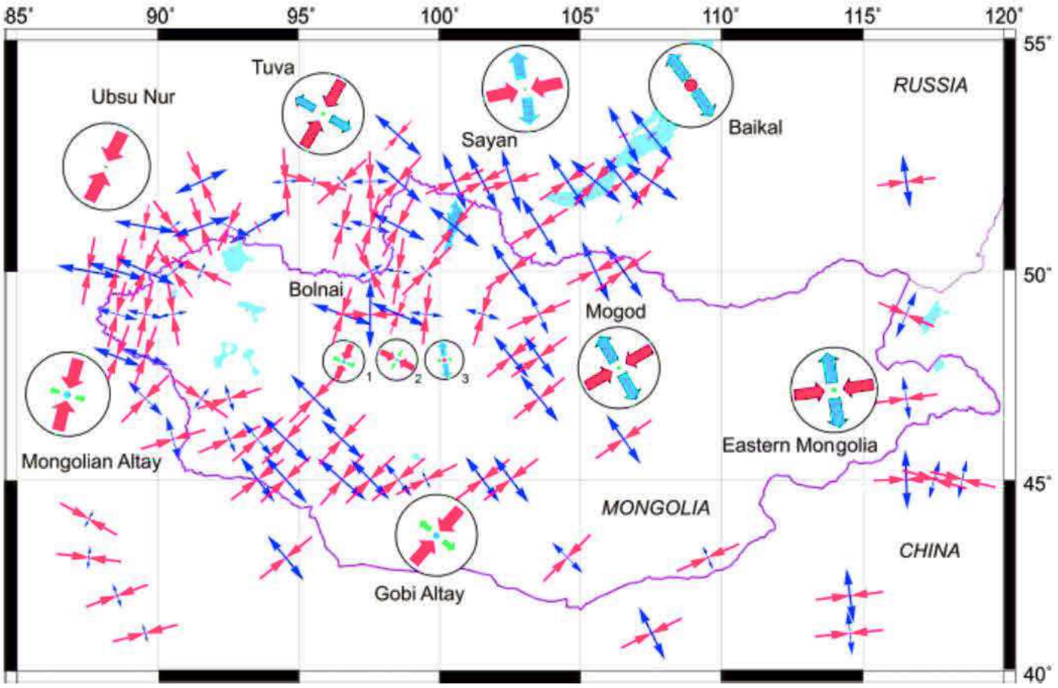

Figure 5.12. Stress inversion results for main active domains (in circles) and after damped stress inversion for 1°-spaced grid. Vectors give orientations of maximum (red) and minimum (blue) compressional horizontal stress SH and Sh. Arrow length depends on inclination to the horizon. Inversion results obtained by Tensor program (in circles) show also intermediate axis orientations (green) (after Radziminovich et al., 2016).

5.3 What is telling us the 1D and 3D velocity models ?

5.3.1 Crustal velocity and depth of the seismicity

The 1D velocity model is not well constrained below ~28 km due to events distribution, then deeper, it is identical to the input model (Figure 5.13). It is impossible to give specific conclusion for the crust structure deeper than 28 km in this area.

A low velocity is observed from surface until 2 km, then until 12 km it is very stable at about 6 km/s and near our NDC model. Below, the velocity is increasing again until 28 km up to 6.7 km/s. It is very near the IASPEI91 model between 20 and 28 km depth. Notice that our 1D velocity model is always higher than the IASPEI91 velocity model.

Most of the seismicity is restricted in the top part of the crust down to 12 km, the main active seismogenic layer. The main part of the seismicity is located in the area of the velocity changes at ≈10-12 km depth. It suggests that this area undergoes some changes in the crust rheological behaviour. The open question is: could this depth be the place of the initiation of large events (hypocentre depths) ?

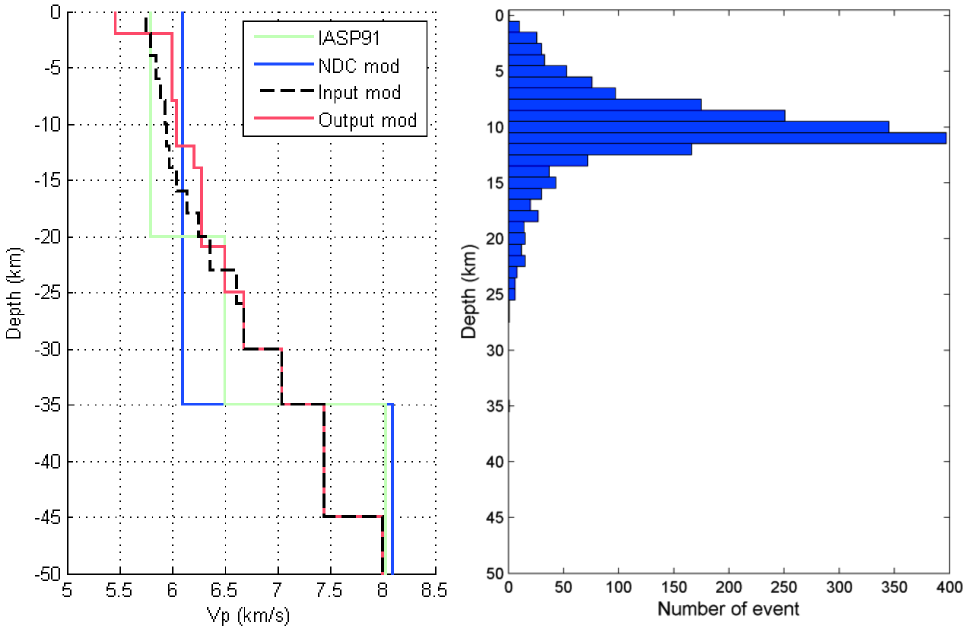

Figure 5.13. Left figure is 1D velocity model and right figure shows depths histogram of seismicity after tomoDD relocation.

In the obtained 3D WAM velocity model, we observe high and low velocities contrasts in the NW part of the MEFZ. Figure 5.14 (A) shows a horizontal cross section of P velocity at 12.5 km depth. From 9 km depth, we start to observe high velocity (7.5 km/s) to the N of EEB and low velocity of about 5.5 km/s to the NW of MEB. This pattern continues until the depth of 17 km of the 3D WAM velocity model with 8 and 5.9 km/s, respectively, for high and low velocities.

Low velocities to the NW of MEB are always observed (C of Figure 5.14). The highest velocities are surrounding the seismicity of the Emeelt fault area and they start at depths of about 9 km. At shallower depths, the velocity is more homogeneous without clear and particular anomalies. The high velocity "raise" to the south of MEB is a local anomaly that is not observed to its south for at least 45 km (Figure 5.15). Another general observation is that we observe high lower-crust velocities (more than 7 km/s) starting from 23 km and deeper (Figure 5.14-15). Notice a low velocity (~5 km/s) observed just above this high velocity zone between 2 and 6 km.

5.3.2 Velocity ratio and fluids

Another interesting observation are the variations of the velocity ratio Vp/Vs with values locally very different from the "average" 1.7 (Figure 5.14B). In fact, Vs is quite stable over the area and thus most of the high (2 and more) or low (1.4 and less) Vp/Vs ratios are related to high and low Vp, respectively (Figure 5.14B and Figure 5.14C). These contrasts are observed only in the area of the observed seismic swarms of the MEB, WEB and EEB. One explanation of low Vp velocity and low Vp/Vs is the presence of regions of water-filled pores (Nugraha et al., 2013). When the seismic activity is located in area with high Vp/Vs, it is considered that the seismicity is mainly controlled by fluid overpressures (e.g., Lindenfeld et al., 2012; Muksin et al., 2013; Leclere et al., 2013).

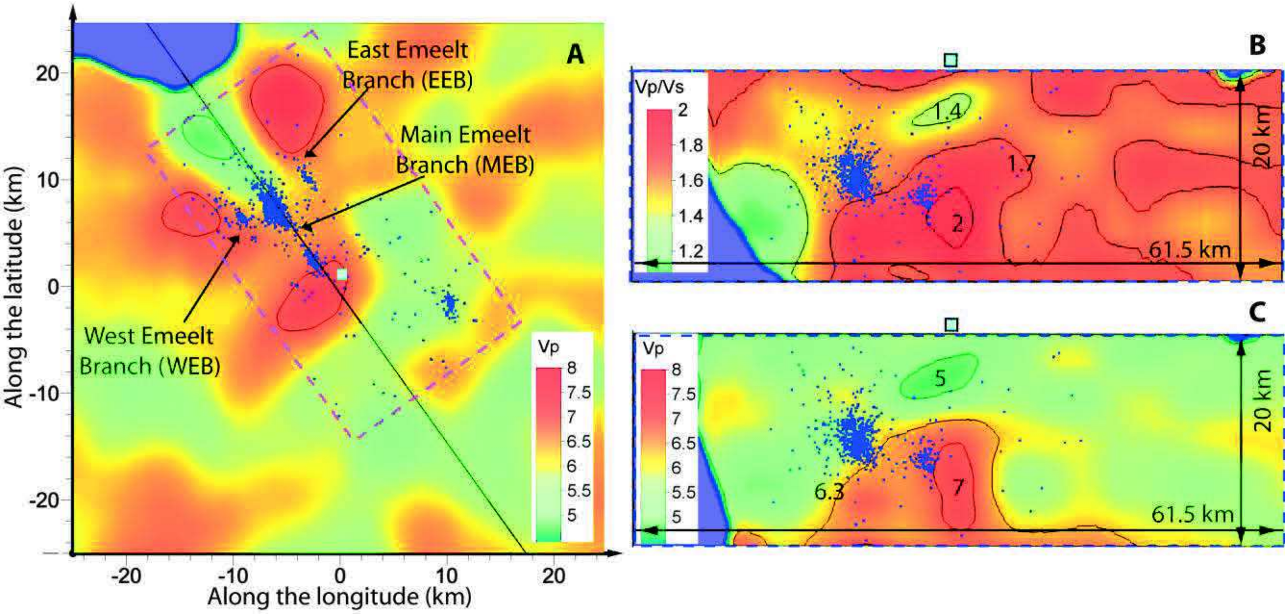

Figure 5.14. A) Horizontal cross section of **Vp velocity** at depth 12.5km, B) Vertical cross section of **Vp/Vs ratio** along line shown in A and C) Vertical cross section of **Vp velocity** along line shown in A (from NW to SE). Aqua square is trench site. Magenta dashed line is limit of TEFZ (only for seismicity observed in TEFZ).

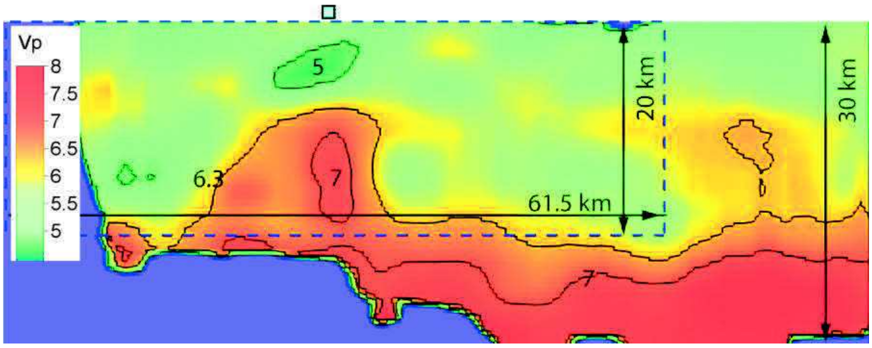

Figure 5.15. Vertical cross section of Vp velocity along line shown in Figure 5.14 A (extension to SE of Figure 5.14C). Color scale is the same as figure 5.14 C.

5.3.3 Are the anomalies related to geological structures ?

Generally, velocity models are consistent with local geology, that can simplified as older rock shows higher velocity than younger rock. The velocity distribution shows (Figure 5.14C) high and low velocity boundaries, that could characterize fault boundaries as observed in other places (Figure 5.16) (Pei et al., 2010; Jo and Hong, 2013). The 3D WAM velocity model of the Emeelt fault zone shows heterogeneous structures along and across the Emeelt fault zone. The highest anomalies are surrounding the area with the seismicity but they are also discontinuous, with 3 high Vp velocity zones raising from its normal depth, 20 km and deeper, to a depth of about 9 km (Figure 5.14A).

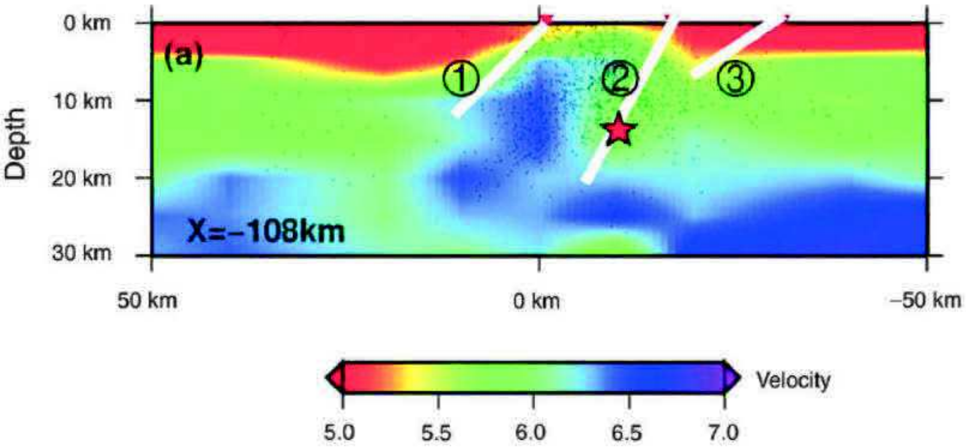

Figure 5.16. NW–SE cross-section slices for Vp across main shock (denoted as a red star) of magnitude Mw7.9 2008 Wenchuan earthquake. Events within 30 km of section are shown. White lines from left to right represent (1) Wenchuan–Maowen fault, (2) Yingxiu–Beichuan fault, and (3) Guanxian–Jiangyou fault, respectively. Star is approximate hypocenter location of Wenchuan earthquake (after Pei et al, 2010).

These anomalies appear to be organized in the direction of the Emeelt fault branches, N147° and more or less perpendicular (N60°), which is the direction of local Mesozoic structures (Figure 5.8). This suggests a direct relation between the contrasts in the 3D WAM velocity model and geological or crustal structure that are activated.

5.4 Evolution of the swarm activity

5.4.1 Space and time migration of swarms

10 swarms are identified in the Emeelt fault area between 2005 and 2014. In chapter 2, I explained how they were identified. Here, I discuss the evolution of these swarms in time and space. Table 5.2 shows some characteristics of the swarms.

Table 5.2. Number of relocated events in seismic swarms of the TEFZ.

Swarm ID	Start date	Continuous days	Number of events	
			By NDC total	By TomoDD relocated
Before swarm 1	2005.01.01	95	15	13
Swarm_1	**2005.04.06**	**5**	**29**	**26**
Between Swarm_1 and Swarm_2	2005.04.11	1753	426	203
Swarm_2	**2010.01.28**	**4**	**79**	**44**
Between Swarm_2 and Swarm_3	2010.02.01	34	19	13
Swarm_3	**2010.03.07**	**2**	**55**	**33**
Between Swarm_3 and Swarm_4	2010.03.09	163	56	36
Swarm_4	**2010.08.19**	**13**	**53**	**32**
Between Swarm_4 and Swarm_5	2010.09.01	846	91	51
Swarm_5	**2012.12.25**	**50**	**1091**	**426**
Between Swarm_5 and Swarm_6	2013.02.13	50	86	54
Swarm_6	**2013.04.04**	**7**	**78**	**42**
Between Swarm_6 and Swarm_7	2013.04.11	186	184	26
Swarm_7	**2013.10.14**	**29**	**544**	**143**
Between Swarm_7 and Swarm_8	2013.11.12	55	90	6
Swarm_8	**2014.01.06**	**9**	**79**	**17**
Between Swarm_8 and Swarm_9	2014.01.15	71	148	15
Swarm_9	**2014.03.27**	**3**	**118**	**36**
Between Swarm_9 and Swarm_10	2014.03.30	265	162	42
Swarm_10	**2014.12.20**	**4**	**32**	**9**
After swarm 10	2014.12.24	8	24	8

The chronology is summarized in Figures 5.17 and Table 5.2. The seismic activity was separated into particular swarms based on the time between two consecutive events and the density of events (upper right corner of Figure 5.17).

Figures 5.18-19-20 show the space and time distribution of events.

The first swarm is the "***column swarm***" near the airport (blue in Figures 5.1-4-6). It took place within few days after *1 April 2005* with about 26 events (relocated number, not total) and was reactivated only during one period *between 2005-04-06 and 2005-04-10* (Figures 5.17-20). Within a crisis the activity is widespread randomly along the column, something also observed late in 2005 (Figure 5.17).

Between the 1st and 2nd swarms, the three branches were activated, **MEB**, **WEB** and **EEB** (Figures 5.17-20). During 2006, the seismic activity remains at the same place as the 1st swarm and **MEB** become activated. During this period (see Appendix 4), between *2005-04-11* and *2010-01-27*, there is a continuous seismic activity along the Emeelt fault branches that was not identified as swarms because they were widespread over the whole period, without concentration of events.

The next three swarms took place in **WEB**, **MEB** and **EEB**, during Swarm_2, Swarm_3 and Swarm_4. These swarms were much more important and activated chronologically the **West Emeelt Branch (WEB)** then **the Main Emeelt Branch (MEB)** and **the East Emeelt Branch (EEB)** (yellow, green and blue on Figures 5.18-20). Regarding the depth distribution, these seismic activities were concentrated between 5 and 15km and became deeper from WEB to the EEB (Figure 5.20). These swarms took place during 7 months of 2010.

The last six swarms activated **mainly the MEB** (Figures 5.18-19). These swarms (from 2012.12 to 2014.12) produced **half of the seismicity recorded since 2005**. The swarm of *2012-12-25* to *2013-02-12* include 426 events that could be relocated with TomoDD (Figure 5.17 - Figure 5.19 and Table 5.2).

The depths of events in the swarm near the airport, active in 2005, were restrained over a range of about 7km (between ≈ 3 to 10km depth). On the MEB, the depth was first restrained in 2010 over 5km (between 7 and 12 km depth), then at the end of 2012 during the swarm_5 it was active over a very large range, about 20km, from the subsurface until 20km depth. From swarm_7 to swarm_10, that all occurred on MEBF, the depth range decreases swarm after swarm from 10km (from ≈7 to 17km deep) to about 5km (from ≈8 to 13km deep). **This shows that the Emeelt fault branches, at least the MEB, are crustal structures that extend down to 20 km at minimum.**

During the 5th swarm, the length of the MEB activated was the longest as well as the depth, from the subsurface until 20 km.

The Emeelt fault branches were activated also between swarms (see epicentres shown in grey colour in Figure 5.17). In the cross-sections parallel and perpendicular to the fault, the seismicity is located at different places year by year. It means that the whole fault area was activated between the swarms.

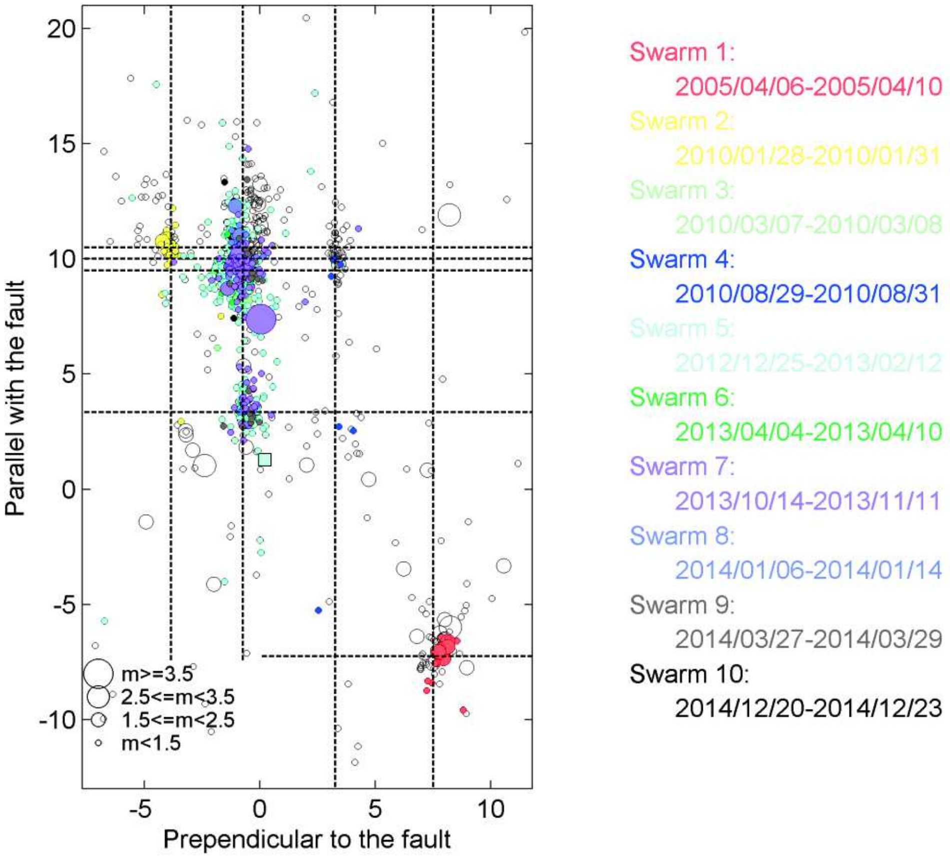

Figure 5.17. Epicenter distribution in map view rotated along orientation of fault (N146^0= vertical) of relocated events of Emeelt fault zone (2005 to 2014). Colour indicates swarms and grey colour empty circles indicate events that occurred between swarms.

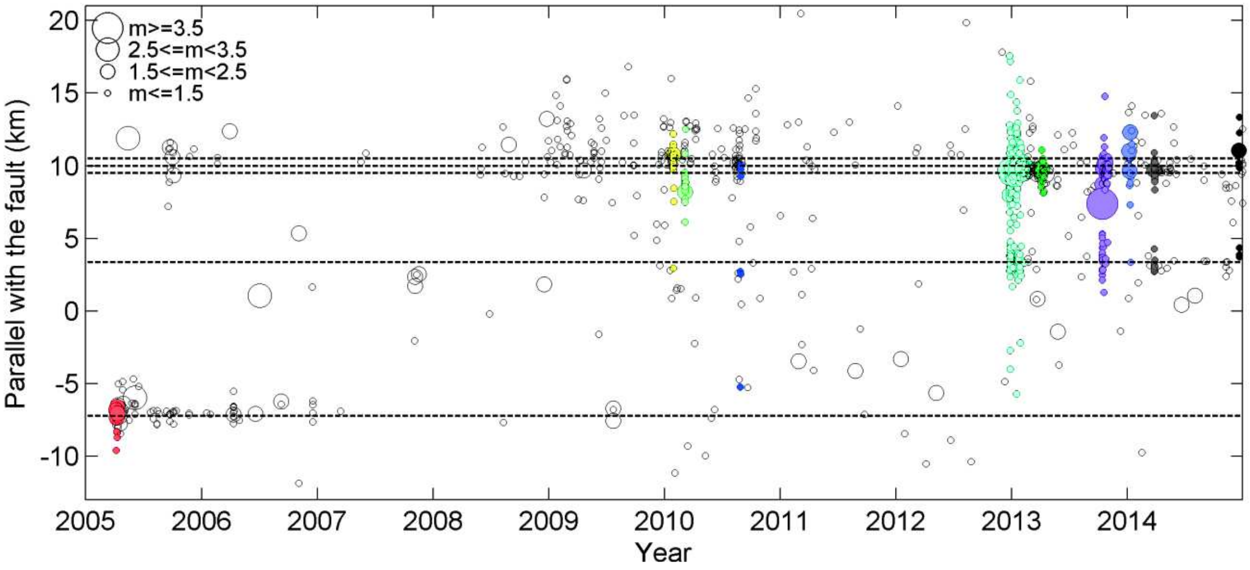

Figure 5.18. Space-time diagrams projected along fault orientation. Corresponding epicenter distribution map and colour indication similar as Figure 5.17.

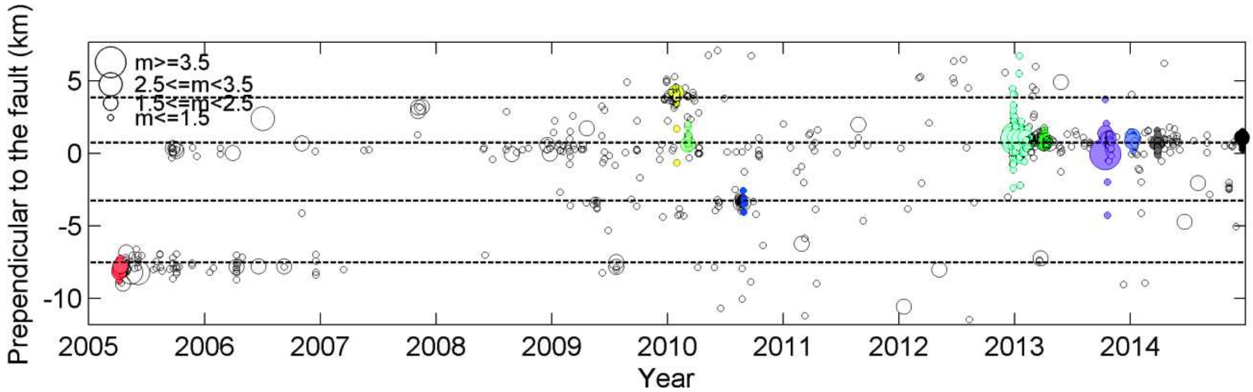

Figure 5.19. Space-time diagram prependiculiar to fault. Corresponding epicenter distribution map and colour indication similar as Figure 5.17.

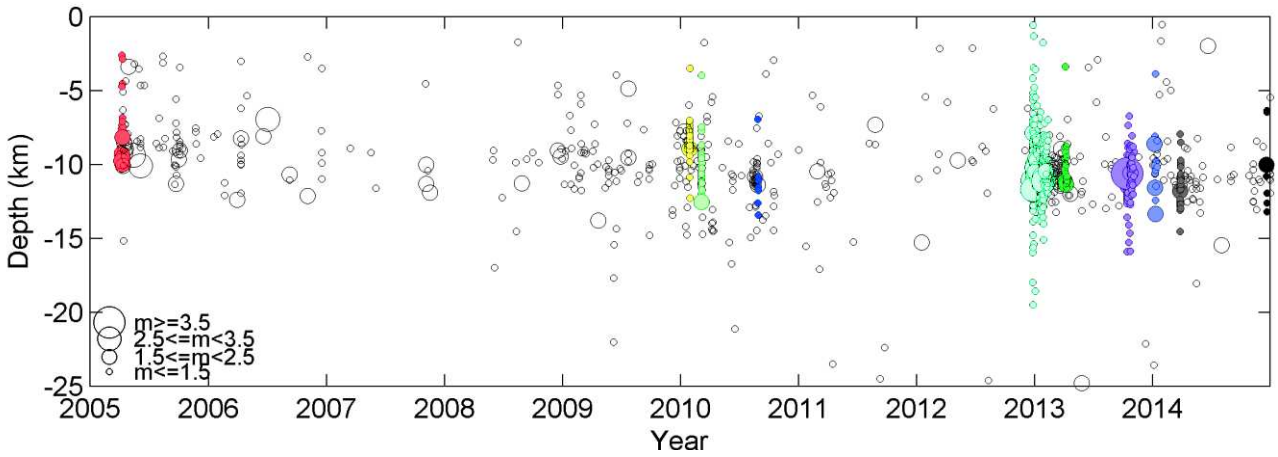

Figure 5.20. Space-time diagram by depth. Corresponding epicenter distribution map and colour indication similar as Figure 5.17.

5.4.2 Decrease of time between two consecutive events

Before the seismic activity started in the Emeelt area (before 2005) the delay time between two events was most of the time larger than 1 day (0.86x10^5 seconds) with very few delay of less than 1 hour (Figure 5.21). At the beginning of the swarm, this delay decreases until about 1 minute. During each crisis, the minimum delay decreases to 4 seconds, like for example during the 2014 crisis. Another observation is that the maximum delay between two consecutive events also decreases, from about 10 days (8.6x10^5 seconds) in 1995 down to about one day in 2005 and only about 12 hours in 2014. This shows that the seismic activity increases regularly over the whole period.

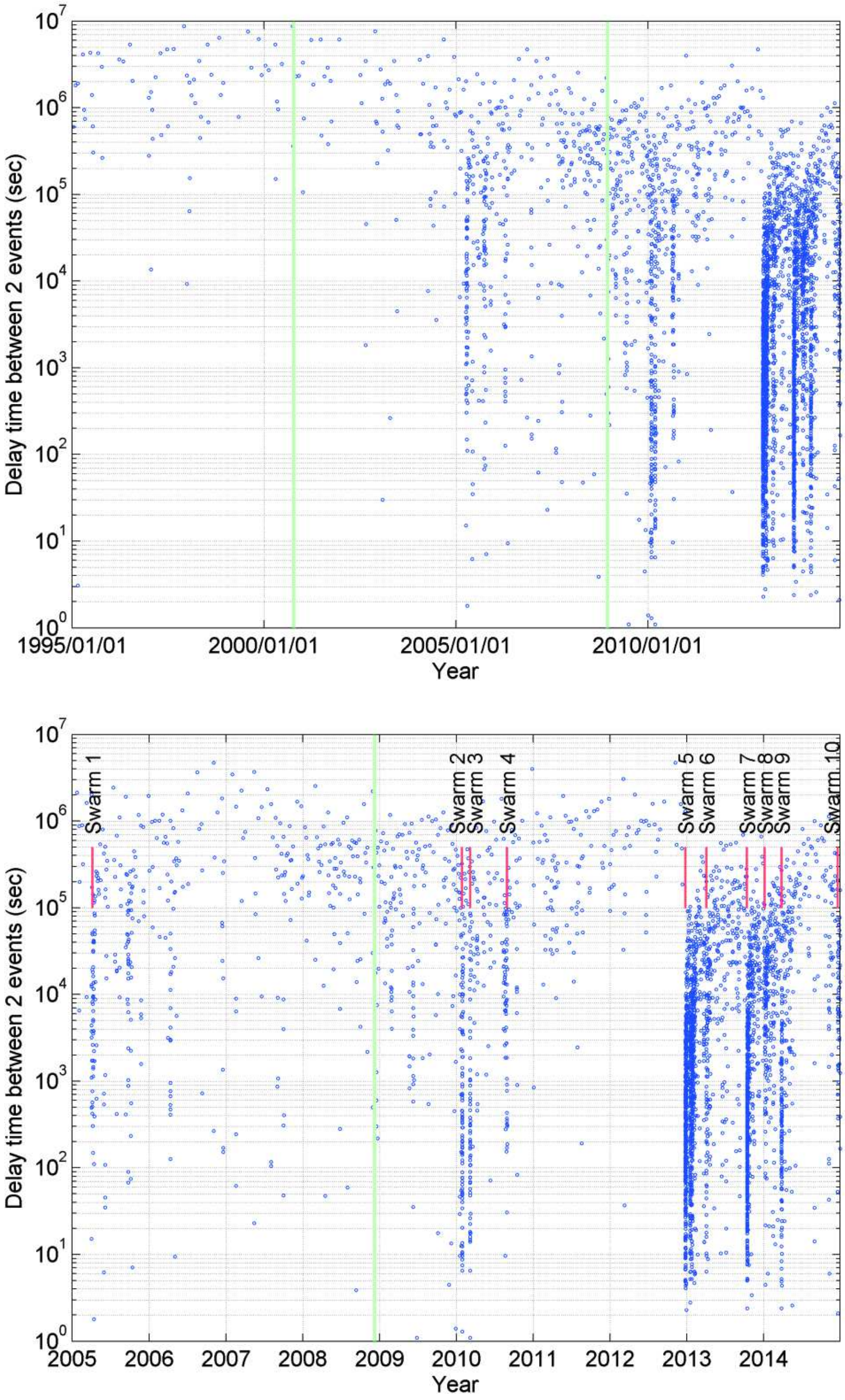

Figure 5.21. Delay time between two consecutive events (in seconds) in the Emeelt fault area of 60x60 km. Top figure is between 1995 and 2014 and bottom figure zoomed between 2005 and 2014. Green line is upgrade time of seismic network (Songino array in 2001 and UB-mobile in 2008). Red line is starting date of swarm (bottom figure).

5.4.3 Relation between swarms and Radon anomalies: observations and perspectives

Nowadays, one of the main studies for the earthquake prediction is based on radon study. Scientists already observed radon anomalies in seismic active areas especially before and after seismic swarms and activation time. For example, before the L'Aquila earthquake in Italy (Mw6.3, 2009) they observed radon anomalies before the seismic swarm and the main shock (Plastino et al., 2010).

Several Radon stations have been installed in the area of the Emeelt surface ruptures since 2009 (Figures 1.34, 5.23 and 5.24) followed by a calibration period. Below, I present very preliminary and simple comparisons between the occurrence of the swarms and the radon records or anomalies.

If we compare the radon records on the three stations (top in Figure 5.22) and occurrence of the swarms (bottom in Figure 5.22) we observe that:

- Some radon anomalies are observed at EM-3 station during Swarm 7 and at the EM-2 and EM-3 stations during Swarm 9 (Figure 5.22)
- There is no anomaly during Swarm 8, which started at 2014.01.06 for 9 days.

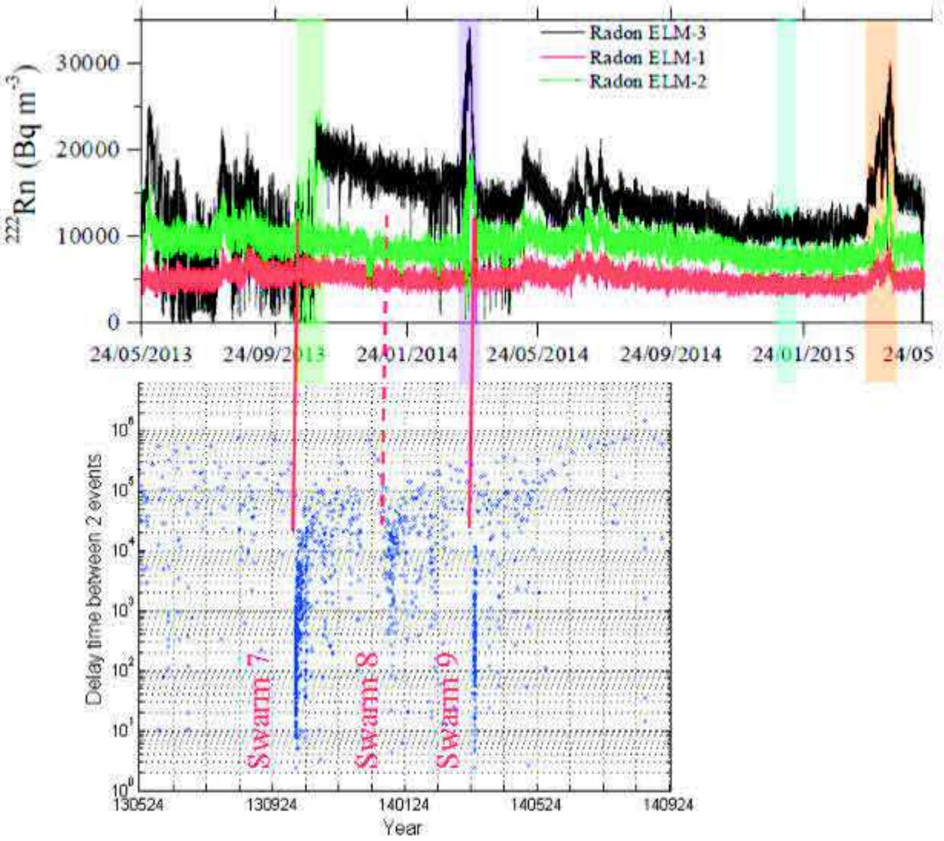

Figure 5.22. Top = Radon measurement versus time (after Richon et al., 2015). Bottom figure is delay time between two events that occurred in the Emeelt fault area of 60x60km between 2013.05.24-2014.09.24.

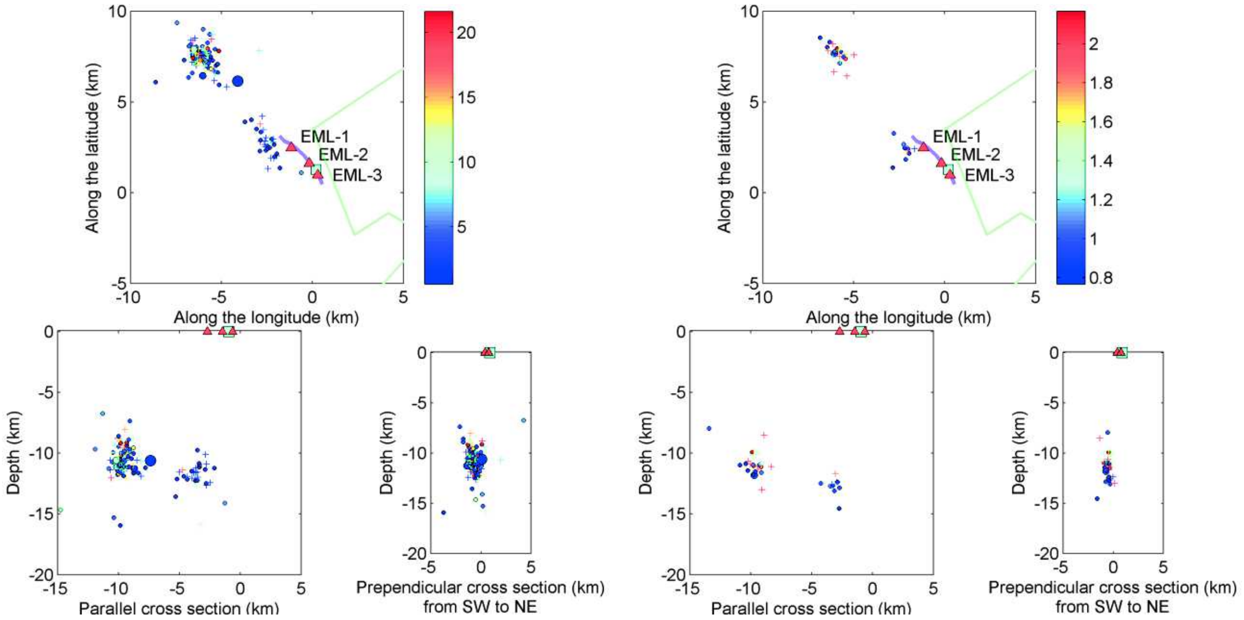

Figure 5.23. Location of Swarm 7 (Colour bar = days since 2013.10.14) and 9 (Colour bar = days since 2014.03.27). Top = epicentral view. Bottom left = cross section along fault (NW to SE). Bottom right = cross section perpendicular to fault (SW to NE). Aqua square = trench site and purple line is observed surface rupture of Emeelt fault, red triangles are locations of radon stations and green line is urban area of Ulaanbaatar city.

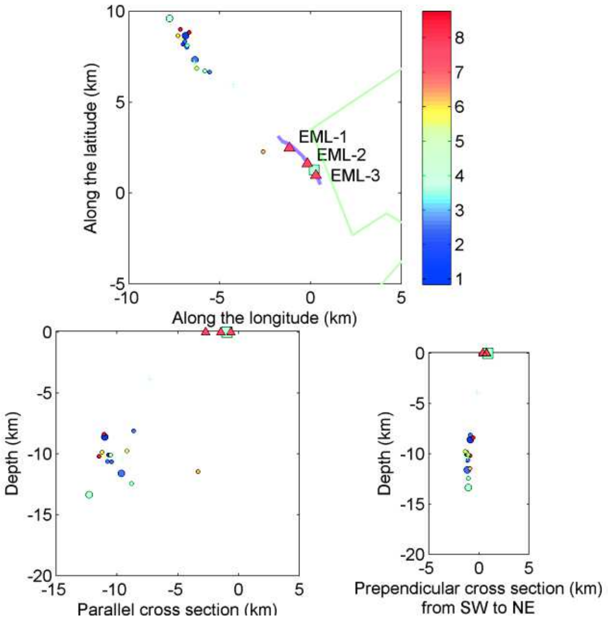

Figure 5.24. Location of Swarm 8. Colour bar = days since 2014.01.06. Top = epicentral view. Bottom left = cross section along fault (NW to SE). Bottom right = cross section perpendicular to fault (SW to NE). Aqua square = trench site and purple line is observed surface rupture of Emeelt fault, red triangles are locations of radon stations and green line is urban area of Ulaanbaatar city.

If we compare the radon records on the three stations and the locations of the swarms (Figures 5.23-24), we observe that:

- The south part of MEB was activated during Swarm_7 and Swarm_9 where we observed surface rupture. These two swarms are at less than 7 km (epicentral distance) from the radon stations. Nevertheless, the signal at the southern radon station is always the strongest (ELM-3).

- Swarm_8 is at to the north of MEB. This activity is about 7 km (epicentral distance) more to the north in comparison with swarm_7 and swarm_9, its distance to the radon station is larger, which could be an explanation of the absence of signal.

The analysis of the occurrence of well localized events and the radon observations is promising but it seems with a first very simple analysis that the distance between the radon station to the seismic activity must be short (less than 10km ?).

The timing between radon anomalies and radon signal varies on a case by case basis. For instance, Swarm_7 occurred before the radon anomaly (characterized by a jump in the radon level of the southern station) and Swarm_9 occurred after the anomaly (characterized by a clear peak on each station).

5.5 Comparison with swarms before the Mw=6.3 L'Aquila earthquake : possible evolution towards a large event ?

A seismic swarm is defined as a sequence of earthquakes clustered in time and space without a mainshock (Mogi, 1963). Swarms are commonly observed in a diverse range of geological settings including volcanic regions (e.g., Waite and Smith, 2002), geothermal areas, and plate boundaries and active fault zones (e.g., Jenatton et al., 2007; Courboulex et al., 2003; Fisher et al., 2014). Waite and Smith (2002) relates the occurrence of swarms to the presence of fluids in the upper crust (5 to 20 km), because fluids tend to reduce the normal stress along pre-existing faults. The fluids thus modulate the strain energy release by favouring the occurrence of small to moderate seismic events that are characterized by a time and space migration. For the L'Aquila event, Papadopoulos et al. (2010) makes the observation of an increase of seismic rate (event/days) and a decrease of the b-value before the mainshock (Figure 5.25). Also, the b-value of the strong foreshock stage (last 10 days before the mainshock, 06 Apr 2009) was significantly lower than that of the aftershocks sequence.

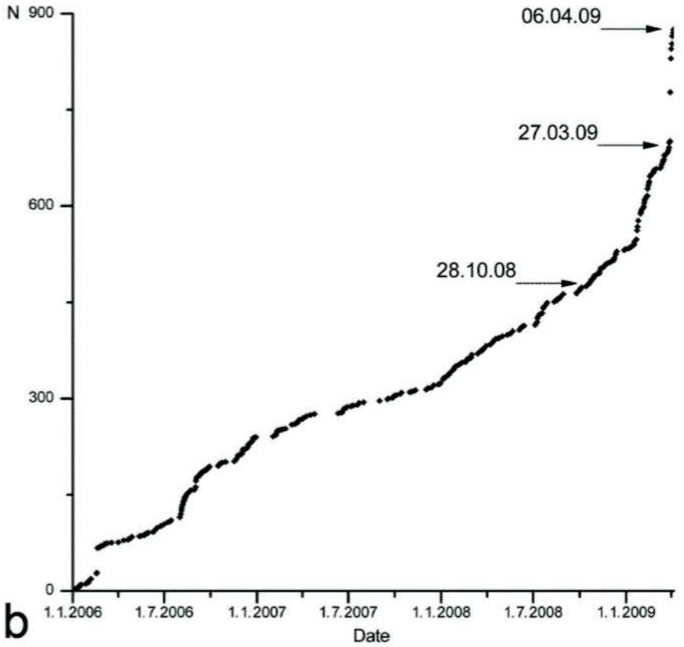

Figure 5.25. Cumulative number of earthquakes of magnitude more than 1.3 as a function of time during the L'Aquilla 2009 sequence. Earthquakes occurring within a 30 km radius target area around mainshock epicenter of 6 April 2009 at L'Aquila (after Papadopoulos et al., 2010).

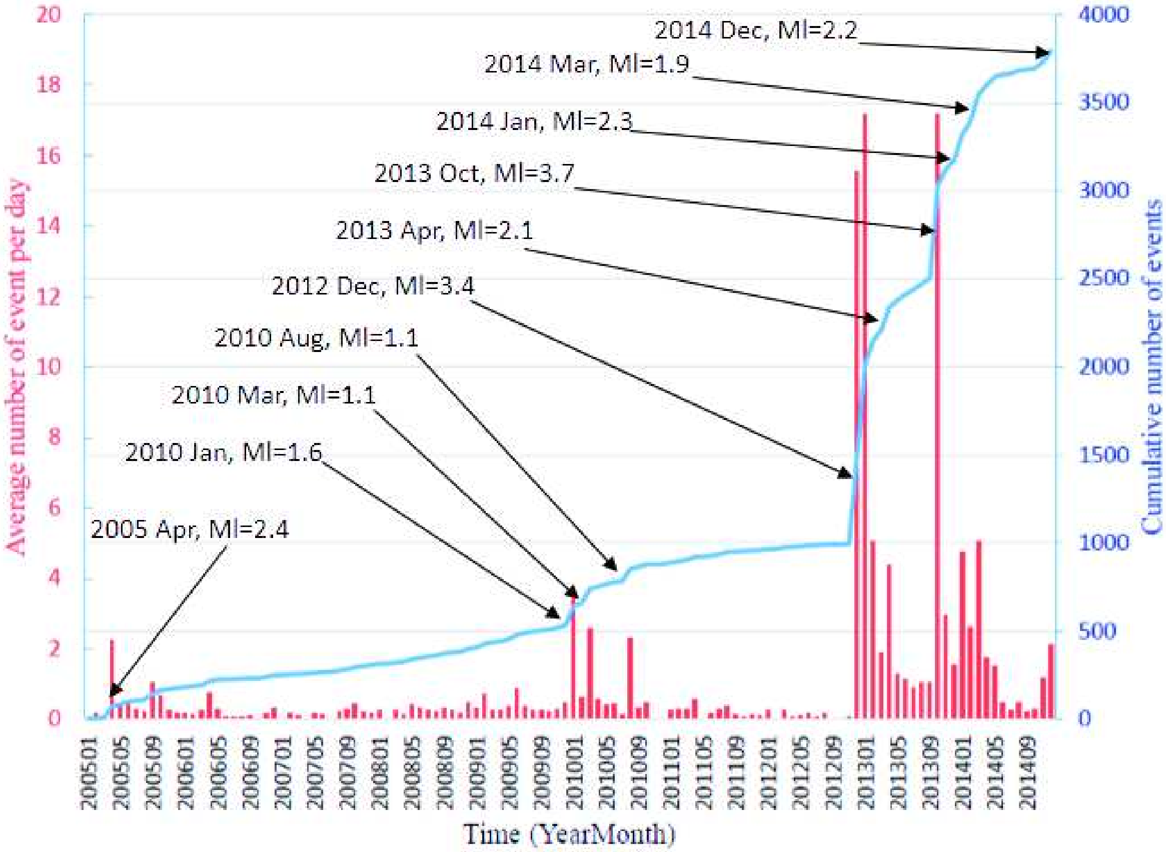

Figure 5.26. Cumulative number of seismic events and average number of event per day during specific months in Emeelt fault area of 60x60km for 2005 and 2014. Biggest event of each swarm noted.

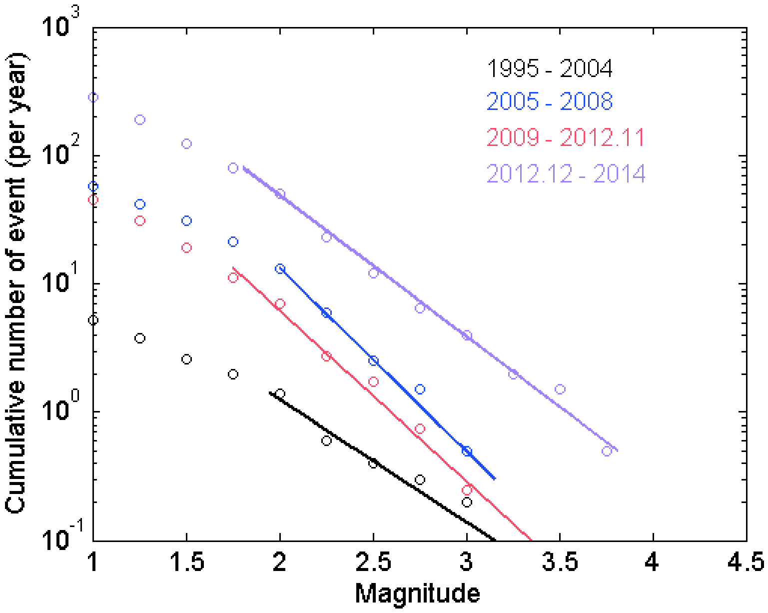

Figure 5.27. Frequency-magnitude distributions (GR) of Emeelt area of 60x60 km centered on Emeelt fault and for 4 time periods.

I represent 4 time periods based on seismic stations upgrade (2008) and swarms periods (2005, 2012.11) from 1995 until 2014 (see chapter 2.4, Figure 2.13 and here Figure 5.27). We observe that the rate of seismicity increases when the swarm activity starts (2005) from 1.7 to 3.9, and stays more or less stable after. For the seismic events more centered on the activity of the Emeelt fault zone, the "b" value moves from 0.8 to 1.4 with the first swarm activity, and then it decreases progressively until a value of 1.1 for the last period. It shows that, first, the number of small events increases more rapidly (2005-2008), then, it is the number of "large" events that is increasing more rapidly. The relation between small and large events changes with time for the swarm activity.

If we compare our observations (Figure 5.26) with the Papadopoulos et al. (2010) analysis (Figure 5.25), we see many similarities. The rate of the seismicity increases over a duration of several years. Notice that they show 3 yrs when we observe that increase already over a period of 10 yrs. Papadopoulos et al. (2010) indicate that in their target area, the earthquake activity increases from October 2008 but the increase became drastic in the last 10 days before the mainshock occurrence. Then they put forward three periods: a period A, before the activity started, from 1 January 2006 up to the end of October 2008 with seismicity level close to background ; a period B from end of October 2008 to 26 March 2009 when the seismicity enters a state of weak foreshock sequence ; and period C of the last 10 days before the mainshock (27 March to 6 April 2009) with a strong foreshock activity.

We plotted the largest events of the swarm periods (Figure 5.26) and we can see that the first change occurs in 2010 with very low magnitudes (M_L =1.1 to 1.6) but the big Swarm_5 of end of 2012 was associated with an event of M_L=3.4 that occurred inside the swarm when the M_L=3.7 event of October 2013 occurred in the second day of the swarm. Therefore, if it is possible to consider the Swarm_5 of 2010, or part of it, as an aftershocks sequence of the M_L=3.4, it is not the case for the 2013 one.

It is clearly difficult to compare between the observed swarms in the Emeelt area and those of L'Aquila. In our case, we already observed the first (A) and second period (B) described by Papadopoulos et al. (2010) We do not know how far we are in the second period but up to now (July 2016) the third period (C) has not started. We still do not know if the Emeelt seismic activity observations are signs of a large event preparation in a short time (days, months or few years) but we know that the Emeelt fault was in the past the place of a large event, between magnitude 6 to 7 (Dujardin et al. 2014) and that it may occur again in the future.

5.6 Impact on the seismic hazard assessment for Ulaanbaatar

5.6.1 Attenuation law used for the region of Ulaanbaatar.

There are two basic approaches for estimating ground motions that are commonly used in practice : deterministic and probabilistic. The selection of either the probabilistic or the deterministic approaches remains controversial. In the deterministic approach individual earthquake scenarios and specified ground motion are selected. In the case of the probabilistic method all the possible earthquake scenarios as well as all the possible ground motion probability levels are considered and the probability that any of the scenarios with ground motion greater than the specific test value is computed. Then a level of ground motion, based on its probability is chosen. Many times, it is considered the level for which the probability of exceedance is 10% for the next 50 years, many time called "475 yrs return period". In this work, I apply the Deterministic seismic hazard assessments approach to discuss the direct impact of the Emeelt fault earthquakes on Ulaanbaatar, including site effects of the area. I will not discuss the way the site effects are calculated as they are included in the procedure developed at IAG and it is not the core of my study. I will use the expertise of my institute, the IAG, for that (Chimed et al., 2014).

To calculate ground motion parameters, like the PGA (Peak Ground Acceleration) that I will use here, induced by a specific earthquake at a given site, knowledge of the attenuation of the PGA with distance is necessary. To be able to define the attenuation of PGA, accelerometric recordings of earthquakes for various distances and various magnitudes are neede, as attenuation relationships are empirically based equations. The predicted ground motion parameters are functions of magnitude, distance, site conditions and other predictor variables, e.g. the type of faulting and the dimensions of the faulting. Moreover, because seismic hazard mainly depends on the potential events at a distance less than 200 km, the attenuation of PGA for short distances is an important parameter. But the observations at most places in the world still suffer of a lack of events at short distances (less than 50 km and even worse at less than 10km).

This calculation has been done with Chimed Odonbaatar who is responsible of the hazard team at the Department of Seismology of the IAG.

In Mongolia, the attenuation of peak ground accelerations is not precisely known today as we still did not collect yet adequate acceleration data to build PGA attenuation, mainly due to lack of records of large events (M>5) at short distances.

According to the research project of the Seismic Hazard Analysis of the capital Ulaanbaatar (Chimed at al., 2014), we compared all acceleration data of ULN stations (starting in 1994) with the most recent published 17 different attenuation functions of International PGA laws, such as listed in 1st column of Table 5.3. We used events with magnitudes of more than 3.5 that occurred in Mongolia since 1994 (Figure 5.28 example for a magnitude 3.8).

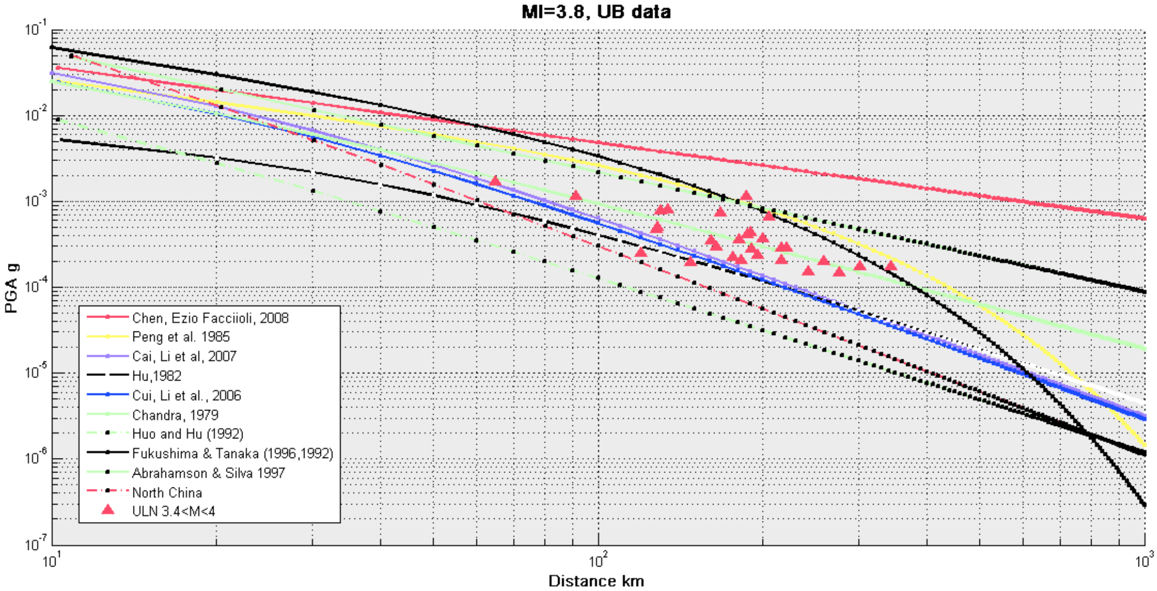

Figure 5.28. Peak Ground Acceleration calculated by different attenuation functions.

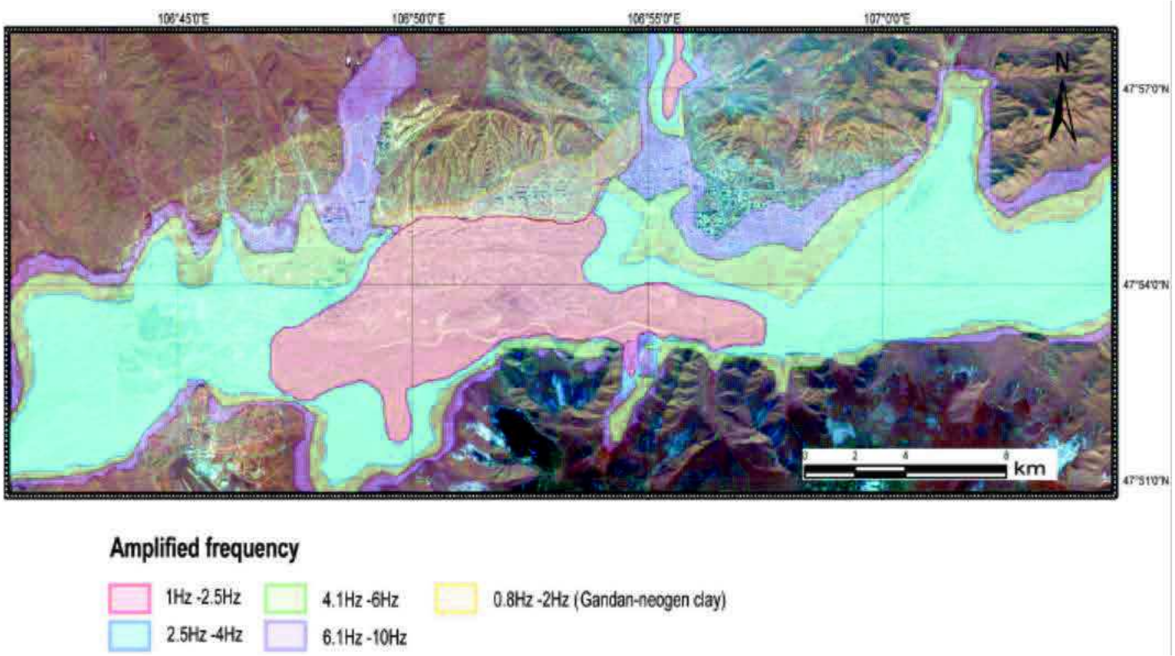

Figure 5.29. Amplified frequency zoning map for Ulaanbaatar basin (after Chimed, 2011).

At the end we selected Chandra (1979) attenuation law, which has the lowest RMS when we compare it to our data (Table 5.3) at the ULN station near Ulaanbaatar (Chimed at al., 2014).

Table 5.3. Root mean square of attenuation laws (after Chimed et al., 2014)

Attenuation law	Root Mean Square			
	Ml=3.8	Ml=4.2	Ml=4.8	Ml=5.8
Chen,Ezio Faccioli, 2008	0.00271478	0.0024482	0.00034459	0.00039497
Peng et al., 1985	0.00095713	0.00093085	0.00027439	0.00032497
Cai Li et al., 2007	0.00029677	0.00176143	0.00015007	0.00056371
Hu, 1982	0.00037418	0.00195532	0.00012532	0.00040705
Cui Li et al., 2006	0.00031944	0.00181517	0.00014574	0.00052949
Chandra 1979	0.0002246	0.00147361	0.00009054	0.00020712
Huo and Hu 1992	0.00050828	0.00222739	0.00017172	0.00050447
Fukushima et al., 2003	0.0013048	0.00143886	0.00022855	0.00049401
Abrahamson &Silva, 1997	0.00081263	0.00096269	0.00050869	0.00291976
North China	0.00042144	0.00189079	0.00014409	0.00045526
Ambraseys et al.,1996	0.00054387	0.00236648	0.00025578	0.00062418
Boore et al., 1997	0.00032543	0.00150841	0.00025742	0.00084713
Nishimura & Horike, 2003	0.00054956	0.00238103	0.00025955	0.00062311
Rinalds et al., 1998	0.00107677	0.00093237	0.00067289	0.00022482
Si and Midorikawa, 1999	0.0543355	0.07103147	0.0218096	0.0084896
Spudich et al., 1999	0.09735078	0.16206637	0.07181229	0.1491669
Takahashi et al., 2000	0.00057567	0.00242212	0.0002732	0.00062658

Therefore, I used Chandra et al.'s (1979) attenuation function to calculate the PGA at Ulaanbaatar for earthquake scenarios on the Emeelt fault. For the calculation, I also included site effects at Ulaanbaatar (Figure 5.29) that were and are studied in details by Chimed (2011) and IAG team under coordination of Chimed.

Constraining the maximum magnitude estimation associated to a fault is important for seismic hazard assessment. In section 5.1.2, I considered three scenarios and associated magnitude based on fault length and Wells and Coppersmith (1994) relation. The minimum is 5.7 using the surface ruptures only. The two others use the extension of the seismicity observed. We then get a magnitude 6.4 the extension along the main three branches are used and magnitude 6.7 if the seismic activity near the airport is included. Moreover, if we consider the right-lateral offset observed along the surface ruptures (2m, Dujardin et al., 2014) and if we consider it has been built by one or two events, then a magnitude of about 7 is possible. This would imply a length of the active fault of about 40 ±5km, 10 to 15 km longer that what we observed yet in the area. In comparison, the 1967 Mogod earthquake, in Mongolia (at about 250 km) produced about 45 km of surface rupture and was associated to a magnitude Mw=7.1 (Bayasgalan and Jackson, 1999). While this hypothesis is probably in the uppermost range of magnitude, we will consider it.

At the end, I chose the magnitudes 6.4 and 7 as the two important scenarios for the area.

This study consists of two parts:

- Validation of the method by comparison of observed intensity and calculated one for an event with magnitude 3.7, the biggest that occurred on the Emeelt fault the 2013.10.14.
- Calculation of PGA with magnitudes of 6.4 and 7 for the Ulaanbaatar area including site effects.

5.6.2 Observed intensities at Ulaanbaatar during the M_L=3.7 Emeelt earthquake of 14/10/2013

The 14th October 2013, an earthquake with a magnitude of 3.7 (M_L) depth of 12 km in the Emeelt fault area. This event was felt by residents of Ulaanbaatar and the Intensities MKS-64 were estimated up to V (largely felt, no damage) (see Appendix 7 and 5th column in Table 5.4). The aim here is to calculate the PGA at the same place than where an Intensity was estimated. To compare them, we have also to convert the PGA into Intensity.

For the calculation of PGA, the attenuation laws use the Ms magnitude scale and we are using M_L at IAG. Therefore, to convert M_L into Ms, I used first a relation between M_L (local magnitude) and Ms (surface magnitude), which was determined during the study of the "Seismic hazard assessment of Ulaanbaatar, capital of Mongolia" by IAG (see Appendix 6).

Then I calculated the PGA, using Chandra (1979) attenuation law at the same point where intensity is estimated during 14 October 2013 event (see the 3rd column in Table 5.4).

Also, using the observed magnitude of the 2013 event, I calculated the intensity directly from the observed local magnitude (M_L) using the relation proposed by Souriau (2006) (see the 6th column in Table 5.4).

We can compare the PGA and the Intensity if we have a conversion between these two parameters of the ground shaking. I took the following relation between PGA and Intensity, which is used by the 2012 Russian Building code (see the 7th column in Table 5.4).

$$Log\ A = 0.301 * I_{msk64} - 0.107 \qquad (1)$$

At the end, we can compare the Intensity observed, with the Intensity calculated (based on Souriau, 2006) and with the Intensity deduced from the PGA calculated using the law of Chandra (1979). The estimated intensities are summarized in Table 5.4 and in Figure 5.30.

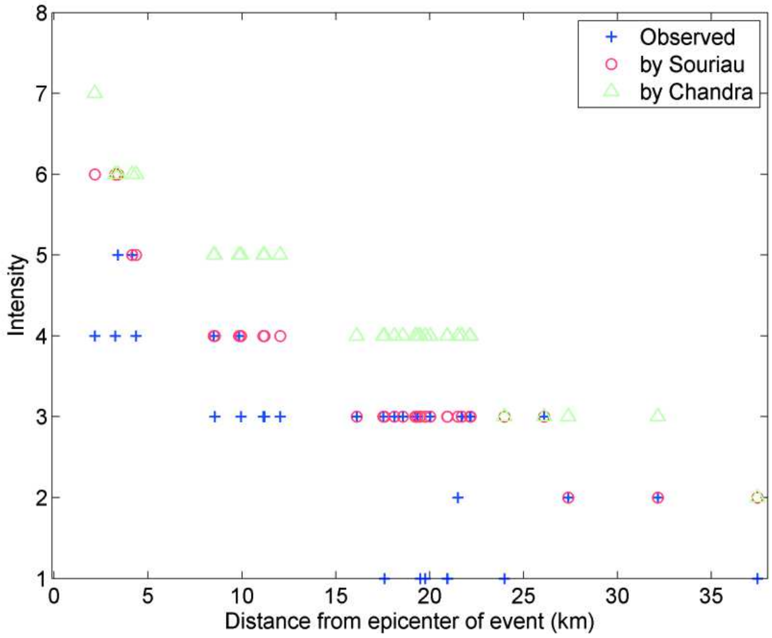

Figure 5.30. Observed and calculated intensity by Souriau (2006) and Chandra (1979) for an event of magnitude 3.7 versus distance.

The observed intensities are lower that the one deduced from Souriau (2006) and the one deduced from Chandra (1979) with the conversion of intensity. The observed Intensity are very near from the Intensity deduced from Souriau (2006) but they have been calculated at the rock based on M_L magnitude when the others, calculated by Chandra (1979) law, include site effects that could increase the intensity of one degree. There is only one site at 26.8 km at a site at the rock (see Table 5.4), where the value are the same (Intensity III) for the three intensities estimated (Observed Intensity, calculated from Souriau and calculated from Chandra).

Table 5.4. Calculated PGA and Intensity for magnitude of Emeelt event. The 1st column is ID of site where observed Intensity (see Appendix 7).

ID of site	Distance between epicenter and observed site (km)	PGA calculated by Chandra		Intensity			
				Observed	Calculated by Souriau	Calculated from PGA showen in column 3 and 4	
		M_L=3.7	Mw=6.4	M_L=3.7		M_L=3.7	Mw=6.4
1	2.16	82.00226	448.5630	4	6	7	9
2	3.25	66.00682	411.3686	4	6	6	9
3	3.39	64.31343	406.9460	5	6	6	9
4	**4.15**	**56.21257**	**384.1976**	**5**	**5**	**6**	**9**
5	**4.35**	**54.34721**	**378.5443**	**4**	**5**	**6**	**9**
6	8.49	30.38104	285.7325	3-4	4	5	9
7	**8.56**	**30.12915**	**284.4830**	**3**	**4**	**5**	**9**
8	9.85	26.01971	262.9189	3-4	4	5	8
9	9.94	25.76649	261.5115	3	4	5	8
10	11.13	22.75376	243.9684	3	4	5	8
11	11.19	22.61678	243.1335	3	4	5	8
12	12.03	20.82823	231.9031	3	4	5	8
13	16.11	14.64576	187.4387	3	3	4	8
14	17.52	13.16357	175.1431	3	3	4	8
15	17.58	13.10582	174.6484	1*[4]	3	4	8
16	**18.13**	**12.59456**	**170.2144**	**3**	**3**	**4**	**8**
17	18.57	12.20787	166.7939	3	3	4	8
18	19.75	11.25862	158.1383	1*	3	4	8
19	20.02	11.05779	156.2575	3	3	4	8
20	20.93	10.42097	150.1718	1*	3	4	8
21	20.95	10.40763	150.0423	1*	3	4	8
22	21.49	10.05739	146.6108	2	3	4	8
23	21.71	9.920021	145.2483	2-3	3	4	8
24	**22.17**	**9.642189**	**142.4631**	**2-3**	**3**	**4**	**8**
25	23.97	8.664944	132.3362	1*	3	3	7
26	26.08	7.705344	121.8443	2-3	3	3	7
27	27.37	7.198739	116.0623	2	2	3	7
28	37.45	4.566072	82.69717	1*	2	2	7

The Intensity deduced from PGA is compared with the observed Intensity (Figure 5.31). The observed intensity are very few in the area of Ulaanbaatar and that they are always below the calculated ones. The calculated PGA and Intensity converted from them take into account site effects.

---

[4] At this point people did not feel this event => associated intensity "1"

Notice that we have only one record of this event at the accelometric station ULN, at an epicentral distance of 37.5 km. The value is very low, 0.623 cm/s^2 , in a place where the observed intensity is "I" (not felt).

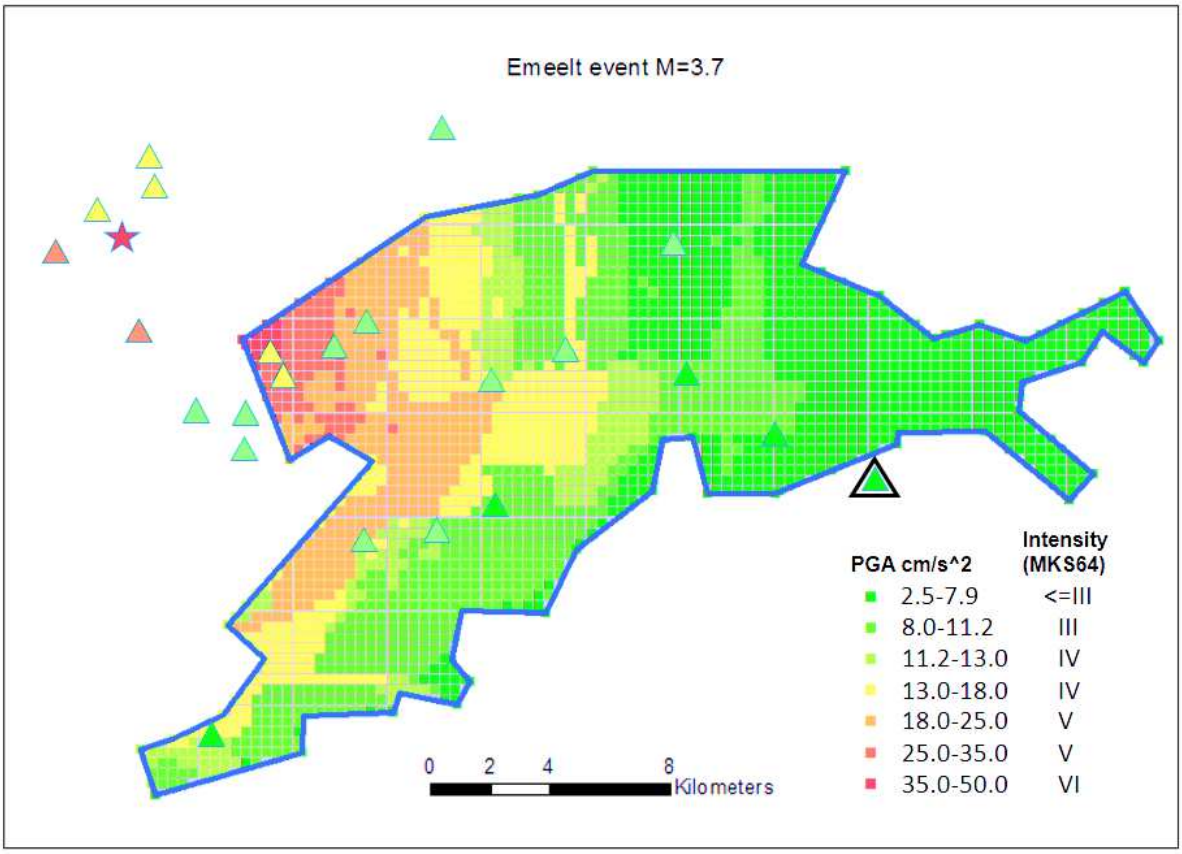

Figure 5.31. Observed intensity (coloured triangle) and calculated intensity (PGA converted into Intensity) of the event of magnitude M_L=3.7 at Emeelt. Red star is epicenter of this event. Black triangle to the SE is the location of ULN station.mpact of large earthquakes along the Emeelt Fault (scenarios with M=6.4 and M=7) on Ulaanbaatar.

In conclusion, with only these very few data, based on a small event, we can say that the intensity calculated using Chandra (1979) attenuation law in PGA and after a conversion into Intensity (by formula 1) seems to be the uppermost value that can be considered. Also an attenuation law is never well constrained at short epicentral distance all over the world. The values calculated at less than 10 km epicentral distance are not confirmed by the observation probably because of unconstrained Chandra law at short ditsance. But that conclusion should be considered as very preliminary for the Emeelt area.

5.6.3 Intensities assessment at Ulaanbaatar for two scenarios: M=6.4 and M=7

We will apply this methodology (Chandra and Intensity relations) to calculate the impact on Ulaanbaatar for the two scenarios considered.

The calculated scenarios for magnitudes 6.4 and 7 are shown in Figures 5.32 and 5.33, respectively. They are based on the PGA calculated using the Chandra (1979) attenuation low for sites at rock and sediment for the whole urban area of Ulaanbaatar. The PGA are converted in Intensity (MSK64) using the intensity formula. We see for the two scenarios that the PGA are increased in the area, with site effects, like in the central basin occupied by the Tuul riverbed and along the more or less NS oriented lateral valleys. Most of the south part of the city is built on sediments.

Scenario M=6.4: The PGA is about 0.41g-0.58g for the closest area of Ulaanbaatar (Figure 5.32). The whole area of the city would be shaken with an intensity of VI and up to IX for the nearest area to the fault. In addition, most of the urban area would be affected with an intensity of VIII minimum (light green and yellow in Figure 5.32). An intensity VIII would already produce partial collapses of weak buildings (high vulnerability) and even some damage, despite moderate, on strong building (low vulnerability). The places with intensity IX would have many collapses of weak buildings (high vulnerability) and even some partial collapses of stronger buildings (low vulnerability).

As an example, such magnitude (Mw=6.4) corresponds to the size of the earthquake (27/05/2006) which happened in Yogyakarta (Indonesia) and killed nearly 6000 people in an area of 200km^2 of maximum intensity of IX - X on the MSK scale. Note that a shallow hypocentre was a possible reason for the widespread structural damage in the affected area (Potter et al., 2015).

Scenario M=7: The result is shown in Figure 5.33. The western part of the city would be shaken with an intensity of X that would induce many collapses on "strong" buildings (low vulnerability). The important result in that case is the wide area associated with high intensity of X and the minimum intensity of the whole city is VIII. This means that such an event will induce at least partial collapses on weak buildings until the east part of the city, situated at about 30 km from the fault and that for most of the city with intensity of IX and more, the impact would be many collapses of weak buildings (high vulnerability) and even some partial collapses on stronger buildings (low vulnerability).

The impact of such event, in the frame of ground shaking (PGA or Intensity MSK64) is important, and the impact on building according to their vulnerability is very important.

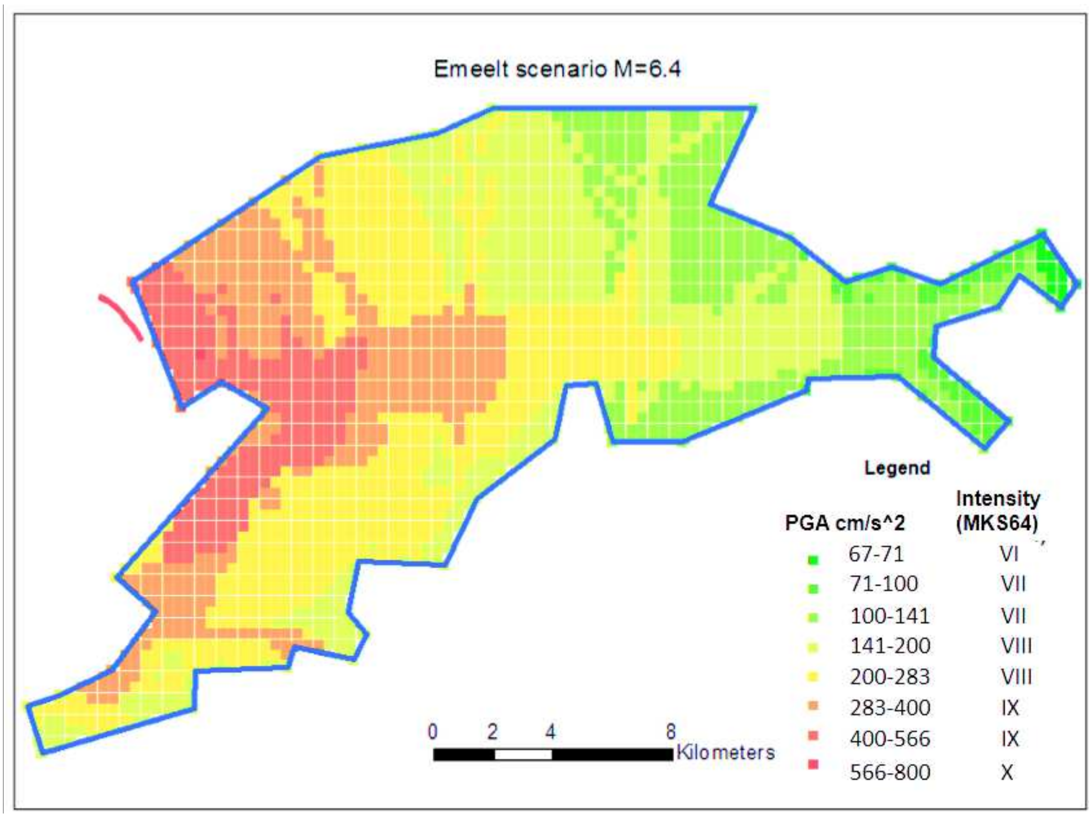

Figure 5.32. PGA calculated by the deterministic approach for Ulaanbaatar city area (M=6.4).

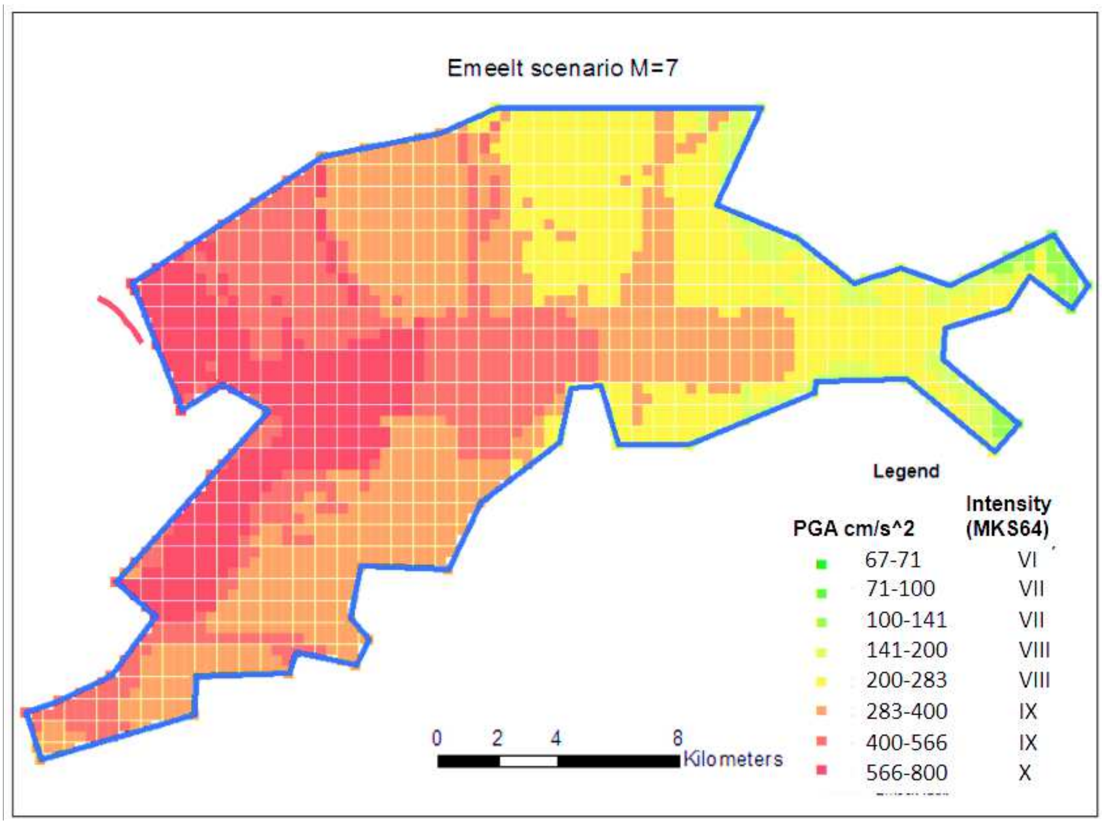

Figure 5.33. PGA calculated by the deterministic approach for Ulaanbaatar city area (M=7).

Based on estimated minimum magnitudes along the Emeelt fault, the whole city area could be affected with intensity MSK64 of VI and more. The western part of the city could even be affected by an intensity of X MSK-64. For the largest scenario, the impact is huge and would affect deeply the city, its infrastructures, the population and probably the whole country. The reason for that is the short distance between the fault and the city, the size of the fault that could induce at least a magnitude 6.4, and the site effects due to the basin fill on which is constructed a large part of the capital.

Even if we consider that the modelled intensities are overestimated by one degree (see observation with a small M=3.7 event at Emeelt), the city would be in the scenario of M=6.4 affected by an intensity up to VIII and IX, and for the largest scenario, M=7, with an intensity of IX for a large part of the city.

Despite larger active faults (Khustai, Sharkhai, Avdar) in the area are observed, they are farther and would all induce lower intensities or PGA in the city than the Emeelt fault. Nevertheless, the eastern extension of the Khustai fault could reach the city, if we consider the Mesozoic fault as its east prolongation and could then become the most "dangerous" structure for Ulaanbaatar. The Emeelt active fault appears to be, or one of, the most dangerous active fault for Ulaanbaatar.

5.7 Perspectives

The Emeelt fault area should be one of our most important target according to the impact on Ulaanbaatar if an important event occurs (M≥6). I will here under propose few perspectives dedicated to the study of the seismicity itself.

In the past, the structure of Emeelt fault area has not been studied in such detail.

Further study must be undertaken to obtain a more detailed knowledge of the crustal structure to resolve the northwestern part of this area and be able to get a precise view of the seismicity in that area. For that we need new seismic stations in that area, which are not available today unfortunately.

The near future work should be dedicated to relocate all possible events in the Emeelt area. In this study, I relocated just 1/3 of the events. During the picking time, I observed that there are many missed small events. To include all these numerous small events we should try to apply some other methods such as wave cross correlation methods to save time for that process and follow more rapidly the evolution of the seismic activity and better identify the migration of tectonic seismic swarms. The increasing number of precisely located events will help to precise the location of active faults and confirm or not the hypothesis we did for some EW active structures in the area.

The next step is to improve the velocity structure in and around the Emeelt fault area. For the time being we can not well constrain the northwestern area as well as the deep crust.

We observed also that the local geology and the tectonic structures of the area are not well known, as east prolongation of Khustai fault, Mezosoic structures (geological fault) and their possible reactivation. Complementary informations have to be collected on the field using detailed geological and geophysical investigations in the area.

In any case, the authorities have to take into account that Ulaanbaatar is surrounded by active faults, like Emeelt at short distance but even bigger ones but at larger distances from the capital (Avdar, Sharkhai, Khustai). The city has to be prepared for strong shaking and the new constructions need to take that hazard into account to mitigate the risk. Also, the emergency procedure should consider the possible occurrence of a destructive events in the region.

5.8 General conclusions

The Emeelt area, located very near the capital of Mongolia is the site of an important seismic activity since 2005, in a place where no active faults was known. At that time, the active faults near Ulaanbaatar were weakly known beside the Khustai fault. Since then, 2 new faults have been identified, the Sharkai and Avdar faults that can produce magnitude of about 7. Short surface ruptures have been observed along the N150 Emeelt fault in 2008. The study of the seismicity of the Emeelt area informs us about many new characteristics.

The seismic activity is regularly increasing. At the beginning of the swarm activity, the delay time between two events decreased until about 1 minute. After each crisis, the minimum delay decreases, down to 4 seconds for the 2014 crisis. The maximum delay also decreased from about 10 days in 1995 down to about one day in 2005 and only about half a day in 2014. The rate of seismicity increases with time but also the b value of the GR law varies. Similar changes have been observed in the years preceding the large L'Aquila earthquake in Italy (2009, Mw=6.3).

During 10 years after the beginning of the seismic activity in 2005, we recorded 3504 earthquakes located in the Emeelt fault zone (blue dashed line in Figure 5.1) but I could precisely relocated only 1968 events by tomoDD despite several mobile stations have been installed in the area. There are two reasons for this low amount of relocated events: 1) I excluded events that were located only by two permanent stations, which exclude many events; 2) after the hypoinverse procedure, I selected events with an RMS lower than 0.5 s and epicentre distance to station of less than 25 km. It shows the importance to improve the seismic network in the area of Ulaanbaatar, especially in the Emeelt area. From this selective datasets, we can analyse the time and space evolution of the activity but also the geometry of the fault and its relation with regional structures.

The relocated events (Figure 5.5) show the seismic activity of the Emeelt fault located mainly NW from the observed surface rupture in the field. The Emeelt fault zone includes at least three parallel branches of an active fault oriented N147. Regarding the depth distribution, these seismic activities were concentrate between 5 and 15km (Figure 5.20). On the cross section parallel to the fault (Figure 5.6), all the seismicity is in the same area, dipping more or less to the NW. It could be an indication of a structure perpendicular of the MEB direction dipping at about 60° to the NNW and cutting the three branches. A structure with this N60 orientation corresponds to a Mesozoic structure that is mapped south of the seismicity. On the cross section perpendicular to the fault (Figure 5.4) it appears that the three branches are not clearly connected based on the seismicity observed until 17km depth for the 3 branches. Only 3 to 4km separate them and it is possible that they are connected deeper. The depth distribution shows that the Emeelt fault branches oriented N147 are crustal structures that extend until 20 km depth at minimum, the clearest one being the MEB. The activated area seems to be located at the intersection with Mesozoic structure. Moreover, the velocity anomalies in the obtained 3D WAM velocity model appears to be organized in the direction of the Emeelt fault branches, N147° and more or less perpendicular (N60°) which is the direction of local Mesozoic structures. This suggests a direct relation between the contrast in 3D WAM velocity model and geological or crustal structure that are activated. Also, Vp/Vs contrast suggests the presence of fluids that could be located in the area of the seismic activity.

I identified 10 swarms between 2005 and 2014 oriented N147. The first swarm started near the airport (blue in Figures 5.1, 5.4 and 5.6). Between the 1st and 2nd swarms, three branches were activated, MEB (Main Emeelt Branch), WEB (West Emeelt Branch) and EEB (East Emeelt Branch) (Figures 5.17 and 5.19). After, during 2006, the seismic activity stays at the same place as the 1st swarm and the MEB becomes activated. During the next period of nearly 5 years, between 2005-04-11 and 2010-01-27, there is a continuous seismic activity along the Emeelt fault branches, but not qualified as swarms (see group1 of Appendix 4). The other swarms activated mainly the MEB (see Appendix 4). The swarms of 2010 were much more important and migrated chronologically from the WEB to the MEB and then to the EEB (yellow, green and blue in Figures 5.17-5.19). Swarm_5, at the end of 2012, was the largest with the deepest activity, down to 20km.

In the field clear ~4-5 km long surface ruptures associated to the Emeelt fault zone, located as the south end part of the seismic activity, are observed. If they break in one earthquake, they would produce a magnitude about 5.7. If we consider the 15 km length of the seismicity along the Main Emeelt Branch (MEB), it would produce an earthquake of magnitude about 6.4. If we include the seismic activity near the airport, the 25 km of rupture considered in that case could produce a magnitude 6.7 event. If we consider the 2m horizontal offset of a paleo-river as the co-seismic displacement during one or two earthquakes, the associated magnitude would be about 7. The fault length, in that case, may reach about 40-45km, a possibility that cannot be excluded as the extent of the observed seismicity may only show a part of the real fault extension.

We estimated the impact (ground shaking level) of events of magnitudes 6.4 and 7 on the city of Ulaanbaatar. For M=6.4, the whole area of the city would be shaken with an intensity of VI and up to IX for the nearest area to the fault and most of the urban area would be affected with an intensity of VIII minimum (Figure 5.29). For M=7 the western part of the city would be shaken with an intensity of X that would induce many collapses on "strong" buildings (low vulnerability). What is important in that case is also the very wide area associated with high intensity X and that the minimum intensity of the whole city would be VIII. Such event would have a huge impact and affect deeply the city, its infrastructures, the population and probably the whole country. The reason is the short distance between the fault and the city, the size of the fault that could induce at least a magnitude 6.4, and the site effects due to the basin on which is constructed a large part of the capital. Despite larger active faults in the area (Khustai, Sharkhai, Avdar) are observed, they are farther and induce all lower intensity or PGA in the city than the Emeelt fault. However, the eastern extension of the Khustai fault could reach the city, if we consider the Mesozoic fault as its eastern prolongation and it could then become the most "dangerous" structure for Ulaanbaatar.

6 Appendixes

6.1 Appendix 1: Seismicity of Mongolia (1900-2000)

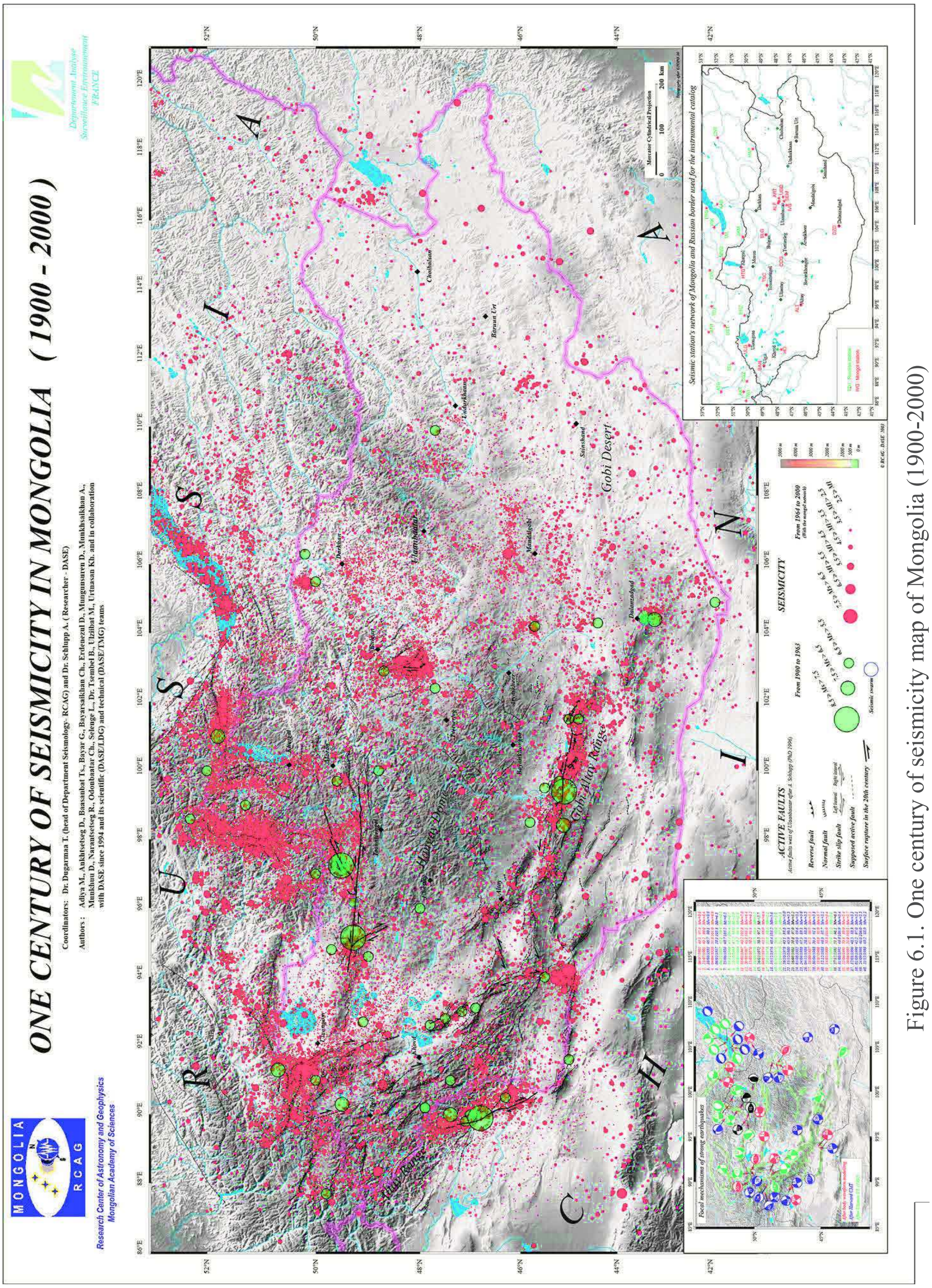

Figure 6.1. One century of seismicity map of Mongolia (1900-2000)

6.2 Appendix 2: Magnitude determination in NDC

From the beginning of the seismological observatory in Mongolia until end of 2000, we used a Russian magnitude scale to determine earthquake size. This magnitude determination is an energy scale (Kl=Log(E)) that derived from the estimation of the seismic energy released by the earthquake.

In 2001, we use a new seismic wave's attenuation relation with distance for the whole database, and obtained the first local magnitude (M_L) scale in Mongolia. This formula was defined by using the digital signals recorded since 1994. However, this formula could not be determined for epicentral distance to station of less than 100km therefore the magnitude of small earthquakes were not estimated. Then we developed a duration magnitude (Md) in 2007 based on M_L (Mungunsuren, 2007). The relationship between local and duration magnitude is M_L=1.05*Md-0.15 with 0.9 correlation (Figure 6.2).

I used this relationship to associate a M_L to all small events of my database if there were associated to an Md.

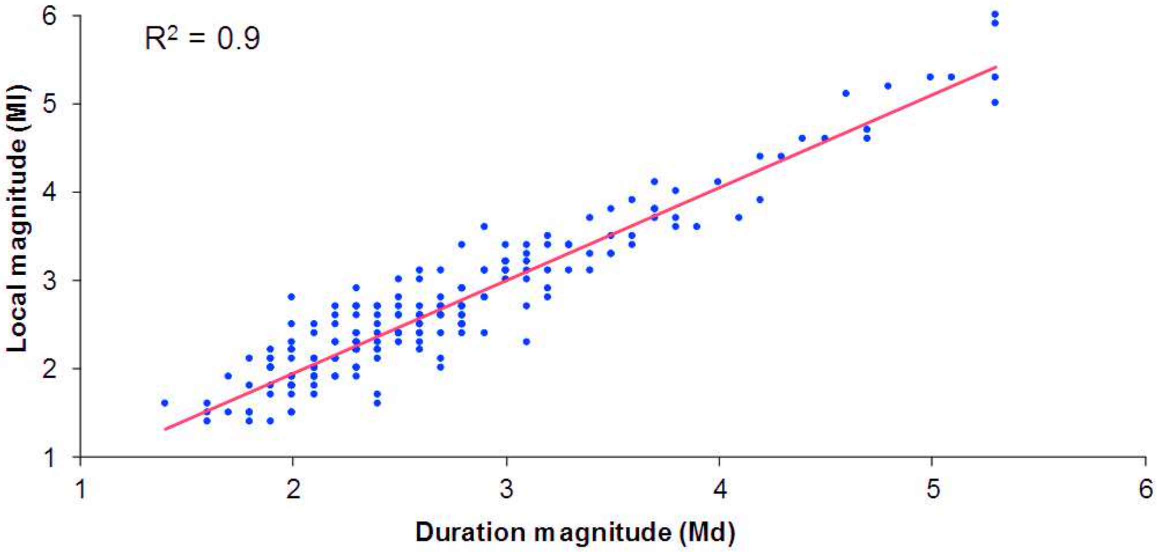

Figure 6.2. Correlation graphic between M_L and Md (after Mungunsuren, 2007).

6.3 Appendix 3: Station correction value

Table 6.1. Station correction value as relative value with respect the the ALF station

Station name	Used event number	Correction value [s]		Station name	Used event number	Correction value [s]	
		For P	For S			For P	For S
ALFM	253	0.00	0.00	ULN	39	0.28	0.48
ARTM	96	0.05	-0.01	IVGM	13	0.17	0.13
SEMM	106	0.08	0.12	UB0M	25	0.16	0.05
UGDM	100	0.08	0.13	UB2M	9	0.15	0.17
SA0M	257	-0.02	-0.02	UB3S	30	0.06	0.16
UB1M	178	0.02	0.07	UB7M	22	0.06	0.01
UB2S	188	0.02	0.00	UB8M	37	0.08	0.07
UB4M	171	0.03	0.04	UB9M	24	0.02	0.09
UB5M	96	-0.03	-0.05	MO5M	2	-0.02	-0.03
UB6M	139	0.09	0.05	MO7M	3	0.04	0.09
				MO8M	3	-0.01	0.04
				UB3M	8	-0.16	0.06
				EM3M	37	0.04	-0.04
				EM4M	42	-0.01	-0.05
				EM9M	34	0.02	0.17

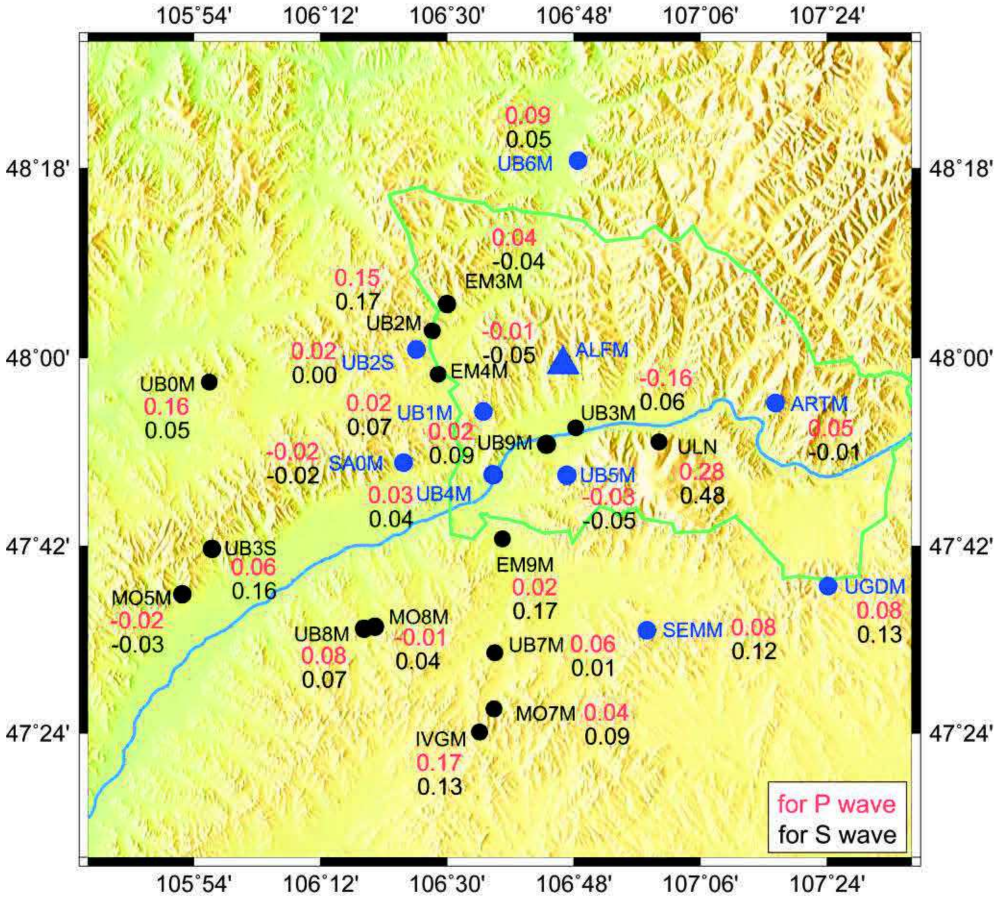

Figure 6.3. Station correction value for each seismic stations. Blue colour names are stations at which we used more than 96 events and black colour names are for stations at which we used less than 42 events. Number value represent, respectively, positive and negative values with respect to reference station (ALFM = triangle).

6.4 Appendix 4: Time and space evolution of seismic swarms

Swarm 1 : Started from 2005-04-06 for 5 days:

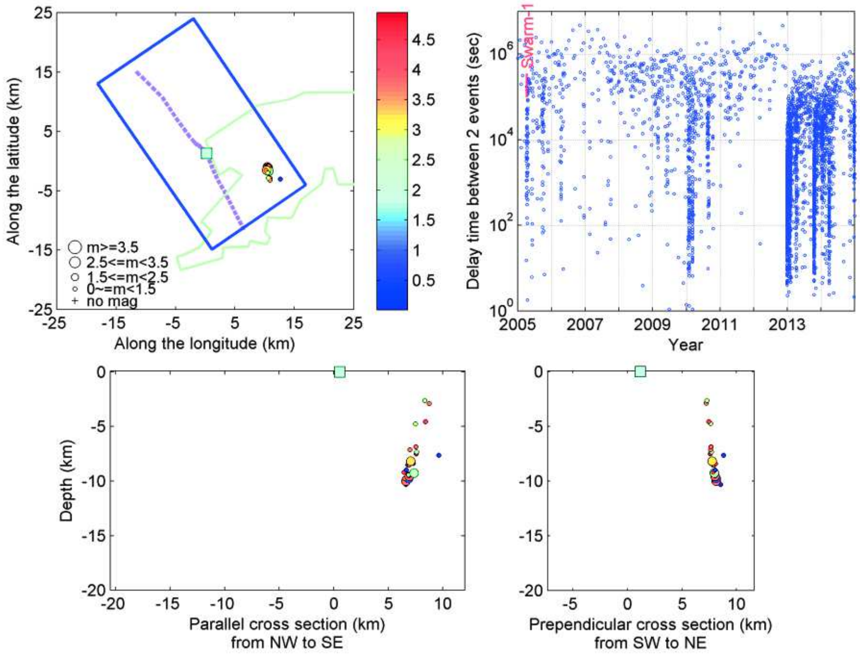

Figure 6.4. Colour bar = days since 2005.04.06. Top = epicentral view. Bottom left = cross section along the fault (NW to SE). Bottom right = cross section perpendicular to the fault (SW to NE). Aqua square = trench site and dashed purple line is estimated fault based on seismic activity determined by NDC.

Group 1: Events between Swarm 1 and Swarm 2: 1734 days 168 events

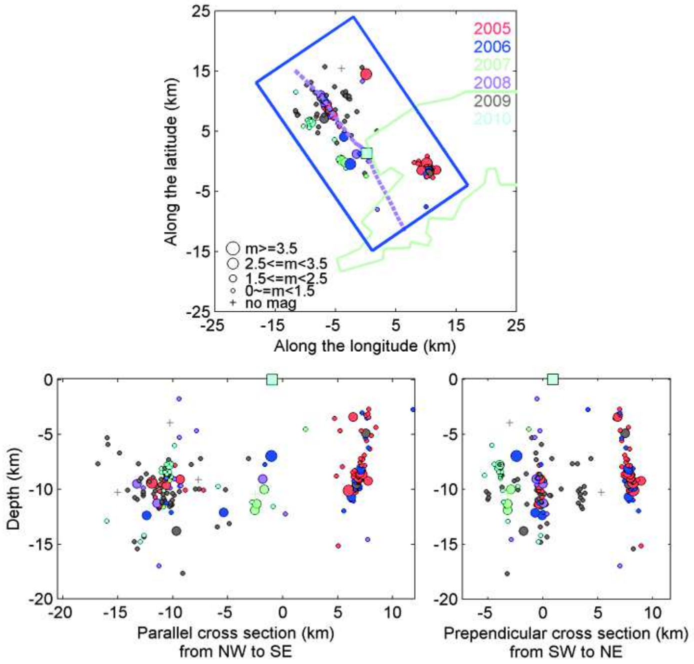

Figure 6.5. Top = epicentral view. Bottom left = cross section along the fault (NW to SE). Bottom rigth = cross section perpendicular to the fault (SW to NE). Aqua square = trench site and dashed purple line is estimated fault based on seismic activity determined by NDC. Colour indicates year.

Swarm 2: Started from 2010-01-28 for 4 days:

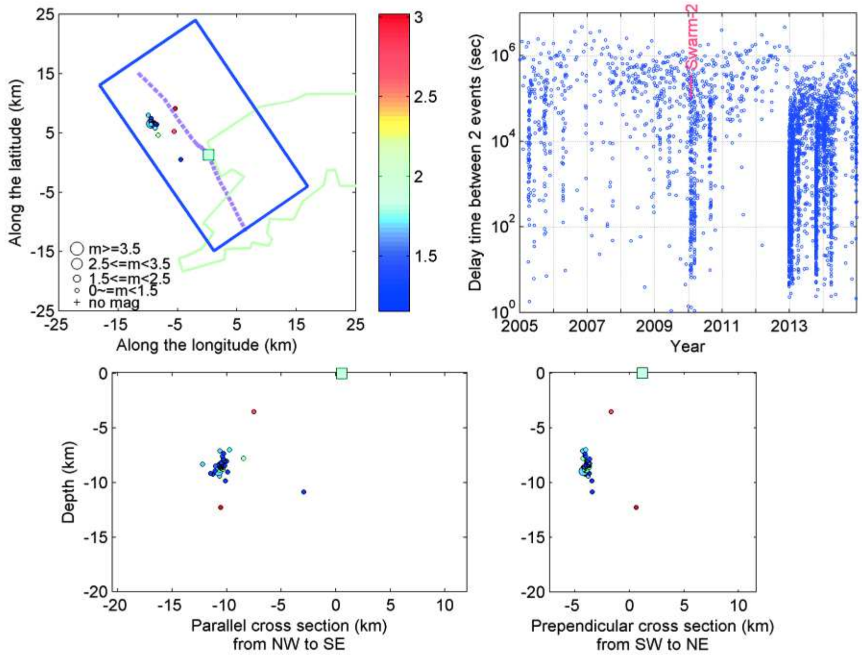

Figure 6.6. Colour bar = days since 2010.01.28. Top = epicentral view. Bottom left = cross section along the fault (NW to SE). Bottom right = cross section perpendicular to the fault (SW to NE). Aqua square = trench site and dashed purple line is estimated fault based on seismic activity determined by NDC.

Swarm 3 : Started from 2010-03-07 for 2 days:

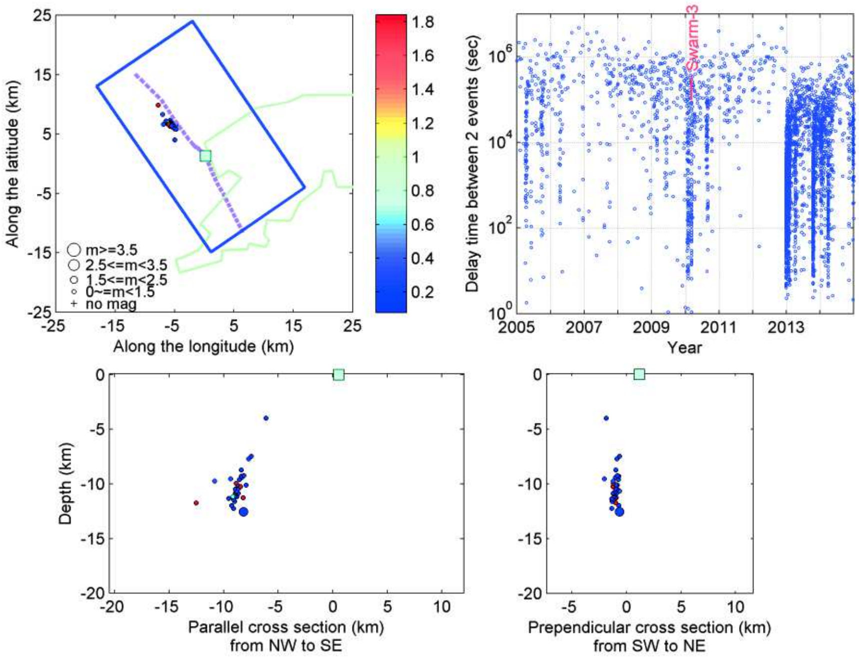

Figure 6.7. Colour bar = days since 2010.03.07. Top = epicentral view. Bottom left = cross section along the fault (NW to SE). Bottom right = cross section perpendicular to the fault (SW to NE). Aqua square = trench site and dashed purple line is estimated fault based on seismic activity determined by NDC.

Swarm 4 : Started from 2010-08-29 for 2 days:

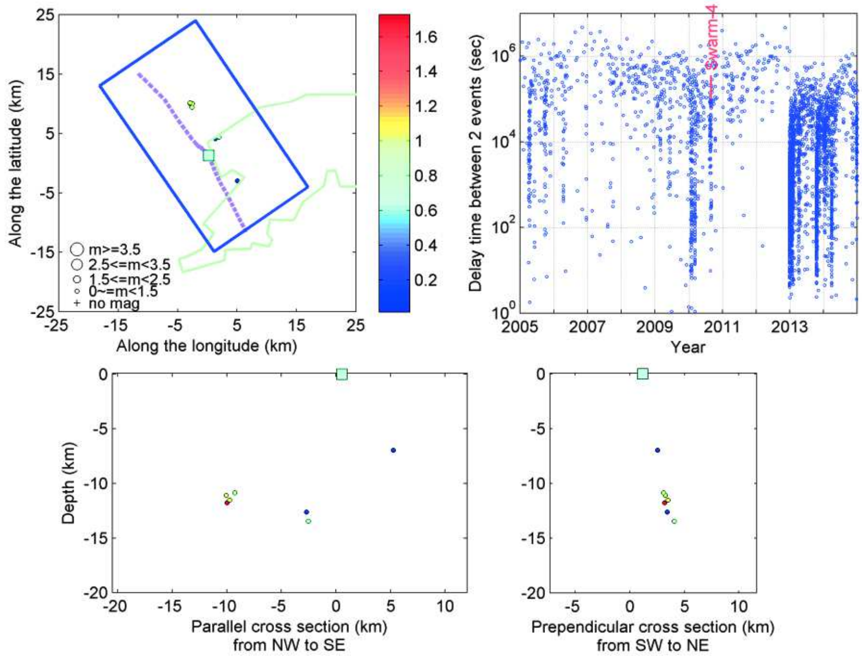

Figure 6.8. Colour bar = days since 2010.08.29. Top = epicentral view. Bottom left = cross section along the fault (NW to SE). bottom right = cross section perpendicular to the fault (SW to NE). Aqua square = trench site and dashed purple line is estimated fault based on seismic activity determined by NDC.

Swarm 5 : Started from 2012-12-25 for 50 days:

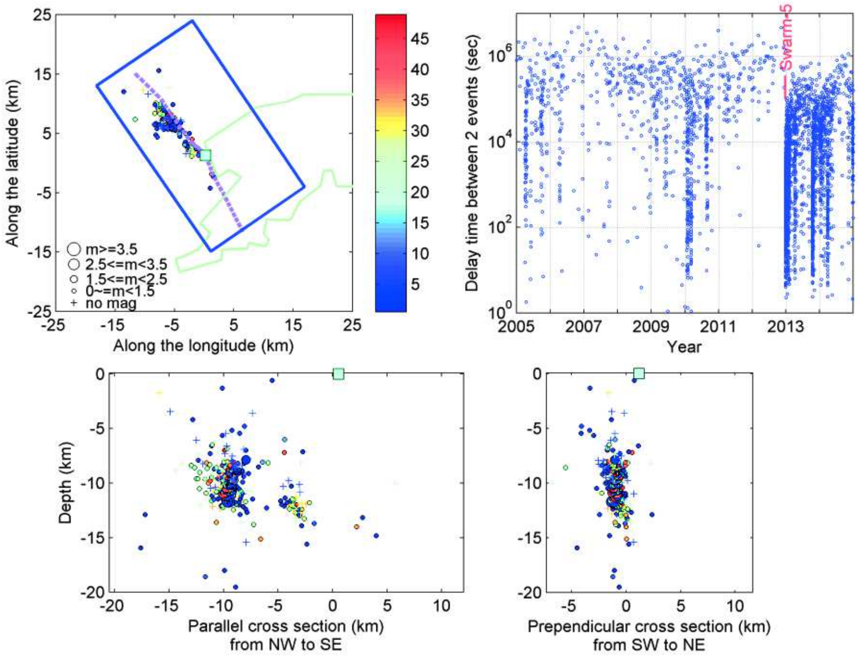

Figure 6.9. Colour bar = days since 2012.12.25. Top = epicentral view. Bottom left = cross section along the fault (NW to SE). Bottom right = cross section perpendicular to the fault (SW to NE). Aqua square = trench site and dashed purple line is estimated fault based on seismic activity determined by NDC.

Swarm 6 : Started from 2013-04-04 for 7 days:

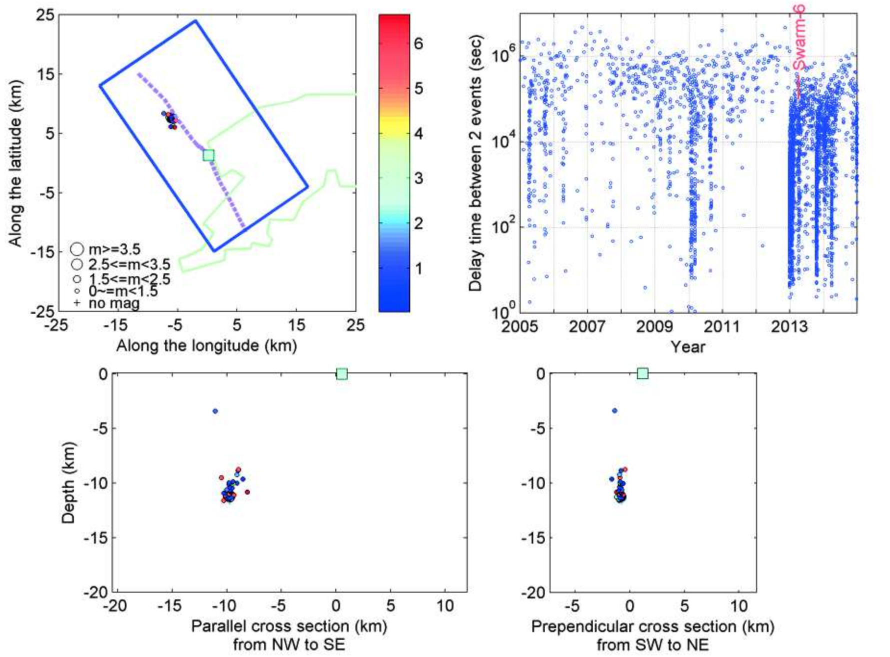

Figure 6.10. Colour bar = days since 2013.04.04. Top = epicentral view. Bottom left = cross section along the fault (NW to SE). Bottom right = cross section perpendicular to the fault (SW to NE). Aqua square = trench site and dashed purple line is estimated fault based on seismic activity determined by NDC.

Swarm 7 : Started from 2013-10-14 for 29 days:

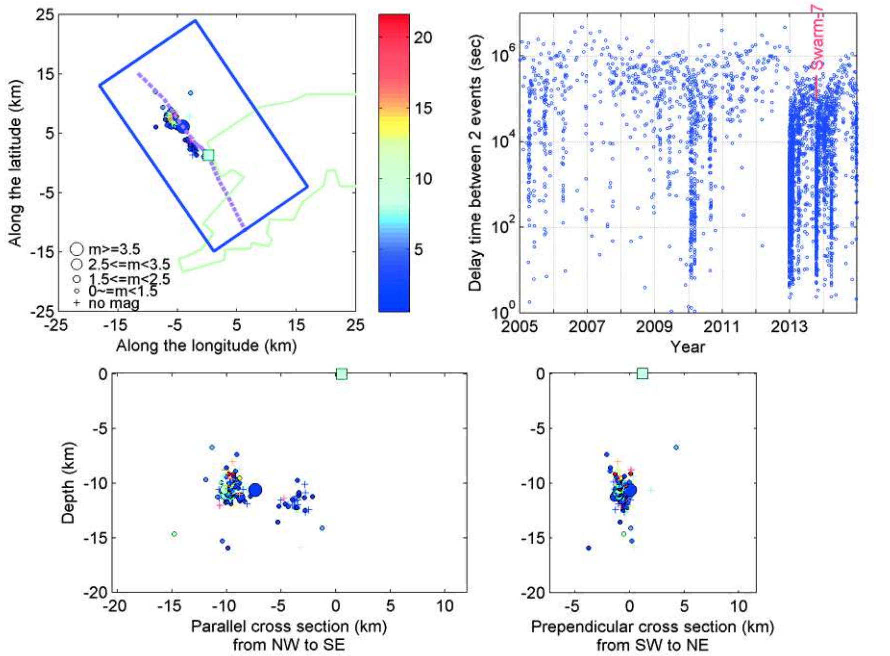

Figure 6.11. Colour bar = days since 2013.10.14. Top = epicentral view. Bottom left = cross section along the fault (NW to SE). Bottom right = cross section perpendicular to the fault (SW to NE). Aqua square = trench site and dashed purple line is estimated fault based on seismic activity determined by NDC.

Swarm 8 : Started from 2014-01-06 for 9 days:

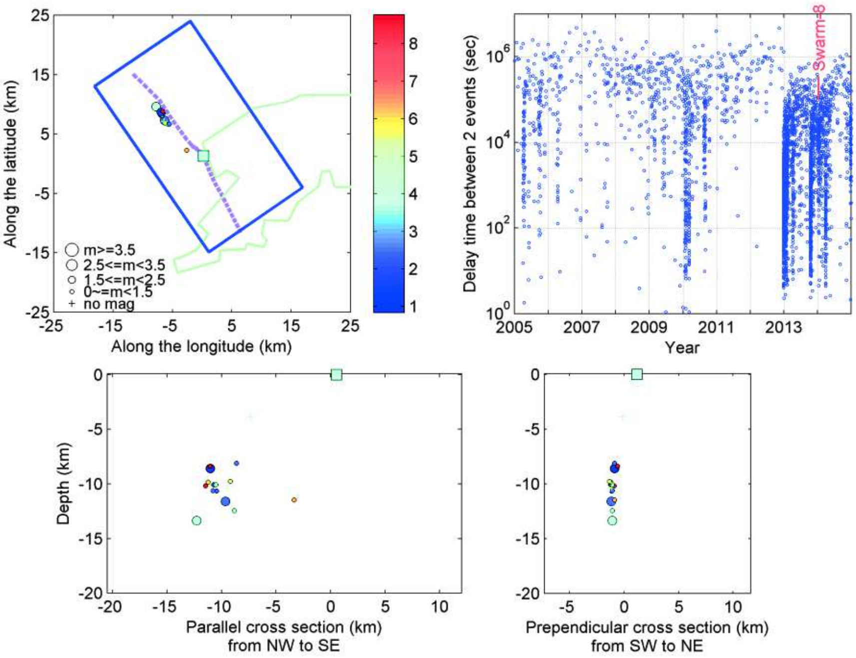

Figure 6.12. Colour bar = days since 2014.01.06. Top = epicentral view. Bottom left = cross section along the fault (NW to SE). Bottom right = cross section perpendicular to the fault (SW to NE). Aqua square = trench site and dashed purple line is estimated fault based on seismic activity determined by NDC.

Swarm 9 : Started from 2014-03-27 for 3 days:

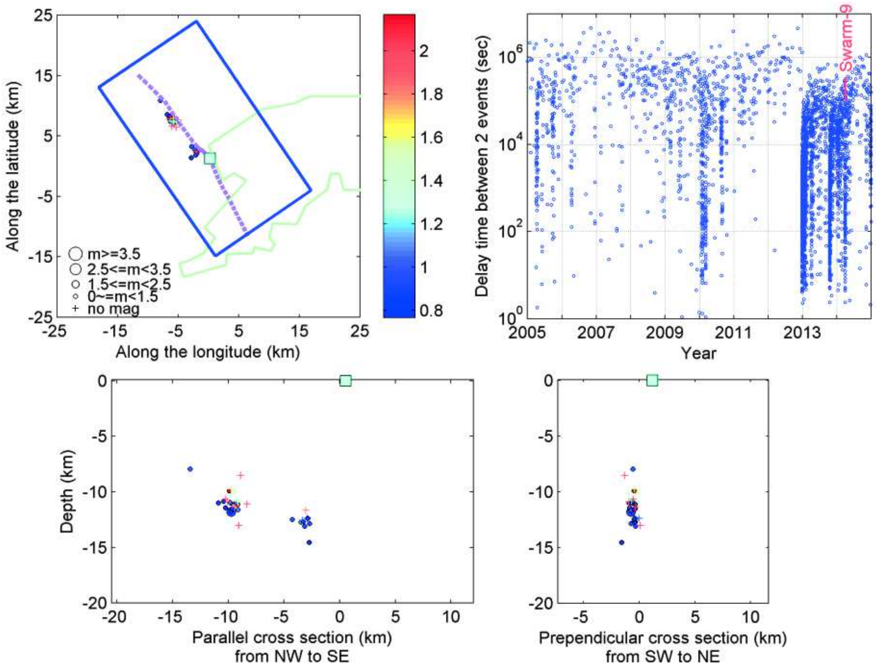

Figure 6.13. Colour bar = days since 2014.03.27. Top = epicentral view. Bottom left = cross section along the fault (NW to SE). Bottom right = cross section perpendicular to the fault (SW to NE). Aqua square = trench site and dashed purple line is estimated fault based on seismic activity determined by NDC.

Swarm 10 : Started from 2014-12-20 for 4 days:

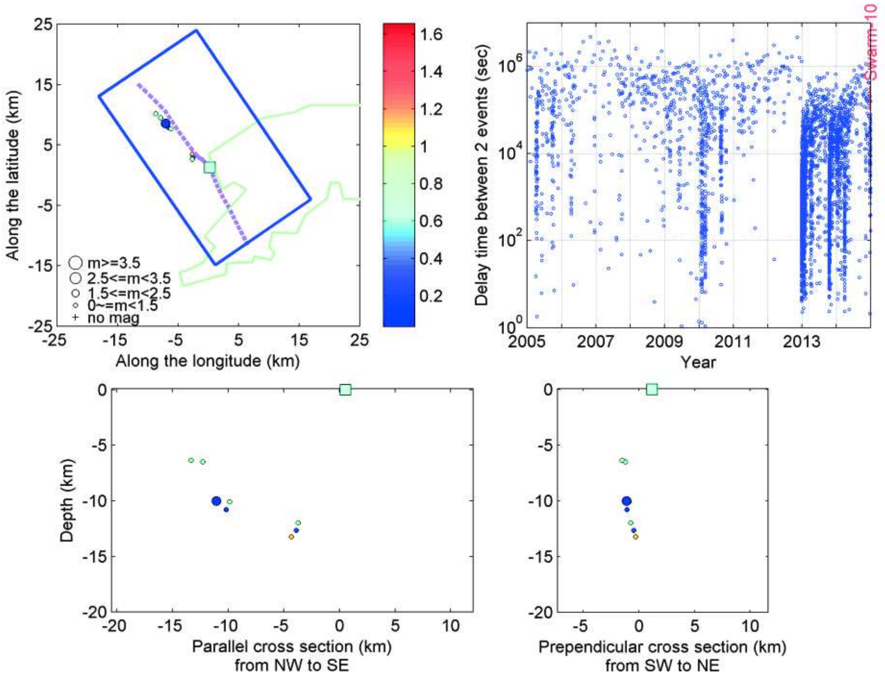

Figure 6.14. Colour bar = days since 2014.12.20. Top = epicentral view. Bottom left = cross section along the fault (NW to SE). Bottom right = cross section perpendicular to the fault (SW to NE). Aqua square = trench site and dashed purple line is estimated fault based on seismic activity determined by NDC.

Group 2: Events included between swarms 2, 3, 4, 5, 6, 7, 8 and 9: 178 events

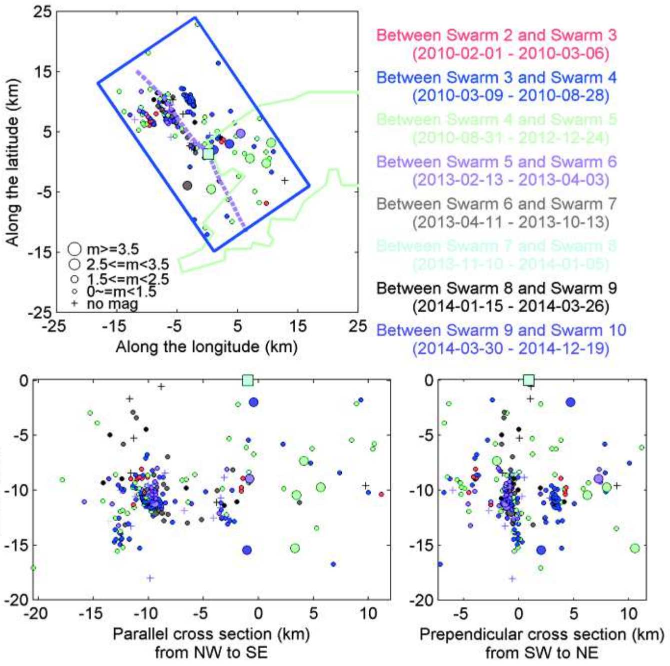

Figure 6.15. Top = epicentral view. Bottom left = cross section along the fault (NW to SE). Bottom rigth = cross section perpendicular to the fault (SW to NE). Aqua square = trench site and dashed purple line is estimated fault based on seismic activity determined by NDC. Colour indicates time between swarms noted in upperright corner of figure.

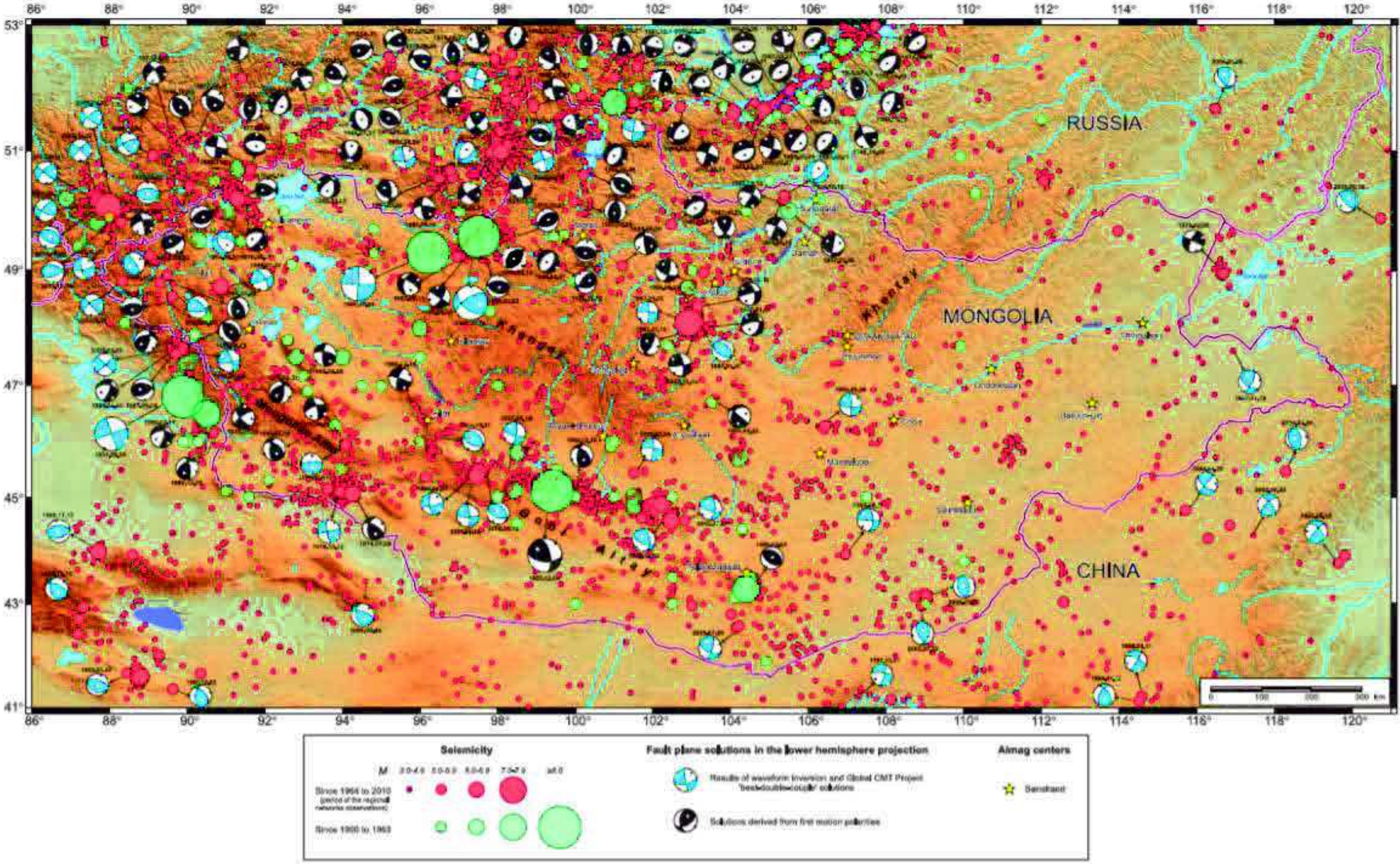

Figure 6.16. Map of focal mechanism of earthquakes in Mongolia (after Gangaadorj et al., 2011)

6.6 Appendix 6: Relation between ML and MS magnitude for Mongolia

The attenuation law uses the Ms magnitude scale, we determine a relation between M_L (local magnitude) and Ms (surface magnitude). We compare the M_L from our NDC catalog with that of Ms from ISC (International Seismological Center) for events referenced in both catalogs.

$$\mathbf{Ms = 0.81 \times M_L + 0.87}$$

After converting our seismological data from Ml to Ms, we compare the results with the Ms published by the ISC with a residual of less than 0.2 in magnitude, which is a small value allowing us to use this conversion (Report of SHAU, 2006).

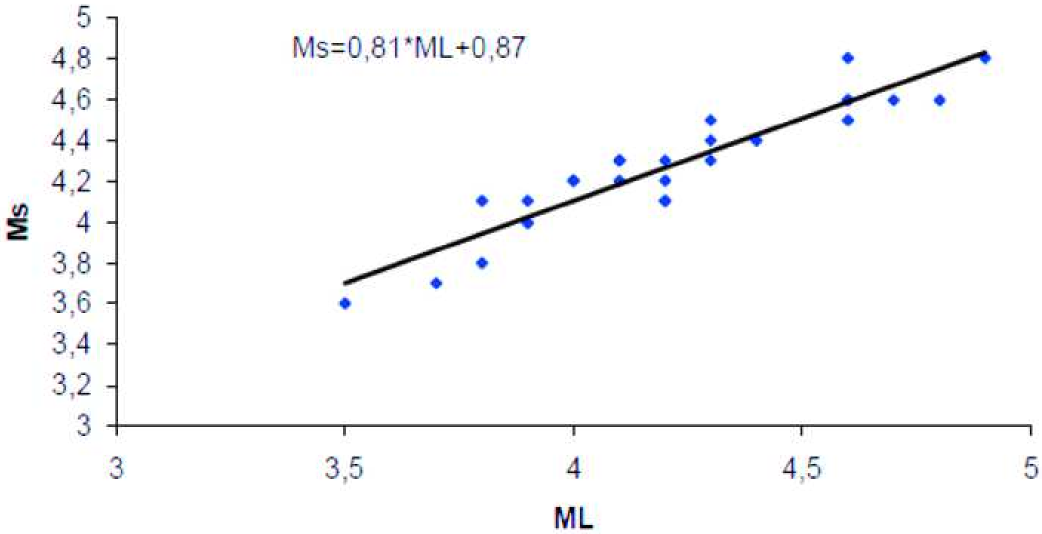

Figure 6.17. Relation between M_L and Ms magnitude for Mongolia (after report of the “Seismic Hazard Assessment of Ulaanbaatar, capital of Mongolia, Seismic micro zoning map”, 2006).

6.7 Appendix 7: Observed intensities at Ulaanbaatar area during the M_L=3.7 Emeelt earthquake of 14/10/2013

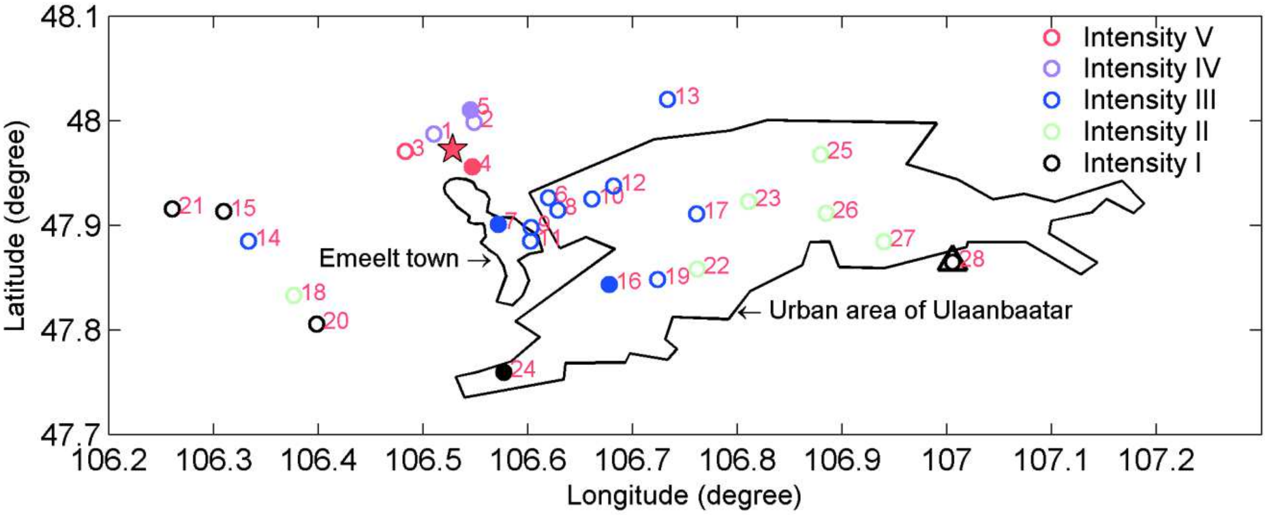

Figure 6.18. Intensities observation for Emeelt event of the 14th October 2013, $M_{L=}3.7$, depth 12 km. Red star is epicenter. Circles are observed intensity sites and numbers are site ID (see Table 5.4). Black triangle is ULN station.

Intensities estimations are based on 10 to 15 individual information at the site 4, 5, 7, 16 and 24 (filled circle in Figure 6.18). Intensities at other sites are based on up to 8 individual information.

6.8 Appendix 8 : Extended abstract in french

Résumé étendu du mémoire de thèse présenté par Munkhsaikhan ADIYA.

Activité sismique de la région d'Oulan Bator : Implication pour l'évaluation de l'aléa sismique

Introduction:

La Mongolie est un pays de 1,57 millions km^2 situé entre la Russie, au nord, la Chine, du sud-ouest au sud-est, et le Kazakhstan à l'ouest. Avec une altitude moyenne de 1580m, elle est composée de montagnes, principalement dans sa moitié ouest, atteignant 3700 à 4000m (Altai, Gobi-Altai, Khangai et Khentey), de larges bassins ou vallées (avec plus de 300 lacs) entre ces montagnes, et de plateaux à l'est et au sud-est.

Avec environ 3 millions d'habitants, la densité de la population est l'une des plus faibles au monde, mais près de la moitié, environ 1,3 million, se concentre dans la capitale, Oulan Bator, la ville stratégique du pays. La Mongolie a été affectée au cours du 20ème siècle par 4 séismes de magnitude 8 et plus dans sa partie occidentale, loin de la capitale. En avril 2005, une activité sismique anormale est observée à 3 km au nord de l'aéroport international, en bordure d'Oulan Bator. Par la suite, elle se localise légèrement plus à l'ouest et se répartit sur une distance de 35 km environ. En 2008, une mission de reconnaissance mongole et française permet de découvrir 4 à 5 km de ruptures de surface très érodées dans le secteur de cette sismicité. L'objectif de cette thèse est de comprendre cette activité, son évolution spatio-temporelle et d'étudier son implication pour l'estimation de l'aléa sismique à Oulan Bator. Pour cela, il est indispensable de localiser précisément la sismicité en 3D, la précision des localisations issues de l'observatoire de sismologie de l'IAG (Institut of Astronomy and Geophysics) étant inadaptée à ce type d'étude à une échelle très locale. Pour cela, il me faudra définir un modèle de vitesse 1D et 3D et réaliser une relocalisation précise avec le modèle de vitesse 3D par TomoDD (Tomographie double différence, code développé par Zhang et Thurber (2003)). Ensuite la relation de cette sismicité avec une ou des structures actives sera étudiée avant de voir son impact sur l'estimation de l'aléa sismique.

Chapitre 1: Contexte géologique de la Mongolie

La Mongolie est localisée au sein de la CAOB (Central Asian Orogenic Belt) (Kröner et al., 2005), une large région entre le craton sibérien et le bloc du Tarim qui a enregistré depuis 800 Ma l'accrétion de microcontinents et d'arcs jusqu'au Paléozoïque.

Les déformations récentes sont associées à la collision Inde-Asie avec une convergence d'environ 4cm/an décrite depuis les années 1970 (Tapponnier and Molnar, 1979). Elle a généré l'extrusion de blocs vers le SE, et en Mongolie, cette extrusion est apparente entre des décrochements senestres orientés EO sur les structures de Bolnay et du Gobi-Altay. La déformation en Mongolie est beaucoup plus faible qu'au sud. Environ 15% de la convergence Inde-Asie est accommodée au nord du Tien Shan avec un raccourcissement NS associé à des décrochements dextres dans l'Altay et senestre sur les structures EO (Calais et al., 2003) (Figure A1).

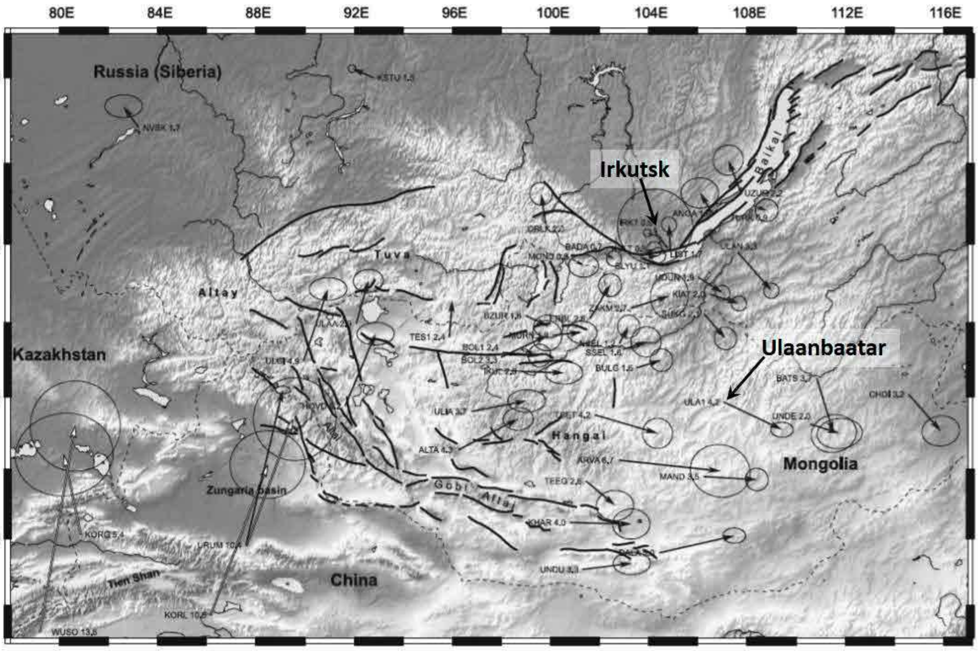

Figure A1: Vitesses issues des mesures GPS par rapport à l'Eurasie. Les ellipses représentent l'intervalle de confiance de 95%. Les nombres sont les vitesses en mm/an par rapport à l'Eurasie (d'après Calais et al., 2003).

Les failles actives principales sont indiquées par des lignes continues. La sismicité de la Mongolie a été marquée par 4 grands séismes de magnitude 8 et plus : (Bulnai 1905/07/09, Tsetserleg 1905/07/23, Altai/Fu-Yun 1931/08/10 et Gobi-Altai 1957/12/04) (Figure A2). Le cumul des ruptures de surface atteint 900 km et les déplacements co-sismiques mesurés sont entre 5 et 12m (Baljinnyam et al., 1993; Schlupp 1996; Schlupp and Cisternas, 2007; Klinger et al., 2011; Choi et al., 2012). Leur période de retour est estimée à plus de 3000ans et les taux de déformation sont entre 1 et 3 mm/an

(Ritz et al., 2006; Calais et al., 2003; Rizza et al., 2015). Une synthèse de chacune de ces structures et de l'activité sismique des grandes régions de la Mongolie occidentale est présentée.

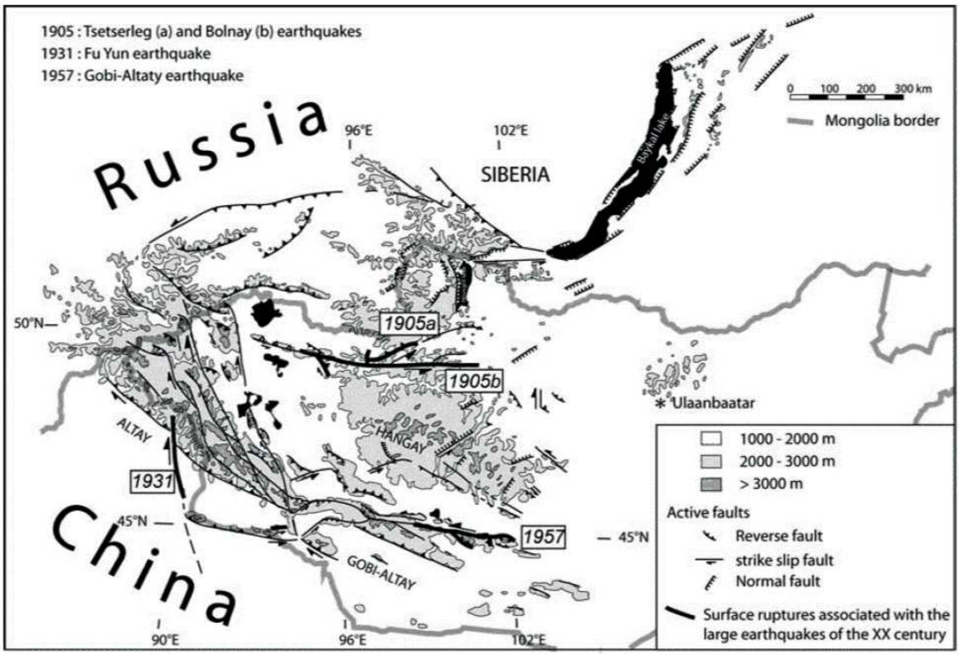

Figure A2. Principales failles actives en Mongolie et les grands séismes du XXème siècle (d'après Schlupp et Cisternas, 2007).

D'un point de vue tectonique, l'est de la Mongolie, où se trouve la capitale, est au sein de la plaque amurienne dont la limite serait entre le massif du Hangay et Oulan Bator en s'étendant selon une direction NS du Baïkal au sud de la Mongolie. Cette limite traversant la Mongolie reste discutée et non validée à ce jour.

La région d'Oulan Bator est marquée par 5 failles actives (Figure A3). La faille de Khustai, connue mais étudiée en détails seulement récemment, de 111 km environ, décrochante senestre pouvant générer un séisme de magnitude 7.5 (Ferry et al., 2010, 2012), la faille de Gunj d'environ 25km de long, dont le dernier paléoséisme est daté à 7800 à 4667 BC (Imaev et al., 2012), les failles de Sharkhay et Avdar, toutes les deux découvertes et étudiées depuis 2011, décrochantes senestres sur environ 46 km, trois paléoseismes ont été identifiés sur la faille de Sharkhay donnant une période de retour de 1195±157ans et une vitesse de glissement entre 0.6±0.2 et 2.14±0.5 mm/an, Al-Ashkar, (2015), et enfin, la faille d'Emeelt, sujet de cette étude (Figure A4). Sur la faille d'Emeelt, un mouvement dextre de 2m a été identifié pouvant correspondre à un ou 2 paleoséismes et un pendage de la faille de 27 à 35° vers le NNE en proche surface (Dujardin et al. 2014.

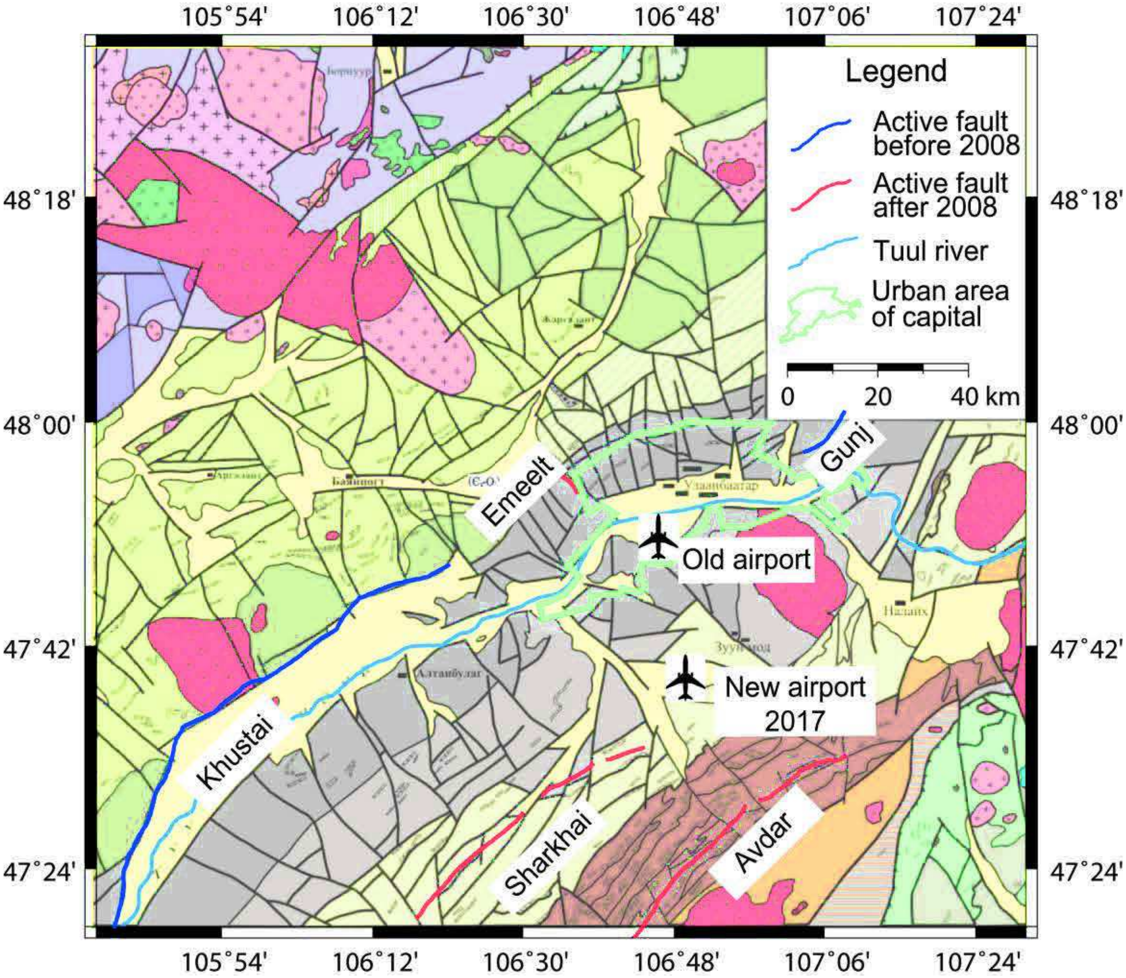

Figure A3: Failles actives principales de la région d'Oulan Bator, capitale de la Mongolie (Pour la légende géologique, voir Figure 1.24).

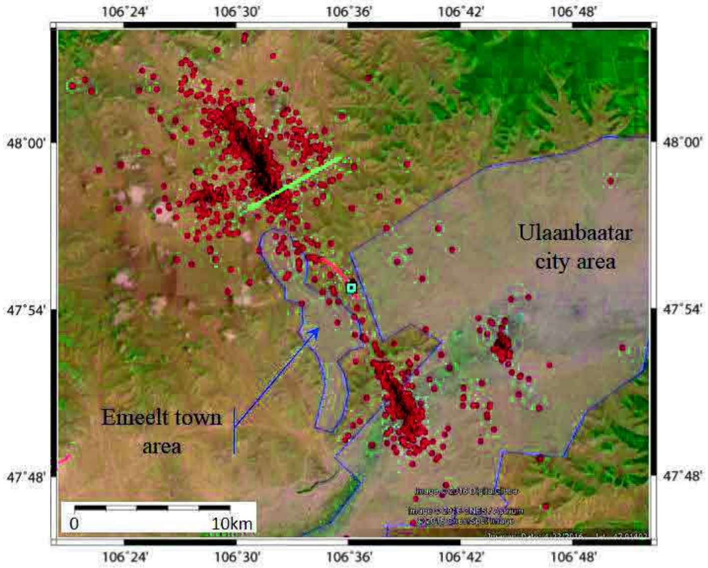

Figure A4: Zone de la faille d'Emeelt et sismicité enregistrée par le National Data Centre de l'IAG, Mongolie. En vert la localisation du profil sismique réalisé par les équipes mongoles et françaises.

Le réseau sismologique instrumental a débuté en 1957 avec une station à Oulan Bator. Ce sera la seule station proche de la ville jusqu'en 1994, la suivante étant à 290 km. Ceci limite fortement la connaissance de la sismicité de la région. Depuis 1994, le réseau s'est développé, principalement dans le cadre d'une collaboration importante avec la France et le CEA/DASE. Mais suite à la sismicité observée dans la région d'Emeelt depuis 2005, et afin de bien localiser la sismicité, diverses stations ont été rajoutées dans la région (Figure A5).

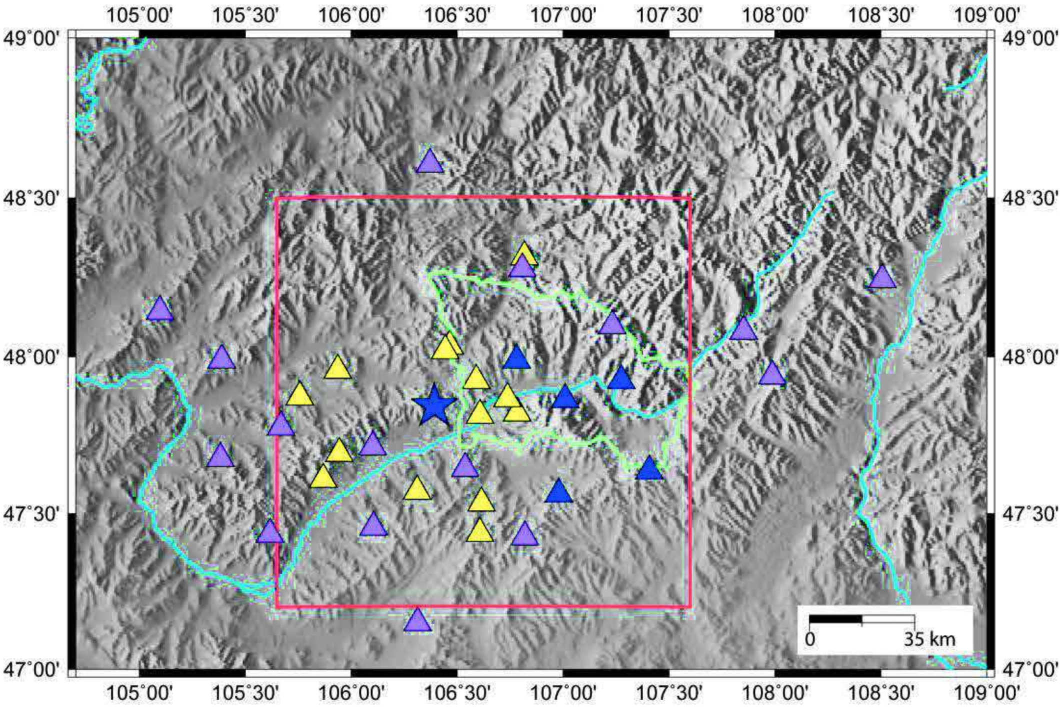

Figure A5: localisation des stations sismologiques ayant fonctionné dans la région d'Oulan Bator depuis 1994. Bleu = Réseau Oulan Bator permanent (Triangle = station, étoile = mini-réseau CTBT); Jaune = stations portables; Rose = réseau Guralp.

La détection de la sismicité a totalement changé depuis 1994 (Figure A6). Le fort changement de sismicité après 2005 intervient dans une période sans changement du réseau et correspond bien à une nouvelle activité avec une augmentation notable du taux de sismicité (Figure A7 et A8). Cependant, le catalogue fourni par le NDC reste très mal contraint en profondeur (Figure A9)

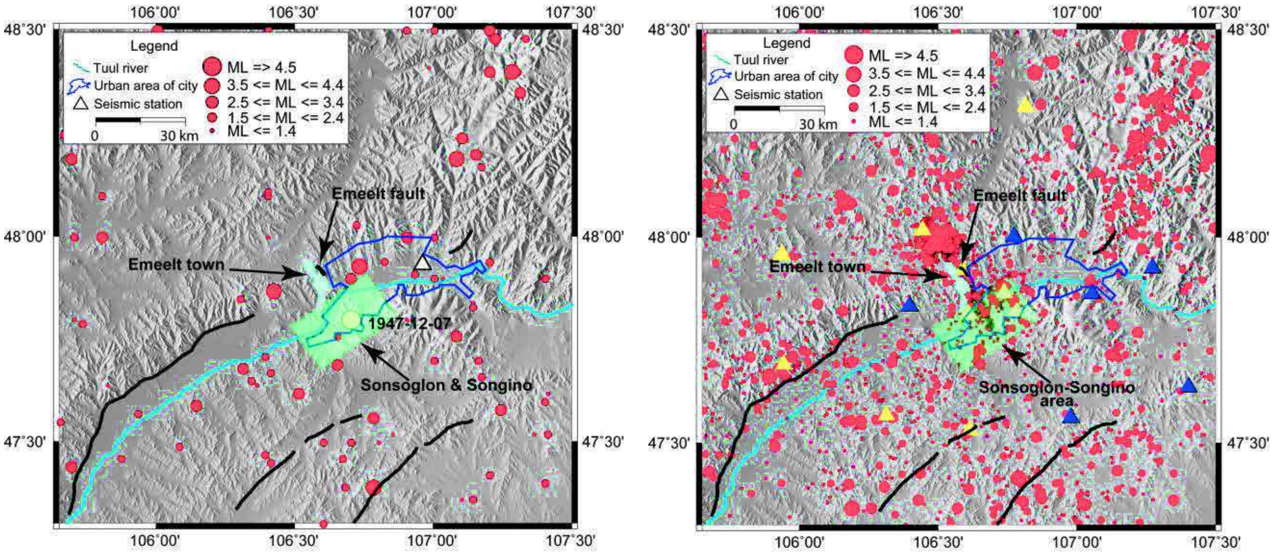

Figure A6: Sismicité observée entre 1964 et 1994 (gauche) et entre 1995 et 2013 (droite) dans la région d'Oulan Bator.

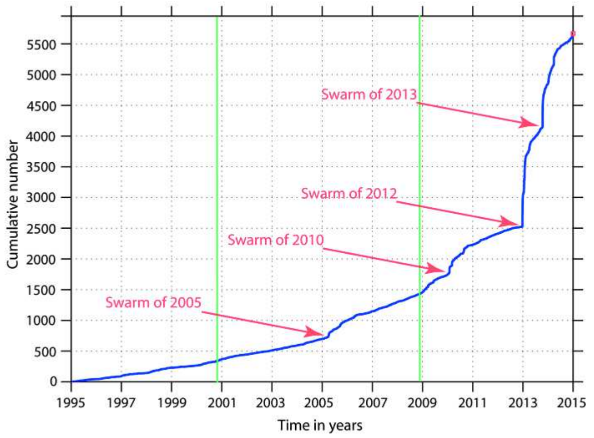

Figure A7: Evolution du nombre de séismes (cumulé) dans la zone d'Emeelt (140X140km) entre 1995 et 2014. Les lignes vertes sont les dates d'évolutions importantes du réseau sismologique (fin 2008 ajout du réseau mobile).

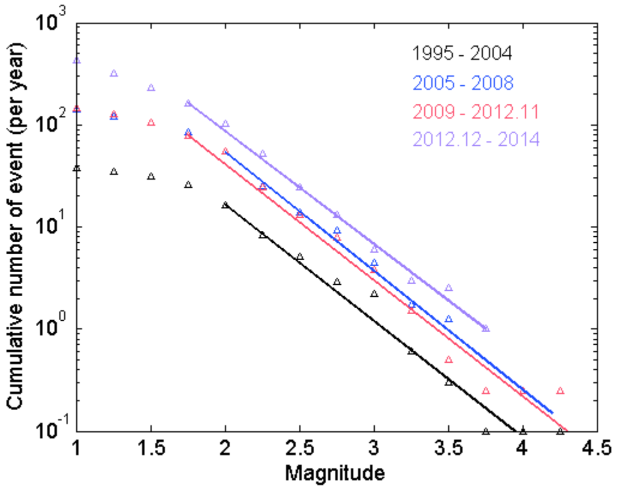

Figure A8: Evolution de la GR dans la zone d'Emeelt (140X140km).

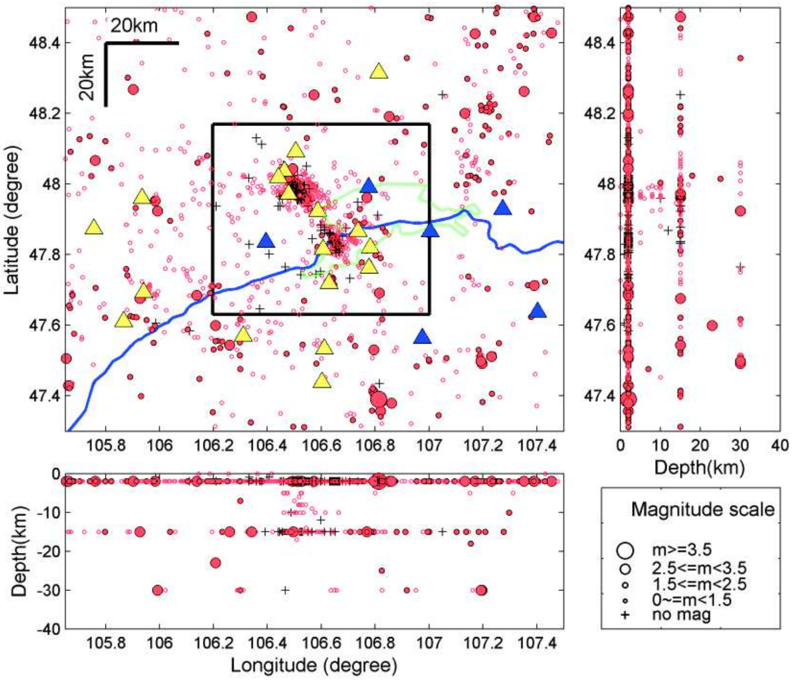

Figure A9: Localisation des hypocentres par le NDC entre décembre 2008 et janvier 2013.

L'analyse de la sismicité a permis d'identifier 10 crises sismiques (Figure A10) qui deviennent très importantes fin 2012.

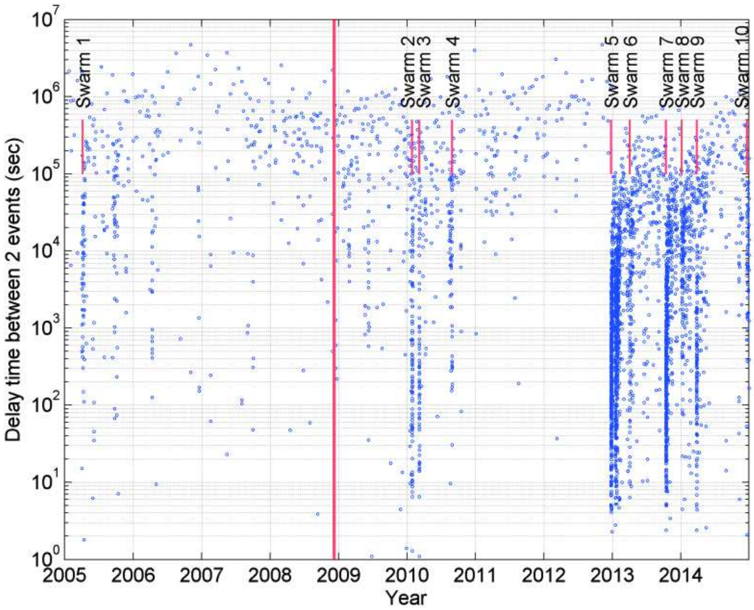

Figure A10: Identification des crises sismiques

Chapitre 3: Inversion du modèle de vitesse 1D et nouvelle localisation de la sismicité dans la région d'Emeelt.

Ce chapitre décrit la procédure de sélection des données puis le calcul du modèle de vitesse 1D. Ce calcul a été précédé par un long travail de contrôle des temps d'arrivées ou phases, par l'intégration de stations portables et l'ajout de nombreuses phases oubliées. (Figure A11). L'ajout de stations a permis de corriger des fausses localisations dues à un effet miroir (cercle violet, Figure A12). Le modèle de vitesse obtenu est contraint jusqu'à environ 28km de profondeur, au-delà il est identique au modèle initial à cause du manque de données (Figure A13).

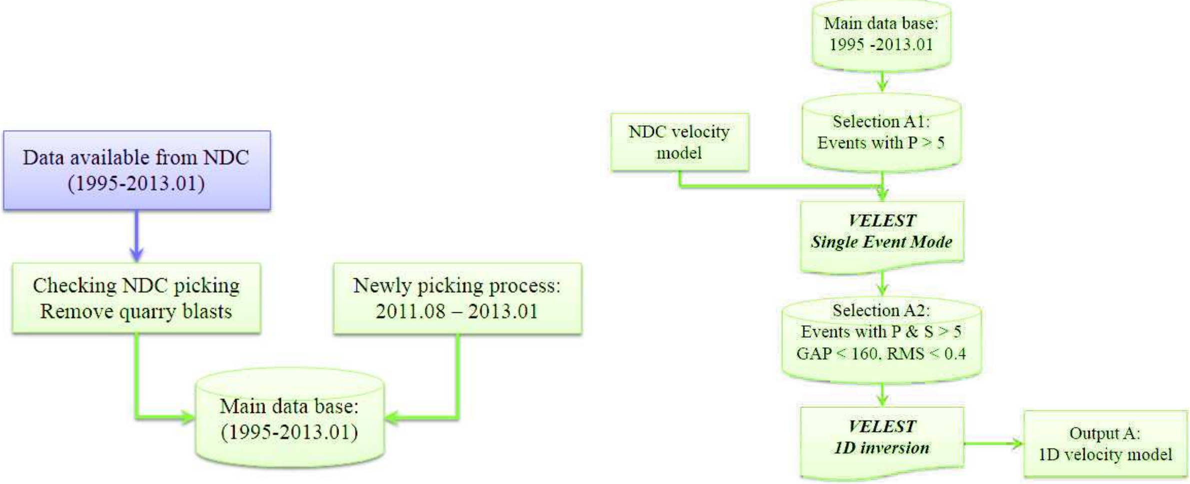

Figure A11: Préparation de la base de données et calcul du modèle de vitesse 1D.

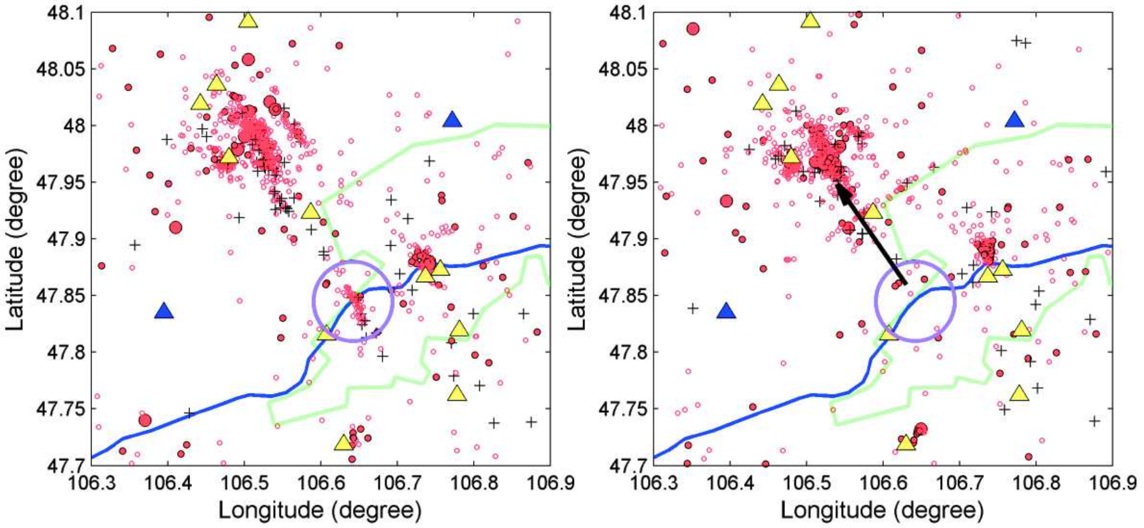

Figure A12: Gauche = localisations issues du catalogue NDC, Droite = localisations SEM (Single event mode) intégrants de nouvelles stations (triangles bleus).

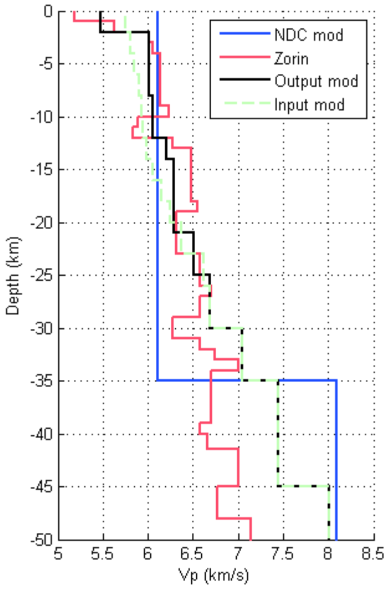

Figure A13: Nouveau modèle de vitesse 1D (Output) comparé à des modèles soit publiés (Zorin et al., 2002) soit utilisés au NDC

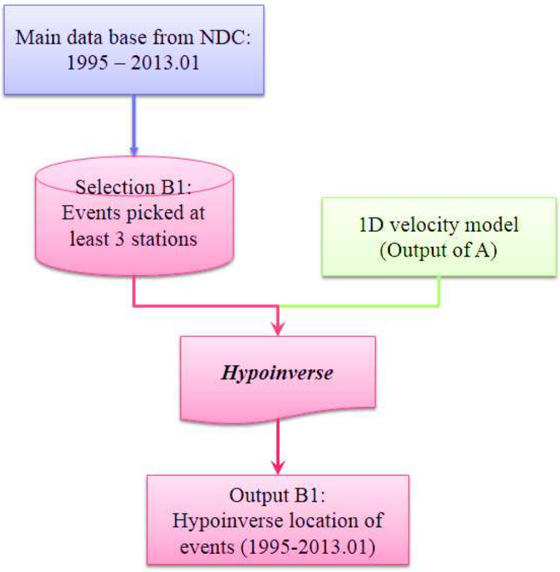

Figure A14: Résumé de la procédure "Hypoinverse" appliquée (Procédure B1).

L'ensemble de la sismicité a été localisé par "Hypoinverse", procédure résumée dans la figure A14. Le résultat est montré en figure A15, comparant la sismicité localisée par le NDC, initiale, et le résultat de la localisation "hypoinverse" avec le nouveau modèle de vitesse 1D. On observe un fort changement de la profondeur des séismes, points faible de la localisation NDC dans le secteur.

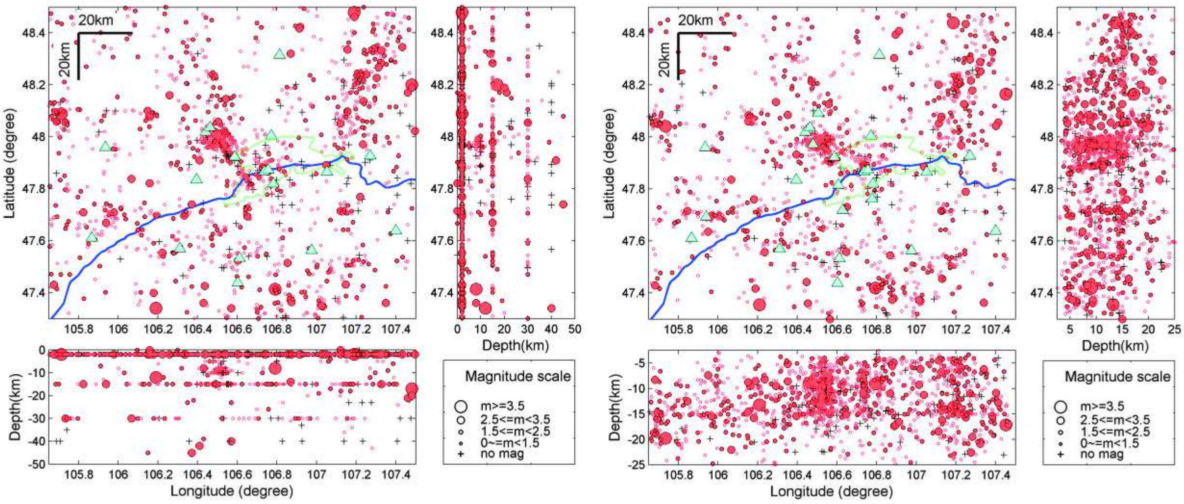

Figure A15: Comparaison de la sismicité localisée par le NDC (gauche) et le résultat de la localisation "hypoinverse" avec le nouveau modèle de vitesse 1D (droite)

La procédure utilisée pour l'élaboration du modèle de vitesse 3D est résumée dans la figure A16. Seule la période de 1995 à 2013.01 a été utilisée car elle a fait l'objet d'un important travail de vérification, correction et intégration de nouvelles données. La sélection C contient 810 évènements dont les paramètres sont résumés dans la figure A16. Elle contient 9982 temps d'arrivée et 148063 mesures de temps différentiel.

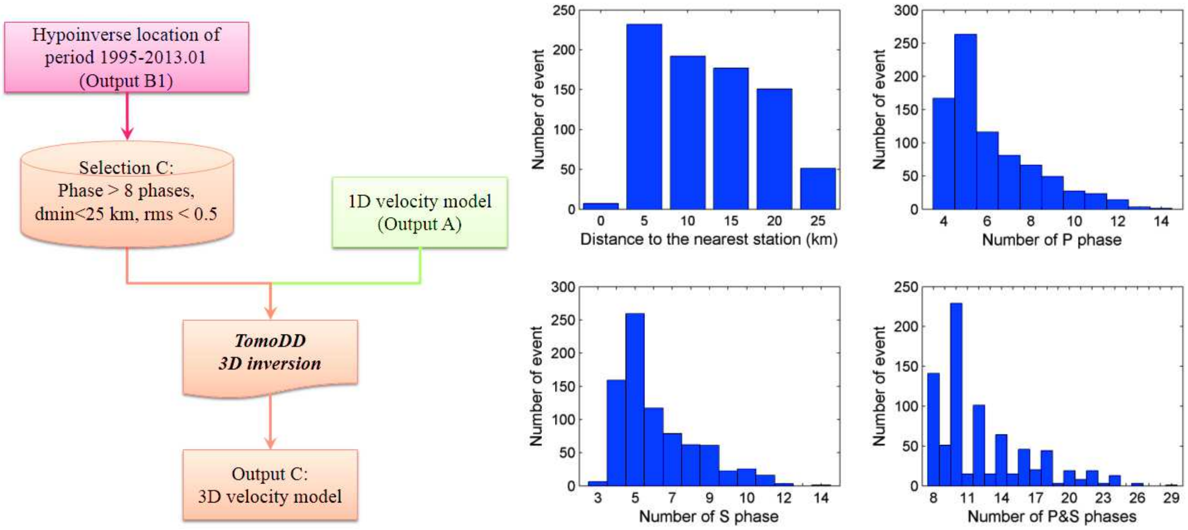

Figure A16: Procédure pour le calcul du modèle 3D et paramètres de la sélection C (droite).

La grille d'inversion est composée de 21x21x12 noeuds séparés de 5km en NS et EO et en vertical à des profondeurs de 0, 2.4, 6, 10 puis tous les 5 km (Figure A17).

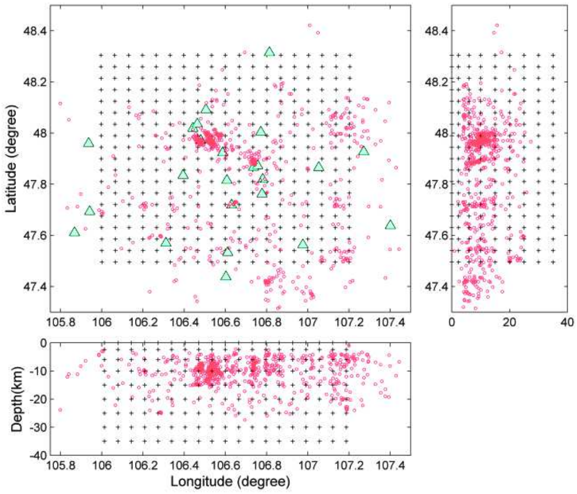

Figure A17: Grille d'inversion utilisée pour le calcul du modèle 3D. Triangles bleus= stations

Pour réduire l'incertitude liée à la géométrie du modèle, 12 autres grilles ont été utilisées, déduites de la grille initiale par des rotations de 15 en 15 degrés et des décalages dans les 3 directions. Différents test ont été réalisés sur ces modèles (dépendance des vitesses Vp, test de résolution "checkerboard"). Les 13 modèles de vitesses 3D obtenus sont alors combinés dans un modèle moyen (WAM, Weighted average model, Calo 2009 et Calo et al., 2012). Le résultat obtenu (Modèle de vitesse 3D WAM) est présenté figure A18 pour diverses profondeurs lorsque le DWS (Derivative Weight Sum) est supérieur à 50. Ce modèle de vitesse sera utilisé pour la relocalisation via TomoDD.

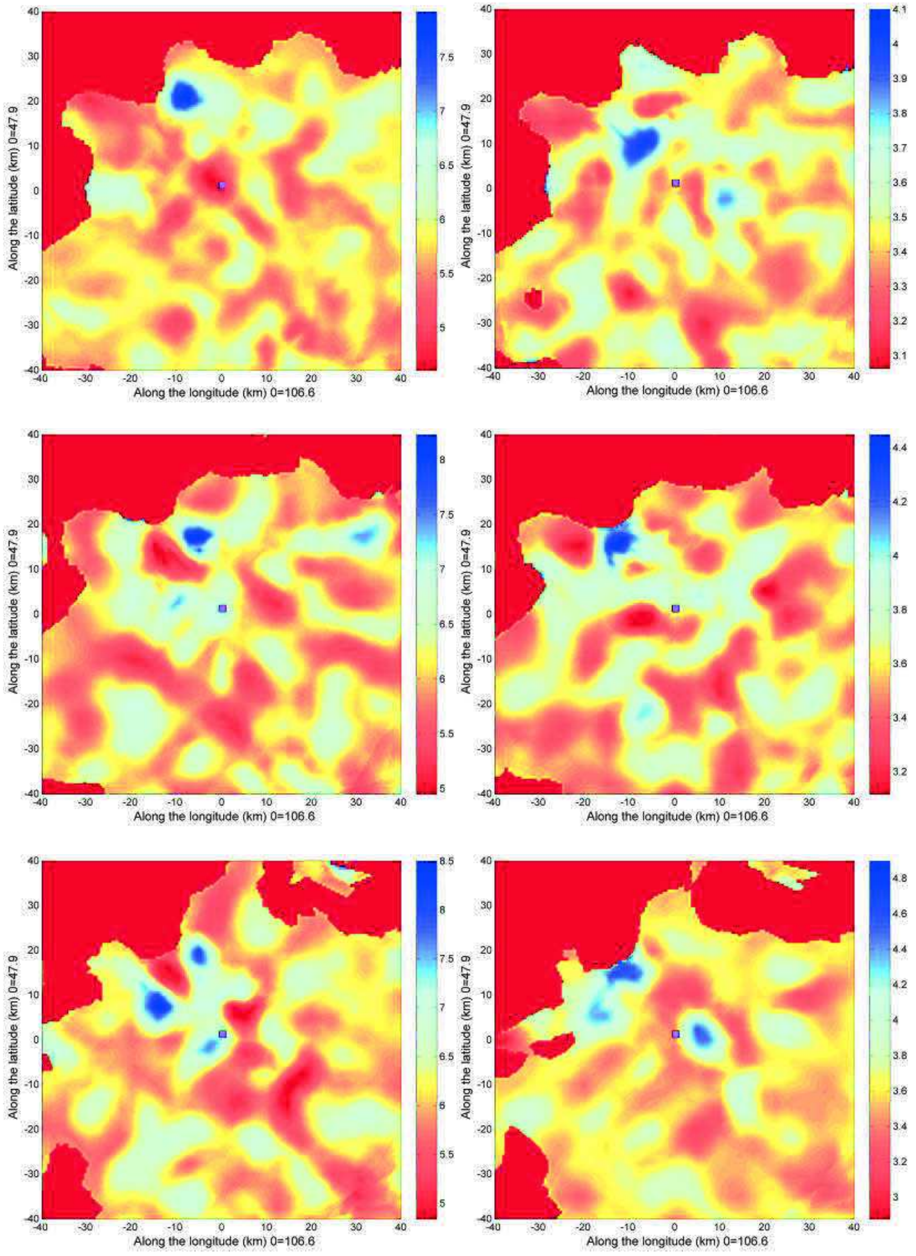

Figure A18: Coupe horizontale du modèle pour le WAMP (gauche) et WAMS (droite) à 5, 10 et 15km de profondeur (haut vers le bas). La zone brune au NO marque la région avec un DWS<50. Le carré violet correspond à la position de la tranchée d'Emeelt.

Avant de réaliser le calcul de relocalisation TomoDD, l'ensemble des évènements respectant les critères de sélection ont été localisés par la méthode Hypoinverse (2817 évènements). Cela couvre deux périodes, la première jusqu'à janvier 2013 avec des données vérifiés en détails et complétées qui ont été utilisées pour le modèle de vitesse 3D WAM et la période entre janvier 2013 et décembre

2014 qui à elle seule représente 50% des évènements de la zone. Cependant, pour cette deuxième période, seuls les temps d'arrivés identifiés par le NDC ont été utilisés. La sélection des données pour le calcul TomoDD a été la même pour les deux périodes avec au final 1986 évènements relocalisés (Figure A19). Les paramètres associés aux données sélectionnées pour les deux périodes sont présentés figure A20.

La figure A21 montre les incertitudes sur les localisations obtenues (RMS, incertitude EO, NS et profondeur) et montre que les localisations sont associées à des incertitudes faibles, inférieurs à 150m en général et une valeur moyenne de 92m. Le résultat régional est donné en figure A23. L'évolution par rapport aux données initiale est majeure, pour la profondeur mais aussi en localisation grâce à l'ajout de stations mobiles. (Figure A23). L'histogramme des profondeurs montre qu'elles sont les plus fréquentes entre 10 et 12km et se répartissent entre 2 et 25km. La répartition de la sismicité est selon 3 branches à quoi l'on peut ajouter la zone de l'aéroport qui peut être associée à une 4ème branche (Cf. Polygones sur la figure A25).

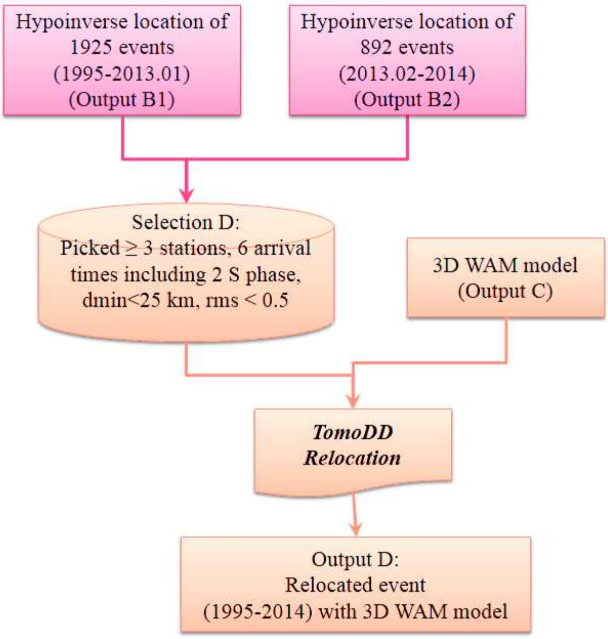

Figure A19: Procédure suivie pour la relocalisation TomoDD.

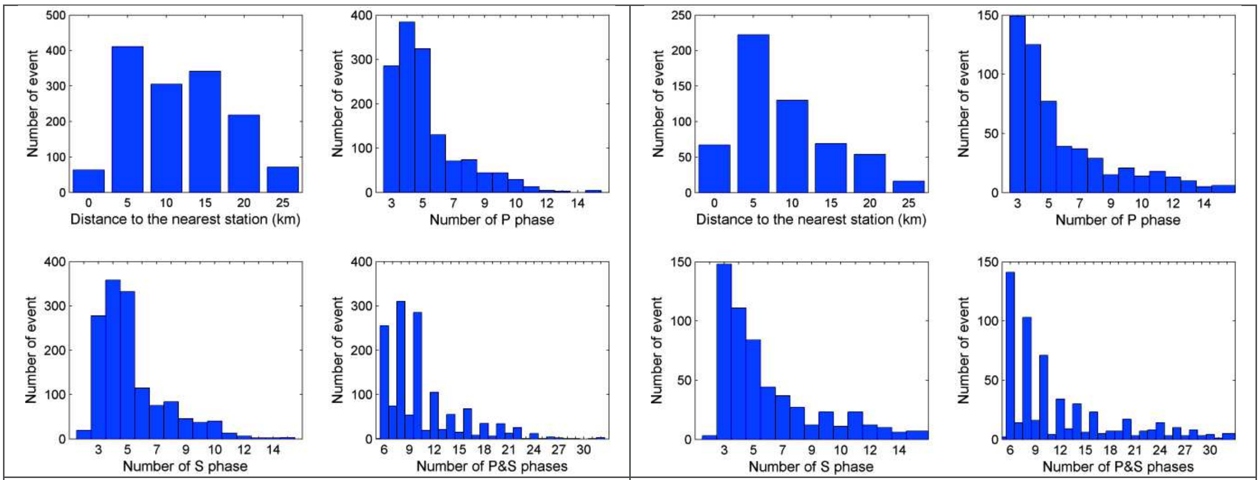

période avant jusqu'à fin janvier 2013

période de fin janvier 2013 à fin 2014

Figure A20: Paramètres associés au données sélectionnées pour les relocalisations 3D (Distance à la station la plus proche, nombre de phase P, S et P+S).

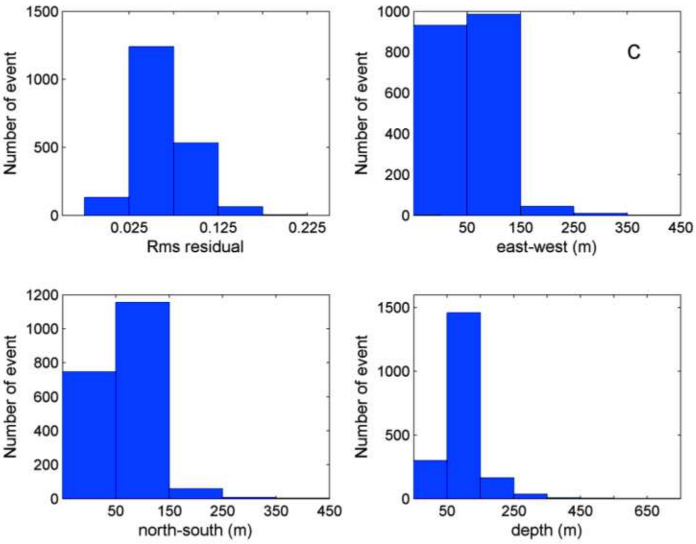

Figure A21: Incertitudes sur les localisations TomoDD (RMS, EO, NS et profondeur).

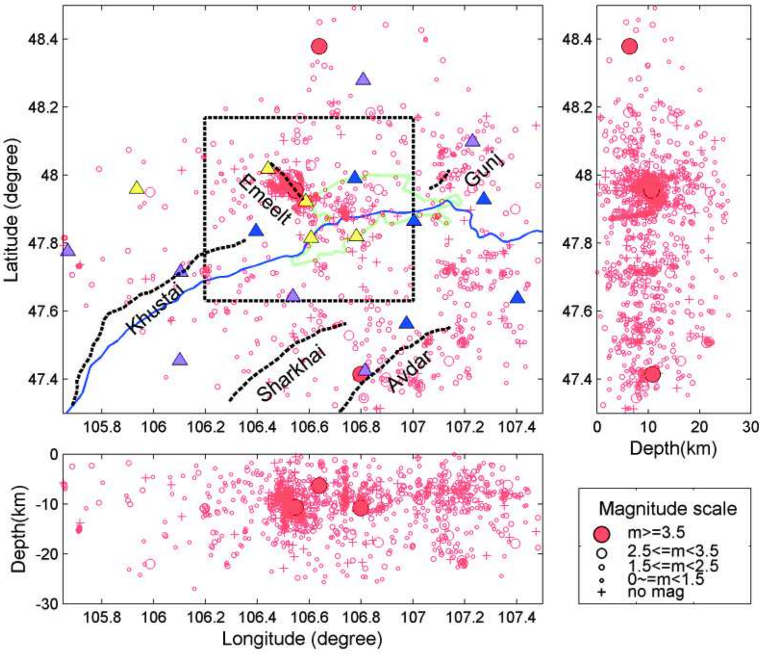

Figure A22: Localisation TomoDD avec un modèle de vitesse 3D WAM sur la période 1995-2014 centré sur la zone d'Emeelt. Le carré noir correspond à l'emprise de la figure A23.

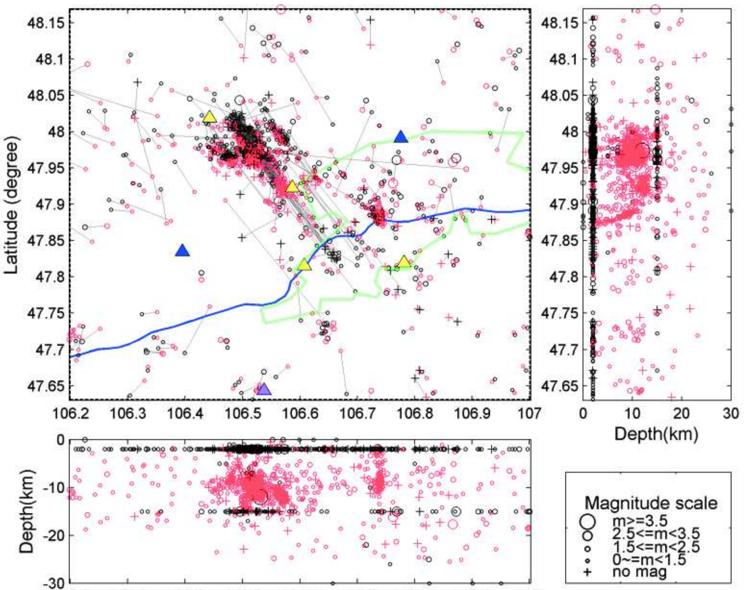

Figure A23: Différence de localisation entre le catalogue NDC (noir) et le résultat de la localisation TomoDD avec un modèle de vitesse 3D WAM (rouge) sur la période 1995-2014 centré sur la zone d'Emeelt. Les lignes en gris indiquent les mouvements des épicentres.

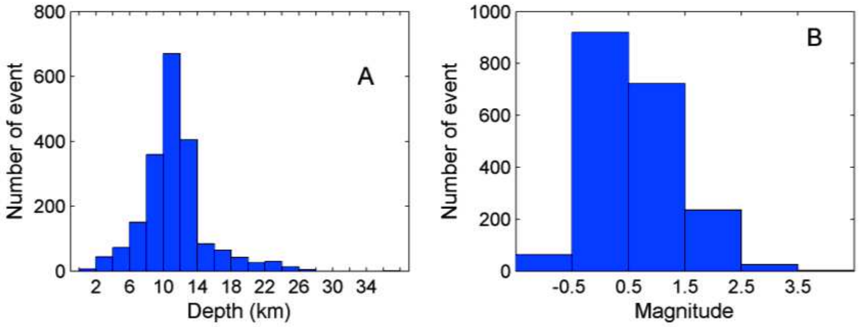

Figure A24: Histogramme des profondeurs et des magnitudes pour les séismes relocalisés par TomoDD.

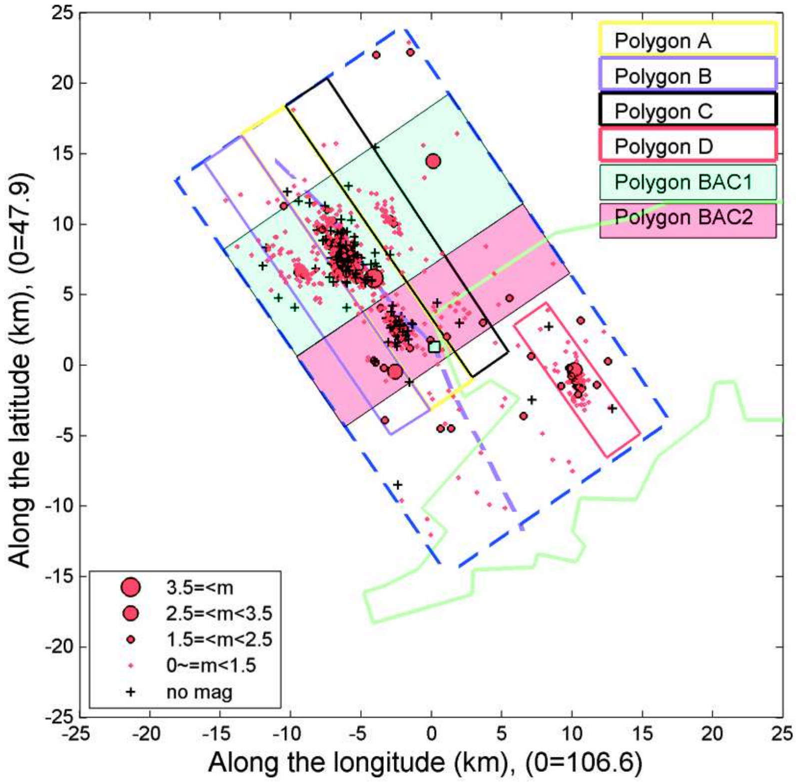

Figure A25: Séparation de la sismicité selon des branches ou polygones (A=WEB, B=MEB, C= EEB, D=aéroport).

Les conclusions principales sont:

- le modèle de vitesse montre une organisation en "boite à oeufs" avec des remontées de fortes vitesses localisées à proximité de la sismicité (Figures A26-1 et A26-2). Des directions N147 et perpendiculaires sont marquées dans ce modèle de vitesse dont la structuration semble être directement liée aux structures actives.
- La sismicité se répartie selon 3 branches orientés N147 (Branche Emeelt ouest - WEB, Branche principale - MEB, branche Est - EEB) et une 4ème si l'on considère la zone de l'aéroport. Elles sont subverticales et séparés de seulement 2 à 4 km.

- La sismicité est répartie sur une longueur de 15 km au lieu des 35 constatés à partir des localisations NDC. Elle peut être étendue à 25km si l'on considère la sismicité à proximité de l'aéroport.
- La MEB est la plus active, sur une longueur de 15 km et une profondeur entre 1 et 18 km principalement, la WEB a une sismicité plus faible sur une région similaire à la MEB mais la profondeur ne dépasse pas 15km. L'activité sur la EEB est plus courte et la profondeur se limite entre 5 et 15km. La sismicité de la zone de l'aéroport a une forme tubulaire
- la profondeur de la sismicité est répartie entre 2 et 25km et est centrée sur 10-12km suggérant une zone sismogénique de 20 à 25 km.

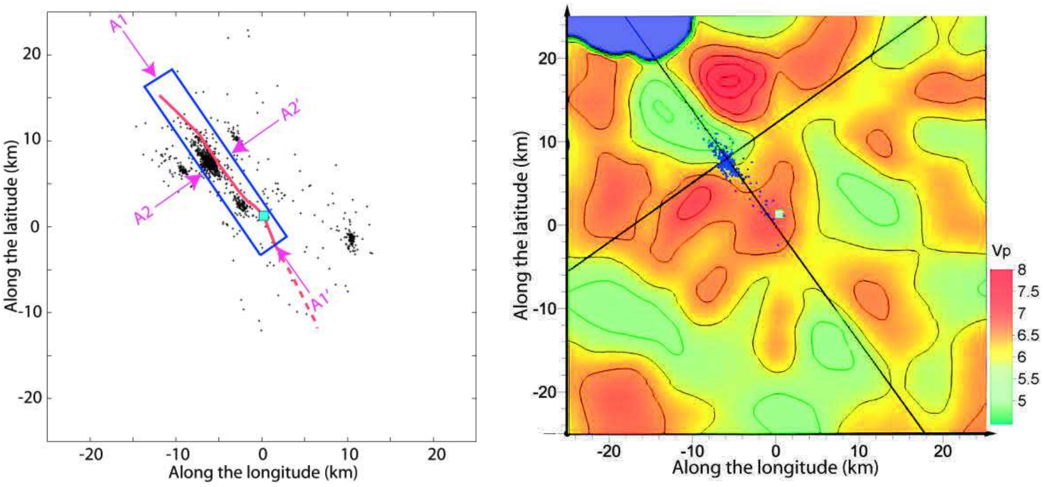

Figure A26-1: Coupe horizontale dans le modèle de vitesse 3D (Vp) à 10 km de profondeur. La sismicité indiquée est limitée à la zone indiquée sur la figure de gauche (MEB). Les lignes sur la figure de droite indiquent les coupes montrées dans la figure A26-2.

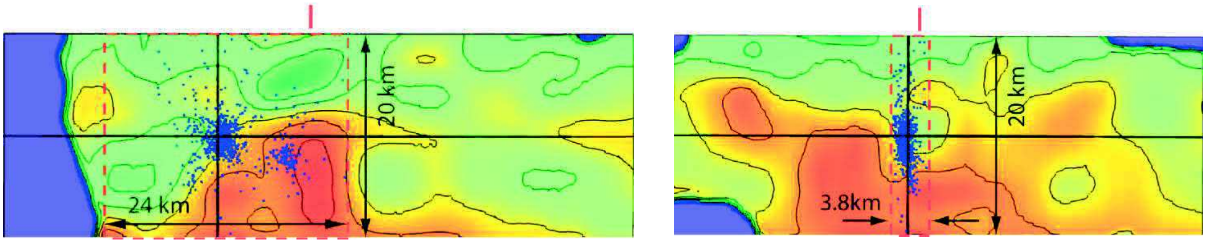

Figure A26-2: Coupe verticale dans le modèle de vitesse 3D (Vp) parallèle à la faille (gauche) et perpendiculaire à la faille (droite), la sismicité indiquée est limitée à la zone indiquée sur la figure A26-1 (MEB). La ligne horizontale indique la profondeur de 10km, au niveau de la coupe présentée figure A26-1.

Pendant les 10 ans qui ont suivi le début de l'activité à Emeelt en 2005, on a observé 3504 séismes dont 1968 on pu être précisément localisés par TomoDD (Figure A27). L'activité est principalement située au nord de la zone des ruptures de surfaces. Elle marque 3 branches (WEB, MEB, EEB) parallèles orientées N147, subverticales, avec un pendage vers le NE (Figure A28). Ces branches ne se raccordent pas en profondeur à moins de 17km, limite principale de la sismicité observée, bien que ces branches ne soient séparées que de 3 à 4km. La branche Est (EEB) se raccorde aux ruptures de surface identifiées sur le terrain et site d'une tranchée (Figures A28 et A29). La branche principale (MEB) se raccorde à la zone de déformation principale vue dans le profil sismique (Figure A30). Aucune observation de surface ne permet de raccorder la branche ouest (WEB). La sismicité s'étend principalement sur une profondeur entre 5 et 15km, et majoritairement entre 10 et 12km.

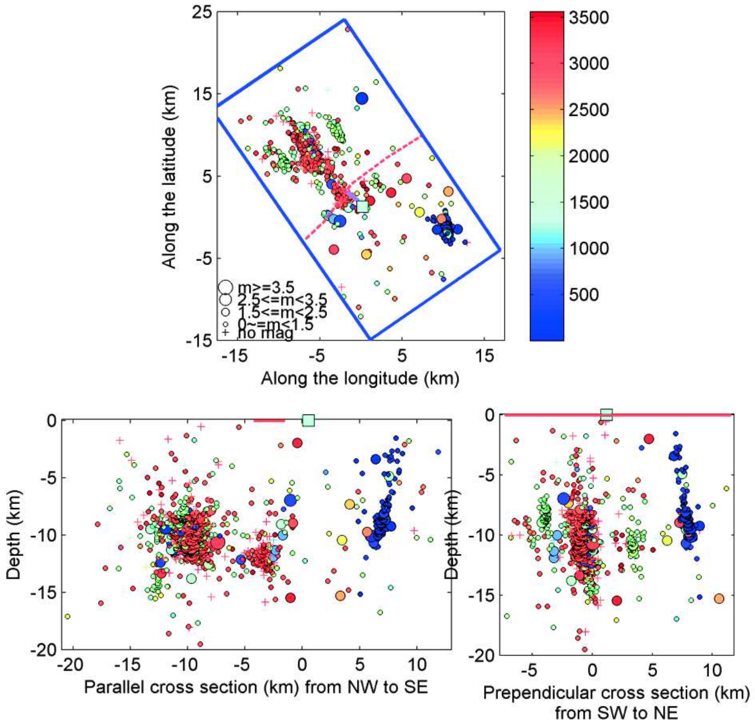

Figure A27: Localisation finale des séismes de la zone d'Emeelt via TomoDD. L'échelle de couleurs indique le nombre de jours depuis le 2005.01.01. En violet= zone des rupture de surface identifiées, carré bleu = tranchée, rouge = position de la faille Mésozoïque en surface.

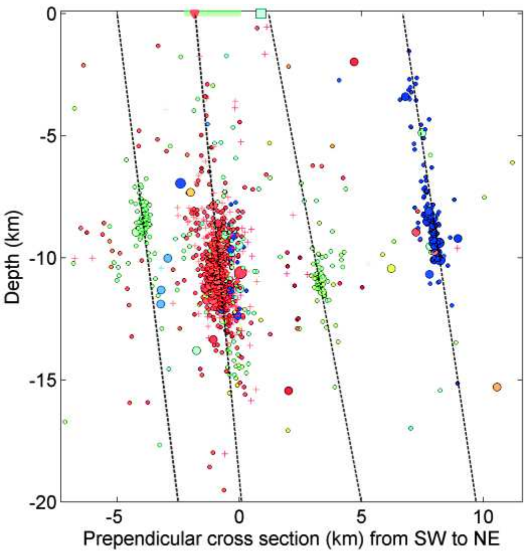

Figure A28.Coupe perpendiculaire à la faille d'Emeelt et extrapolation de la sismicité vers la surface. Carré vert = tranchée; ligne verte=position du profil sismique

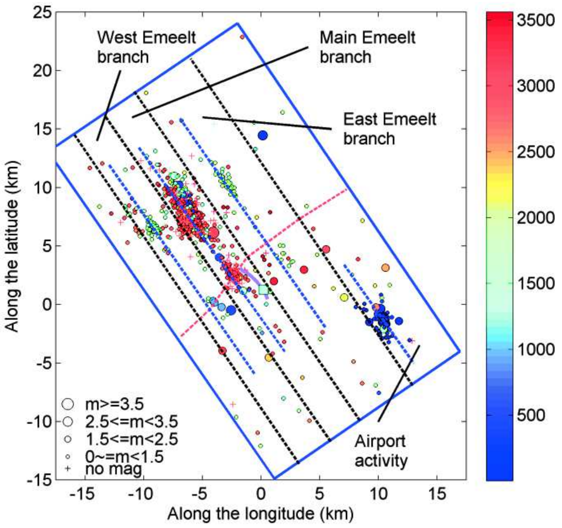

Figure A29. Localisation de la sismicité en cartographie, marquée en profondeur par les ligne bleues (environ 10km de profondeur) et leur extrapolation en surface en noir (cf. figure A28). L'échelle de couleurs indique le nombre de jours depuis le 2005.01.01.

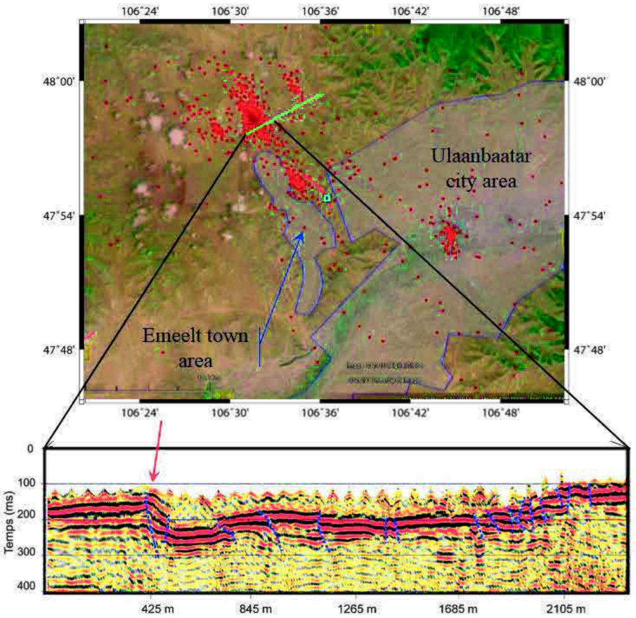

Figure A30: Profil sismique traité par Bolaty (2015). La flèche rouge indique la zone de déformation maximale et en bleu les ruptures identifiées.

Le nuage nord, partie la plus active sur les 3 branches, montre au cours des crises sismiques une organisation selon un pendage vers le NO de 55 à 60° (Figure A31). C'est une indication d'une faille perpendiculaire qui semble correspondre à une structure Mésozoïque orienté N60 (Figure A27) dans la prolongation Est de la faille de Khustai. L'activité serait donc concentrée à leur intersection. Les contrastes de vitesses Vp et les rapport Vp/Vs obtenus dans le modèle de vitesse 3D WAM suggèrent la présence de fluides dans les zones activées et d'une faille qui pourrait être la structure Mesozoïque (Figure A32).

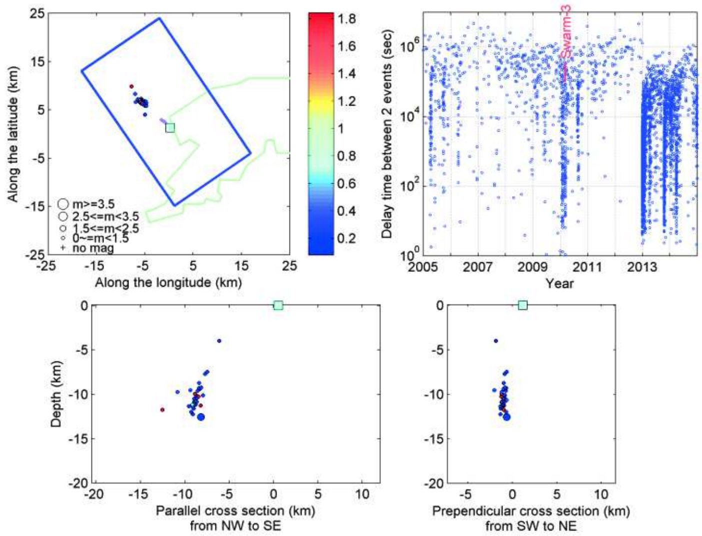

Figure A31: Exemple d'une crise sismique montrant le pendage vers le NO de la sismicité.

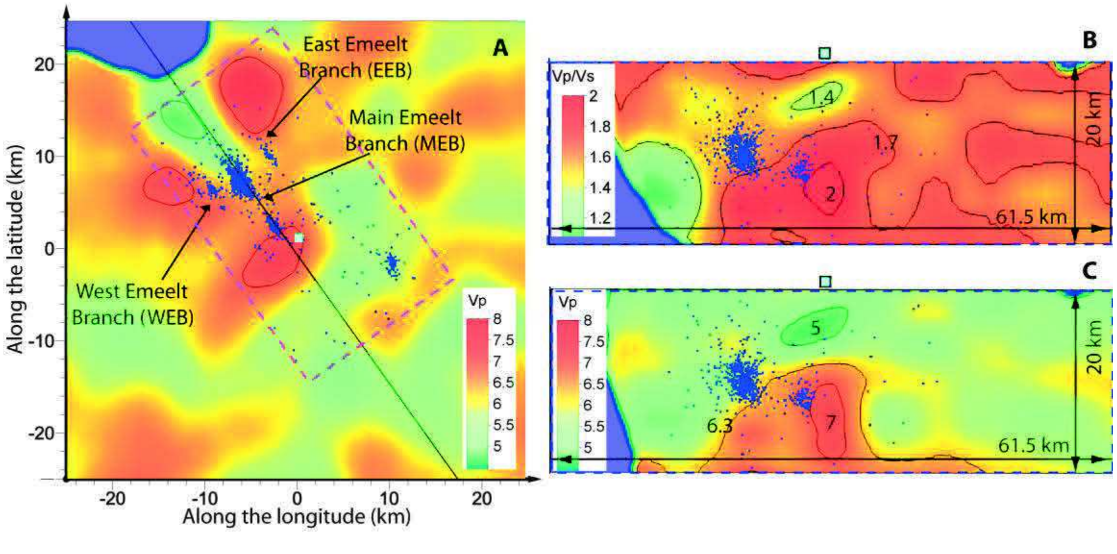

Figure A32: A) Coupe horizontale dans le modèle de vitesse 3D (Vp) à 12,5 km de profondeur. Les lignes sur la figure indiquent les coupes B et C. A droite, coupe verticale dans le modèle de vitesse 3D (Vp) parallèle à la faille (B) et perpendiculaire à la faille (C).

Dix crises sismique ont été identifiées entre 2005 et 2014, avec une activation en premier de la zone de l'aéroport, puis des trois branches et enfin de la branche principale (branche centrale) avec une crise très forte fin 2012 début 2013 qui a activé la plus grande surface de la faille parmi l'ensemble des crises, et ce jusqu'à 20 km en profondeur (Figure A33). L'activité sismique a augmenté régulièrement et le temps le plus court séparant deux séismes consécutif s'est réduit au fil du temps, de 1 minutes en 2005 jusqu'à 4 secondes dans les dernières crises. De même, la durée la plus longue entre deux séismes passe de 10 jours en 2005 à 0.5 jour en 2014. Le taux de sismicité varie sur la période mais aussi la valeur "b" de la GR montrant l'instabilité sismique. Des changements comparables ont été observés dans les années précédant une série de séismes ressentis sur une durée de 10 jours qui a précédé le séisme de l'Aquila en Italie (Avril 2009), Mw=6.3 (Papadopoulos et al., 2010) (Figure A34).

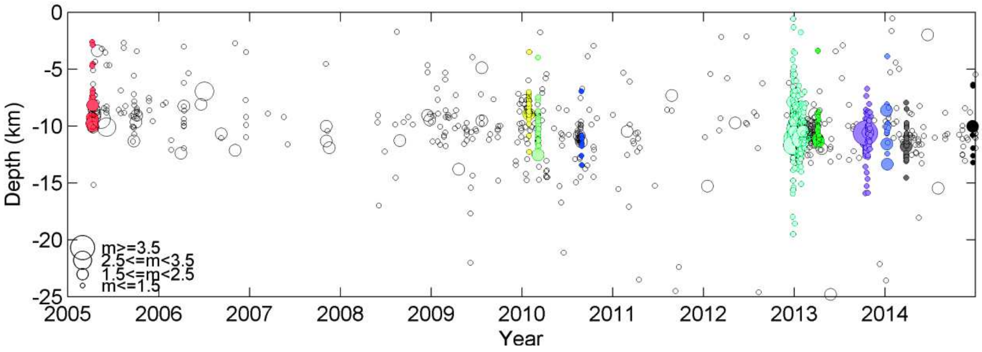

Figure A33. Diagramme espace temps en profondeur de la zone des failles d'Emeelt.

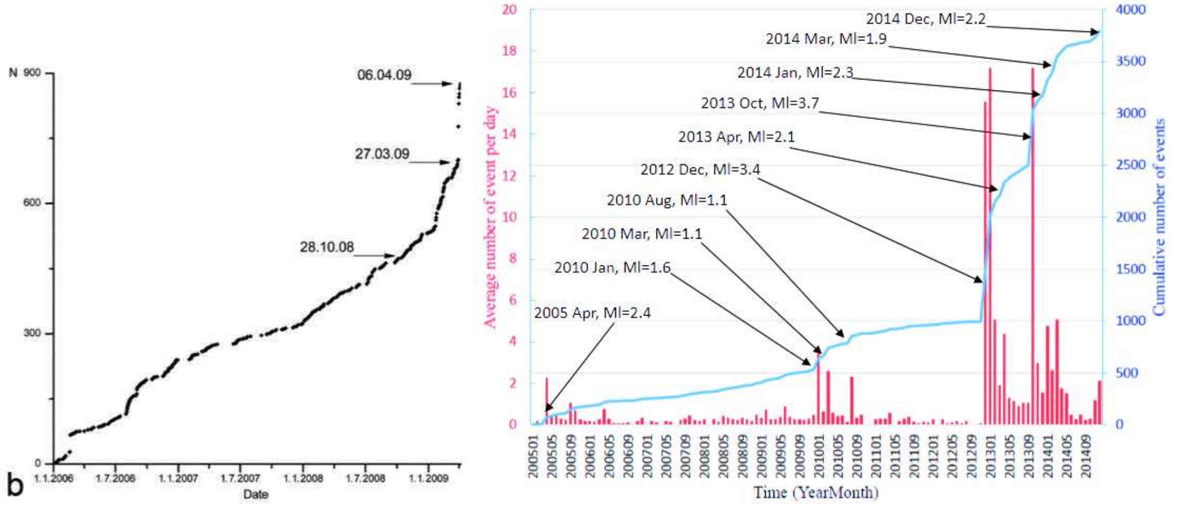

Figure A34: Nombre cumulatif de séismes avant le séisme de l'Aquila, Italie, Mw=6.3 (Papadopoulos et al., 2010, à gauche) et celui observé dans la zone d'Emeelt avec les plus forts séismes indiqués (à droite) .

En terme de magnitude potentielle, la longueur des ruptures de surface, de 4 à 5km, suggère une magnitude de 5.7 (d'après les relations de Wells et Coppersmith, 1994). En tenant compte de la longueur de 15 km de la sismicité observée sur les 3 branches principales d'Emeelt, la magnitude serait de 6.4 (Figure A35) et si l'on considère que le déplacement horizontal de 2m d'une paleo-rivière correspond au déplacement co-sismique d'un ou deux séismes, la magnitude serait d'environ 7.

L'impact sur Oulan Bator d'une magnitude 6.4 et 7 sur la faille d'Emeelt a été estimé en tenant compte d'une amplification due aux effets de site (Figure A36). Pour M=6.4, l'intensité minimale serait de VI avec localement une intensité de IX dans sa partie ouest, la plus proche de la faille, mais une grande partie de la zone urbaine d'Oulan Bator serait marquée par une intensité VIII. Pour une magnitude de 7, une large partie ouest de la ville subirait une intensité X mais surtout l'intensité minimale serait de VIII sur l'ensemble de la ville. Ces séismes auraient donc un impact majeur sur la ville et la population avec des effondrements de bâtiments vulnérables.

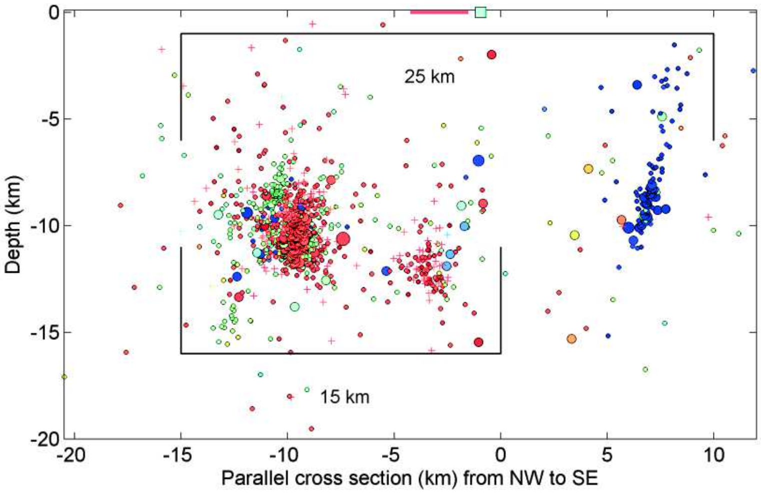

Figure A35. Coupe parallèle à la faille. Les crochets indiques les longueurs de la zone active en tenant compte des 3 branches (15km) et en intégrant la sismicité dans la zone de l'aéroport (25km).

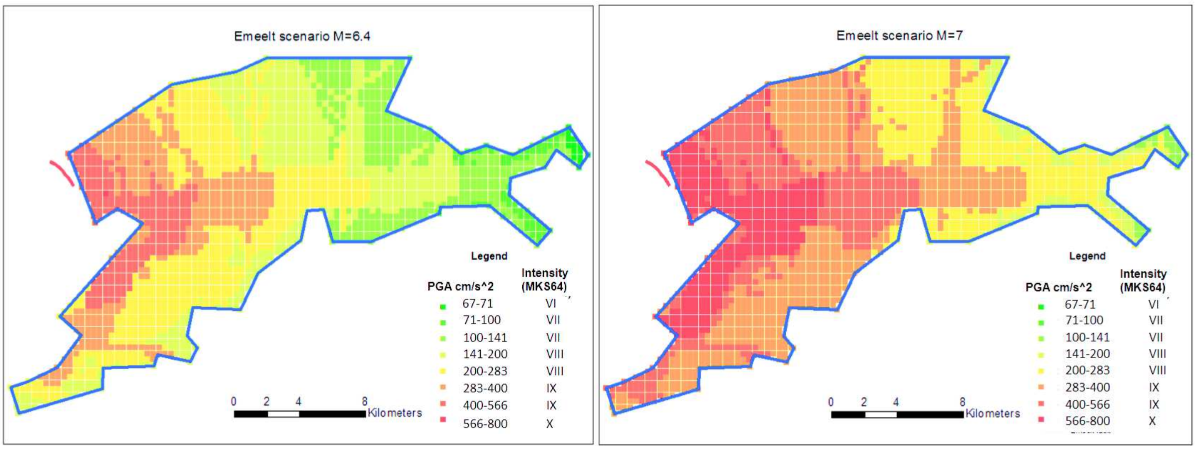

Figure A36. Calcul déterministe du PGA dans la capitale Oulan Bator pour un scenario de M=6.4 (gauche) et 7 (droite) sur la faille d'Emeelt.

7 References

Abrahamson N.A., and W. J. Silva., 1997. Empirical Response Spectral Attenuation Relations for Shallow Crustal Earthquakes. Seismological Research Letters, 68-1, 94-127.

Al Ashkar A., 2015. Tectonique active de la région d'Oulan Bator, Mongolie: Analyse morphotectonique et paléosismologique. Institute de Physique du Globe de Strasbourg, École et observatoire des sciences de la Terre, PhD Thesis, 249 pages.

Ambraseys, N., 1974. Notes on engineering seismology. in J. Solnes (ed.), Engineering Seismology and Earthquake Engineering, NATO Advanced study, 33-54.

Badarch G., Cunningham W.D., and Windley B.F., 2002. A new terrane subdivision for Mongolia: implications for the Phanerozoic crustal growth of Central Asia. Journal of Asian Earth Sciences, 21, 87-110.

Baljinnyam I., Bayasgalan A., Borisov B.A., Cisternas A., Dem'yanovich B.A., Ganbaatar L., Kochetkov V.M., Kurushin R.A., Molnar P., Philip P., and Vashchilov Y.Y., 1993. Ruptures of Major Earthquakes and Active Deformation in Mongolia and its Surroundings. The Geological Society of America, 181, 64.

Baljinnyam I., Munkhuu D., Tsembel B., Dugarmaa T., Adiya M., and Bayar G., 1975. Seismicity of Mongolia (in Mongolian language). Mongolian Academy of Sciences, B-55957, 461/74, 105 pages.

Bayasgalan A, 1999. Active tectonic of Mongolia. University of Cambridge, PhD Thesis, 182 pages.

Bayasgalan A., and J. A. Jackson, 1999. A re-assessment of the faulting in the 1967 Mogod earthquakes in Mongolia. Geophysical Journal International, 138, 784-800.

Barruol G., Deschamps A., Deverchere J., Mordvinova V., Ulziibat M., Perrot J., Ertemiev A., Dugarmaa T., and Bokelmann G.H.R., 2008. Upper mantle flow beneath and around the Hangay dome, Central Mongolia. Earth and Planetary Science Letters, 278, 221-233.

Bird P., 2003. An updated digital model of plate boundaries. Geochemistry Geophysics Geosystems, 4, 1027.

Bolaty J.-M., 2015. Retraitement de données de sismique réflexion dans le cadre d'une etude sismotectonique en Mongolie. Master thesis, 38 pages.

Boore D.M., William B. Joyner, and Thomas E. Fumal, 1997. Equations for Estimating Horizontal Response Spectra and Peak Acceleration from Western North American Earethquakes: A Summary of recent Work, Seismological Research Letters. 68-, 128-153.

Cai, H., Li, Y., Zheng, S., and Zheng, Q., 2007. Attenuation relations for acceleration peak and response spectrum of horizontal earthquake motion in Chongqing and its adjacent region. Earthquake Research in Sichan, 2-11-15. (In Chinese).

Calais E., and Amarjargal Sh., 2000. New constraints on current deformation in Asia from continuous GPS measurements at UlanBaatar, Mongolia. Geophysical Research Letters, 27, 1527-1531.

Calais E., Vergnolle M., Sankov V., Lukhnev A., Miroshnitchenko A., Amarjargal S., and Deverchere J., 2003. GPS measurements of crustal deformation in the Baikal–Mongolia area (1994–2002): implications for current kinematics of Asia. Geophysical Research Letters, 108, 2501-.

Calais E., Dong L., Wang M., Shen Z., and Vergnolle M., 2006. Continental deformation in Asia from a combined GPS solution. Geophysical Research Letters, 33, L24319.

Calo M., Dorbath C., Luzio D., Rotolo S., and D'Anne G., 2009. Local Earthquake Tomography in the Southern Tyrrhenian Region of Italy: Geophysical and Petrological Inferences on the Subducting Lithosphere. Frontiers in Earth Sciences, 276, 85-99.

Calo M., Parisi L., and Luzio D., 2013. Lithospheric P and S wave velocity models of the Sicilian area using WAM tomography. Geophysical Journal International, doi: 10.1093/gji/ggt252

Chandra U., 1979. Attenuation in the united states. Bulletin of the seismological Society of America, 69, 2003-2024.

Chery J., Carretier S., and Ritz J-F., 2001. Postseismic stress transfer explains time clustering large earthquakes in Mongolia. Earth and Planetary Science Letters, 194, 277-286.

Chen L., and Faccioli E., 2008. Ground motion attenuation relationships based on Chinese and Japanese strong ground motion data European school for advanced studies reduction of Seismic Risk, Rose University.

Chen M., Niu F., Liu Q., and Tromp J., 2015. Mantle-driven Uplift of Hangai Dome: New Seismic Constraints from Adjoint Tomography. doi: 10.1002/2015GL065018

Chimed O., 2011. Characterisation des effets de sites dans le basin d''OulanBator. University of Strasbourg, PhD Thesis, 152 pages.

Chimed O., and Team of IAG., 2014. Seismic Hazard Assessment for the proposed Combined Heat Power Plant-CHP 5. Report of IAG, Mongolia.

Choi J-H., Jin K., Enkhbayar D., Davaasambuu B., Bayasgalan A., and Kim Y-S., 2012. Rupture propagation inferred from damage patterns, slip distribution, and segmentation of the 1957 Mw 8.1 Gobi-Altai earthquake rupture along the Bogd fault, Mongolia. Journal of Geophysical Research, 117, B12401.

Cui J.W., Li S.C., Gao D, Zhao Y.Q., and Bao Y.F., 2006. Ground motion attenuation relations in the Yunnan area. Japanese Seismological Research 29(14), 386–391. (in Chinese with English abstract).

Cunningham, W.D., 2001, Cenozoic normal faulting and regional doming in the southern Hangay region, Central Mongolia: Implications for the origin of the Baikal rift province. Tectonophysics, 331, 389–411.

Cunningham, W.D., Davies S.J., and Badarch G., 2003. Crustal Architecture and Active Growth of the Sutai Range, Western Mongolia: A Major Intracontinental, Intraplate Restraining. Journal of Geodynamics,36,169-191.

Courboulex F., Larroque Ch., Deschamps A., Gelis G., Charreau J., and Stephan JF., 2003. An unknown active fault revealed by microseismicity in the south-east of France. Geophysical Research Letters, 30, NO. 15, 1782, doi:10.1029/2003GL017171

Dujardin J.R., Bano M., Schlupp A., Ferry M., Ulziibat M., Nyambayar Ts., and Bayarsaikhan E., 2014. GPR measurement to assess the Emeelt active fault's characteristics in a highly smooth topographic context, Mongolia., Geophysical Journal International, doi:10.1093/gji/ggu130.

Dobrynina A.A., Sankov V.A., Chechelnitsky V.V., and Deverchere J., 2016. Spatial changes of seismic attenuation and multiscale geological heterogeneity in the Baikal rift and surroundings from analysis of coda waves. Tectonophysics, 578, 50-68.

Dorbath C., J. Van der Woerd., Sergei S.A., Eugene A.R., and Janna Y.A., 2008. Geological and Seismological Field Observations in the Epicentral Region of the 27 September 2003 *M*w 7.2

Gorny Altay Earthquake (Russia). Bulletin of the Seismological Society of America, 2008, 98, 2849-2865, doi:10.1785/0120080166.

Eenjin G., Tomurtogoo O., Odgerel D., Erdenejargal Ch., and Buyanjargal Kh., 2009. Universal geological structure around Ulaanbaatar. Research report of the Institute of Geology and Mineralogy of MAS (in Mongolian).

Eberhart-Phillips, D., 1990. Three-dimensional P and S velocity structure in the Coalinga region, California. Journal of Geophysical Research, 95, 15343-15363, doi:10.1029/90JB01292.

Ferry M., Schlupp A., Munkhuur U., Munschy M., Fleury S., Baatarsuren G., Erdenezula D., Munkhsaikhan A., and Ankhtsetseg D., 2010. Tectonic Morphology of the Hustai Fault (Northern Mongolia), A Source of Seismic Hazard for the city of Ulaanbaatar. EGU General Assembly, Vienna, Austria.

Ferry M., Schlupp A., Munkhuu U., Munschy M., and Fleury S., 2012. Tectonic Morphology of the Hustai Fault (Northern Mongolia). EGU General Assembly, Vienna, Austria.

Fisher T., Horalek J., Hrubcova P., Vavrycuk V., Brauer K., and Kampf H., 2014. Intra-continental earthquake swarms in West-Bohemia and Vogtland: A review. Tectonophysics 611, 1-27.

Fleury S., Munschy M., Schlupp A., Ferry M., Bano M., and Munkhuu U., 2012. High resolution magnetic survey to study Hustay Fault (northern Mongolia). AGU Fall Meeting, San Francisco, California, USA.

Fleury S., Munschy M., Schlupp A., Ferry M., and Munkhuu U., 2012. High resolution magnetic survey across the Emeelt and Hustai faults near Ulaanbaatar, Mongolia.GEU General Assembly, Vienna, Austria.

Florensov N.A., Solonenko V.P., 1963. The Gobi-Altai earthquake. Akademie Nauk, Moscow, 424. (English translation, U.S Department, Washington D.C, 1965).

Fukushima Y., Berge-Thierry C., Volant Ph., Griot-Pomera D.A. and Cotton F, 2003. Attenuation relation for west Eurasia determined with recent near-fault records from California, Japan and Turkey, Journal of Earthquake Engineering, 7-4, 573-598.

Gangaadorj B., Munkhuu U., Davaasuren G., Danzansan E., Daram M., Tsembel B., Majig A., Lodon S., Melnikova V., Radziminovich Ya., 2011. Map of focal mechanisms of earthquakes in Mongolia. Research Centre of Astronomy & Geophysics of the Mongolian Academy of Sciences (RCAG), Mongolia.

Gutenberg B., and Richter C.F., 1944. Frequency Earthquakes in California. Bulletin of the Seismological Society of America, 34, 1985-1988.

He J., Wu Q.J., Gao M.T., Zhang R.Q., Yu D.X., Ulziibat., and Demberel S., 2014. Crustal structure and poisson ratio beneath the central and southern Mongolia derived from receiver functions. Chinese journal of Geophysics, 57(7), 2386-2394.

Hu Y., 1982. Inverse analysis of structural vibration. In Collected Papers on Earthquake Engineering, Science Press. 79-025,179.

Hunt A.C., Parkinson I.J., Harris B.W., Rogers N.W., and Yondon M., 2012. Cenozoic Volcanism on Hangai Dome, Central Mongolia: Geochemical Evidence for Changing Melt Source and Implications for Mechanisms of Melting. Journal of Petrology, 202, 1-30.

Huo, J. and Hu, Y., 1992, Study on attenuation laws of ground motion parameters. Earthquake Engineering and Engineering Vibration. 12.2, 1-11.

Jeanne L.H., Andrew J.M., and Thomas M.B., 2007. Seismic velocity structure and seismotectonics of the eastern San Francisco Bay region, California. Bulletin of the Seismological Society of America, 97, 826-842.

Jenatton L., Guiguet R., Thouvenot F., and Daix N., 2007. The 16000 event 2003-2004 earthquake swarm in Ubaye (French Alps). Journal of Geophysical Research, 112, B11304.

Jo Eunyoung and Hong T-K., 2013. Vp/Vs ratios in the upper crust of the southern Korean Peninsula and their correlations with seismic and geophysical properties. Journal of Asian Earth Sciences, 66, 204-214.

Khilko S.D., Kurushin R.A., Kochetkov V.M., Misharina L.A., Melnikova V.I., Gilyova N.A., Lastochkin S.V., Baljinnyam I., and Monhoo D., 1985. Earthquakes and the base of the seismic zoning of Mongolia. Vol. 41 of The joint Soviet-Mongolian scientific - Reasearch Geological Expedition. 225 pages.

Kissling E., 1978. Hypocenter location program Hypoinverse. Users Guide to versions 1,2,3 and 4, U.S Geological Survey, open file report, 78/694.

Kissling E., 1988. Geotomography with local earthquake data. Rev Geophysics, 26, 659-698.

Kissling E., Ellworth W.L., Eberhart-Phillips D., and Kradolfer U., 1994. Initial reference models in local earthquake tomography. Journal of Geophysical Research, 99, 19635-19646.

Kissling E., 1995. VELEST, User's Guide. International report 26, Institute of Geophysics, ETH Zurich, Switzerland.

Klinger Y., Etchebes M., Tapponnier P., and Narteau C., 2011. Characteristic slip for five great earthquakes along the Fuyun fault in China. Nature Geoscience, 4, 389-392.

Kröner A., Windley B.F., Badarch G., Tomurtogoo O., Hegner E., Jahn B.M., Gruschka S., Khain E.V., Demoux A., and Wingate M.T.D., 2007. Accretionary growth and crust formation in the Central Asian Orogenic Belt and comparison with the Arabian-Nubian shield. Geological Society of America, 200, 181-209.

Kurihara T., Tsukada K., Otoh S., Kashiwagi K., Minjin Ch., Dorjsuren B., Bujinlkham B., Sersmaa G., Manchuk N., Niwa M., Tokiwa T., Hikichi G., and Kozuka T., 2009. Upper Silurian and Devonian pelagic deep-water radiolarian chert from the Khangai-Khentei belt of Central Mongolia: Evidence for Middle Paleozoic subduction-accretion activity in the Central Asia Orogenic Belt. Journal of Asian Earth Sciences, 34, 209-225.

Lindenfeld M., Rumpker G., Link K., Koehn D., and Batte A., 2012. Fluid-triggered earthquake swarms in the Rwenzoni region, East African Rift-Evidence for rift initiation. Tectonophysics, 566-567, 95-104.

Leclere H., Daniel G., Fabbri O., Cappa F and Thouvenot F., 2013. Tracking fluid pressure buildup from focal mechanisms during the 2003-2004 Ubaye seismic swarm, France. Journal of geophysical research, 118, 4461-4476.

Majig A., Dorjsuren A., Tsagaan B., Gangaadorj B., Chimedtseren B., Danzansan E., Dashdondog M., Adiya M., Daram M., Rentsen N., Chimed O., Lodon S., Tsembel B., Munkhuu U., Khukhuudei U. and with DASE/LDG team., 2003. Map of "ONE CENTURY OF SEISMICITY IN MONGOLIA (1900 - 2000)". Coordinators : Dugarmaa T., and Schlupp A. Research Centre of Astronomy & Geophysics of the Mongolian Academy of Sciences (RCAG), Mongolia and Laboratoire de Télédétection et Risque Sismique, BP12, Bruyиres le Chatel, France.

Minjin Ch., Tomurtogoo O., and Dorjsuren B., 2006. Devonian-Carboniferous accretionary complex of the Ulaanbaatar terrane. (Second International Workshop and Field Excursions for IGC Project 480), abstract and excursion guidebook, 100-106.

Moretti M., Gori D.P., and Chiarabba C., 2009. Earthquake relocation and three dimentional Vp and Vp/Vs models along the low angle Alto Tiberina fault (Central Italy): evidence for fluid overpressure. Geophysical Journal International, 176, 833-846.

Mogi K., 1963. Some discussion of aftershocks, foreshocks and earthquake swarms - the fracture of a semi-infinite body caused by an inner stress origin and its relation to earthquake phenomena. Bulletin of the Earthquake Research Institute, 41, 625-658.

Mordvinova V.V., Zorin Y.A., Gao S., and Davis P.M., 1996. Thickness of crust along the Irkutsk-Ulan-Bator-Undurshil profile from spectral ratios of body seismic waves. Physics of solid earth, 31-9, 727-234.

Mordvinova V.V., Deschamps A., Dugarmaa T., Deverchere J., Ulziibat M., Sankov V.A., Artemiev A.A., and Perrot J., 2007. Velocity structure of the lithosphere on the 2003 Mongolian-Baikal transect from SV waves. Izvestiya Phys. Solid Earth, 43-2, 119-129, ISSN 1069-3513.

Muksin U., Bauer K., and Haberland C, 2013. Seismic Vp and Vp/Vs structure of the geothermal area around Tarutung (North Sumatra, Indonesia) derived from local earthquake tomography. Journal of Volcanology and Geothermal Research, 26,0, 27-42.

Mungunsuren D., 2007. Estimating Magnitude of local earthquakes from signal duration, Ulaanbaatar State University, Mongolia, Master thesis, 57 pages.

Munkhuu U., 2006. The 2003 Chuya sequence (North Altay range): tectonic context and seismological study. University of Nice Sophia Antipolis, PhD Thesis, 200 pages.

Munkhuu U., Adiya M., Batkhuu B., Sèbe O., Schlupp A., Usnikh S., Sodnomsambuu D., 2010. The Emeelt active fault, revealed by the outbreak of micro seismicity, and its impact on the PSHA of Ulaanbaatar, capital of Mongolia. Part II: Time and spatial behavior of the regional seismicity. ESC General Assembly, Montpellier, France.

Nakamichi H., Watanabe H., and Ohminato T., 2007. Three-dimentional velocity structures of Mount Fuji and the South Fossa Magna, central Japan. Journal of geophysical research, 112, B03310.

Natsag-Yum I., Balzhinnyam J and Monkho D., 1971. Earthquake in Mongolia, in Seismic Regionalization of Ulan-Bator. Nauk, Moscow, 54-82.

Nishimura T., and Horike M., 2003. The Attenuation Relationships of Peak Ground Accelerations for the Horizontal and the Vertical Components Inferred from Kyoshin Network Data, Journal of Struct. Construct. Eng. (Transactions of AIJ), 571, 63-70 (in Japanese).

Nugraha A.D., Ohmi S., Mori J., and Shibutani T., 2013. High resolution seismic velocity structure around the Yamasaki fault zone of southwest Japan as revealed from travel time tomography. Earth planets space, 65, 871-881.

Papadopoulos A.G., Charalampakis M., Fokaefs A., and Minadakis G., 2010. Strong foreshock signal preceding the L'Aquila (Italy) earthquake (Mw6.3) of 6 April 2009. Natural hazard and earth system sciences, 10, 19-24.

Pei Sh., Su J., Zhang H., Sun Y., Nafi Toksoz M., Wang Z, Gao X Liu-Zeng J., and He J., 2010. Three dimentional seismic velocity structure across the 2008 wenchuan Ms8.0 earthquake, Sichuan, China. Tectonophysics, 491, 211-217.

Peng K.Z., Wu F.T., and Song, L.1985. Attenuation characteristics of peak horizontal acceleration in north east and southwest China. Earthquake Engineering and Structural Dynamics. 13(3), 337-350.

Petit C., and Fournier M., 2005. Present-day velocity and stress fields of the Amurian plate from thin-shell finite-element modelling. Geophysical Journal International, 160, 357-369.

Petit C., Tiberi C., Deschamps A., and Déverchère J., 2008. Teleseismic traveltimes, topography and lithospheric structure across central Mongolia. Geopgysical Research Letters, 35, doi:10.1029/2008GL033933.

Plastino W., Povinec P.P., De Luca G., Doglioni C., Nisi S., Ioannucci L., Balata M., Laubenstein M., Bella F., and Coccia E., 2010. Uranium groundwater anomalies and L'Aquila earthquake, 6th April 2009 (Italy). Journal of Environmental Radioactivity, 101, 45-50.

Potter S.H., Becker J.S., Johnston D.M., and Rossiter K.P., 2015. An overview of the impact of the 2010-2011 Canterbury earthquakes. International Journal of Disaster Risk Reduction. 14, 6-14.

Pujol J., 2011. Tomography, Seismic (Chapter 50 of the "Extreme environmental events: Complexity in forecasting and early warning"). Springer, 928-966.

Radziminovich N.A., Gileva N.A., Melnikova V.I., and Ochkovskaya M.G., 2013. Seismicity of the Baikal rift system from regional network observations. Journal of Asian Earth Sciences, 62, 146-161.

Radziminovich N.A., Bayar G., Miroshnichenko A.I., Demberel S., Ulziibat M., Ganzorig D.,and Lukhnev A.V., 2016. Focal mechanisms of earthquakes and stress field of the crust in Mongolia and its surroundings. Geodynamics & Tectonophysics, 7, 23-38.

Rautian T.G., 1964. On the estimation of earthquake energy at distances up to 3000 km. Trudi, IFZ.AN.SSSRn32, 88-93, Moscow.

Rinaldis D., Berardi R., Theodulidis N., and Margaris B., 1998. Empirical predictive models based on a joint Italian & Greak strong-motion database: I, Peak ground acceleration and velocity. in Proc of the Eleventh European Conf. on Earthquake Engineering, Paris, France, 6–11 September.

Richon, P., Heritier, T., Sebe, O., Maffat, I., Holtzappfel, T., Le Hesran, E., Geber, O., Ulziibat, M., Demberel, S., Oyun-Erdene, M., & Bilguun, M. (2015). Is radon 222 an appropriate tracer for the study of seismic precursors?. Chocs Focus, (4), 32-33.

Ritz, J.-F., Bourlès, D., Brown, E.T., Carretier, S., Chery, J., Enhtuvushin, B., Galsan, P., Finkel, R.C., Hanks, T.C., Kendrick, K.J., Philip, H., Raisbeck, G., Schlupp, A., Schwartz, D.P., and Yiou, F., 2003. Late Pleistocene to Holocene slip rates for the Gurvan Bulag thrust fault (Gobi-Altay, Mongolia) estimated with Be10 dates. Journal of Geophysical Research, 108, 2162.

Ritz J-F., Vassallo R., Braucher R., Brown E.T., Carretier S., and Bourles D.L., 2006. Using in situ–produced 10Be to quantify active tectonics in the Gurvan Bogd mountain range (Gobi-Altay, Mongolia). Geological Society of America, 415, 87-110.

Rizza M., Ritz J-F., Braucher R., Vasallo R., Prentice C., Mahan S., Mc Gill S., Chauvet A., Marco S., Todbileg M., Demberel S., Bourles D., 2011. Slip rate and slip magnitudes of past earthquakes along the Bogd left-lateral strike-slip fault (Mongolia), Geophysical Journal International, 186, 897-927.

Rizza M., Ritz J-F., Prentice C., Vassallo R., Braucher R., Larroque C., Arzhannikova S., Arzhannikov S., Mahan S., Massault M.., Michelot J-L., Todbileg M., and ASTER Team, 2015.

Erathquake Geology pf the Bulnai fault (Mongolia). Bulletin of the Seismological Society of America, 105, 72-93.

San'kov, V., Déverchère, J., Gaudemer, Y., Houdry, F., Filippov, A., 2000. Geometry and rate of faulting in the North Baikal rift, Siberia. Tectonics, 19, 707-722.

Sankov V.A., Lukhnev A.V., Miroshnitchenko A.I., Dobrynina A.A., Ashurkov S.V., Byzov L.M., Dembelov M.G., Galais E., and Déverchère J., 2014. Contemporary Horizontal Movements and Seismicity of the South Baikal Basin (Baikal Rift System). Physics of the Solid Earth, 50, 785–794.

Schlupp A., 1996. Neotectonic of western Mongolia using field, seismological and remote sensing data. Laboratoire de Sismologie et de Physique de la Terre, Ecole et Observatoire de Physique du Globe de Strasbourg- Université Louis Pasteur de Strasbourg, PhD Thesis, 270 pages.

Schlupp A., 2007. Seismic hazard assessment in Mongolia and at Ulaanbaatar. The Asian Science and Technology Seminar on Seismic Disaster Mitigation in Mongolia. March 6-8, Ulaanbaatar, Mongolia.

Schlupp A., Ferry M., Munkhuu U., Munschy M., Fleury S., 2010. Tectonic Morphology of the Hustai Fault (Northern Mongolia): Implications for Regional Geodynamics. AGU Fall Meeting, San Francisco, USA.

Schlupp A., Ferry M., Munkhuu U., Munschy M., Fleury, S., Adiya M., Bano M., and Baatarsuren G., 2010. The Emeelt active fault, revealed by the outbreak of microseismicity, and its impact on the PSHA of Ulaanbaatar, capital of Mongolia. Part I: seismotectonic analysis. ESC General Assembly, Montpellier, France.

Schlupp A., Ferry M., Ulziibat M., Baatarsuren G., Munkhsaikhan A., Bano M., Dujardin J-M., Nyambayar Ts., Sarantsetseg L., Munschy M., Fleury S., Mungunshagai M., Tserendug Sh., Nasan-Ochir T., Erdenezul D., Bayarsaikhan E., batsaikhan Ts., and Demberel S., 2012. Investigation of active faults near Ulaanbaatar, Implication for seismic hazard assessment. ASC General Assembly-2012, Ulaanbaatar, Mongolia.

Schlupp A., Ferry M., Munkhuu U., Sodnomsambuu D., Fleury S., and l-Ashkar A., 2013. Active faults system and related potential seismic events near Ulaanbaatar, capital of Mongolia. ESC General Assembly, Vienna, Austria.

Schlupp A., and Cisternas A., 2007. Source history of the 1905 great Mongolian earthquakes (Tsetserleg, Bolnay). Geophisical Journal International, 169, 1115-1131.

Si H., and Midorikawa S., 1999. Attenuation Relations for Peak Ground Acceleration and Velocity Considering Effects of Fault Type and Site Condition, Journal of Struct. Construct. Eng. (Transactions of AIJ), No. 523, 63-70 (in Japanese).

Sodnomsambuu D., Schlupp A., and Munkhuu U., 2014. A century of aftershocks related to large intracontinental earthquakes: A seismic behavior for hazard assessment. AGU Fall Meeting, San Francisco, USA.

Souriau A., 2006. Quantifying felt events: A joint analysis of intensities, accelerations and dominant frequencies. Journal of Seismology, 10, p23-38, doi:10.1007/s10950-006-2843-1.

Spudich P., Joyner W.B., Lindh A.G., Boore D.M., Margaris B.M., and Fletcher J.B., 1999. A Revised Ground Motion Prediction Relation for Use in Extensional Tectonic Regimes, Bulletin Seismological Society America. 89-5, 1156-1170.

Takahashi T., Kobayashi S., Fukushima Y, Zhao J.X, Nakamura H., and Somerville P.G., 2000. A Spectral Attenuation Model for Japan using Strong Ground Motion Data Base, Proceedings of 6th International Conference on Seismic Zonation, CD-ROM.

Takeuchi M., Tsukada K., Suzuki T., Nakane Y., Sersmaa G., Manchuk N., Kondo T., Matsuzawa N., Bacht N., Khishigsuren S., Onon G., Katsurada Y., Hashimoto M., Yamasaki S., Matsumoto A., Oyu-Erdene B., Bulgantsetseg M., Kundyz S., Enkhchimeg L., Ganzorig R., Myagmarsuren G., Jamiyandagva O., Molomjamts M., 2012. Stratigraphy and geological structure of the Paleozoic system around Ulaanbaatar, Mongolia. Bulletine of the Nagoya University Museum, 28, 1-18.

Tapponnier P., and Molnar P, 1979. Active faulting and Cenozoic tectonics on the Tien Shan, Mongolia and Baikal regions. Journal of Geophysical Research, 84, 3425-3459.

Tapponnier P., Peltzer G., Le Dain A.Y., Armijo R., and Cobbold P., 1982. Propagating extrusion tectonics in Asia: New insights from sim-ple experiments with plasticine. Geology, 10, 611–616.

Tomurtogoo O., Byamba J., Badarch G., Minjin Ch., Orolmaa D., Khosbayar P., and Chuluun D., 1998. Geologic map of Mongolia. Scale 1:1000000 and summary, Mineral Resources Authority of Mongolia, Ulaanbaatar.

Tomurtogoo O., 2009. Tectonic and Geological map of Ulaanbaatar, Scale 1:500,000. (in Mongolian).

Tectonic map of Mongolia, scale 1:1000000., 2002. Institute of Geology and Mineral Resources of MAS, Mongolia..

Thurber, C.H., 1993. Local earthquake tomography: velocities and Vp/Vs-theory, in H. M. Iyer & K. Hirahara, ed., 'Seismic Tomography: Theory and practice', Chapman and Hall, London, 563-583.

Tiberi C., Deschamps A., Devegchere J., Petit C., Perrot J., Appriou D., Mordvinova V.V., Dugarmaa T., Ulziibat M. and Artemiev A.A., 2008. Asthenospheric imprints on the lithosphere in Central Mongolia and southern Siberia from a joint inversion of gravity and seismology (MOBAL experiment). Geophysical Journal International.

Tomomi O., Tadashi Y., Norihito U., Toru M., Akira H., Haijiang Z., and Clifford H.T., 2006. Detailed imaging of the fault planes of the 2004 Niigata-Chuetsu, central japan, earthquake sequence by double-difference tomography. Earth and Planetary Science Letters, 244,1-2, 32-43.

Vassallo R., Jolivet M., Ritz J-F., Braucher R., Larroque C., Sue C., Todbileg M., Javkhanbold D., and Bourlès D. L., 2007. Uplift age and rates of the Gurvan Bogd system (Gobi-Altay) by apatite fission tracks analysis, EPSL, 259, 333–346.

Vergnolle M., Pollitz F., and Calais E., 2003. Constraints on the viscosity of the continental crust and mantle from GPS measurements and postseismic deformation models in western Mongolia. Journal of Geophysical Research, 108, B10, 2502, doi:10.1029/2002JB002374.

Wadati K., 1933. On the travel time of earthquake waves. Part II, Geophysical Magazine, 7, 101-111.

Waite GP., and Smith R.B., 2002. Seismic evidence for fluid migration accompanying subsidence of the Yellowstone caldera. Journal of Geophysical Research, 107,2177

Waldhauser F and Ellsworth W.L., 2000. Double-Difference Earthquake Locations Algorithm: Method and Application to the Northern Hayward fault, California. Bulletin of the seismological Society of America, 90-6, 1353-1368.

Waldhauser, F., 2001. HypoDD: A computer program to compute double-difference earthquake locations. UGSG open file report, 01-113.

Walker R.T., Nissen E., Molor E., and Bayasgalan A., 2007. Reinterpretation of the active faulting central Mongolia. Geology, 759-762.

Walker R.T., Molor E., Fox M., and Bayasgalan A., 2008. Active tectonics of an apparently aseismic region: distributed active strike-slip faulting in the Hangay Mountains of central Mongolia. Geophisical Journal International, 174, 1121-1137.

Webb L.E and Johnson C.L., 2006. Tertiary strike-slip faulting in southeastern Mongolia and implications for Asian tectonics. Earth and planetary Science letters, 241, 323-335.

Wei D and Seno T., 1998. Determination of the Amurian plate motion in Mantle Dynamics and Plate Interaction in East Asia. 337-346.

Wells, D.L., and Coppersmith, K.J., 1994. New empirical relationships among magnitude, rupture length, rupture width, rupture area and surface displacement. Bulletin of the Seismological Society of America, 84, 974-1002.

Yin A., Rumelhart, P., Butler, R., Cowgill, E., Harrison, T., Foster, D., Ingersoll, R., Qing, Z., Xian-Qiang, Z., and Xiao-Feng, W., 2002, Tectonic history of the Altyn Tagh fault system in northern Tibet inferred from Cenozoic sedimentation: Geological Society of America Bulletin, 114, 1257-1295.

Zhang, H., and Thurber, C.H., 2003. Double-difference tomography: method and application to the Hayward fault, California. Bulletin of the Seismological Society of America, 93, 1875-1889.

Zorin Yu.A., 1993. The South Siberia – Central Mongolia transect. Tectonophysics, 225, 361-378.

Zorin Yu.A., Belichenko B.G., Turutanov E.K, Turutanov Y.K., Mordvinova V.V., Kozhenikov V.M., Khosbayar P., Tomurtogoo O., Arvisbaatar N., Gao S.S. and Davis P., 1994. Baikal-Mongolia transect. Russian Geology and Geophysics, 35, 78-92.

Zorin Yu.A., Mordvinova V.V., Turutanov E.Kh., Belichenko B.G., Artemyev A.A., Kosarev G.L. and Gao S.S., 2002. Low seismic velocity layers in the Earth's crust beneath Eastern Siberia (Russia) and Central Mongolia: receiver function data and their possible geological implication. Tectonophysics, 359, 3-4, 307-327.

Zelt C. A., 1998. Lateral velocity resolution from three-dimensional seismic refraction data. Geophysical Journal International, 135, 1101-1112.

8 List of figures

9 List of tables

Munkhsaikhan ADIYA

Activité sismique de la région d'Oulan Bator:
Implication pour l'évaluation de l'aléa sismique

Résumé

Mots clés : Mongolie, Oulan-Bator, aléa sismique, essaim, modèle de vitesse, tomographie double différence, faille d'Emeelt,

On observe depuis 2005 une sismicité intense à 10 km d'Oulan Bator ce qui a permis d'identifier une faille active, Emeelt, sur le terrain.

Après le calcule d'un modèle de vitesse 3D, j'ai appliqué la tomographie double différence pour obtenir une localisation précise des séismes. Ils marquent au moins trois branches parallèles orientées N147° comme la faille vue en surface. L'activité sur la faille principale d'Emeelt (MEF) s'étend sur 15 km, les branches Ouest et Est, moins actives, sur 10 km. La profondeur de l'activité s'étend entre 4 et 15 km. L'activité sismique semble concentrée à l'intersection avec des failles Mésozoïques et les contrastes Vs/Vs suggèrent la présence de fluides. Les 10 essaims identifiés montrent une activité croissante et une migration spatiale avec le temps.

Le calcul de 2 scénarios possibles, un M ~ 6.4 et un M ~ 7, indique un important impact sur la ville d'Oulan Bator, avec une intensité minimum de VIII et localement IX pour M=6.4 et X pour M=7.

Résumé en anglais

Key words: Mongolia, Ulaanbaatar, seismic hazard, swarm, velocity model, Double-Difference tomography, Emeelt fault.

We observe since 2005 a high seismic activity at 10 km from Ulaanbaatar that allowed us to identify a new active fault, Emeelt, on the field.

After computing a 3D velocity model, I applied Double-Difference tomography to obtain a precise localization of earthquakes. They trace at least three parallel branches oriented N147^0 like the fault seen at surface. The seismic activity on the Main Emeelt Fault (MEF) is along at least 15 km, on the West and East branches, less active, along 10 km. The depth of the seismicity extends between 4 and 15 km. The activity seems concentrated at the intersection with Mesozoic faults and Vp/Vs contrast suggests the presence of fluids. The 10 swarms identified show an increasing activity and a spatial migration with time.

The calculation of 2 possible scenarios, one M ~ 6.4 and one M ~ 7, shows an important impact on Ulaanbaatar, with a minimum intensity of VIII and IX for M=6.4 and X for M=7.